UNIVERSITÀ
DEGLI STUDI
DI PADOVA

Head Office: Università degli Studi di Padova

Department of Physics and Astronomy

Ph.D. COURSE IN: Physics
SERIES: 36th

Multicomponent Superfluidity and Josephson Dynamics in Ultracold Atomic Systems

Thesis written with the financial contribution of Fondazione Cassa di Risparmio di Padova e Rovigo

Coordinator: Prof. Giulio Monaco
Supervisor: Prof. Luca Salasnich

Ph.D. student : Koichiro Furutani

Università degli Studi di Padova

Dipartimento di Fisica e Astronomia "Galileo Galilei"

Ph.D. Thesis in Physics

Multicomponent Superfluidity and Josephson Dynamics in Ultracold Atomic Systems

Supervisor
Prof. Luca Salasnich

Ph.D. Candidate
Koichiro Furutani

Academic Year
2022/2023

Abstract

Multicomponent superfluidity exhibits fruitful physics in contrast to single-component superfluids. In a binary superfluid with two different hyperfine states, the vorticity is modified from the single-component case and the circulation is no longer quantized, which affects thermodynamics and phase transitions. Josephson junctions prepared by trapping superfluids in a double-well potential are a platform to investigate the dynamics of multicomponent superfluids. Several experiments of Bose Josephson junctions or superconducting Josephson circuits enable us to clarify the quantum effects on the relaxation dynamics. In this Thesis, we analyzed quantum effects on multicomponent superfluidity from the viewpoints of phase transitions in a binary Bose superfluid and the dynamics in Josephson junctions.

In Chap. 1, we start with an introduction to superfluidity and ultracold atomic physics. We present comprehensive ideas on why we focus on ultracold atoms and their advantages. Then, we conclude the introduction by presenting the motivation and outline of this Thesis.

In Chap. 2, we present the fundamental overview of quantum fluids including the occurrence of Bose-Einstein condensation, superfluid hydrodynamics, quantized vortices, and Berezinskii-Kosterlitz-Thouless transitions, which are the basis of the discussions in the following chapters.

In Chap. 3, we provide analyses of sound velocities in a single-component collisional Bose superfluid in D-dimension. Including the beyond-mean-field correction, we discuss the quasicrossing behavior of the first and second sound velocities in collisional Bose superfluids.

In Chap. 4, we discuss Berezinskii-Kosterlitz-Thouless transitions in a Rabi-coupled binary Bose superfluid in two dimensions. Starting from the miscibility condition and vortex excitations, which are distinct from a single-component superfluid, we discuss the Berezinskii-Kosterlitz-Thouless transition in the binary Bose superfluid. Since it is a phase transition originating from vortex excitations, the different vortex excitations peculiar to multicomponent superfluids play a crucial role. We give the comprehensive behaviors of the superfluid density, superfluid transition temperature, and sound modes. In particular, the sound modes show significantly different behavior from the single-component case analyzed in Chap. 3, and we propose experimental verification of our result based on the sound velocities.

In Chap. 5, we discuss quantum effects on the dynamics in multicomponent superflu-

ids focusing on Josephson junctions. We reveal that a Bose Josephson junction can be mapped to a Caldeira-Leggett-type model and it exhibits damped Langevin dynamics. Such a damped Langevin dynamics can be also observed in a superconducting Josephson circuit. However, due to the different types of coupling between the Josephson mode and bath modes, the correlation functions exhibit different relaxation dynamics. We clarify the effects of quantum fluctuations on the correlation functions. Finally, we conclude Chap. 5 by showing the quantum correction also to the Josephson frequency.

In Chap. 6, we summarize this Thesis.

Contents

Chapter 1

Introduction

Multicomponent quantum many-body systems are the central target in modern physics, offering diverse novel physics including fundamental physics such as quantum phases or dynamical responses, and applications to quantum computation with qubits. Quantum many-body physics deals with a system composed of a huge amount of particles obeying quantum theory and collective phenomena manifesting quantum nature on the macroscopic scale. If the system has additional degrees of freedom, such as spins, species, or colors, it exhibits a much richer variety of physics. This Thesis aims to establish a comprehensive understanding of the multicomponent quantum many-body physics with a special focus on superfluidity.

1.1 Superfluidity

One of the most striking and fundamental phenomena in quantum many-body physics is *superfluidity*. It dates back to Onnes' first realization of liquid ^{4}He in 1908. In 1937, Kapitza, Allen, and Misener first observed an inviscid flow in a liquid ^{4}He below the λ point, which is the significant property of superfluidity [1, 2]. After the observation, Tisza and Landau proposed superfluid hydrodynamics describing superfluidity in 1941 [3, 4, 5, 6, 7]. In modern interpretations, superfluidity is also related to Bose-Einstein condensation (BEC) theoretically predicted by Bose and Einstein in 1925 [8, 9]. This connection between superfluidity and BEC was first indicated by London in 1938 [10]. However, the realization of BEC requires an ultralow temperature around the order of $1\,\mu$K and high density. Note that even in outer space without starlight, we still have the temperature of $2.7\,$K due to the cosmic microwave background. For a long time, it was a highly challenging issue to develop a cooling mechanism to realize Bose-Einstein condensation at ultralow temperatures.

In 1995, Cornell, Ketterle, and Wieman succeeded in experimentally realizing atomic BEC with a ^{87}Rb atomic cloud cooled to around $1\,\mu$K [11, 12, 13]. The atomic gases are trapped by a magneto-optical trap, and cooled by laser cooling and evaporative cooling technology. This seminal achievement was a milestone in ultracold atomic physics

and the realization of BEC was awarded by Nobel Prize in Physics in 2001 [11, 12, 13]. Recently, a wide variety of superfluidity and superconductivity have been reported such as driven-dissipative superfluids realized in exciton-polariton systems composed of electrons and holes in a cavity [14, 15, 16, 17, 18], topological superconductors hosting topologically nontrivial phases [19, 20], and laser-induced superconductors [21, 22].

1.2 Ultracold atomic physics

Since the successful achievement of BEC in 1995 [11, 12, 13], ultracold atomic systems have offered a versatile platform to study quantum many-body physics. In ultracold atomic systems, neutral atomic gases are magnetically or optically trapped in a vacuum and cooled down to ultralow temperatures lower than the order of 1 μK. Ultracold atomic systems have several advantages compared to other quantum systems. In this section, we explain the five aspects in particular: (I) ultracold temperature, (II) diluteness, (III) neutral charge, (IV) isolated system, and (V) optical lattice.

First of all, (I) ultracold temperature allows us to achieve a quantum degeneracy regime of the order of 10 nK, which contributes to the realization of an atomic BEC. This ultralow temperature is also useful to investigate the effects of quantum fluctuations at low temperatures. Furthermore, (I) ultracold temperature and (II) dilute density result in a small energy scale of the order of 1 kHz compared to the strongly-correlated electron systems with the large energy scale eV $\sim 10^{14}$ Hz. It enables us to observe the real-time quantum dynamics and the momentum distribution through the time-of-flight (TOF) method [23]. Indeed, the experimental realization of BEC with ^{87}Rb atoms has been observed via the measurement of the momentum distribution with the TOF [11, 12, 13].

In addition, (III) charge neutrality simplifies the inter-atomic interactions and enables us to tune the interaction strength in a controllable manner by the technique of Feshbach resonance [24, 25]. Let us consider the scattering of an incoming atom with momentum $\hbar k$ where $\hbar$ is the reduced Planck constant, and a scatterer ball with the radius r_0. For a particle with the orbital angular momentum $L_{\rm in} = b\hbar k \simeq \hbar l$ with b being the impact parameter and $l = 0, 1, 2, \cdots$ being the quantum number of angular momentum, the necessary condition for the scattering is $b < r_0$, which reads $l < kr_0$. For a ^{6}Li atomic gas cooled down to 100 nK, for instance, $k^{-1} \sim 10^4 a_0$ and $r_0 \simeq 62.5 a_0$ allow us to describe the atomic gas only with the s-wave inter-atomic interaction with a_0 the Bohr radius because only the s-wave channel $l = 0$ is allowed. The s-wave scattering length a_s associated with the three-dimensional effective inter-atomic interaction potential

$$U_{\rm 3D}(r) = \frac{4\pi\hbar^2 a_s}{m}\delta(r), \tag{1.1}$$

can be controlled by an external magnetic field by the technique of Feshbach resonance. Feshbach resonance refers to the formation of a resonant bound state when two atoms collide with each other. The Hamiltonian of the single atom coupled with a magnetic

field $\boldsymbol{B} = (0, 0, B)$ associated with the hyperfine structure is given by [26]

$$\hat{H}_{\rm hf} = A_{\rm hf}\hat{\boldsymbol{I}} \cdot \hat{\boldsymbol{J}} - \frac{\mu_{\rm I}}{I} B\hat{I}_z + g_{\rm L}\mu_{\rm B} B\hat{J}_z, \tag{1.2}$$

where $\hat{\boldsymbol{I}}$ and $\hat{\boldsymbol{J}}$ are the nuclear and electronic spin angular momentum operators, respectively. The first term in Eq. (1.2) stands for the hyperfine interaction between the nuclear spin and electron spin with the coupling strength $A_{\rm hf}$. The second and third terms are the Zeeman terms for the nuclear spin and electron spin, respectively, where $\mu_{\rm I}$ is the nuclear magneton, $\mu_{\rm B}$ is the Bohr magneton, and $g_{\rm L}$ is the Landé g-factor. The second term is usually negligible compared to the third term. The total spin $\hat{\boldsymbol{F}} = \hat{\boldsymbol{I}} + \hat{\boldsymbol{J}}$ is a good quantum number with a weak magnetic field. The hyperfine coupling between the nuclear spin and the electron spin makes the Zeeman energies of the resonant bound state and the unbound state different. As a result, the effective interaction (1.1) depends on the external magnetic field and the inter-atomic scattering length in the collision is related to the magnetic field as

$$a_s(B) = a_{\rm bg}\left(1 + \frac{W_{\rm res}}{B - B_0}\right). \tag{1.3}$$

Here, $W_{\rm res}$ is the resonance width and $a_{\rm bg}$ is the s-wave scattering length associated with the triplet scattering. Figure 1.1 shows the dependence of the s-wave scattering length on the external magnetic field in a ^{87}Rb atomic gas [27]. By irradiating a laser, the resonant magnetic field B_0 changes as shown in Fig. 1.1. By tuning the external magnetic field B, one can change the magnitude and the sign of the s-wave scattering length a_s according to Eq. (1.3), which controls the repulsive or attractive inter-atomic interaction strength as in Eq. (1.1). This high tunability of interaction by Feshbach resonance with an external magnetic field and a locally irradiated laser beam allows us to systematically investigate the strong-coupling effects on physical quantities in quantum many-body systems. In Fermi systems such as electrons, the formation of Cooper pairs due to the attractive interaction results in the Bardeen-Cooper-Schrieffer (BCS) superfluidity. With Fermi atoms by tuning the inter-atomic attractive interaction strength, the BCS-BEC crossover, which is a continuous crossover from the BCS superfluids to the tightly bound molecular BEC, was achieved experimentally [28, 29]. In Bose systems, the inter-atomic repulsive interaction plays an important role in the formation of solitons as well as superfluidity [30, 31, 32, 33, 34, 35, 36, 37, 38, 39, 40].

Since the atoms are confined by a magneto-optical trap in a vacuum, one can realize a highly isolated system, which is clean without any disorder or impurity atoms. Thanks to this feature, ultracold atomic systems are useful to demonstrate the relaxation dynamics in isolated quantum systems [41]. One example is the Josephson dynamics in atomic superfluids [42], as introduced shortly. We can utilize the atomic hyperfine spin states to trap an atomic cloud with a magnetic field. For an alkaline atom with nuclear spin $I = 3/2$, for instance, there are two split levels of $F = I + 1/2 = 2$ and $F = I - 1/2 = 1$. The Hamiltonian (1.2) leads to the energy eigenvalues of the two states $|F = 2, m_F\rangle$ and

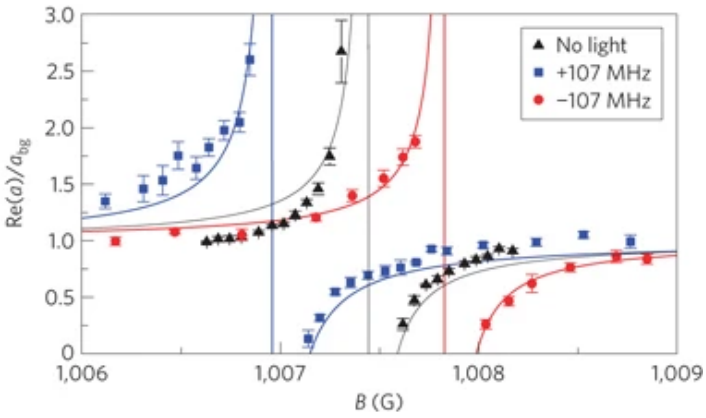

Figure 1.1: Control of inter-atomic s-wave scattering length scaled by $a_{\rm bg}$ by the Feshbach resonance in a ^{87}Rb Bose gas [27]. The vertical lines represent the resonant magnetic fields for each frequency of the irradiated laser.

$|F=1,m_F\rangle$ as

$$\begin{aligned} E_{2,m_F} &= \frac{3A_{\rm hf}}{4} + \frac{m_F}{4} g_{\rm L}\mu_{\rm B}B - \frac{m_F^2-4}{32A_{\rm hf}}(g_{\rm L}\mu_{\rm B}B)^2, \\ E_{1,m_F} &= -\frac{5A_{\rm hf}}{4} - \frac{m_F}{4} g_{\rm L}\mu_{\rm B}B + \frac{m_F^2-4}{32A_{\rm hf}}(g_{\rm L}\mu_{\rm B}B)^2, \end{aligned} \tag{1.4}$$

respectively up to the second order in B with the total spin magnetic quantum number $m_F = -F, -F+1, \cdots, F-1, F$. The energy eigenvalues of the atomic states $|2,2\rangle$, $|2,1\rangle$, and $|1,-1\rangle$ are increasing functions in terms of B. They are subject to a force in the direction of the weaker magnetic field and are called weak field seeking states (WFSSs). As a result, alkaline atoms of these states can be trapped at a spot with the minimum magnetic field.

Although atomic gases are continuous in space, one can introduce (V) optical lattices to implement a spatially periodic potential [23]. When the atoms are irradiated by an off-resonant optical field, the atomic levels are effectively shifted due to virtual absorption and emission of photons (AC Stark effect). The level shift can be regarded as a potential for the atoms given by

$$V(\boldsymbol{r}) = -\frac{1}{2}\alpha(\omega)\left|\bar{\boldsymbol{E}}(\boldsymbol{r})\right|^2, \tag{1.5}$$

where $\alpha(\omega)$ is the AC polarizability and $\bar{\boldsymbol{E}}(\boldsymbol{r})$ is the time-averaged AC electric field with frequency ω. When the optical field is a standing wave $\left|\bar{\boldsymbol{E}}(\boldsymbol{r})\right|^2 = E^2\cos(\boldsymbol{k}\cdot\boldsymbol{r})$, the potential (1.5) plays a role of a periodic lattice. In this way, one can implement various configurations of lattices and band structures in atomic systems, which is useful to simulate the Hubbard model, a theoretical model of strongly correlated electron systems. In the atomic Hubbard model, the tunneling rate between the nearest neighbor sites can

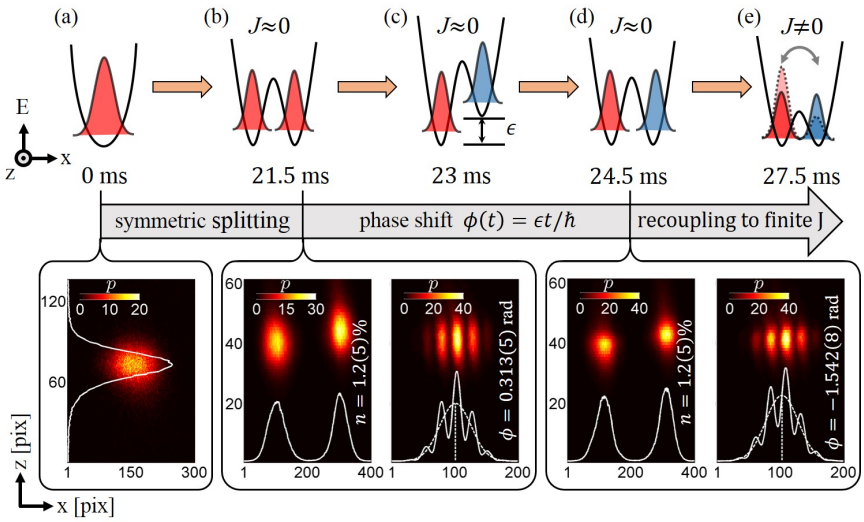

Figure 1.2: Schematic figures of the Bose Josephson junction prepared in a double-well potential with ^{87}Rb atoms [42]. (a,b) Splitting of the original Bose gas into two separated ones. (c,d) Implementation of the phase shift. (e) Recoupling between the two Bose gases. The lower panels show the TOF images of the atomic density after 46 ms and the white curves stand for the integrated profiles.

be tuned by the depth of the optical lattice, and the onsite interaction strength can be controlled by the Feshbach resonance. Indeed, the superfluid-Mott insulator quantum phase transition at zero temperature has been experimentally observed with ^{87}Rb atoms [43]. Optical traps can also create tight confinement in specific directions to realize quasi-2D systems or quasi-1D systems. In the latter part of this Thesis, we focus on two superfluids separated by a potential barrier. This configuration can be achieved by a double-well optical potential. Figure 1.2 shows the preparation of the Bose Josephson junction composed of two one-dimensional ^{87}Rb atomic gases confined in a double-well potential [42]. The observed relaxation dynamics are reported in Fig. 1.3. It shows the damped oscillation dynamics of both the relative phase and the population imbalance.

1.3 Multicomponent physics

In addition to the five advantages explained in Sec. 1.2, it is easier to manipulate additional degrees of freedom in ultracold atomic systems to investigate multicomponent physics. There are numerous number of multicomponent physical systems in the world. The superconducting Josephson junctions and the atomic Josephson junctions illustrated in Fig. 1.2 are one of the examples of multicomponent systems. Metallic superconductors consist of Cooper pairs made of spin-up and spin-down electrons. Two-component ultracold Fermi gases with two different hyperfine states are similar examples exhibiting BCS-BEC crossover. Currently, they are utilized as a quantum simulator of a neutron

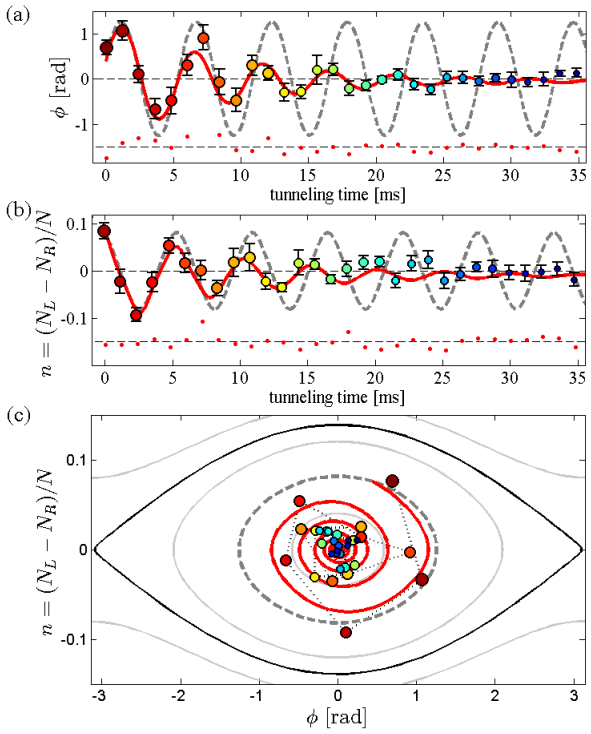

Figure 1.3: Damped oscillation dynamics of (a) relative phase ϕ and (b) population imbalance n measured in the setup of Fig. 1.2 with the number of atoms $N = 3300$ [42]. The red curves are the fits resulting in $U/h = 0.71\,\mathrm{Hz}$ and $J/h = 8\,\mathrm{Hz}$. The dashed curves are the mean-field predictions of the two-mode Bose-Hubbard model. (c) shows the contour plot with respect to the population imbalance and the relative phase.

superfluid realized in neutron stars. Exciton-polariton systems are also multicomponent systems composed of electrons and holes coupled with photons in a cavity. It is a driven-dissipative system and hosts several phases including the electron-hole plasma, electron-hole BCS phase, exciton BEC phase, exciton-polariton BEC phase, and photon laser phase in which electrons and holes play the role of a gain medium [44]. A ^{3}He atom is a fermion and ^{3}He superfluidity also exhibits fruitful superfluid phases such as ^{3}He-A, ^{3}He-B, and ^{3}He-A$_1$ phases due to the internal degrees of freedom in Cooper pairs in contrast to ^{4}He superfluidity [45, 46, 47]. In multicomponent Bose superfluids that we focus on in Chap. 4, there are several specific properties such as the Andreev-Bashkin entrainment effect describing the mutual drag among the components [48, 49, 50, 51, 52, 53, 54, 55], and the emergence of fractional circulation of vorticity in contrast to a single-component superfluid [56, 57, 58, 59, 60, 61, 62, 63, 64, 65, 66, 67, 68, 69, 70, 71, 72, 73, 74]. As a three-component system, a quark system may be a familiar example in high-energy physics. Quarks have three colors and interact with each other by exchanging gluons. The theoretical framework of these quark systems is quantum chromodynamics (QCD).

The QCD hosts a rich phase diagram with respect to the temperature and baryon chemical potential: hadronic phase, quark-gluon plasma, color superconducting phase, and nuclear superfluid phase [75]. Recently, the analogue of quark systems has been investigated with three-component Fermi atoms [76, 77, 78]

From these points of view, in general, multicomponent quantum many-body systems exhibit a broader variety of phases compared to single-component systems. Within ultracold atom setups, one can easily control the internal degrees of freedom such as the atomic species and hyperfine spin states. In a recent development, in particular, the first realization of a BEC in a ^{87}Rb-^{41}K mixture in space has been reported [79]. These experiment of quantum gases in space paves the way to have a shell-shaped bubble trap potential in microgravity conditions [80, 81, 82, 83, 84, 85, 86, 87, 88, 89]. Based on these developments of ultracold atomic setups, multicomponent ultracold atomic gases open new paths to demonstrate and engineer novel quantum many-body physics which has never been explored in single-component systems.

1.4 Our motivation

The high controllability of ultracold atomic systems introduced in Sec. 1.2 is useful to study multicomponent superfluidity. The motivation of this Thesis is to reveal novel physics including both thermodynamics and dynamical properties in multicomponent quantum many-body systems. In particular, we consider a binary Bose superfluid with two different hyperfine states and a one-dimensional Bose Josephson junction. In a binary Bose superfluid with different hyperfine states, in contrast to a single-component superfluid, exotic vortex excitations are stable. In 2D, in particular, these topological excitations play a crucial role in the superfluid-normal phase transition. It indicates that the exotic vortex excitations contribute to novel types of superfluid-normal phase transitions in multicomponent superfluids. Furthermore, the superfluid-normal phase transitions induced by vortex excitations are topological phase transitions without spontaneous symmetry breaking. In other words, a specific symmetry in a system is not necessarily important and the physics of topological excitations are expected to occur in a broad range of energy scales. Indeed, the exotic vortex excitations have similarities with the quark matters as to be mentioned in Chap. 4. Therefore, these analyses would be useful in a wide range of physics including high-energy physics. In addition to the superfluid phase transitions, the dynamical properties in multicomponent superfluids are also expected to exhibit interesting properties depending on the interaction strength and tunnel coupling. The experiment in Ref. [42] reported damped oscillation dynamics shown in Fig. 1.3 in a Bose Josephson junction, but the damping mechanism was not clear since the ultracold atomic setup is an ideal isolated system as mentioned in Sec. 1.2. The clarification of the damping mechanism in comparison with a superconducting Josephson junction is meaningful work and is expected to contribute to a broad range of transport phenomena in junction systems.

1.5 Outline of this Thesis

This Thesis consists of 6 chapters. Chapter 2 is a review part. We overview the physics of quantum fluids with a special focus on Bose superfluids. In Chap. 3, we show the behavior of first and second sound modes in a D-dimenional single-component Bose superfluid in the hydrodynamic regime. The presented results are based on our work in Ref. [90]. Chapter 4 is devoted to the study of superfluid-normal phase transitions in a 2D binary Bose superfluid with two hyperfine spin states. In particular, we show the novel behavior of superfluid transition temperature and sound modes in stark contrast to single-component superfluids discussed in Chap. 3 based on our work [91]. Chapter 5 presents analyses of the dynamical properties of multicomponent superfluids focusing on Josephson junctions. Based on our work [92], we see that the damped Josephson dynamics in a Bose Josephson junction can be derived without introducing any external thermal bath. The dynamics are governed by both quantum and thermal fluctuations analogous to a superconducting Josephson circuit and we clarify the difference by elucidating the effects of quantum fluctuations [93, 94]. The last chapter summarizes the Thesis.

Chapter 2

Overview of quantum fluids

In this chapter, we overview the fundamentals of quantum hydrodynamics. We first review the notion of superfluidity and Gross-Pitaevskii theory which describes superfluids in ultracold atomic systems. Then, we see the hydrodynamics of superfluids and the emergence of quantized vortices. In a classical fluid, vorticity has a continuous value because vortices are continuous and can be disconnected. On the other hand, in a single-component superfluid, the circulation of vorticity is quantized with a unit proportional to the Planck constant. From this point of view, we can understand that superfluids are *quantum fluids*.

2.1 Bose-Einstein condensation and spontaneous symmetry breaking

First, we review Bose-Einstein condensation as a manifestation of quantum effects on the macroscopic scale in this section. We see that the occurrence of the Bose-Einstein condensation is accompanied by spontaneous symmetry breaking.

2.1.1 Bose-Einstein condensation

We start with the quantum many-body system described by

$$\begin{aligned}\hat{H} &= \hat{H}_0 + \hat{H}_{\rm int} \\ &= \int \mathrm{d}\boldsymbol{r}\, \hat{\Psi}^\dagger(\boldsymbol{r}) \left[-\frac{\hbar^2}{2m}\boldsymbol{\nabla}^2 + V_{\rm ext}(\boldsymbol{r}) \right] \hat{\Psi}(\boldsymbol{r}) \\ &\quad + \frac{1}{2}\int \mathrm{d}\boldsymbol{r} \int \mathrm{d}\boldsymbol{r}'\, \hat{\Psi}^\dagger(\boldsymbol{r})\hat{\Psi}^\dagger(\boldsymbol{r}')U(\boldsymbol{r}-\boldsymbol{r}')\hat{\Psi}(\boldsymbol{r}')\hat{\Psi}(\boldsymbol{r}), \end{aligned} \tag{2.1}$$

where $\hat{\Psi}(\boldsymbol{r})$ is the field operator. For bosons, it satisfies the commutation relation

$$[\hat{\Psi}(\boldsymbol{r}), \hat{\Psi}^\dagger(\boldsymbol{r}')] = \delta(\boldsymbol{r}-\boldsymbol{r}'), \quad [\hat{\Psi}(\boldsymbol{r}), \hat{\Psi}(\boldsymbol{r}')] = [\hat{\Psi}^\dagger(\boldsymbol{r}), \hat{\Psi}^\dagger(\boldsymbol{r}')] = 0. \tag{2.2}$$

In Eq. (2.1), $V_{\rm ext}(\boldsymbol{r})$ is the external potential and $U(\boldsymbol{r}-\boldsymbol{r}')$ is the two-body interaction potential.

Bose systems manifest macroscopic occupation of a lowest-lying state called *Bose-Einstein condensation* (BEC) in the thermodynamic limit due to the Bose statistics in Eqs. (2.2). To discuss BEC in an interacting Bose system, it is convenient to follow the approach of Penrose and Onsager by introducing the single-body density matrix [95]

$$\rho_1(\boldsymbol{r},\boldsymbol{r}') = \langle \hat{\Psi}^\dagger(\boldsymbol{r})\hat{\Psi}(\boldsymbol{r}')\rangle, \tag{2.3}$$

where $\langle\cdots\rangle$ denotes the grand canonical ensemble average. The single-body density matrix (2.3) represents the probability amplitude of finding a particle annihilated at position $\boldsymbol{r}'$ and created at position $\boldsymbol{r}$ simultaneously. It can be time-dependent in nonequilibrium systems. The diagonal component $\rho_1(\boldsymbol{r},\boldsymbol{r}) = n(\boldsymbol{r})$ is the number density at position $\boldsymbol{r}$. The normalization is given by the total number of bosons $N = \int {\rm d}\boldsymbol{r}\, n(\boldsymbol{r}) = \int {\rm d}\boldsymbol{r}\, \rho_1(\boldsymbol{r},\boldsymbol{r})$ where the volume integral is performed within the system size V. The off-diagonal component represents the long-range correlation.

The hermiticity of the single-body density matrix $\rho_1^*(\boldsymbol{r}',\boldsymbol{r}) = \rho_1(\boldsymbol{r},\boldsymbol{r}')$ guarantees that it is diagonalizable and can be expanded with an orthonormal basis $\{\phi_j(\boldsymbol{r},t)\} = \{e^{i\boldsymbol{k}_j\cdot\boldsymbol{r}}/\sqrt{V}\}$ with $\boldsymbol{k}_j = (k_x,k_y,k_z) = (j_x,j_y,j_z)\pi/\sqrt{V}$ where $j_{x,y,z}$ are integers as

$$\rho_1(\boldsymbol{r},\boldsymbol{r}') = \sum_j n_j(t)\phi_j^*(\boldsymbol{r})\phi_j(\boldsymbol{r}'), \tag{2.4}$$

with $\{n_j\}$ the real eigenvalues. BEC is a thermodynamic phase in which the eigenvalue for the lowest-lying microscopic state $j=0$ is $\mathcal{O}(N)$ and the other eigenvalues are $\mathcal{O}(1)$ in the thermodynamic limit. To see this, we decompose Eq. (2.3) as

$$\rho_1(\boldsymbol{r},\boldsymbol{r}') = N_0\phi_0^*(\boldsymbol{r})\phi_0(\boldsymbol{r}') + \sum_{j\neq 0} n_j\phi_j^*(\boldsymbol{r})\phi_j(\boldsymbol{r}'), \tag{2.5}$$

where $n_0 = N_0 = \mathcal{O}(N)$ is the maximum eigenvalue and $n_{j\neq 0} = \mathcal{O}(1)$. In the thermodynamic limit $N\to\infty$ and $V\to\infty$ under $N/V = $ const., due to $\phi_j \propto V^{-1/2}$, only the first term in Eq. (2.5) remains finite. Then, we define *off-diagonal long-range order* (ODLRO) by a finite $\rho_1(\boldsymbol{r},\boldsymbol{r}')$ in $|\boldsymbol{r}-\boldsymbol{r}'|\to\infty$. By introducing the order parameter or *condensate wavefunction* $\Psi(\boldsymbol{r}) \equiv \sqrt{N_0}\phi_0(\boldsymbol{r})$, the occurrence of ODLRO is defined by the condition

$$\lim_{|\boldsymbol{r}-\boldsymbol{r}'|\to\infty} \rho_1(\boldsymbol{r},\boldsymbol{r}') = \Psi^*(\boldsymbol{r})\Psi(\boldsymbol{r}') \neq 0. \tag{2.6}$$

In our case of Bose systems, this occurrence of ODLRO states the emergence of BEC. Here, $N_0 = \int {\rm d}\boldsymbol{r}\, |\Psi(\boldsymbol{r})|^2$ represents the number of bosons in the condensate. A macroscopic number of bosons occupying a single quantum state, BEC is a manifestation of quantum effects at the macroscopic scale. In this sense, $\Psi(\boldsymbol{r})$ is also called *macroscopic wavefunction*.

In an ideal Bose gas in thermal equilibrium at temperature T, the momentum distribution function is given by

$$f_T(\varepsilon_p - \mu) = \frac{1}{e^{\beta(\varepsilon_p - \mu)} - 1}, \tag{2.7}$$

in the grand canonical ensemble where $\varepsilon_p = p^2/2m$ is the kinetic energy, μ is the chemical potential determined by $N = \sum_{\boldsymbol{p}} f_T(\varepsilon_p - \mu)$, and $\beta = 1/k_{\rm B}T$ is the inverse temperature with $k_{\rm B}$ being the Boltzmann constant. The positivity of distribution function $f_T(\varepsilon_p - \mu) \geq 0$ requires $\varepsilon_p - \mu \geq 0$. Since the lowest-lying state is $\boldsymbol{p} = 0$, $\mu \leq 0$ is required. When the chemical potential is identical to the lowest-lying level $\varepsilon_0 = 0$, Eq. (2.7) diverges implying the macroscopic occupation of the lowest-lying state. To see this, we write the single-body density matrix in the momentum domain as

$$\rho_1(\boldsymbol{p}) = \int \mathrm{d}\boldsymbol{s}\, e^{-i\boldsymbol{p}\cdot\boldsymbol{s}/\hbar} \rho_1(\boldsymbol{r}, \boldsymbol{r} + \boldsymbol{s}), \tag{2.8}$$

which is identical to Eq. (2.7) in a free Bose gas and gives the number of bosons as

$$N = \sum_{\boldsymbol{p}} \rho_1(\boldsymbol{p}) = N_0 + N' = \frac{1}{e^{-\beta\mu} - 1} + \sum_{\boldsymbol{p}} \frac{1}{e^{\beta(\varepsilon_p - \mu)} - 1}, \tag{2.9}$$

where N_0 is the number of bosons occupying the lowest-lying mode $\boldsymbol{p} = 0$ and N' is the one occupying other excitation modes. In 3D, the latter contribution can be evaluated as

$$N' = \frac{V}{\lambda_T^3} g_{3/2}(-\beta\mu), \tag{2.10}$$

with

$$\lambda_T \equiv \sqrt{\frac{2\pi\hbar^2}{m k_{\rm B} T}}, \tag{2.11}$$

being the thermal de Broglie wavelength and

$$g_\alpha(z) \equiv \frac{1}{\Gamma(\alpha)} \int_0^\infty \mathrm{d}x\, \frac{x^{\alpha-1}}{e^{x+z} - 1}, \tag{2.12}$$

where $\Gamma(\alpha)$ is the Gamma function and $g_\alpha(0) = \zeta(\alpha)$ is the Riemann's zeta function. In the high-temperature regime, most bosons occupy the excited states and $N_0 = \mathcal{O}(1)$ and $N' \simeq N$. As one decreases the temperature, λ_T increases and to keep $N' \simeq N$, $g_{3/2}(-\beta\mu)$ must increase. Here, $g_{3/2}(z)$ is monotonically increasing with respect to z and consequently, monotonically decreasing in terms of $|\mu|$. In the limit of $\mu \to 0$, therefore, the BEC transition temperature $T_{\rm BEC}$ is determined by

$$\frac{V}{\lambda_{T_{\rm BEC}}^3} g_{3/2}(0) = N, \tag{2.13}$$

which reads

$$T_{\mathrm{BEC}} = \frac{2\pi\hbar^2}{mk_{\mathrm{B}}} \left(\frac{N}{\zeta(3/2)V} \right)^{2/3}. \tag{2.14}$$

Equation (2.13) states that the thermal wavelength becomes the same order of the interparticle distance $(V/N)^{1/3}$ in a BEC.

2.1.2 Spontaneous symmetry breaking

The original Hamiltonian (2.1) is invariant under the global U(1) transformation $\hat{\Psi}(\boldsymbol{r}) \to \hat{\Psi}(\boldsymbol{r})e^{i\alpha}$ and $\hat{\Psi}^\dagger(\boldsymbol{r}) \to \hat{\Psi}^\dagger(\boldsymbol{r})e^{-i\alpha}$. The occurrence of BEC defined by Eq. (2.6) allows us to write the field operator as a classical variable $\Psi(\boldsymbol{r}) = \sqrt{N_0}e^{i\theta(\boldsymbol{r})}$. It indicates that the occurrence of BEC determined the U(1) phase $\theta(\boldsymbol{r})$ and the U(1) symmetry is spontaneously broken. Indeed, this U(1) phase plays a crucial role in creating superflow as we will see in Sec. 2.3. This *spontaneous symmetry breaking* (SSB) characterizes phase transitions in general. In the high-temperature regime $T > T_{\mathrm{BEC}}$, thermal fluctuations prevent the ordered phase and the long-range order decays exponentially. In the low-temperature regime $T < T_{\mathrm{BEC}}$, thermal fluctuations are suppressed and ordered phases are favored, which fixes the U(1) phase of the order parameter. It is analogous to the ferromagnet transition in a spin system. Below a transition temperature $T < T_{\mathrm{c}}$, the orientation of spins is ordered to realize a ferromagnet. Indeed, the universality class of the BEC transition and the ferromagnet transition in spin systems are identical.

Hohenberg-Mermin-Wagner theorem rules out the occurrence of ODLRO due to the SSB of a continuous symmetry in a D-dimensional system in thermal equilibrium at finite temperatures for $D \leq 2$ [96, 97]. It is because the degeneracy originating from the continuous symmetry results in large fluctuations and in low dimensions, in particular, less spatial degrees of freedom cannot suppress the fluctuations to sustain ODLRO. Hence, in a 2D Bose gas in thermal equilibrium at finite temperatures, BEC cannot occur. However, the single-body density matrix decays algebraically in the long-range limit instead of exponentially. This quasi-long-range order is called *algebraic long-range order* (ALRO). It is closely related to the Berezinskii-Kosterlitz-Thouless transition, which is a superfluid-to-normal phase transition peculiar to 2D, as to be addressed in Sec. 2.6.

2.2 Gross-Pitaevskii equation

In dilute atomic gases, as explained in Sec. 1.2, it is a good approximation to assume the inter-particle interaction as a contact interaction as

$$U(\boldsymbol{r} - \boldsymbol{r}') = g\delta(\boldsymbol{r} - \boldsymbol{r}'), \tag{2.15}$$

where g is the coupling constant. The grand canonical Hamiltonian is then given by

$$\begin{aligned}\hat{K} &= \hat{H} - \mu\hat{N} \\ &= \int \mathrm{d}\boldsymbol{r}\, \hat{\Psi}^\dagger(\boldsymbol{r}) \left[-\frac{\hbar^2}{2m}\boldsymbol{\nabla}^2 + V_{\mathrm{ext}}(\boldsymbol{r}) - \mu \right] \hat{\Psi}(\boldsymbol{r}) + \frac{g}{2}\int \mathrm{d}\boldsymbol{r}\, \hat{\Psi}^\dagger(\boldsymbol{r})\hat{\Psi}^\dagger(\boldsymbol{r})\hat{\Psi}(\boldsymbol{r})\hat{\Psi}(\boldsymbol{r}),\end{aligned} \tag{2.16}$$

with μ the chemical potential and $\hat{N} = \hat{\Psi}^\dagger\hat{\Psi}$ the number operator. The Hamiltonian (2.16) gives the Heisenberg equation

$$\begin{aligned}i\hbar\partial_t\hat{\Psi}(\boldsymbol{r},t) &= [\hat{\Psi}(\boldsymbol{r},t), \hat{K}] \\ &= \left[-\frac{\hbar^2}{2m}\boldsymbol{\nabla}^2 + V_{\mathrm{ext}}(\boldsymbol{r}) - \mu + g\hat{\Psi}^\dagger(\boldsymbol{r},t)\hat{\Psi}(\boldsymbol{r},t) \right] \hat{\Psi}(\boldsymbol{r},t).\end{aligned} \tag{2.17}$$

In a BEC, we decompose the field operator $\hat{\Psi}$ into the classical order parameter field Ψ and the other non-condensed part as

$$\hat{\Psi}(\boldsymbol{r},t) = \Psi(\boldsymbol{r},t) + \delta\hat{\Psi}(\boldsymbol{r},t). \tag{2.18}$$

It is called *Bogoliubov ansatz*. If the non-condensed component $\delta\hat{\Psi}$ is negligible, the field operator is equivalent to the classical field. In this case, Eq. (2.17) can be written as

$$i\hbar\partial_t\Psi(\boldsymbol{r},t) = \left[-\frac{\hbar^2}{2m}\boldsymbol{\nabla}^2 + V_{\mathrm{ext}}(\boldsymbol{r}) - \mu + g|\Psi(\boldsymbol{r},t)|^2 \right] \Psi(\boldsymbol{r},t), \tag{2.19}$$

which is the Gross-Pitaevskii (GP) equation. It was first introduced by Gross and Pitaevkii in 1961 to describe an ultracold inhomogeneous Bose gas [98, 99]. The contact interaction strength g can be tuned by the Feshbach resonance as explained in Sec. 1.2. This interaction term makes the GP equation nonlinear. This nonlinearity is crucial also in the formation of solitons [40] as well as in superfluids as to be shown in Sec. 2.5.3. The chemical potential in the right-hand-side of Eq. (2.19) can be eliminated by the U(1) transformation $\Psi(\boldsymbol{r},t) \to \Psi(\boldsymbol{r},t)e^{i\mu t/\hbar}$. The GP equation can be obtained also by extremizing

$$L[\Psi,\Psi^*] = \int \mathrm{d}\boldsymbol{r}\, \frac{i\hbar}{2}\left[\Psi^*(\boldsymbol{r},t)\partial_t\Psi(\boldsymbol{r},t) - \Psi(\boldsymbol{r},t)\partial_t\Psi^*(\boldsymbol{r},t)\right] - E[\Psi,\Psi^*], \tag{2.20}$$

with the energy functional

$$E[\Psi,\Psi^*] = \int \mathrm{d}\boldsymbol{r}\left[\frac{\hbar^2}{2m}|\boldsymbol{\nabla}\Psi(\boldsymbol{r},t)|^2 + V_{\mathrm{ext}}(\boldsymbol{r})|\Psi(\boldsymbol{r},t)|^2 + \frac{g}{2}|\Psi(\boldsymbol{r},t)|^4 \right]. \tag{2.21}$$

By setting $\partial_t\Psi(\boldsymbol{r},t) = 0$ in Eq. (2.19), the steady-state solution of the GP equation (2.19) is obtained by

$$\left[-\frac{\hbar^2}{2m}\boldsymbol{\nabla}^2 + V_{\mathrm{ext}}(\boldsymbol{r}) + g|\Psi(\boldsymbol{r})|^2 \right] \Psi(\boldsymbol{r}) = \mu\Psi(\boldsymbol{r}). \tag{2.22}$$

The chemical potential μ is determined by

$$N_0 = \int \mathrm{d}\boldsymbol{r}\, |\Psi(\boldsymbol{r})|^2, \tag{2.23}$$

where N_0 is the condensate density.

2.3 Hydrodynamic equations

We consider performing a polar decomposition of the classical field as

$$\Psi(\boldsymbol{r}, t) = \sqrt{n(\boldsymbol{r}, t)} e^{i\theta(\boldsymbol{r}, t)}, \tag{2.24}$$

which is also called Madelung transformation, with $n(\boldsymbol{r}, t)$ the condensate density and $\theta(\boldsymbol{r}, t)$ the phase. By multiplying Ψ^* to Eq. (2.19) and subtracting its complex conjugate, we get the continuity equation

$$\partial_t n(\boldsymbol{r}, t) + \boldsymbol{\nabla} \cdot \boldsymbol{j}(\boldsymbol{r}, t) = 0, \tag{2.25}$$

where the current density

$$\begin{aligned} \boldsymbol{j}(\boldsymbol{r}, t) &= \frac{\hbar}{2im} \left[\Psi^*(\boldsymbol{r}, t) \boldsymbol{\nabla} \Psi(\boldsymbol{r}, t) - \Psi(\boldsymbol{r}, t) \boldsymbol{\nabla} \Psi^*(\boldsymbol{r}, t)\right] \\ &= n(\boldsymbol{r}, t) \frac{\hbar}{m} \boldsymbol{\nabla} \theta(\boldsymbol{r}, t), \end{aligned} \tag{2.26}$$

is related to the phase $\theta(\boldsymbol{r}, t)$. The velocity field

$$\boldsymbol{v}_\mathrm{s}(\boldsymbol{r}, t) \equiv \frac{\hbar}{m} \boldsymbol{\nabla} \theta(\boldsymbol{r}, t), \tag{2.27}$$

is called *superfluid velocity* and plays the central role in the superfluid component in two-fluid hydrodynamics introduced later.

By inserting Eq. (2.24) into Eq. (2.19), the real part coincides with the continuity equation (2.25). The imaginary part, on the other hand, provides

$$m \partial_t \boldsymbol{v}_\mathrm{s}(\boldsymbol{r}, t) + \boldsymbol{\nabla} \left[\mu(\boldsymbol{r}, t) + \frac{m v_\mathrm{s}^2}{2}\right] = 0, \tag{2.28}$$

with

$$\mu(\boldsymbol{r}, t) \equiv g n + V_\mathrm{ext}(\boldsymbol{r}) - \frac{\hbar^2}{2m\sqrt{n(\boldsymbol{r}, t)}} \boldsymbol{\nabla}^2 \sqrt{n(\boldsymbol{r}, t)}. \tag{2.29}$$

Equation (2.28) is the Euler equation for the superfluid. The last term in Eq. (2.29) is the quantum pressure term that stems from the density gradient. Compared to the Navier-Stokes equation for a viscid fluid

$$m \partial_t \boldsymbol{v} + \boldsymbol{\nabla} \left[\mu + V_\mathrm{ext}(\boldsymbol{r}) + \frac{m v^2}{2}\right] = \nu \boldsymbol{\nabla}^2 \boldsymbol{v} + m \boldsymbol{v} \times (\boldsymbol{\nabla} \times \boldsymbol{v}), \tag{2.30}$$

where ν is the viscosity and the second term in the right-hand-side represents the rotational term, one can observe that Eq. (2.28) describes inviscid and irrotational flow.

2.4 Quantized vortex

The rotation of a velocity field $\boldsymbol{\omega} = \boldsymbol{\nabla} \times \boldsymbol{v}$ is called vorticity. The line integral of the velocity field along a closed loop C surrounding a region Ω

$$\Gamma = \oint_C \mathrm{d}\boldsymbol{r} \cdot \boldsymbol{v} = \int_\Omega \mathrm{d}\boldsymbol{S} \cdot \boldsymbol{\omega}, \tag{2.31}$$

is called circulation and is related to vorticity $\boldsymbol{\omega}$ from the Stokes theorem. The vorticity and circulation vanish for a potential flow such as the superfluid velocity in Eq. (2.27). If Ω includes a region in which the superfluid density is absent, Eq. (2.31) can lead to a finite value. In this case, because $\Psi = \sqrt{n}e^{i\theta}$ must be a single-valued function, Eq. (2.31) gives

$$\Gamma = \oint_C \mathrm{d}\boldsymbol{r} \cdot \boldsymbol{v}_\mathrm{s} = \frac{\hbar}{m} \oint_C \mathrm{d}\boldsymbol{r} \cdot \boldsymbol{\nabla}\theta = \kappa q, \tag{2.32}$$

with q the integer vortex charge or, in general, winding number. This is Feynman-Onsager's quantization of circulation with the quantum of circulation $\kappa = h/m$. The notion of the quantized vortex was first examined theoretically by Onsager and Feynman [100, 101], and experimentally observed later by Vinen in 1961 [102]. Onsager considered whether a superfluid rotates. Under the condition of $\boldsymbol{\nabla} \times \boldsymbol{v}_\mathrm{s} = 0$ and incompressibility $\boldsymbol{\nabla} \cdot \boldsymbol{v}_\mathrm{s} = 0$, with the boundary condition $\boldsymbol{v}_{\mathrm{s},\perp} = 0$ at the edge of a simply connected container, it allows only $\boldsymbol{v}_\mathrm{s} = 0$. In a rotating cylinder, however, Onsager found a solution of $\boldsymbol{v}_\mathrm{s} \neq 0$ with a finite circulation under the same boundary condition [100]. In 1955, Feynman developed Onsager's idea and proposed the notion of the quantized vortex with the quantized circulation κ [101]. To experimentally realize a multiply connected domain, Vinen set a lead at the center of a cylinder filled with liquid helium. An AC electric current makes the lead oscillate due to the Lorentz force. Without any rotational flow, the two oscillation modes in clockwise and anticlockwise directions degenerate. If vortices are winding the lead with a rotational flow, a Magnus force split the degeneracy generating a beat. One can find the circulation around the lead by the observation of the difference in frequency in the beat. Vinen observed the quantized circulation of the rotational flow in liquid helium II below the lambda temperature 1.3 K, which was the first observation of the quantized circulation.

Let us consider a vortex line stretched along the z-axis illustrated in Fig. 2.1(a). The velocity field induced by the vortex line is given by

$$\boldsymbol{v} = \left(0, \frac{\kappa q}{2\pi r}, 0\right) \tag{2.33}$$

in the cylindrical coordinate (r, ϕ, z). At $r = 0$, the velocity v diverges creating a large kinetic energy cost. It is cancelled by $n(r = 0) = 0$, which is the vortex core. This is the case that the circulation of vorticity (2.31) gives a nonzero value. The GP equation (2.22) provides a better understanding of this vortex core structure. For simplicity, we ignore the external potential V_ext assuming a large enough radius of the cylinder. By

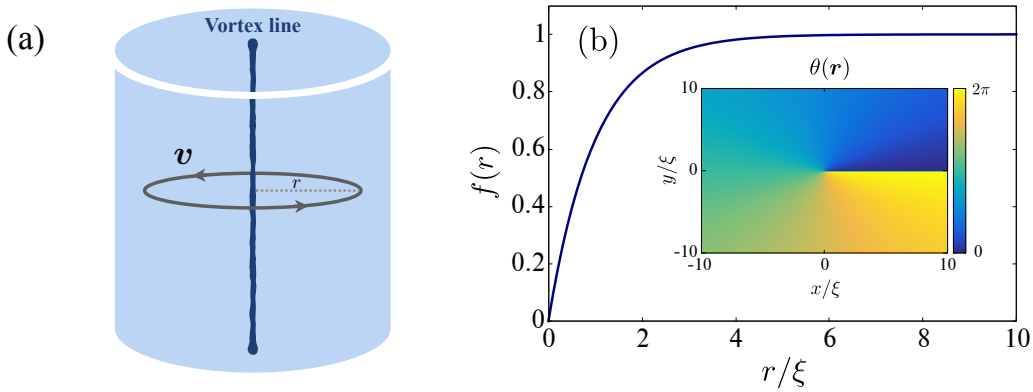

Figure 2.1: Vortex with a unit charge $q = 1$ in a cylinder. (a) illustrates the vortex line in a cylinder with the velocity (2.33). (b) shows the amplitude of the density numerically solved from Eq. (2.34) under the boundary conditions $f(0) = 0$ and $f(r \to \infty) = 1$. The inset shows the superfluid phase $\theta(\boldsymbol{r})$.

assuming $\Psi(r, \phi) = \sqrt{n} f(r) e^{iq\phi}$, Eq. (2.22) gives

$$-\frac{\hbar^2}{2mr}\frac{\mathrm{d}}{\mathrm{d}r}\left(r\frac{\mathrm{d}f}{\mathrm{d}r}\right) + \frac{\hbar^2 q^2}{2mr^2} f + gnf^3 = \mu f. \tag{2.34}$$

Here, $n = \mu/g$ is the bulk density in $r \to \infty$. Equation (2.34) is not analytically solvable. However, with a large r, the asymptotic solution can be obtained as

$$f(r) \sim 1 - \frac{q^2\xi^2}{r^2}, \tag{2.35}$$

with

$$\xi = \frac{\hbar}{\sqrt{2mgn}}, \tag{2.36}$$

the healing length. Equation (2.35) indicates that the vortex core size is the same as the healing length ξ, which is also confirmed by the numerical solution displayed in Fig. 2.1(b). It shows a numerical solution of Eq. (2.34) under the boundary conditions $f(0) = 0$ and $f(r \to \infty) = 1$, which is the bulk value. The inset of Fig. 2.1(b) shows the superfluid phase. The line $y = 0$ for $x \geq 0$ corresponds to the branch cut and the vortex core $(x, y) = (0, 0)$ corresponds to the singular point of the superfluid phase. The vortex core size ξ is the order of $\sim$ Å in ^{4}He, and $\sim 0.1\,\mu$m in atomic superfluids.

According to Eq. (2.21), the leading contribution to the vortex energy with the vortex charge q reads [50]

$$E_{\mathrm{vor}}[\Psi] = \int \mathrm{d}^2\boldsymbol{r}\frac{1}{2}mnv_{\mathrm{s}}^2 = q^2\frac{\pi n\hbar^2}{m}\ln\left(\frac{L}{\xi}\right) + (\text{core energy}), \tag{2.37}$$

which is proportional to the square of the vortex charge q^2 with the system length L. It indicates that a vortex with a larger charge is unstable and splits into two vortices with

smaller charges. For instance, the energy of a vortex with a charge $q = 2$ is proportional to $q^2 = 4$. If it splits into two vortices with charges $q = 1$ separated by a large distance, the energy is then proportional to $2 \times q^2 = 2$, which is energetically favored. Therefore, we can consider stable vortices only with the unit vortex charge $q = 1$.

Let us consider the interaction between two vortices with charge q_1 and q_2 separated by a distance R. Under the Abrikosov ansatz [103]

$$\Psi(\boldsymbol{r}; \boldsymbol{r}_1, \boldsymbol{r}_2) = \Psi_1(\boldsymbol{r} - \boldsymbol{r}_1)\Psi_2(\boldsymbol{r} - \boldsymbol{r}_2), \tag{2.38}$$

the inter-vortex interaction energy can be computed as [50]

$$E_{\rm int} = E_{\rm vor}[\Psi] - E_{\rm vor}[\Psi_1] - E_{\rm vor}[\Psi_2] = -q_1 q_2 \frac{2\pi n\hbar^2}{m} \ln R. \tag{2.39}$$

The inter-vortex force is

$$F_{\rm int} = -\frac{\partial E_{\rm int}}{\partial R} = q_1 q_2 \frac{2\pi n\hbar^2}{mR}. \tag{2.40}$$

In 2D, this force proportional to $1/R$ is equivalent to the Coulomb force. Indeed, via the Hubbard-Stratonovich transformation, a vortex can be interpreted as a charged particle subject to the Coulomb force. It allows us to discuss the vortices by moving on to the Coulomb gas model in 2D. This correspondence is useful also to analyze the phase transition caused by the vortices in 2D as to be discussed in Sec. 2.6.

2.5 Elementary excitations and Landau instability

To understand the thermodynamic properties of quantum fluids, we need to know the elementary excitations. In this section, we provide the derivation of the Bogoliubov spectrum, which is the elementary excitations in a weakly interacting Bose gas. One can follow two approaches for the derivation. One is the linear analysis of the hydrodynamic equations. The other way is the Bogoliubov-de Gennes (BdG) equation.

2.5.1 Bogoliubov spectrum via hydrodynamic equations

First, we consider the linear analysis of the hydrodynamic equations in a uniform Bose gas $V_{\rm ext} = 0$. We write the deviations from the equilibrium by

$$n(\boldsymbol{r}, t) = n_0 + \delta n\, e^{i(\boldsymbol{k}\cdot\boldsymbol{r} - \omega t)}, \quad \boldsymbol{v}_{\rm s}(\boldsymbol{r}, t) = \delta \boldsymbol{v}_{\rm s}\, e^{i(\boldsymbol{k}\cdot\boldsymbol{r} - \omega t)}. \tag{2.41}$$

Inserting Eqs. (2.41) into Eqs. (2.25) and (2.27), we obtain

$$m\omega^2 \delta n = \left(g n_0 k^2 + \frac{\hbar^2}{4m} k^4 \right) \delta n, \tag{2.42}$$

up to the linear order in δn. Then, the excitation spectrum in a uniform weakly-interacting Bose gas reads

$$E_k = \hbar\omega = \sqrt{\varepsilon_k \left(\varepsilon_k + 2gn_0\right)}. \tag{2.43}$$

In an ideal Bose gas $g = 0$, Eq. (2.43) reduces to the quadratic dispersion $\varepsilon_k = \hbar^2 k^2/2m$. With $g \neq 0$ in the long-wavelength limit $k \to 0$, Eq. (2.43) gives a linear phononic dispersion $E_k = c_{\mathrm{B}}\hbar k$ with

$$c_{\mathrm{B}} = \sqrt{\frac{gn_0}{m}}, \tag{2.44}$$

being the Bogoliubov speed of sound. This change of dispersion from quadratic to linear one occurs at $k \sim \sqrt{2mgn_0}/\hbar = \xi^{-1}$.

2.5.2 Bogoliubov spectrum via Bogoliubov-de Gennes equation

We can derive Eq. (2.43) also through the BdG equation. We follow this approach also in a multicomponent case as to be discussed in Sec. 4.2. Let us consider the deviation from the steady state solution of the GP equation (2.19) with $V_{\mathrm{ext}} = 0$ as

$$\Psi(\boldsymbol{r}, t) = \left[\Psi(\boldsymbol{r}) + \delta\Psi(\boldsymbol{r}, t)\right] e^{-i\mu t/\hbar}, \tag{2.45}$$

with

$$\delta\Psi(\boldsymbol{r}, t) = \sum_{\boldsymbol{k}} e^{i\boldsymbol{k}\cdot\boldsymbol{r}} \left(u_k e^{-i\omega t} + v_k^* e^{i\omega t}\right). \tag{2.46}$$

Inserting Eq. (2.45) into Eq. (2.19), we obtain

$$E_k \begin{pmatrix} u_k \\ v_k \end{pmatrix} = \mathcal{M} \begin{pmatrix} u_k \\ v_k \end{pmatrix}, \tag{2.47}$$

with

$$\mathcal{M} = \begin{pmatrix} h + 2g|\Psi|^2 & g\Psi^2 \\ -g\Psi^{*2} & -h - 2g|\Psi|^2 \end{pmatrix}, \tag{2.48}$$

and $h = \varepsilon_k - \mu$. By substituting $\Psi = \sqrt{n_0}$ and $\mu = gn_0$, the eigenvalue equation (2.47) results in the Bogoliubov spectrum (2.43).

2.5.3 Landau instability and Landau criterion

The elementary excitations allow us to analyze the stability of a steady state. If the excitation spectra are positive $E_k > 0$ for any k (except for the Nambu-Goldstone mode), the steady state is thermodynamically stable because the excitation from the steady state increases the energy. On the other hand, if $E_k < 0$ for a mode k, the steady state is unstable because one can decrease the energy by exciting the mode. This mechanism is called *Landau instability*. Even with the Landau instability, the GP equation provides just oscillation around the steady state because the time evolution of

the GP equation preserves the total energy. If a dissipation mechanism is introduced to decrease the energy, we can observe another more stable steady state favored according to the Landau instability instead of the unstable state.

Based on the knowledge, let us consider a superflow in a weakly-interacting Bose superfluid. A steady state of the superfluid moving with a constant superfluid velocity $\boldsymbol{v}$ is given by

$$\Psi(\boldsymbol{r}) = \sqrt{n_0} e^{im\boldsymbol{v}\cdot\boldsymbol{r}/\hbar}, \tag{2.49}$$

with the chemical potential $\mu = gn_0 + mv^2/2$. Under this steady state, the BdG equation gives

$$E'_k = E_k + \hbar\boldsymbol{k}\cdot\boldsymbol{v}, \tag{2.50}$$

where E_k is the excitation spectrum without the superflow $\boldsymbol{v}$. If the superflow $\boldsymbol{v}$ makes the energy E'_k negative, the superfluid is subject to Landau instability. In other words, the thermodynamic stability condition of superfluidity is

$$E'_k \geq 0. \tag{2.51}$$

Because $\boldsymbol{k}\cdot\boldsymbol{v}$ takes its minimum if $\boldsymbol{k}$ and $\boldsymbol{v}$ are antiparallel with each other, the critical velocity for the stability condition (2.51) reads

$$v_\mathrm{c} = \min_k \left(\frac{E_k}{\hbar k} \right), \tag{2.52}$$

which is the *Landau criterion*. In particular, for the phononic dispersion in the long-wavelength limit $k \to 0$, Eq. (2.52) gives $v_\mathrm{c} = c_\mathrm{B}$. Note that, however, the critical velocity just gives a sufficient condition for the stability of superfluidity. Indeed, in experiments with superfluid helium and ultracold atoms, it has been observed that superfluidity undergoes an instability with a velocity lower than the critical velocity because of the roton or nucleation of quantized vortices [104]. For an ideal Bose gas $g = 0$, Eq. (2.52) gives $v_\mathrm{c} = 0$. It indicates an important consequence that an ideal Bose gas cannot exhibit superfluidity because the parabolic excitation energy $\varepsilon_k = \hbar^2k^2/2m$ cannot satisfy the stability condition (2.51) for any k.

If the excitation spectrum involves an imaginary part, according to Eq. (2.46), the fluctuations exponentially grow and the steady state is no longer stable. This instability is called *dynamical instability*. An example subject to dynamical instability is an attractively interacting Bose gas. With an attractive contact interaction $g < 0$, the Bogoliubov dispersion (2.43) has a finite imaginary part in the long wavelength limit $k \to 0$ indicating dynamical instability. It results in the collapse of the attractively interacting Bose gas [26].

2.6 Berezinskii-Kosterlitz-Thouless transition

Hohenberg-Mermin-Wagner theorem rules out the occurrence of the off-diagonal long-range order in 2D thermal equilibrium [96, 97]. However, superfluidity can emerge also

in 2D and it is subject to a topological phase transition called *Berezinskii-Kosterlitz-Thouless* (BKT) *transition* [105, 106, 107]. It is a phase transition originating from the vortex excitations without SSB. 2D superfluidity has been realized in a thin films of ^{4}He [108, 109, 110, 111, 112, 113, 114, 115, 116, 117, 118, 119, 120, 121, 122, 123], ultracold atoms [87, 124, 125, 126, 127, 128, 129, 130, 131, 132, 133, 134, 135, 136, 137, 138, 139, 140, 141, 142, 143], and exciton-polariton systems [15, 16, 144, 145]. The BKT transition was first observed in a thin ^{4}He film [118], and later observed also in superconducting films [146, 147, 148] and ultracold atoms [143]. To see this phase transition, it is instructive to consider the free energy of a vortex. By ignoring the core structure of vortices by neglecting the vortex core contribution in Eq. (2.37), the energy for a single vortex with a unit charge is given by

$$E_{\rm vor} = \pi J \ln\left(\frac{L}{\xi}\right), \tag{2.53}$$

with $J = n\hbar^2/m$ being the phase stiffness. Since we are ignoring the core structure of a vortex, the short-range cutoff is determined by the vortex core size ξ. The number of states for the configurations of vortices can be evaluated as $\Omega = L^2/\xi^2$ and the entropy reads

$$S = k_{\rm B} \ln \Omega = k_{\rm B} \ln\left(\frac{L^2}{\xi^2}\right). \tag{2.54}$$

Then, the free energy for a single vortex at temperature T reads

$$F = E_{\rm vor} - TS = (\pi J - 2k_{\rm B}T) \ln\left(\frac{L}{\xi}\right). \tag{2.55}$$

The free energy (2.55) classifies the thermodynamic phase into two distinct phases. If $J < 2k_{\rm B}T/\pi$, $F < 0$ and the proliferation of free vortices occurs. On the other hand, if $J > 2k_{\rm B}T/\pi$, the vortices form a bound vortex-antivortex pair without any free vortex. These physical pictures are summarized in Fig. 2.2. In the following section, we review the BKT transition in a 2D Bose superfluid through the renormalization group analysis.

2.6.1 Nelson-Kosterlitz renormalization group equations

We saw that interacting vortices are equivalent to a Coulomb gas model in Sec. 2.4. It allows us to construct renormalization group (RG) equations with respect to the phase stiffness and the vortex fugacity. To see that, let us start with a 2D superfluid described by the Euclidean action

$$S_{\rm E}[\Psi, \Psi^*] = \int_0^{\hbar\beta} {\rm d}\tau \int {\rm d}^2\boldsymbol{r} \left[\hbar\Psi^* \partial_\tau \Psi + \frac{\hbar^2}{2m}|\boldsymbol{\nabla}\Psi|^2 + \frac{g}{2}|\Psi|^4\right], \tag{2.56}$$

with $\beta = 1/k_{\rm B}T$ and $\tau = it$ being the imaginary time. To discuss the vortex configurations, we assume a uniform density and time-independent phase as

$$\Psi(\boldsymbol{r}, \tau) = \sqrt{n} e^{i\theta(\boldsymbol{r})}. \tag{2.57}$$

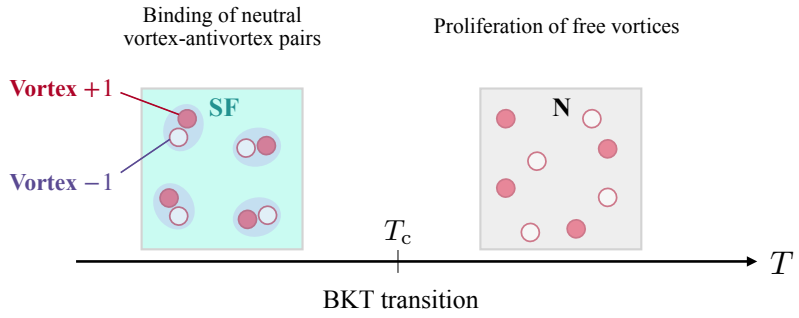

Figure 2.2: Schematic picture of the BKT transition in a single-component Bose superfluid.

Here, we ignored the density fluctuations. In a 2D Bose gas, indeed the density fluctuations turn out to be negligible and Eq. (2.57) is justified at sufficiently low temperatures. For details of the suppression of density fluctuations, see Appendix A.1. Inserting Eq. (2.57) into the action (2.56), one obtains

$$S_{\mathrm{XY}}[\theta] = \frac{\hbar K}{2} \int \mathrm{d}^2\boldsymbol{r}\, (\boldsymbol{\nabla}\theta)^2 \,, \tag{2.58}$$

where $K = \hbar^2 n_{\mathrm{s}}/mk_{\mathrm{B}}T = \beta J$ with $J = \hbar^2 n_{\mathrm{s}}/m$ being the superfluid phase stiffness. Here, we have explicitly substituted the superfluid density for the density $n \to n_{\mathrm{s}}$. This is indeed a reasonable substitution and can be shown through Popov's treatment (see Appendix A.2). The phase action (2.58) is equivalent to the XY model in the continuum limit.

With vortices with charge $\{q_i\}$ at locations $\{\boldsymbol{r}_i\}$ in a closed region Ω, the distortion field $\boldsymbol{\nabla}\theta$ satisfies

$$\oint_{\partial\Omega} \mathrm{d}\boldsymbol{r} \cdot \boldsymbol{\nabla}\theta = 2\pi \sum_i q_i, \tag{2.59}$$

which leads to

$$\boldsymbol{\nabla}\theta = \boldsymbol{\nabla}\phi - \boldsymbol{\nabla} \times [\boldsymbol{e}_z f(\boldsymbol{r})] \,, \tag{2.60}$$

with $\phi(\boldsymbol{r})$ being a regular function. The second term in Eq. (2.60) guarantees $\boldsymbol{\nabla} \times \boldsymbol{\nabla}\theta = 2\pi \sum_i q_i \delta^2(\boldsymbol{r} - \boldsymbol{r}_i)$, which represents the presence of vortices with the stream function $f(\boldsymbol{r}) = \sum_i q_i \ln|\boldsymbol{r} - \boldsymbol{r}_i|$. Since a vortex with a higher charge is energetically unstable as mentioned in Sec. 2.4, we can assume $q_i = \pm 1$. Inserting Eq. (2.60) into the XY action (2.58), we obtain

$$S_{\mathrm{XY}} = \frac{\hbar K}{2} \int \mathrm{d}^2\boldsymbol{r} \left[(\boldsymbol{\nabla}\phi)^2 + (\boldsymbol{\nabla} \times \boldsymbol{e}_z f)^2 \right] = S_{\mathrm{SW}}[\phi] + S_{\mathrm{top}}[\{\sigma_i\}], \tag{2.61}$$

with

$$S_{\rm SW}[\phi] = \frac{\hbar K}{2}\int {\rm d}^2\boldsymbol{r}\,(\boldsymbol{\nabla}\phi)^2\,, \tag{2.62}$$

being the spin-wave contribution while

$$\begin{aligned} S_{\rm top}[\{q_i\}] &= \frac{\hbar K}{2}\int {\rm d}^2\boldsymbol{r}\,(\boldsymbol{\nabla}\times\boldsymbol{e}_z f)^2 = -2\pi^2\hbar K\sum_{i,j} q_i q_j C(\boldsymbol{r}_i-\boldsymbol{r}_j) \\ &= \sum_i S_i^{\rm core} - 4\pi^2\hbar K\sum_{i<j} q_i q_j C(\boldsymbol{r}_i-\boldsymbol{r}_j), \end{aligned} \tag{2.63}$$

being the topological contribution due to the vortices. Here, $C(\boldsymbol{r}) = \ln|\boldsymbol{r}|/2\pi$ is the 2D Coulomb potential. The infrared divergence originating from the Coulomb potential for $\boldsymbol{r}=0$ is absorbed into the vortex core contribution $\sum_i S_i^{\rm core}$. The partition function is then obtained as

$$Z = \int \mathcal{D}\theta\, e^{-S_{\rm XY}/\hbar} = Z_{\rm SW} Z_{\rm top}, \tag{2.64}$$

with

$$Z_{\rm SW} = \int \mathcal{D}\phi\, e^{-S_{\rm SW}[\phi]/\hbar}, \tag{2.65}$$

and

$$\begin{aligned} Z_{\rm top} &= \sum_{N=0}^{\infty}\frac{1}{(N!)^2}\int\left(\prod_{i=1}^{2N}{\rm d}^2\boldsymbol{r}_i\right) e^{-S_{\rm top}[\{q_i\}]/\hbar} \\ &= \sum_{N=0}^{\infty}\frac{y^{2N}}{(N!)^2}\int\left(\prod_{i=1}^{2N}{\rm d}^2\boldsymbol{r}_i\right)\exp\left[4\pi^2 K\sum_{i<j} q_i q_j C(\boldsymbol{r}_i-\boldsymbol{r}_j)\right], \end{aligned} \tag{2.66}$$

where $y = \exp[-S^{\rm core}_{q=\pm1}/\hbar]$ is the vortex fugacity. The combinatorial factor $1/(N!)^2$ in Eq. (2.66) cancels the overcounting of the vortices. Since the spin-wave contribution in $Z_{\rm SW}$ is Gaussian and analytic, any phase transition must originate from the topological contribution $Z_{\rm top}$ which is equivalent to a 2D Coulomb gas.

To obtain the RG equations describing the superfluid phase transition, we have two possible ways. One is to directly consider the effective Coulomb interaction screened by other vortices using Eq. (2.66). Another slightly different path is to utilize the equivalence with the sine-Gordon model. In this section, we show the former derivation. The latter approach is also given in Appendix A.3.

In Eq. (2.66), $C(\boldsymbol{r}_i-\boldsymbol{r}_j)$ represents the Coulomb interaction potential between two vortices located at $\boldsymbol{r}_i$ and $\boldsymbol{r}_j$. Let us consider the screening effect on the Coulomb interaction between two vortices of charges $+1$ and -1 due to the other vortices. With the ensemble average in terms of the topological action

$$\langle O(\boldsymbol{r})\rangle_{\rm top} \equiv \frac{1}{Z_{\rm top}}\sum_{N=0}^{\infty}\frac{1}{(N!)^2}\int\left(\prod_{i=1}^{2N}{\rm d}^2\boldsymbol{r}_i\right) O(\boldsymbol{r}) e^{-S_{\rm top}[\{q_i\}]/\hbar}, \tag{2.67}$$

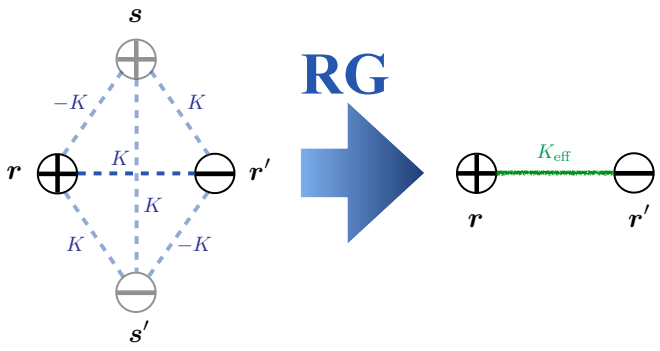

Figure 2.3: RG procedure of intervortex interactions between a vortex at $\boldsymbol{r}$ and an antivortex at $\boldsymbol{r}'$ calculated in Eq. (2.68).

the effective interaction can be written as

$$\begin{aligned} e^{-4\pi^2 K_{\text{eff}} C(\boldsymbol{r}-\boldsymbol{r}')} &\equiv \left\langle e^{-4\pi^2 K C(\boldsymbol{r}-\boldsymbol{r}')} \right\rangle_{\text{top}} \\ &= e^{-4\pi^2 K C(\boldsymbol{r}-\boldsymbol{r}')} \left[1 + y^2 \int \mathrm{d}^2\boldsymbol{s}_1\, \mathrm{d}^2\boldsymbol{s}_2\, e^{-4\pi^2 K C(\boldsymbol{s}_1-\boldsymbol{s}_2)} e^{4\pi^2 K D(\boldsymbol{r},\boldsymbol{r}';\boldsymbol{s}_1,\boldsymbol{s}_2)} + \mathcal{O}\big(y^4\big)\right] \\ &\times \left[1 + y^2 \int \mathrm{d}^2\boldsymbol{s}_1\, \mathrm{d}^2\boldsymbol{s}_2\, e^{-4\pi^2 K C(\boldsymbol{s}_1-\boldsymbol{s}_2)} + \mathcal{O}\big(y^4\big)\right]^{-1} \\ &= e^{-4\pi^2 K C(\boldsymbol{r}-\boldsymbol{r}')} \left[1 + y^2 \int \mathrm{d}^2\boldsymbol{s}_1\, \mathrm{d}^2\boldsymbol{s}_2 \left[e^{4\pi^2 K D(\boldsymbol{r},\boldsymbol{r}';\boldsymbol{s}_1,\boldsymbol{s}_2)} - 1\right] + \mathcal{O}\big(y^4\big)\right], \end{aligned} \tag{2.68}$$

with $D(\boldsymbol{r},\boldsymbol{r}';\boldsymbol{s}_1,\boldsymbol{s}_2) \equiv C(\boldsymbol{r}-\boldsymbol{s}_1) - C(\boldsymbol{r}-\boldsymbol{s}_2) - C(\boldsymbol{r}'-\boldsymbol{s}_1) + C(\boldsymbol{r}'-\boldsymbol{s}_2)$ describing the interaction among the internal and external vortex dipoles as sketched in Fig. 2.3. Using $\bar{\boldsymbol{s}} \equiv (\boldsymbol{s}_1+\boldsymbol{s}_2)/2$ and $\boldsymbol{s} = \boldsymbol{s}_2 - \boldsymbol{s}_1$ and assuming $|\boldsymbol{s}|$ much smaller than any other length scale $\boldsymbol{r}-\bar{\boldsymbol{s}}$ and $\boldsymbol{r}'-\bar{\boldsymbol{s}}$, one can write

$$\begin{aligned} e^{-4\pi^2 K_{\text{eff}} C(\boldsymbol{r}-\boldsymbol{r}')} &= e^{-4\pi^2 K C(\boldsymbol{r}-\boldsymbol{r}')} \left[1 + 16\pi^5 K^2 y^2 C(\boldsymbol{r}-\boldsymbol{r}') \int_1^\infty \mathrm{d}x\, x^{3-2\pi K} + \mathcal{O}\big(y^4\big)\right] \\ &= e^{-4\pi^2 K C(\boldsymbol{r}-\boldsymbol{r}') + 16\pi^5 K^2 y^2 C(\boldsymbol{r}-\boldsymbol{r}') \int_1^\infty \mathrm{d}x x^{3-2\pi K}}, \end{aligned} \tag{2.69}$$

with a short-range cutoff a and $x = r/a$. The short-range cutoff length corresponds to the vortex core size ξ in Eq. (2.36). See Appendix A.3.2 for the details of the above computation. Consequently, one obtains the relation

$$K_{\text{eff}} = K - 4\pi^3 K^2 y^2 \int_1^\infty \mathrm{d}x\, x^{3-2\pi K}, \tag{2.70}$$

or equivalently, up to $\mathcal{O}(y^2)$,

$$K_{\rm eff}^{-1} = K^{-1} + 4\pi^3 y^2 \int_1^\infty \mathrm{d}x\, x^{3-2\pi K}. \tag{2.71}$$

By splitting the spatial integral at a boundary $b = e^{\mathrm{d}l} = 1 + \mathrm{d}l$ with l the dimensionless RG scale and introducing

$$\tilde{K}^{-1} \equiv K^{-1} + 4\pi^3 y^2 \int_1^b \mathrm{d}x\, x^{3-2\pi K}, \qquad \tilde{y} \equiv y b^{2-\pi K}, \tag{2.72}$$

Eq. (2.71) can be written as

$$K_{\rm eff}^{-1} = \tilde{K}^{-1} + 4\pi^3 \tilde{y}^2 \int_1^\infty x^{3-2\pi \tilde{K}}, \tag{2.73}$$

after rescaling $x \to x/b$. Finally, with $\partial_l K(l)^{-1} = [\tilde{K}^{-1}(l) - K(l)^{-1}]/\,\mathrm{d}l$ and $\partial_l y(l) = [\tilde{y}(l) - y(l)]/\,\mathrm{d}l$, Eqs. (2.72) read

$$\partial_l K(l)^{-1} = 4\pi^3 y(l)^2, \tag{2.74a}$$

$$\partial_l y(l) = [2 - \pi K(l)]\, y(l). \tag{2.74b}$$

The RG equations (2.74) are referred to as Nelson-Kosterlitz (NK) RG equations. As we have seen, this renormalization procedure includes the effects of additional vortices screening the bare inter-vortex Coulomb interaction strength K. We can therefore understand that the RG equations (2.74) incorporate the many-body effect to the phase stiffness and vortex fugacity taking into account a number of vortices occupying the system. The fixed point is determined by

$$K_{\rm c} = \frac{2}{\pi}, \tag{2.75}$$

which is referred to as the NK criterion. It indeed implicitly determines the BKT transition temperature $T_{\rm c}$ as

$$k_{\rm B} T_{\rm c} = \frac{\pi \hbar^2}{2m} n_{\rm s}(T_{\rm c}). \tag{2.76}$$

2.6.2 Discontinuous jump in superfluid density

As a consequence of the renormalization, the superfluid density exhibits a discontinuity at the BKT transition temperature (universal jump) in the thermodynamic limit. Figure 2.4(a) shows the RG flow of Eqs. (2.74). At low temperatures below $T_{\rm c}$, $2 - \pi K$ can be negative and the vortex fugacity y is irrelevant flowing to $y^* = 0$. It implies that vortex excitations can appear only in the form of neutral pairs as depicted in Fig. 2.2. The Coulomb interaction strength is renormalized as $K_{\rm eff} = K(l \to \infty) \geq K_{\rm c}$. At higher

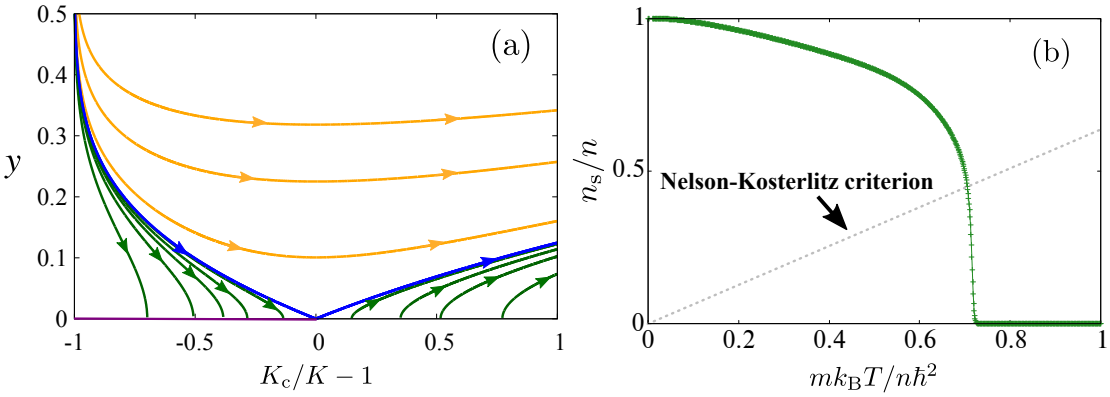

Figure 2.4: (a) NK RG flow and (b) superfluid fraction calculated with Eqs. (2.74) under $L = 200\xi$. The violet line $K_c/K - 1 \leq 0$ corresponds to the fixed line. The gray thin dotted line in (b) stands for $k_B T = \pi\hbar^2 n_s(T)/2m$ which intersects with the superfluid density at $T = T_c$ in the thermodynamic limit $L \to \infty$.

temperatures than T_c, on the other hand, $2 - \pi K$ is positive and the vortex fugacity y is a relevant variable flowing to infinity as $\sim K_c/K - 1$. It implies a proliferation of vortices and K is renormalized to zero. In summary, below T_c, the superfluid density is finite and decreases by increasing the temperature. At the BKT transition temperature T_c, it discontinuously jumps to zero. Figure 2.4(b) shows the superfluid fraction as a function of temperature. The maximum RG scale is related to the system size as $l_{\max} = \ln(L/\xi)$. We set $L = 200\xi$ in Fig. 2.4(b). In a finite-size system with $l_{\max} < \infty$, the superfluid density exhibits a continuous drop at the BKT transition temperature. The sharp drop changes to a discontinuous jump in the thermodynamic limit $l_{\max} \to \infty$. This starkly contrasts the condensate density in a 3D BEC, which continuously vanishes at the BEC transition temperature.

2.6.3 Algebraic long-range order

One can show that the 2D Bose superfluid exhibits algebraic decay of the long-range order. To see it, let us consider the single-body density matrix in Eq. (2.3). Under Eqs. (2.57) and (2.58), we can write

$$\rho_1(\boldsymbol{r}, \boldsymbol{r}') = \langle \Psi^\dagger(\boldsymbol{r})\Psi(\boldsymbol{r}')\rangle = n \left\langle e^{-i[\theta(\boldsymbol{r})-\theta(\boldsymbol{r}')]} \right\rangle_{\rm XY}, \tag{2.77}$$

where $\langle \cdots \rangle_{\rm XY}$ stands for the ensemble average with respect to Eq. (2.58). We can show

$$\lim_{|\boldsymbol{r}-\boldsymbol{r}'|\to\infty} \rho_1(\boldsymbol{r}, \boldsymbol{r}') \propto \left|\boldsymbol{r} - \boldsymbol{r}'\right|^{-\eta(T)}, \tag{2.78}$$

with

$$\eta(T) = \frac{1}{2\pi K}. \tag{2.79}$$

For details of the above calculation, see Appendix B. Equation (2.78) indicates the algebraic decay of the long-range order instead of the exponential one. Several experimental reports of $\eta(T)$ in 2D systems such as exciton-polariton systems and superconducting thin films show the exponent at the BKT transition temperature $\eta(T_{\mathrm{BKT}}) \simeq 0.25$ [144, 146, 147, 148, 149], which supports Eq. (2.75).

Chapter 3

Sound propagation in quantum fluids

This Chapter presents an introduction to theoretical tools to study sound propagation in dilute Bose gases. We first see the transport in a classical fluid described by the Boltzmann equation focusing on the hydrodynamic regime, which provides classical hydrodynamic equations. Introducing superfluidity, we derive Landau's two-fluid equations resulting in the second sound due to the propagation of entropy wave as well as the first sound associated with density fluctuations in quantum fluids.

3.1 Boltzmann equation and hydrodynamic sound in classical fluids

Physical kinetics can be described by following the time evolution of a distribution function of a fluid $f(\boldsymbol{r}, \boldsymbol{p}, t)$ at a point $(\boldsymbol{r}, \boldsymbol{p})$ in phase space at time t. Let us consider atoms with mass m occupying a cell of volume $\mathrm{d}\boldsymbol{r}\,\mathrm{d}\boldsymbol{p}$ at $(\boldsymbol{r}, \boldsymbol{p})$ at time t. In the absence of collisions under an external conservative force $\boldsymbol{F} = -\boldsymbol{\nabla} U(\boldsymbol{r}, t)$, under the equation of motion

$$\dot{\boldsymbol{r}} = \frac{\boldsymbol{p}}{m}, \qquad \dot{\boldsymbol{p}} = \boldsymbol{F}, \tag{3.1}$$

the atoms evolve to $(\boldsymbol{r}' = \boldsymbol{r} + \boldsymbol{v}\delta t, \boldsymbol{p}' = \boldsymbol{p} + \boldsymbol{F}\delta t)$ at time $t + \delta t$ and the volume of the occupied cell is invariant $\mathrm{d}\boldsymbol{r}'\,\mathrm{d}\boldsymbol{p}' = \mathrm{d}\boldsymbol{r}\,\mathrm{d}\boldsymbol{p}$. Then, the number of atoms in the cell is conserved as

$$f\left(\boldsymbol{r} + \frac{\boldsymbol{p}}{m}\delta t, \boldsymbol{p} + \boldsymbol{F}\delta t, t + \delta t\right) \mathrm{d}\boldsymbol{r}'\,\mathrm{d}\boldsymbol{p}' = f(\boldsymbol{r}, \boldsymbol{p}, t)\,\mathrm{d}\boldsymbol{r}\,\mathrm{d}\boldsymbol{p}\,. \tag{3.2}$$

Up to the linear order in δt, Eq. (3.2) provides the *Boltzmann equation*

$$\left(\partial_t + \frac{\boldsymbol{p}}{m} \cdot \boldsymbol{\nabla} + \boldsymbol{F} \cdot \boldsymbol{\nabla}_{\boldsymbol{p}}\right) f(\boldsymbol{r}, \boldsymbol{p}, t) = I_{\mathrm{coll}}[f], \tag{3.3}$$

where the right-hand-side $I_{\rm coll}[f]$ is the collision integral term which describes the atoms flowing into the cell or drifting outside the cell due to interatomic collision. The collision integral is given by

$$\begin{aligned} I_{\rm coll}[f] &= \sum_{\boldsymbol{p}_1,\boldsymbol{p}_1',\boldsymbol{p}'} \left[w(\boldsymbol{p}',\boldsymbol{p}_1'|\boldsymbol{p},\boldsymbol{p}_1) f(\boldsymbol{r},\boldsymbol{p}',t) f(\boldsymbol{r},\boldsymbol{p}_1',t) - w(\boldsymbol{p},\boldsymbol{p}_1|\boldsymbol{p}',\boldsymbol{p}_1') f(\boldsymbol{r},\boldsymbol{p},t) f(\boldsymbol{r},\boldsymbol{p}_1,t) \right] \\ &= \sum_{\boldsymbol{p}_1,\boldsymbol{p}_1',\boldsymbol{p}'} w(\boldsymbol{p}',\boldsymbol{p}_1'|\boldsymbol{p},\boldsymbol{p}_1) \left[f(\boldsymbol{r},\boldsymbol{p}',t) f(\boldsymbol{r},\boldsymbol{p}_1',t) - f(\boldsymbol{r},\boldsymbol{p},t) f(\boldsymbol{r},\boldsymbol{p}_1,t) \right], \end{aligned} \tag{3.4}$$

with $w(\boldsymbol{p}',\boldsymbol{p}_1'|\boldsymbol{p},\boldsymbol{p}_1)$ being the transition rate between the momentum states describing the scattering in and out of momentum states. For elastic scattering, $w(\boldsymbol{p}',\boldsymbol{p}_1'|\boldsymbol{p},\boldsymbol{p}_1)$ satisfies momentum conservation and energy conservation. In the second equality of Eq. (3.4), we assumed the time-reversal symmetry and parity symmetry leading to $w(\boldsymbol{p}',\boldsymbol{p}_1'|\boldsymbol{p},\boldsymbol{p}_1) = w(\boldsymbol{p},\boldsymbol{p}_1|\boldsymbol{p}',\boldsymbol{p}_1')$. The detailed-balance condition

$$f(\boldsymbol{r},\boldsymbol{p}',t) f(\boldsymbol{r},\boldsymbol{p}_1',t) = f(\boldsymbol{r},\boldsymbol{p},t) f(\boldsymbol{r},\boldsymbol{p}_1,t) \tag{3.5}$$

cancels the collision integral (3.4). In addition to the diffusive term, the Boltzmann equation (3.3) has two terms relaxing the fluids toward equilibrium. One is the third term in the left-hand-side associated with the external force $\boldsymbol{F} = -\boldsymbol{\nabla} U$. The other is the collision integral $I_{\rm coll}$. The regime in which the latter contribution is dominant compared to the former one is referred to as *collisional regime* or *hydrodynamic regime*. If the former contribution plays the major role, the regime is called *collisionless regime*. To discuss the regimes, it is convenient to introduce *collisional time* $\tau_{\rm coll}$ via the following relaxation time approximation

$$I_{\rm coll} = -\frac{f(\boldsymbol{r},\boldsymbol{p},t) - f_0(\boldsymbol{r},\boldsymbol{p})}{\tau_{\rm coll}}, \tag{3.6}$$

where $f_0(\boldsymbol{r},\boldsymbol{p})$ is the distribution function in equilibrium. If the collisional time is much shorter than the typical time scale of the fluid ω^{-1}, the fluid is in the collisional regime. If the collisional time is much longer than the typical time scale, the fluid is in the deep collisionless regime. In this Thesis, we mainly focus on the collisional regime.

For a D-dimensional classical fluid of volume V in thermal equilibrium depicted in Fig. 3.1(a), the Maxwell-Boltzmann distribution function

$$f_0^{\rm MB}(\boldsymbol{p}) = \exp\left[-\beta \left(\frac{p^2}{2m} - \mu \right) \right] \tag{3.7}$$

satisfies the detailed-balance condition (3.5) with $\beta = 1/k_{\rm B}T$ being the inverse temperature and the chemical potential μ is determined from the number equation

$$n = \frac{N}{V} = \left(\frac{k_{\rm B}T}{2m} \right)^{3/2} \sum_{\boldsymbol{p}} f_0^{\rm MB}(\boldsymbol{p}). \tag{3.8}$$

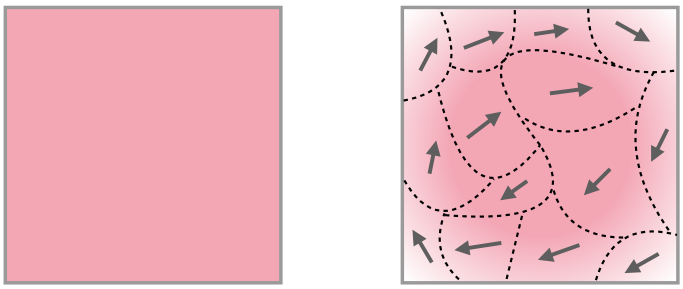

$T(\boldsymbol{r},t)=T$
$\mu(\boldsymbol{r},t)=\mu$
$\boldsymbol{u}(\boldsymbol{r},t)=0$
(a) Global equilibrium

$T(\boldsymbol{r},t)$
$\mu(\boldsymbol{r},t)$
$\boldsymbol{u}(\boldsymbol{r},t)$
(b) Local equilibrium

Figure 3.1: Schematic figures of (a) global equilibrium and (b) local equilibrium.

Note that the vanishing collision integral does not mean a collisionless regime. It implies a collisional regime in which sufficient collisions of atoms keep the distribution equilibrium to cancel Eq. (3.4) even with a small collisional time $\omega\tau_{\rm coll}\ll 1$.

The Maxwell-Boltzmann distribution in *local equilibrium* given by

$$f^{\rm MB}(\boldsymbol{r},\boldsymbol{p},t)=\exp\left[-\beta(\boldsymbol{r},t)\left[\frac{(\boldsymbol{p}-m\boldsymbol{u}(\boldsymbol{r},t))^2}{2m}-\mu(\boldsymbol{r},t)\right]\right] \tag{3.9}$$

also satisfies the detailed-balance condition (3.5) though Eq. (3.9) is different from thermal equilibirum. The local equilibrium illustrated in Fig. 3.1(b) is specified by the local temperature $T(\boldsymbol{r},t)$ and the local chemical potential $\mu(\boldsymbol{r},t)$ in addition to the local velocity $\boldsymbol{u}(\boldsymbol{r},t)$. The chemical potential $\mu(\boldsymbol{r},t)$ is determined from

$$n(\boldsymbol{r},t)=\left(\frac{k_{\rm B}T(\boldsymbol{r},t)}{2m}\right)^{3/2}\sum_{\boldsymbol{p}}f^{\rm MB}(\boldsymbol{r},\boldsymbol{p},t). \tag{3.10}$$

The Boltzmann equation with the local equilibrium distribution (3.9) leads to several conservation laws by multiplying p^k and performing the momentum integral of Eq. (3.3). With $k=0$, one obtains the continuity equation

$$\partial_t n(\boldsymbol{r},t)+\boldsymbol{\nabla}\cdot\boldsymbol{j}(\boldsymbol{r},t)=0, \tag{3.11}$$

corresponding to the number conservation with

$$\boldsymbol{j}(\boldsymbol{r},t)=\sum_{\boldsymbol{p}}\frac{\boldsymbol{p}}{m}f^{\rm MB}(\boldsymbol{r},\boldsymbol{p},t), \tag{3.12}$$

being the current density. With $k=1$, the Boltzmann equation gives the momentum conservation law

$$m\partial_t\boldsymbol{j}(\boldsymbol{r},t)+\sum_{\boldsymbol{p}}(\boldsymbol{p}\cdot\boldsymbol{\nabla})\frac{\boldsymbol{p}}{m}f^{\rm MB}(\boldsymbol{r},\boldsymbol{p},t)=-\boldsymbol{\nabla}U(\boldsymbol{r},t)n(\boldsymbol{r},t). \tag{3.13}$$

Finally, $k = 2$ provides the energy conservation

$$\partial_t \mathcal{E}(\boldsymbol{r}, t) + \boldsymbol{\nabla} \cdot \sum_{\boldsymbol{p}} \frac{\boldsymbol{p}}{m} \frac{p^2}{2m} f^{\mathrm{MB}}(\boldsymbol{r}, \boldsymbol{p}, t) = -\boldsymbol{\nabla} U(\boldsymbol{r}, t) \cdot \boldsymbol{j}(\boldsymbol{r}, t), \tag{3.14}$$

with $\mathcal{E}(\boldsymbol{r}, t) = \sum_{\boldsymbol{p}} p^2/(2m) f^{\mathrm{MB}}(\boldsymbol{r}, \boldsymbol{p}, t)$ the energy density.

To describe sound waves, we decompose the hydrodynamic quantities into the equilibrium part and fluctuating part as $n(\boldsymbol{r}, t) = n_0 + \delta n(\boldsymbol{r}, t)$ and $\boldsymbol{j}(\boldsymbol{r}, t) = n_0 \boldsymbol{v}(\boldsymbol{r}, t)$ with $\boldsymbol{v}(\boldsymbol{r}, t)$ being the velocity field which vanishes in thermal equilibrium. The hydrodynamic equations (3.11), (3.13), and (3.14) reduce to

$$\partial_t n(\boldsymbol{r}, t) + n_0 \boldsymbol{\nabla} \cdot \boldsymbol{v}(\boldsymbol{r}, t) = 0, \tag{3.15a}$$

$$m \partial_t \boldsymbol{j}(\boldsymbol{r}, t) = -\boldsymbol{\nabla} \mathcal{P}(\boldsymbol{r}, t) - n_0 \boldsymbol{\nabla} U(\boldsymbol{r}, t), \tag{3.15b}$$

$$\partial_t \mathcal{E}(\boldsymbol{r}, t) = -\left(\mathcal{E}_0 + \mathcal{P}_0\right) \boldsymbol{\nabla} \cdot \boldsymbol{v}(\boldsymbol{r}, t), \tag{3.15c}$$

up to the linear order of the fluctuation fields. Here, $\mathcal{P}(\boldsymbol{r}, t) = 2\mathcal{E}(\boldsymbol{r}, t)/3$ is the hydrodynamic pressure in a classical fluid and $\mathcal{P}_0 = 2\mathcal{E}_0/3 = n_0 k_{\mathrm{B}} T$ is the pressure in thermal equilibrium. They yield a wave equation

$$\partial_t^2 n(\boldsymbol{r}, t) - c_{\mathrm{cl}}^2 \boldsymbol{\nabla}^2 n(\boldsymbol{r}, t) = n \boldsymbol{\nabla}^2 U(\boldsymbol{r}, t), \tag{3.16}$$

where

$$c_{\mathrm{cl}} = \sqrt{\frac{5 k_{\mathrm{B}} T}{3m}} = \sqrt{\frac{1}{m} \left(\frac{\partial \mathcal{P}}{\partial n}\right)_s}, \tag{3.17}$$

is the classical sound velocity. It corresponds to the adiabatic sound velocity as in the second equality of Eq. (3.17). Indeed, Eqs. (3.15a) and (3.15c) give $n^{-1} \partial_t n = 3\mathcal{P}^{-1} \partial_t \mathcal{P}/5$, which reads the Poisson's relation $\mathcal{P} V^{5/3} = \text{const.}$ indicating adiabatic sound propagation.

3.2 Superfluidity and Landau's two-fluid model

To construct superfluid hydrodynamics, we start with Tisza-Landau's two-fluid model

$$n = n_{\mathrm{s}} + n_{\mathrm{n}}, \quad \boldsymbol{j} = n_{\mathrm{s}} \boldsymbol{v}_{\mathrm{s}} + n_{\mathrm{n}} \boldsymbol{v}_{\mathrm{n}}. \tag{3.18}$$

It reads that the fluid is composed of two components: normal fluid and superfluid. Here, n_{n} and n_{s} are the normal density and superfluid density, respectively, and $\boldsymbol{v}_{\mathrm{n}}$ and $\boldsymbol{v}_{\mathrm{s}}$ are the normal velocity and superfluid velocity, respectively. For the total density n and current density $\boldsymbol{j}$, we have the classical hydrodynamic equations given by

$$\partial_t n + \boldsymbol{\nabla} \cdot \boldsymbol{j} = 0, \tag{3.19a}$$

$$m\partial_t \boldsymbol{j} + \boldsymbol{\nabla} P = 0. \tag{3.19b}$$

The first equation (3.19a) is the continuity equation as in Eq. (3.11), and the latter one (3.19b) reads the momentum conservation with P the pressure as in Eq. (3.13) under $\boldsymbol{\nabla} U = 0$.

For superfluid, we have two additional hydrodynamic equations as

$$\partial_t(ns) + ns\boldsymbol{\nabla} \cdot \boldsymbol{v}_{\mathrm{n}} = 0, \tag{3.20a}$$

$$m\partial_t \boldsymbol{v}_{\mathrm{s}} + \boldsymbol{\nabla}\mu = 0, \tag{3.20b}$$

where s is the entropy per mass unit and μ is the chemical potential. The first equation (3.20a) reflects that only the normal fluid is responsible for the entropy flow, and the latter one (3.20b) reads the irrotational flow in the superfluid. The two-fluid hydrodynamics was first introduced by Tisza to explain Helium superfluidity in 1938 [3, 6, 7]. He claimed that the inviscid superfluid component corresponds to the condensed atoms, while the viscous normal component corresponds to the non-condensed atoms responsible for entropy flow. Later in 1941, Landau considered the quantization of fluids by imposing nontrivial commutation relations with Poisson brackets and proposed the two-fluid model and Landau criterion on the stability of superfluidity explained in Sec. 2.5.3 [4]. Landau's two-fluid model has several common features with Tisza's one. However, the major difference is that he interpreted the viscous normal component as the Bogoliubov quasiparticles due to the elementary excitations, which turned out to be a precise interpretation. Nowadays, the two-fluid model is referred to as Tisza-Landau's two-fluid model. Combining these four sets of hydrodynamic equations (3.19a), (3.19b), (3.20a), and (3.20b), one can derive two wave equations as

$$m\partial_t^2 n - \boldsymbol{\nabla}^2 P = 0, \tag{3.21}$$

which describes the propagation of a density wave common also in a classical fluid, and

$$\partial_t^2 s - \frac{n_{\mathrm{s}}}{n_{\mathrm{n}}} s^2 \boldsymbol{\nabla}^2 T = 0. \tag{3.22}$$

This second wave equation (3.22) is peculiar to the superfluid and describes the propagation of entropy wave. Note that, in classical fluids, the entropy just contributes to heat diffusion and does not propagate as a wave. Inserting the plane-wave solutions $n = n_0 + \delta n e^{\,i\omega(x/c-t)}$ and $s = s_0 + \delta s\, e^{i\omega(x/c-t)}$, one obtains

$$\begin{cases} \left(1 - c^2 \dfrac{\partial n}{\partial P}\right) \delta P - \omega^2 \dfrac{\partial n}{\partial T} \delta T = 0, \\ \left(\dfrac{n_{\mathrm{s}}}{n_{\mathrm{n}}} s^2 - c^2 \dfrac{\partial s}{\partial T}\right) \delta T - \omega^2 \dfrac{\partial s}{\partial P} \delta P = 0, \end{cases} \tag{3.23}$$

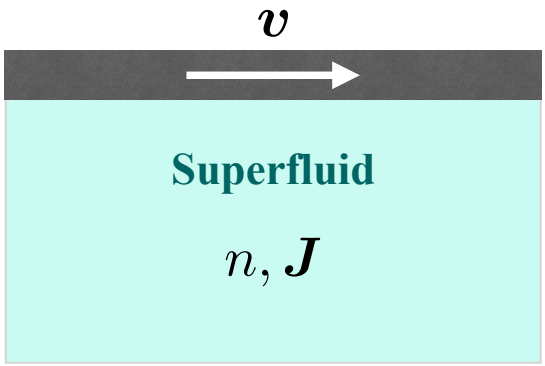

Figure 3.2: Setup we consider to derive the formula of the normal density (3.29b).

which results in the two-fluid equation

$$c^4 - \left(v_s^2 + v_{\rm L}^2\right) c^2 + v_T^2 v_{\rm L}^2 = 0, \tag{3.24}$$

with

$$v_T = \frac{1}{\sqrt{mn\kappa_T}}, \quad v_s = \frac{1}{\sqrt{mn\kappa_s}}, \quad v_{\rm L} = \sqrt{\frac{n_{\rm s} T s^2}{n_{\rm n} c_V}}, \tag{3.25}$$

the isothermal, adiabatic, and Landau velocities, respectively where κ_T and κ_s are the isothermal and adiabatic compressibilities, and c_V is the specific heat at constant volume [150]. The two-fluid equation (3.24) indicates two positive roots due to the additional entropy wave propagation. The larger velocity c_1 is called the first sound and the lower velocity c_2, which originates from the entropy wave propagation in the superfluid phase, is called *second sound*. The second sound was first predicted by Landau in 1941 [4]. In Sec. 3.3, we examine further details of the second sound in 3D, 2D, and 1D Bose gas.

3.2.1 Thermodynamic quantities and Landau's formula of normal density

Using a Helmholtz free energy $F[T, V, N]$, one can calculate the thermodynamic quantities as

$$\kappa_{T/s} = \frac{1}{n}\left(\frac{\partial n}{\partial P}\right)_{T/s}, \quad s = \frac{1}{mN}\left(\frac{\partial F}{\partial T}\right)_{N,V}, \quad c_V = T\left(\frac{\partial s}{\partial T}\right)_{N,V}. \tag{3.26}$$

Let us consider how to obtain the normal density in Eqs. (3.18). First, let us assume a uniform D-dimensional superfluid moving with velocity $\boldsymbol{v}$ in thermal equilibrium with the system size L^D in contact with a flat plate moving with the parallel velocity $\boldsymbol{v}$ as illustrated in Fig. 3.2. Galilean invariance guarantees the independence of the thermodynamic properties from the velocity $\boldsymbol{v}$. Next, by gradually decreasing the velocity of

the plate up to $\boldsymbol{v} = 0$, the velocity of the viscous normal fluid $\boldsymbol{v}_{\rm n}$ also decreases and ends up with $\boldsymbol{v}_{\rm n} = 0$. On the other hand, the inviscid superfluid remains at its velocity $\boldsymbol{v}_{\rm s} = \boldsymbol{v}$. Then, the current density $\boldsymbol{J}$ can be written as

$$\boldsymbol{J} = n_{\rm s}\boldsymbol{v}, \tag{3.27}$$

with $n_{\rm s}$ the superfluid density. The Bogoliubov theory gives the current density as

$$\begin{aligned}\boldsymbol{J} &= \frac{1}{mL^D}{\rm Re}\int {\rm d}\boldsymbol{r}\left\langle\hat{\Psi}^\dagger(\boldsymbol{r})(-i\hbar\boldsymbol{\nabla})\hat{\Psi}(\boldsymbol{r})\right\rangle \\ &= n\boldsymbol{v} + \frac{1}{mL^D}\sum_{\boldsymbol{p}}\boldsymbol{p}f_T(E'_p),\end{aligned} \tag{3.28}$$

with $\langle\cdots\rangle$ being the grand canonical ensemble average, E'_p being the excitation energy with the Doppler shift in Eq. (2.50), and $f_T(E)$ being the Bose distribution function given by Eq. (2.7). In the second equality of Eq. (3.28), we used Eqs. (2.49) and $n = L^{-D}\int {\rm d}^D\boldsymbol{r}\,\langle\hat{\Psi}^\dagger(\boldsymbol{r})\hat{\Psi}(\boldsymbol{r})\rangle$. By expanding the second term in Eq. (3.28) with respect to $\boldsymbol{v}$ up to the first order, the lowest term of the zeroth-order vanishes by the momentum summation $\sum_{\boldsymbol{p}}$ and Eq. (3.28) reads

$$\boldsymbol{J} = n_{\rm s}\boldsymbol{v} = (n - n_{\rm n})\boldsymbol{v}, \tag{3.29a}$$

$$n_{\rm n}(T) = -\frac{1}{DmL^D}\sum_{\boldsymbol{p}}p^2\frac{\partial f_T(E_p)}{\partial E_p}. \tag{3.29b}$$

The formula of the normal density in Eq. (3.29b) is called Landau's formula. It is consistent with the Landau criterion (2.52). Indeed, for an ideal Bose gas $g = 0$ with the parabolic dispersion $E_p = \varepsilon_p = p^2/2m$, the normal density in Eq. (3.29b) reads

$$\begin{aligned}n_{\rm n}^{\rm (free)}(T) &= -\frac{\Omega_D(2m)^{D/2+1}}{2D(2\pi)^D}\int_0^\infty {\rm d}\varepsilon\,\varepsilon^{D/2}\frac{\partial f_T(\varepsilon)}{\partial\varepsilon} = \frac{\Omega_D(2m)^{D/2+1}}{4(2\pi)^D}\int_0^\infty {\rm d}\varepsilon\,\varepsilon^{D/2-1}f_T(\varepsilon) \\ &= \frac{1}{L^D}\sum_{\boldsymbol{p}}f_T(\varepsilon_p) = n,\end{aligned} \tag{3.30}$$

where $\Omega_D = D\pi^{D/2}/\Gamma(D/2+1)$ is the volume of the D-dimensional unit sphere. Equation (3.30) indicates that the fluid totally behaves as a normal fluid and the superfluid density vanishes $n_{\rm s}^{\rm (free)}(T) = n - n_{\rm n}^{\rm (free)}(T) = 0$, which is consistent with the absence of superfluidity in an ideal Bose gas as mentioned below Eq. (2.52).

Hydrodynamics requires the assumption of the local equilibrium in a fluid depicted in Fig. 3.1(b) and assumes the sufficiently gradual spatial and temporal variations of the local physical quantities. Under these conditions, the current density and the number density can be extended as $\boldsymbol{J} \to \boldsymbol{j}(\boldsymbol{r}, t)$ and $n \to n(\boldsymbol{r}, t)$ appeared in Eqs. (3.18).

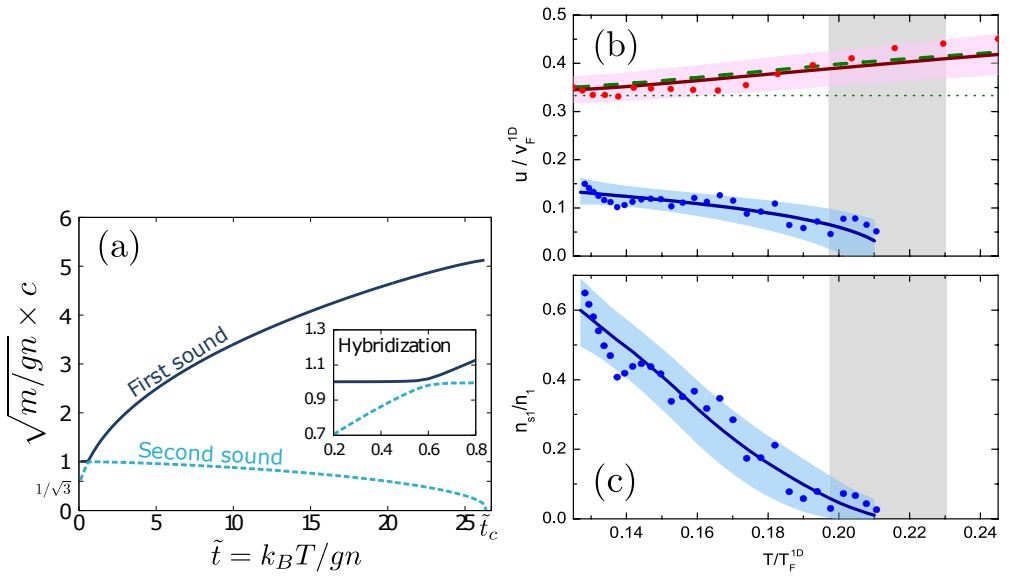

Figure 3.3: Quasicrossing behavior of first and second sound velocities at low temperatures in a 3D weakly-interacting Bose gas (left panel (a)) [151] and in a 3D unitary Fermi gas (right panel (b)) [152]. The right bottom panel (c) shows the superfluid density in the 3D unitary Fermi gas.

3.2.2 Quasicrossing of first and second sound modes

Before moving on to the discussion of sound modes in each dimension, we give a general insight from the two-fluid equation (3.24). First, in the normal phase above the superfluid phase transition temperature T_c, the superfluid density vanishes and $v_L \to 0$ indicating no propagation of entropy wave. The only remaining sound wave is the density mode corresponding to the first sound $c_1 = v_s$. It coincides with the speed of sound in classical fluids in Eq. (3.17). Below T_c, the density and entropy modes are coupled to each other as in Eqs. (3.23). This coupling is negligible if the cross-coupling coefficient is small $\alpha T \ll 1$ where

$$\alpha \equiv -\frac{1}{n}\left(\frac{\partial n}{\partial T}\right)_P = \frac{1}{T}\left(\frac{v_s^2}{v_T^2}-1\right), \tag{3.31}$$

is the thermal expansion coefficient. In this case, the two coupled equations (3.23) yield two independent wave equations for the propagation of density and entropy waves respectively. The incompressibility condition $\alpha T \ll 1$ is satisfied generally in the vicinity of zero temperature in which $v_T \simeq v_s$. The first and second sound velocities determined from Eq. (3.24) exhibit quasicrossing behavior in the low-temperature regime related to the compressibility of the fluid. The quasicrossing characterizes the temperature at which the density and entropy modes start to mix. In a 3D weakly-interacting Bose superfluid, the mean-field analysis in the low-temperature regime predicts the quasicrossing behavior as shown in Fig. 3.3(a) [151]. In a unitary Fermi gas, on the other hand, such quasicrossing behavior cannot be observed as in Fig. 3.3(b) because the

incompressibility makes the two sound modes uncoupled in a wide range of temperatures [152]. In the next section, we include quantum fluctuations in the free energy to consider the quantum effects on the sound velocities in a collisional Bose superfluid in D-dimension.

3.3 Sound modes in dilute Bose gases

In this section, we give our predictions of first and second sound velocities in 3D, 2D, and 1D Bose superfluids including the beyond-mean-field quantum correction. To this end, first of all, we prepare the Helmholtz free energy in a D-dimensional weakly-interacting Bose superfluid given by

$$\begin{aligned} F &= F_0 + F_{\rm Q} + F_T \\ &= \frac{gN^2}{2L^D} + \frac{1}{2}\sum_{\boldsymbol{p}} E_p + k_{\rm B}T \sum_{\boldsymbol{p}} \ln\left(1 - e^{-E_p/k_{\rm B}T}\right), \end{aligned} \tag{3.32}$$

where F_0 is the mean-field zero-temperature free energy with g the Bose-Bose contact interaction strength, L^D the system size, and F_T is the free energy at finite temperature associated with the Bogoliubov spectrum $E_p = \sqrt{\varepsilon_p\left(\varepsilon_p + 2gn\right)}$ with $n = N/L^D$ the D-dimensional number density. For convenience, we define a gas parameter

$$\eta_D \equiv \frac{mg}{2\pi\hbar^2} n^{1-2/D}, \tag{3.33}$$

which is indeed identical to $gn/[k_{\rm B}T_{\rm c}\zeta(D/2)^{2/D}]$ for $D = 3$ where $T_{\rm c}$ is the BEC transition temperature $T_{\rm BEC}$ in an ideal Bose gas given in Eq. (2.14). The quantum correction $F_{\rm Q}$ corresponds to the zero-point fluctuations and requires regularization to remove the ultraviolet divergence. Dimensional regularization results in [153, 154]

$$F_{\rm Q} = \begin{cases} L^3 \dfrac{8}{15\pi^2\hbar^3} m^{3/2} (gn)^{5/2} & (D = 3), \\ -L^2 \dfrac{m}{8\pi\hbar^2} \left[\ln\left(\dfrac{\epsilon_\Lambda}{gn}\right) - \dfrac{2}{\eta_2}\right] (gn)^2 & (D = 2), \\ -L \dfrac{2}{3\pi\hbar} m^{1/2} (gn)^{3/2} & (D = 1), \end{cases} \tag{3.34}$$

for each spatial dimension. For details of the dimensional regularization, see Appendix C. For 2D, it involves an ultraviolet energy cutoff $\epsilon_\Lambda = 4\hbar^2 e^{-2\gamma-1/2}/(ma_{\rm 2D}^2) \gg gn$ with $a_{\rm 2D}$ the 2D scattering length and $\gamma = 0.577\cdots$ is the Euler-Mascheroni's constant.

Denoting $P_{\rm MF}$ as the pressure which includes the mean-field plus the thermal contributions, and $P_{\rm Q}$ as the quantum correction to the pressure, one can obtain

$$v_T = \sqrt{\frac{1}{m}\left(\frac{\partial\left(P_{\rm MF} + P_{\rm Q}\right)}{\partial n}\right)_T} = \sqrt{v_{T,\rm MF}^2 + v_{\rm Q}^2}, \tag{3.35}$$

where $v_{T,\mathrm{MF}}$ is the isothermal velocity within the mean-field theory and

$$v_{\mathrm{Q}}^2 \equiv \frac{1}{m}\left(\frac{\partial P_{\mathrm{Q}}}{\partial n}\right)_T, \tag{3.36}$$

is the beyond-mean-field correction to the isothermal velocity. Since F_{Q} is the zero-temperature free energy, it does not affect the Landau velocity v_{L} and the quantum correction to the adiabatic velocity is identical to that of the isothermal one as

$$v_s = \sqrt{v_{s,\mathrm{MF}}^2 + v_{\mathrm{Q}}^2}, \tag{3.37}$$

where $v_{s,\mathrm{MF}}$ is the adiabatic velocity within the mean-field theory. The explicit expressions of the quantum correction v_{Q}^2 are given by

$$v_{\mathrm{Q}}^2 = \begin{cases} \dfrac{2\left(2\pi\eta_3\right)^{3/2}}{\pi^2} c_{\mathrm{B}}^2 & (D=3), \\ -\dfrac{\eta_2}{2}\left[\ln\left(\dfrac{\epsilon_\Lambda}{gn}\right) - \dfrac{2}{\eta_2} - \dfrac{1}{2}\right] c_{\mathrm{B}}^2 & (D=2), \\ -\sqrt{\dfrac{\eta_1}{2\pi}} c_{\mathrm{B}}^2 & (D=1), \end{cases} \tag{3.38}$$

Figure 3.4 represents the quantum correction v_{Q}^2 to the gas parameter η_D in each dimension. One can see that v_{Q}^2 vanishes as $\eta_D \to 0$ in any dimension. The quantum correction v_{Q}^2 is positive in 3D while it is negative in 1D. In 2D, it is positive for $\eta_2 > \pi/\left(2eN\right)$ and in the thermodynamic limit $N \to \infty$, one can assume $v_{\mathrm{Q}}^2 > 0$.

Zero temperature

Within the mean-field level at zero temperature, the Bogoliubov dispersion can be simplified as a linear phononic one $E_p = c_{\mathrm{B}} p$. It yields analytic expressions of both first and second sound velocities. Under $g \neq 0$, the free energy in Eq. (3.32) can be written as

$$\frac{F}{N} = \frac{gn}{2} - \frac{\Omega_D \Gamma(D)\zeta(D+1)}{(2\pi\hbar)^D} \frac{m^{D/2}}{g^{D/2} n^{D/2+1}} (k_{\mathrm{B}}T)^{D+1}. \tag{3.39}$$

It provides the thermodynamic quantities as

$$P = \frac{gn^2}{2} + \left(\frac{D}{2}+1\right) \frac{\Omega_D \Gamma(D)\zeta(D+1)}{(2\pi\hbar)^D} \frac{m^{D/2}}{g^{D/2} n^{D/2}} (k_{\mathrm{B}}T)^{D+1}, \tag{3.40a}$$

$$s = (D+1) \frac{\Omega_D \Gamma(D)\zeta(D+1)}{(2\pi\hbar)^D} \frac{m^{D/2-1}}{g^{D/2} n^{D/2+1}} (k_{\mathrm{B}}T)^{D}, \tag{3.40b}$$

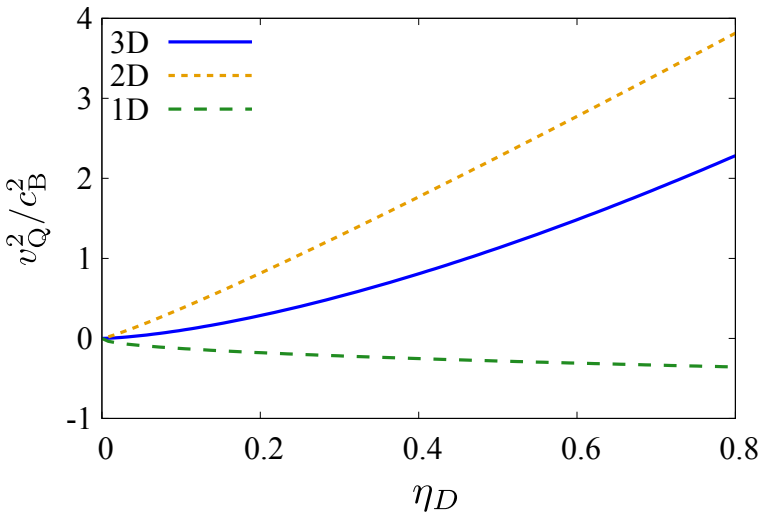

Figure 3.4: The beyond-mean-field correction to the isothermal and adiabatic velocity $v_{\rm Q}^2$ for $D = 1, 2, 3$ scaled by the Bogoliubov velocity $c_{\rm B} = \sqrt{gn/m}$ [90]. The horizontal axis is the gas parameter $\eta_D = mgn^{1-2/D}/2\pi\hbar^2$. For $D = 2$, the number of particles is set to $N = 10^4$.

$$c_V = D(D+1)\frac{\Omega_D \Gamma(D)\zeta(D+1)}{(2\pi\hbar)^D}\frac{m^{D/2-1}}{g^{D/2}n^{D/2+1}}(k_{\rm B}T)^D, \tag{3.40c}$$

$$n_{\rm n} = (D+1)\frac{\Omega_D \Gamma(D)\zeta(D+1)}{(2\pi\hbar)^D}\frac{m^{D/2+1}}{g^{D/2+1}n^{D/2+1}}(k_{\rm B}T)^{D+1}. \tag{3.40d}$$

They give

$$c_1 = v_{T,\rm MF} = v_{s,\rm MF} = c_{\rm B}, \quad c_2 = v_{\rm L} = \frac{1}{\sqrt{D}}c_{\rm B}. \tag{3.41}$$

Hydrodynamic conditions

Our theoretical framework is reliable in the collisional regime in which the hydrodynamic description of the system is valid. As discussed below Eq. (3.6), the condition is $\omega\tau_{\rm coll} \ll 1$ with $\tau_{\rm coll}$ being the collisional time and $\omega \simeq c_{\rm B}k$ being the frequency of the excited phononic mode. The collisional time is given by

$$\tau_{\rm coll} \sim \frac{l_{\rm mfp}}{v_{\rm th}} \sim \frac{1}{n\sigma v_{\rm th}}, \tag{3.42}$$

where $l_{\rm mfp} \sim 1/(n\sigma)$ is the mean-free-path and $v_{\rm th} = \sqrt{2k_{\rm B}T/m}$ is the thermal velocity. For $D = 3$, the cross-section is given by $\sigma = 4\pi a^2 = m^2g^2/(4\pi\hbar^4)$, which leads to

$$\omega\tau_{\rm coll} \sim N^{-1/3}\sqrt{\frac{gn}{2k_{\rm B}T}}\eta_3^{-2}. \tag{3.43}$$

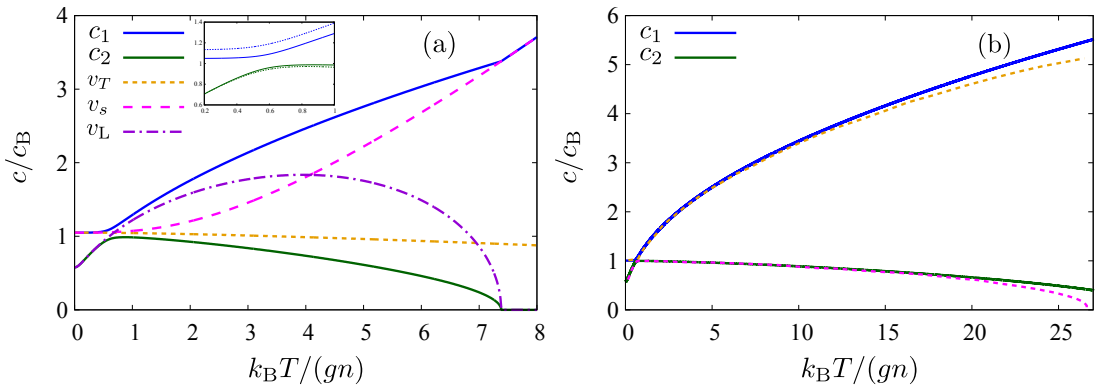

Figure 3.5: Sound velocities in a weakly-interacting Bose gas for $D = 3$ and $\eta_3 = 0.1$ (panel (a)) and the comparison with the first and second sound velocities in Ref. [151] for $\eta_3 = 0.02$ (panel (b)) [90]. The horizontal axis is the reduced temperature $k_BT/(gn)$. Inset of panel (a): The hybridization of the first sound and second sound modes at low temperatures. The dotted lines represent the results for $\eta_3 = 0.2$. The dotted lines in panel (b) represent the results of Ref. [151].

Equation (3.43) indicates that our hydrodynamic description is valid at high temperatures, for a large gas parameter, or for a large number of particles. Taking into account the Bogoliubov theory under the low-temperature approximation we employed, our theory would be valid under low temperature, small gas parameters, and a large number of particles. The cross-section for $D = 2$ is given by $\sigma \sim (2\pi\eta_2)^2 \hbar/(mv_{\rm th})$ and the adimensional collisional time is independent of the temperature as

$$\omega\tau_{\rm coll} \sim \frac{1}{2\sqrt{2\pi N}}\eta_2^{-3/2}. \tag{3.44}$$

Equation (3.44) indicates that the hydrodynamic description for $D = 2$ is valid for a large gas parameter or a large number of particles. As in the 3D case, working with the Bogoliubov theory under the low-temperature approximation, our 2D theory is valid under the conditions of low temperature, a small gas parameter, and a large number of particles. In the experimental observation reported in Ref. [143], the gas parameter and the number of particles are $\eta_2 \simeq 0.10$ and $N \simeq 2178$ respectively, and one obtains $\omega\tau_{\rm coll} \simeq 0.13$, in which our hydrodynamic description is reliable.

3.3.1 Three-dimensional Bose superfluid

Let us discuss the propagation of the first sound and second sound in $D = 3$. The velocities of these modes are shown in Fig. 3.5, where the temperature is rescaled as $k_BT/(gn)$. In Fig. 3.5(a), we set the gas parameter to $\eta_3 \equiv mgn^{1/3}/2\pi\hbar^2 = 0.1$. The dotted, dashed, and dotted-dashed lines in Fig. 3.5(a) indicate the isothermal, adiabatic, and Landau velocities for $D = 3$, respectively. At $T = 0$ within the mean-field theory,

as discussed in Eqs. (3.41), we reproduce the well-known result:

$$c_1 = v_{T,\mathrm{MF}} = v_{s,\mathrm{MF}} = c_{\mathrm{B}}, \qquad c_2 = v_{\mathrm{L}} = \frac{c_{\mathrm{B}}}{\sqrt{3}}. \tag{3.45}$$

By including the quantum correction in Eq. (3.38), the velocities deviate from Eqs. (3.45) as shown in Fig. 3.5. Around $k_{\mathrm{B}}T = 0.6gn$, it exhibits a hybridization of the two sound modes with a small gap, which has been pointed out by Refs. [151, 155, 156, 157, 158] for a weakly-interacting 3D Bose gas. This phenomenon characterizes the hybridization of density and entropy modes as discussed in Sec. 3.2.2. In the incompressible regime $\alpha T \ll 1$, the biquadratic Landau equation of Eq. (3.24) gives $c_1 = v_s$ and $c_2 = v_{\mathrm{L}}$, which indicates that the first sound and second sound mode correspond to the density mode and the entropy mode respectively. The hybridization temperature T_{hyb} characterizes this incompressible regime as $T \lesssim T_{\mathrm{hyb}}$. Experimentally, above the hybridization temperature, the second sound can be probed by density perturbations while only the first sound can be probed below the hybridization temperature since the second sound corresponds to the entropy mode uncoupled from the density oscillation. At a higher temperature than the critical temperature at which the Landau velocity vanishes, one can check that the first sound velocity coincides with the adiabatic one $c_1 = v_s$. The inset of the left panel shows the first sound and second sound velocities for $\eta_3 = 0.1$ and $\eta_3 = 0.2$. It exhibits that a larger gas parameter opens the gap larger as $\eta_3^{3/4}$ [151]. In 3D, hybridization occurs for any gas parameters. The normal density n_{n} in Eq. (3.29b) within Landau's prescription does not include the effects of interactions among elementary excitations and is a low-temperature approximation. In addition, the Bogoliubov theory is not applicable at a high-temperature regime comparable with T_{c} so that the critical temperature at which n_{s} vanishes cannot exactly coincide with the superfluid phase transition temperature T_{c} [151]. We can also qualitatively reproduce the results of Ref. [151] as shown in Fig. 3.5(b) while our framework ignored the Lee-Huang-Yang correction [159], which is included in Ref. [151]. Since Ref. [151] employed perturbation theory based on Beliaev diagrammatic technique in the higher temperature regions for better prediction, we find deviations in this regime.

To precisely discuss the detectability of the second sound, we need to examine the dynamic structure factor for the density response function. In the deep hydrodynamic regime in our consideration, sound propagation is not accompanied by damping. It results in the dynamic structure factor in the form of two delta-peaks as [158]

$$S(q,\omega) = \frac{nq^2}{2m} Z_1 \delta(\omega - c_1 q) + \frac{nq^2}{2m} Z_2 \delta(\omega - c_2 q). \tag{3.46}$$

Here, the amplitudes $Z_{1,2}$ are chosen so that they satisfies the f-sum rule $Z_1 + Z_2 = 1$. The relative amplitudes $W_{1,2} \equiv Z_{1,2}/c_{1,2}^2$ are obtained as

$$W_1 = \frac{1 - c_2^2/v_T^2}{c_1^2 - c_2^2}, \quad W_2 = \frac{c_1^2/v_T^2 - 1}{c_1^2 - c_2^2}. \tag{3.47}$$

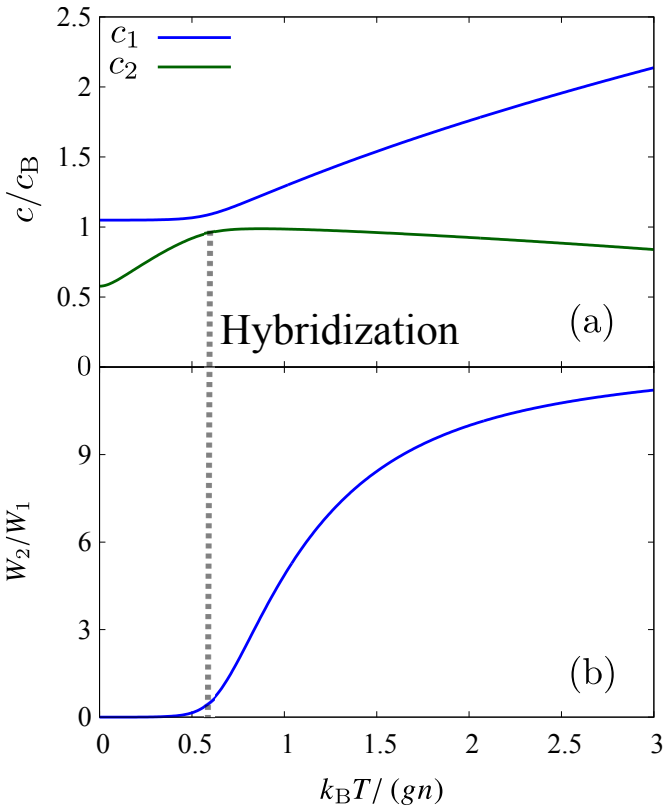

Figure 3.6: First and second sound velocities (panel (a)) and the amplitude ratio W_2/W_1 (panel (b)) for $\eta_3 = mgn^{1/3}/2\pi\hbar^2 = 0.1$.

If the ratio W_2/W_1 is larger than one, the second sound can be excited by density perturbations. Otherwise, only the first sound can be detected by a density probe. We show the ratio in Fig. 3.6(b) in comparison with the first and second sound velocities in Fig. 3.6(a). We can see that the hybridization temperature corresponds to the temperature at which the ratio W_2/W_1 starts to increase from unity.

3.3.2 Two-dimensional Bose superfluid

As discussed in Sec. 2.6, the superfluid properties of a 2D Bose gas are crucially different from those of the 3D case due to the BKT transition [105, 106, 107]. The theoretical framework developed in Sec. 3.3, where the topological excitations of the bosonic fluid are not taken into account, cannot describe the BKT transition. These excitations are responsible for the universal jump of the superfluid density at BKT transition temperature, $T_{\rm BKT}$. To include it in our theory, we employ the NK criterion (2.76). The superfluid density $n_{\rm s}$ in Eq. (2.76) is calculated from the Landau formula given in Eq. (3.29b). A good approximation in an infinite-size weakly-interacting system is to set to zero the superfluid density fraction for $T \geq T_{\rm BKT}$.

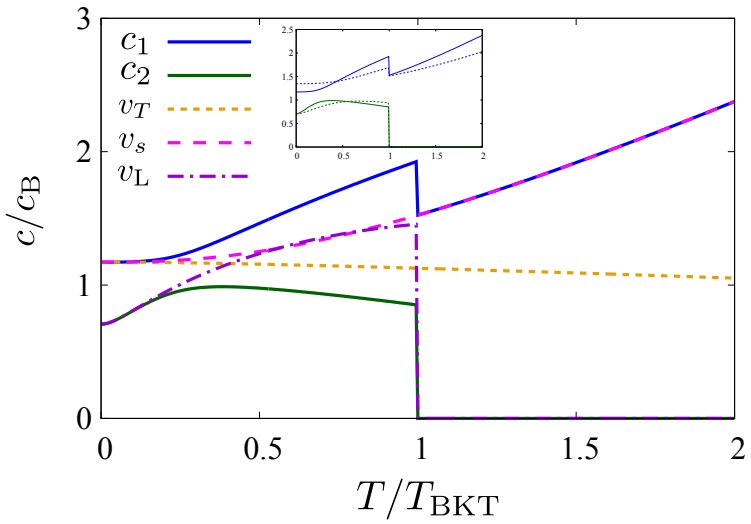

Figure 3.7: Results of sound velocities for $D = 2$ and $\eta_2 = 0.1$ [90]. The number of particles is set to be $N = 10^4$. The horizontal axis is the reduced temperature scaled by the BKT transition temperature $T_{\rm BKT}$, which is determined by the NK criterion Eq. (2.76) for the superfluid density in the two-fluid model while the normal density is computed by Eq. (3.29b). Inset: The first sound and second sound velocities. The solid curves represent the results for $\eta_2 = 0.1$ and the dotted ones represent those for $\eta_2 = 0.2$

We show the sound velocities in a 2D Bose gas in Fig. 3.7. Due to the jump of the superfluid density at $T = T_{\rm BKT}$, the first sound and second sound velocities exhibit discontinuities. One can see that the hybridization of c_1 and c_2 occurs around $T_{\rm hyb} \simeq 0.4gn/k_{\rm B}$ for $\eta_2 = 0.1$. Figure 3.8 displays the dependence on the gas parameter η_D of the hybridization temperature $T_{\rm hyb}$, which is determined by the temperature at which the difference between the first and second sound velocities starts to increase. Note that in 2D, for $\eta_2 \gtrsim 0.6$, $T_{\rm hyb}$ coincides with the BKT transition temperature. In the region of $\eta_2 \gtrsim 0.6$, at which $T_{\rm hyb} = T_{\rm BKT}$ in 2D, we infer from Fig. 3.8 that the first and second sound modes are decoupled, respectively, to density and entropy modes, because the first sound corresponds to the density mode $c_1 = v_s$ and the second sound vanishes $c_2 = 0$ in the absence of the superfluid density above $T_{\rm BKT}$.

Our theoretical approach, based on the Bogoliubov theory, is reliable to describe the propagation of sound in low-temperature Bose gases, and its predictions are as better as the gas parameter $mg/\hbar^2$ is smaller than 1. The recent experiments of Ref. [143] with 2D weakly-interacting bosonic superfluids adopt the value of $mg/\hbar^2 = 0.64$, and, therefore, can be described with our Bogoliubov theory. However, since these experiments focus on the high-temperature regime near $T_{\rm BKT}$, it is useful to extend our previous results to improve the agreement in this specific temperature regime. In particular, the sound velocities are strongly dependent on the superfluid density and the one derived from the Landau formula (3.29b) has, strictly speaking, a simplified behaviour near $T_{\rm BKT}$.

To improve our theory in the high-temperature regime of the experiments, we eval-

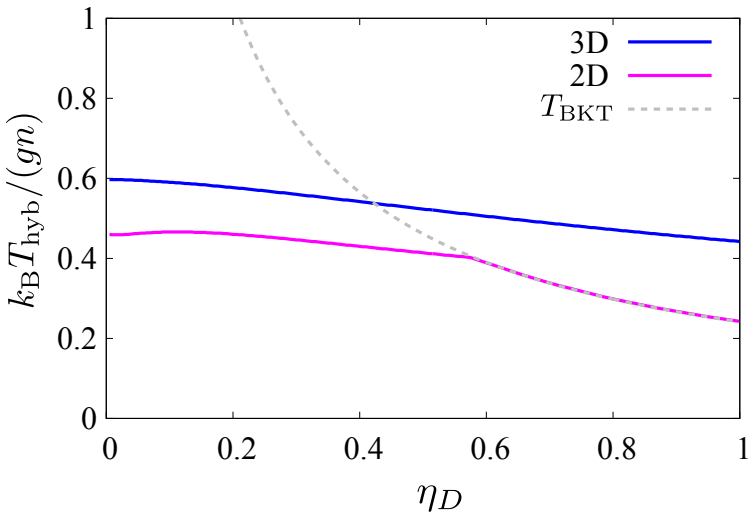

Figure 3.8: Hybridization temperature for $D = 3$ and $D = 2$ as a function of the gas parameter $\eta_D = mgn^{1-2/D}/2\pi\hbar^2$ [90]. In the latter case, the particle number is set to $N = 10^4$. In 2D, moreover, the hybridization temperature coincides with the BKT transition temperature for $\eta_2 \gtrsim 0.6$.

uate the renormalized superfluid density by solving the NK RG equations (2.74) [107]. These differential equations describe the renormalization of the superfluid density due to the presence of vortex-antivortex excitations, which are not taken into account by the Landau formula of Eq. (3.29b). To describe consistently the finite-size experiments, we solve numerically these equations up to a finite scale, $l_{\rm max} = \ln(L/\xi)$, where L^2 is the area of the system. In the solution of Eqs. (2.74) the choice of the initial conditions is quite delicate: we choose the chemical potential of the bare vortices as $\mu_{\rm v}(0) = \pi^2\hbar^2 n_{\rm s}^{(0)}(T)/2m$ [160], and for the initial value of $K(0)$ we use $K(0) = \hbar^2 n_{\rm s}^{(0)}(T)/mk_{\rm B}T$, with $n_{\rm s}^{(0)}(T) = n - n_{\rm n}^{(0)}(T)$. It is important to point out that the bare normal density which we introduce here, $n_{\rm n}^{(0)}(T)$, is formally the same as Eq. (3.29b), but is calculated with the Popov spectrum:

$$E_{{\rm Pop},p} = \sqrt{\frac{p^2}{2m}\left(\frac{p^2}{2m} + 2\mu\right)}, \tag{3.48}$$

where μ is the chemical potential of the system. We derive this chemical potential as a function of N and of T by inverting numerically the grand canonical equation of state, which reads (see Ref. [161])

$$N = \frac{m\mu L^D}{4\pi\hbar^2}\ln\left(\frac{4\hbar^2}{m\mu a_{\rm 2D}^2 e^{2\gamma+1}}\right) + \sum_{\boldsymbol{p}}\frac{p^2}{2m}\frac{f_T(E_{{\rm Pop},p})}{E_{{\rm Pop},p}}. \tag{3.49}$$

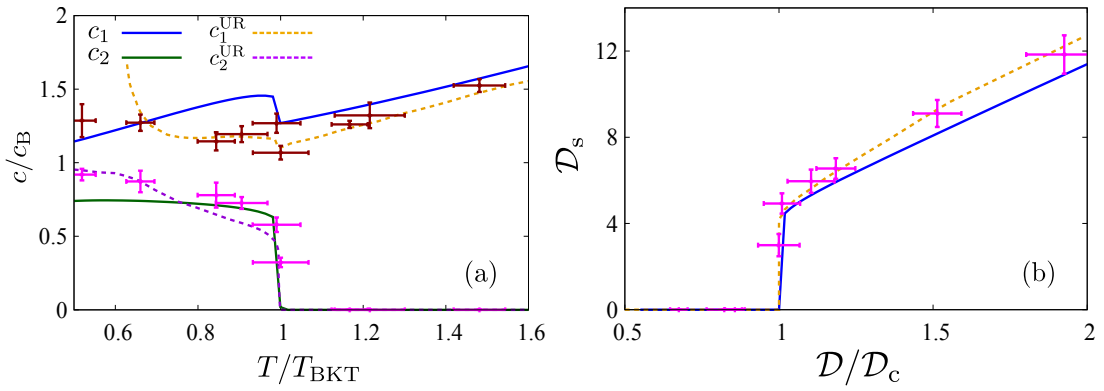

Figure 3.9: First sound and second sound velocities (panel (a)) and rescaled superfluid density $\mathcal{D}_{\rm s} = n_{\rm s}\lambda_T^2$ in 2D (panel (b)) for $mg/\hbar^2 = 0.64$, plotted in comparison with the experimental data of Ref. [143] where $\mathcal{D}/\mathcal{D}_{\rm c} = T_{\rm BKT}/T$ [90]. The particle number is set to be $N = 2178$ [143]. The blue and green solid curves represent our results using the renormalized superfluid density [107] calculated with the chemical potential obtained from Eq. (3.49). The orange and violet dashed curves represent the results with the universal relations [129, 143, 163, 164, 165, 166, 167, 168].

In particular, we evaluate $a_{\rm 2D}$ as [162]

$$a_{\rm 2D} = 2.092\, a_z \ln\left(-\sqrt{\frac{\pi}{2}}\frac{a_z}{a_{\rm 3D}}\right), \tag{3.50}$$

where a_z is the characteristic length of the transverse harmonic confinement and $a_{\rm 3D}$ is the three-dimensional s-wave scattering length, which is directly controlled in the experiment [143]. The procedure described above allows us to have reliable results near $T_{\rm BKT}$ for $n_{\rm s}^{\rm (R)} \equiv n_{\rm s}^{(l_{\rm max})}(T)$. Given the renormalized superfluid density $n_{\rm s}^{\rm (R)}$ for every temperature T, we use it as an input to calculate the sound velocities.

Our results are outlined in Fig. 3.9, which shows, in comparison with the experimental data [143], c_1 and c_2 in panel (a) and the superfluid density $\mathcal{D}_{\rm s} = n_{\rm s}\lambda_T^2$ in panel (b). As in the experiment, here we use $mg/\hbar^2 = 0.64$, the number density of $n = 3\,\mu{\rm m}^{-2}$ and the system area of $L^2 = 33\times 22\,\mu{\rm m}^2$ [143]. We also emphasize that, within our finite-size renormalization group calculation, we find a critical BKT temperature of 37 nK, which is practically coincident with the result $T_{\rm BKT} = 2\pi n/\left[m\ln\left[380\hbar^2/(mg)\right]\right]$ of Ref. [163], and compatible with the critical temperature of the experiments of 42 nK [143]. Figure 3.9(a) indicates that the results using the renormalized superfluid density with the exact chemical potential, represented by the blue and green solid curves, are in reasonable agreement with the experimental values. Note that our first sound velocity also describes the behaviour towards low temperature in a satisfactory way. The slight deviation of our second sound velocity from the experimental one at low temperature is ascribed to the inconsistency between the thermodynamic quantities that appear in Eq. (3.25), calculated under the low-temperature approximation $\mu = gn$, and the renormalized superfluid density $n_{\rm s}^{\rm (R)}$ calculated with the improved μ. While this approximation is not

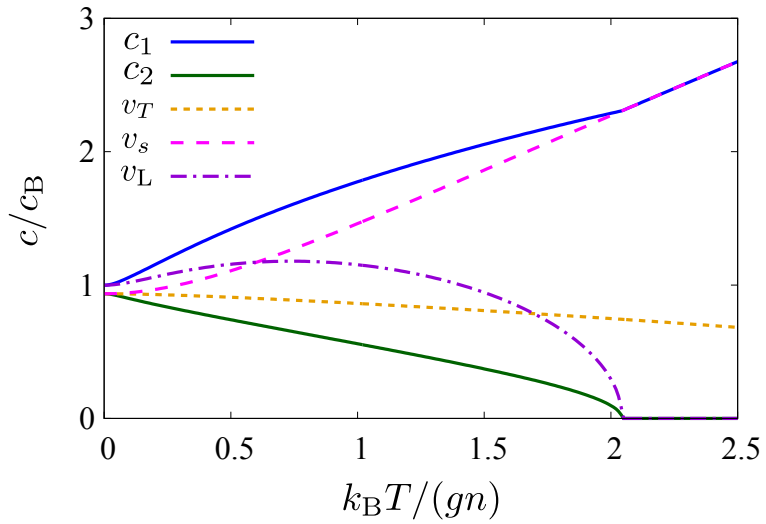

Figure 3.10: Results of sound velocities for $D = 1$ and $\eta_1 = 0.1$ [90]. The horizontal axis is the reduced temperature $k_{\rm B}T/(gn)$.

particularly problematic near $T_{\rm BKT}$, it does not allow us to extend the present theory at low temperatures, where the sound velocities are more sensitive to the normal density. Figure 3.9(b) displays that the renormalized superfluid density $\mathcal{D}_{\rm s} = n_{\rm s}\lambda_T^2$ obtained with the beyond-mean-field chemical potential agrees well with the experimental values. From this last figure, thus, we can expect that the corrections due to the interaction between Bogoliubov quasiparticles, which will be more relevant in the high-temperature regime and outside the very weakly-interacting regime of $mg/\hbar^2 \ll 1$, are, at least for the superfluid density, not particularly relevant. This suggests that future works in 2D with the full evaluation of the improved thermodynamics could be a solid benchmark for the sound velocities both in the low and high-temperature regimes.

3.3.3 One-dimensional Bose superfluid

On the basis of the Hohenberg-Mermin-Wagner theorem [96, 97], the critical temperature $T_{\rm BEC}$ below which there is Bose-Einstein condensation, or equivalently below which there is ODLRO, is positive in 3D, it is zero in 2D, and it is absent in 1D. Instead, the critical temperature $T_{\rm c}$ below which there is superfluidity, or equivalently below which there is ALRO, is equal to $T_{\rm BEC}$ in 3D, it is equal to $T_{\rm BKT}$ in 2D, and it is zero in 1D. Thus, in the thermodynamic limit and with $T > 0$, for a 1D weakly-interacting Bose gas there is neither ODLRO nor ALRO. However, a finite 1D system of spatial size L is effectively superfluid if [50]

$$T \ll T_\phi \equiv \frac{E_\phi}{k_{\rm B}} \ln\left(\frac{L}{\xi}\right), \tag{3.51}$$

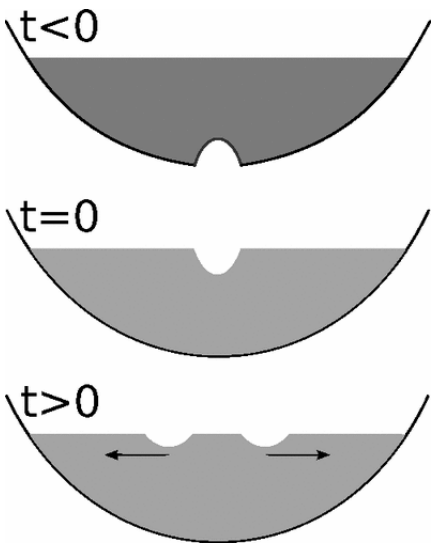

Figure 3.11: Experimental protocol to excite density waves [172]. At $t < 0$, a repulsive laser is irradiated into the trapped atomic clouds to create a density depletion. The laser is suddenly switched off at $t = 0$, and the density defect propagates as density waves at $t > 0$.

where $E_\phi \simeq n\hbar^2/(m\xi)$ is the energy to create a phase slip (black soliton) and ξ is the corresponding healing length. Note that, for $\eta_1 \ll 1$, the adimensional temperature $k_{\rm B}T_\phi/gn$ can be quite large.

In Fig. 3.10, we show the results of c_1 and c_2 in an 1D Bose gas for $\eta_1 = 0.1$. Since the Bogoliubov theory in 1D well describes the thermodynamics in the weakly-interacting regime up to $\eta_1 \sim 1$ at low temperatures [169, 170], our 1D results would be reliable in this regime. It exhibits no hybridization of c_1 and c_2 because of $c_1 = c_2 = c_{\rm B}$ at zero-temperature within the mean-field and the gap opening at zero-temperature between c_1 and c_2 by the quantum correction. In the incompressible regime within the mean-field theory, one can obtain $c_1 = c_2 = c_{\rm B}$ in 1D, which indicates that the decoupled density mode and entropy mode degenerate. Hence, $T = 0$ corresponds to the hybridization temperature at which the first and second sound modes are closest to each other in 1D. The beyond-mean-field correction decreases v_s and results in $c_1 = v_{\rm L}$ and $c_2 = v_s$, namely the first and second sound correspond to entropy and density mode respectively due to the negative quantum correction $v_{\rm Q}^2 < 0$, unlike 3D or 2D case.

3.4 Experiments of sound modes

Before concluding this Chapter, we mention the experimental protocol to detect sound modes in atomic superfluids. The first experimental observation of sound waves in an ultracold atomic gas was achieved in Ketterle's group at MIT in 1997 [171]. The experimental setup is sketched in Fig. 3.11 [172]. First, they inject a repulsive laser beam into the center of the atomic cloud confined in a harmonic trap to create a density

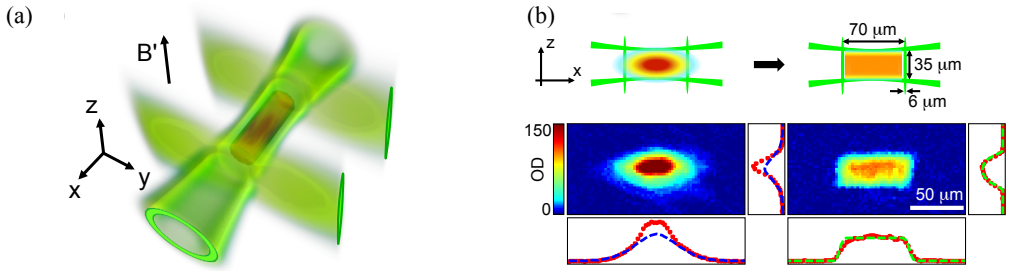

Figure 3.12: Illustration of a box trap [173]. (a) A sketch of the box trap configuration composed of laser beams. The atoms are confined in the dark cylindrical region. The magnetic field B' cancels the gravitational force. (b) The upper sketches show the slice of the trapped atomic cloud in the z-x plane before (left) and after (right) loading into the box trap. The lower panel shows the corresponding in-situ images of the optical density of the atomic gases. The blue dashed curves in the left panel are the fits of the optical density in a Bose gas trapped by a harmonic potential. The green dashed curves in the right panel are the fits for a uniform Bose gas.

defect at $t < 0$. Then, at $t = 0$, they turned off the laser suddenly, and the created density depletion propagates at $t > 0$. In this manner, one can observe the propagation of density waves.

In recent experiments, a box trap composed of laser beams is realized and enables us to experimentally realize a uniform gas as illustrated in Fig. 3.12 [173]. It is more useful than the conventional harmonic trap to compare the experimental data and theoretical predictions, in particular with respect to nonlinearity. The experiment measuring the first and second sound velocities in a 2D ^{39}K atomic gas shown in Fig. 3.9 and more recent experiment measuring them in a compressible 3D Bose fluid also used the box trap and they shook the box to induce density perturbations [143, 174]. As shown in Fig. 3.9, the first and second sound velocities in a 2D Bose superfluid have been measured only around the BKT transition temperature. In this regime above the hybridization temperature, both the first and second sound modes can be excited by density perturbations because the density and entropy modes are mixed. Below the hybridization temperature, the density probe can detect only the first sound and the detection of the second sound requires thermal perturbations by heating the Bose gas. We expect that the measurements at much lower temperatures would be useful to verify our result of the hybridization temperatures.

Chapter 4

Berezinskii-Kosterlitz-Thouless transition in binary superfluids

This Chapter is devoted to the discussion of multicomponent superfluidity and BKT transitions in a binary Bose mixture in the presence of a Rabi coupling. In contrast to the single-component superfluid, the multicomponent superfluidity exhibits fruitful properties. First, we review some fundamental aspects and practical examples of multicomponent superfluids in ultracold atomic systems. Then, we move on to the analysis of a binary Bose superfluid and show two distinct ground states: miscible state and phase separation. We also show that a Rabi coupling exchanging the two species of Bose atoms results in a rich variation of vortex configurations. The exotic vortex excitations are also responsible for the new type of BKT transition in 2D. The last section shows our renormalization group analysis of the BKT transition in a Rabi-coupled binary Bose mixture [91].

4.1 Multicomponent superfluidity

In ultracold atomic systems, multicomponent superfluidity is relatively easy to realize. In addition to the density and superfluid phase, in a multicomponent superfluid, we also have additional degrees of freedom such as the population imbalance or relative phase between the two species, which gives rise to a rich variety of superfluidity. One example of a multicomponent superfluid is a superfluid that includes two different species of atoms with different atomic masses such as a mixture of ^{23}Na and ^{87}Rb. Another way to realize a multicomponent superfluid is to simultaneously trap the same atoms in different hyperfine spin states [175, 176, 177, 178, 179, 180]. For instance, by magnetically trapping alkaline atoms in two WFSSs $|F = 2, m_F = 1\rangle$ and $|F = 1, m_F = -1\rangle$ explained in Sec. 1.2 simultaneously, one can realize a binary superfluid with the same mass. In the latter case with the same atomic species in different hyperfine states, one can make the two states coherently coupled by injecting an external electromagnetic field with a frequency corresponding to the energy difference of the two hyperfine states

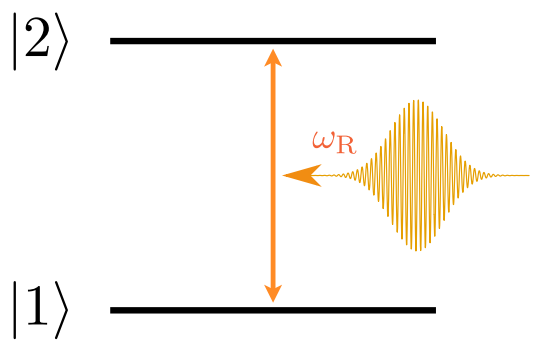

Figure 4.1: Schematic diagram of two hyperfine states coherently coupled with a Rabi coupling.

as illustrated in Fig. 4.1. With the Rabi frequency ω_{R} determined by the coupling between the atoms and the injected electromagnetic field, such a binary Bose superfluid is described by

$$\begin{aligned}\hat{H} = \sum_{a=1,2} \Bigg[& \int \mathrm{d}\boldsymbol{r}\, \hat{\Psi}_a^\dagger(\boldsymbol{r}) \left(-\frac{\hbar^2}{2m}\boldsymbol{\nabla}^2 + V_{\mathrm{ext}}^{(a)}(\boldsymbol{r}) \right) \hat{\Psi}_a(\boldsymbol{r}) \\ & + \frac{1}{2} \int \mathrm{d}\boldsymbol{r} \int \mathrm{d}\boldsymbol{r}'\, \hat{\Psi}_a^\dagger(\boldsymbol{r}) \hat{\Psi}_a^\dagger(\boldsymbol{r}') V_{aa}(\boldsymbol{r}-\boldsymbol{r}') \hat{\Psi}_a(\boldsymbol{r}') \hat{\Psi}_a(\boldsymbol{r}) \Bigg] \\ & + \int \mathrm{d}\boldsymbol{r} \int \mathrm{d}\boldsymbol{r}'\, \hat{\Psi}_1^\dagger(\boldsymbol{r}) \hat{\Psi}_2^\dagger(\boldsymbol{r}') V_{12}(\boldsymbol{r}-\boldsymbol{r}') \hat{\Psi}_2(\boldsymbol{r}') \hat{\Psi}_1(\boldsymbol{r}) \\ & - \hbar\omega_{\mathrm{R}} \int \mathrm{d}\boldsymbol{r} \left[\hat{\Psi}_1^\dagger(\boldsymbol{r}) \hat{\Psi}_2(\boldsymbol{r}) + \hat{\Psi}_2^\dagger(\boldsymbol{r}) \hat{\Psi}_1(\boldsymbol{r}) \right], \end{aligned} \tag{4.1}$$

where $\hat{\Psi}_{a=1,2}(\boldsymbol{r})$ denotes the annihilation operator of a-boson at a position $\boldsymbol{r}$ and $V_{\mathrm{ext}}^{(a)}(\boldsymbol{r})$ is the external potential for a-boson. The atomic masses are the same $m = m_1 = m_2$ because we are assuming a single atomic species. In addition to the two-body interaction potential between the same species $V_{aa}(\boldsymbol{r}-\boldsymbol{r}')$, we also have inter-species interaction potential $V_{12}(\boldsymbol{r}-\boldsymbol{r}')$. We consider the case of contact interactions $V_{ab}(\boldsymbol{r}-\boldsymbol{r}') = g_{ab}\delta(\boldsymbol{r}-\boldsymbol{r}')$ with g_{ab} the coupling constant. The last term in Eq. (4.1) corresponds to the coherent Rabi coupling term. For simplicity, we set the detuning, which is the difference of frequencies between the resonant frequency of the two hyperfine spin states and the electromagnetic field frequency, to be zero. To deal with the Rabi-coupled binary system described by Eq. (4.1), we have mainly two possible strategies. One is to analyze it directly with the component basis $\{|a\rangle\} = \{|1\rangle, |2\rangle\}$. Another possible approach is to move on to the *dressed states* by a unitary transformation so that it diagonalizes the single-body terms in Eq. (4.1). In this way, for binary fermions, one can find that this unitary transformation also keeps the two-body interaction terms invariant in the dressed basis [181]. It is because the spin-singlet states, which are the only allowed states for fermions to interact with each other under contact interactions, are invariant under the

rotation on the Bloch sphere corresponding to the unitary transformation. Consequently, the dressed states are convenient to easily analyze the Rabi-coupled binary fermion system and the Rabi coupling plays the role of an effective magnetic field splitting the energy levels of the dressed states. For binary bosons, however, the two-body interaction terms transform into more complicated terms, which are difficult to treat except for the rotating-wave approximation [182]. Therefore, we follow the former approach in this Thesis to analyze the binary Bose mixture.

Under the Bogoliubov ansatz $\langle\hat{\Psi}_a^\dagger(\boldsymbol{r})\hat{\Psi}_a(\boldsymbol{r}')\rangle \to \Psi_a^*(\boldsymbol{r})\Psi_a(\boldsymbol{r}')$ for $|\boldsymbol{r}-\boldsymbol{r}'|\to\infty$, the energy functional with respect to (Ψ_1,Ψ_2) is obtained as

$$E = \int \mathrm{d}\boldsymbol{r}\Bigg[\sum_{a=1,2}\left(\frac{\hbar^2}{2m}|\boldsymbol{\nabla}\Psi_a|^2 + V_{\mathrm{ext}}^{(a)}|\Psi_a|^2 + \frac{g_{aa}}{2}|\Psi_a|^4\right) + g_{12}|\Psi_1|^2|\Psi_2|^2 \\ - \hbar\omega_{\mathrm{R}}\left(\Psi_1^*\Psi_2 + \Psi_2^*\Psi_1\right)\Bigg]. \tag{4.2}$$

Equation (4.2) provides the GP equations

$$i\hbar\partial_t\Psi_1 = \left(-\frac{\hbar^2}{2m}\boldsymbol{\nabla}^2 + V_{\mathrm{ext}}^{(1)} + g_{11}|\Psi_1|^2 + g_{12}|\Psi_2|^2\right)\Psi_1 - \hbar\omega_{\mathrm{R}}\Psi_2, \tag{4.3a}$$

$$i\hbar\partial_t\Psi_2 = \left(-\frac{\hbar^2}{2m}\boldsymbol{\nabla}^2 + V_{\mathrm{ext}}^{(2)} + g_{22}|\Psi_2|^2 + g_{12}|\Psi_1|^2\right)\Psi_2 - \hbar\omega_{\mathrm{R}}\Psi_1, \tag{4.3b}$$

Equations (4.3) indicate the two species of bosons interact with each other through the inter-species two-body interaction g_{12} and they exchange with each other through the coherent Rabi coupling ω_{R}. By inserting the Madelung transformation

$$\Psi_a(\boldsymbol{r},t) = \sqrt{n_a(\boldsymbol{r},t)}e^{i\theta_a(\boldsymbol{r},t)}, \tag{4.4}$$

into Eqs. (4.3), the imaginary parts of Eqs. (4.3) provide

$$\partial_t n_1 + \boldsymbol{\nabla}\cdot\boldsymbol{j}_1 = 2\hbar\omega_{\mathrm{R}}\sqrt{n_1 n_2}\sin\left(\theta_1-\theta_2\right), \tag{4.5a}$$

$$\partial_t n_2 + \boldsymbol{\nabla}\cdot\boldsymbol{j}_2 = 2\hbar\omega_{\mathrm{R}}\sqrt{n_1 n_2}\sin\left(\theta_2-\theta_1\right), \tag{4.5b}$$

respectively, with $\boldsymbol{j}_a = n_a\boldsymbol{v}_a$ and $\boldsymbol{v}_a = \hbar\boldsymbol{\nabla}\theta_a/m$ the each superfluid velocity. It indicates that the densities of each component are not conserved with a finite Rabi coupling. The total density $n = n_1 + n_2$ is, however, conserved:

$$\partial_t n + \boldsymbol{\nabla}\cdot\boldsymbol{j} = 0, \tag{4.6}$$

with

$$\boldsymbol{j} = \boldsymbol{j}_1 + \boldsymbol{j}_2 = \frac{\hbar}{m}\left(n_1\boldsymbol{\nabla}\theta_1 + n_2\boldsymbol{\nabla}\theta_2\right). \tag{4.7}$$

4.2 Miscibility and elementary excitations

Let us consider the ground state of the binary Bose mixture in the absence of the external potential. In a uniform and stationary system, Eq. (4.4) gives the interaction energy

$$E_{\rm int} = \int \mathrm{d}\boldsymbol{r} \left[\frac{1}{2} g_{11} n_1^2 + \frac{1}{2} g_{22} n_2^2 + g_{12} n_1 n_2 - 2\hbar\omega_{\rm R} \cos\gamma \sqrt{n_1 n_2} \right]. \tag{4.8}$$

The relative phase $\gamma = \theta_2 - \theta_1$ is fixed to be $\gamma = 0$ by minimizing the energy. With the symmetric interaction strength $g = g_{11} = g_{22}$, in particular, the derivative with respect to the population imbalance $\zeta = (n_1 - n_2)/n$ reads

$$\frac{\partial E_{\rm int}}{\partial \zeta} = \int \mathrm{d}\boldsymbol{r} \, \frac{n^2 \zeta}{2} \left(g - g_{12} + \frac{2\hbar\omega_{\rm R}}{n\sqrt{1-\zeta^2}} \right). \tag{4.9}$$

It admits two possible configurations of the ground state. Since Eq. (4.8) is symmetric in terms of n_1 and n_2, we assume $\zeta \geq 0$ or equivalently $n_1 \geq n_2$ without loss of generality. For $g_{12} < g + 2\hbar\omega_{\rm R}/n$, the derivative (4.9) is positive with an infinitesimal increase of ζ from zero. In this case, the *miscible state* with

$$n_1 = n_2, \tag{4.10}$$

is stable. For $g_{12} > g + 2\hbar\omega_{\rm R}/n$, on the other hand, the derivative (4.9) is negative with an infinitesimal increase of ζ from zero and the energy is minimized by maximizing ζ^2. To achieve it, the configuration that $n_1 = 0$ and n_2 is maximized, or n_1 is maximized and $n_2 = 0$, is required. It is the *phase separation* state, in which the species 1 and species 2 exist separately, favored as the ground state with

$$n_1 - n_2 = \pm n \sqrt{1 - \left(\frac{2\hbar\omega_{\rm R}}{(g - g_{12})n} \right)^2}. \tag{4.11}$$

The sign depends on whether $n_1 > n_2$ or $n_1 < n_2$. In the phase separation state, we have a boundary between the two regions occupied by each component breaking the homogeneity of the system. In the vicinity of the boundary, we should also have the gradient energy originating from the boundary, which is, however, negligible in the thermodynamic limit. In a finite-size system, the configuration of the phase separation state is realized so that the area of the boundary is minimized. The phase diagram of the ground state is shown in Fig. 4.2.

To consider the stability of the ground state, let us consider the BdG equation. Due to the conserved total number of atoms $N = \int \mathrm{d}\boldsymbol{r} \, |\Psi_a|^2$, the chemical potential of each component is equal. It allows us to write

$$\Psi_a(\boldsymbol{r}, t) = e^{-i\mu t/\hbar} e^{i\theta_a(\boldsymbol{r},t)} \left[\sqrt{n_a(\boldsymbol{r}, t)} + \delta\Psi_a(\boldsymbol{r}, t) \right], \tag{4.12}$$

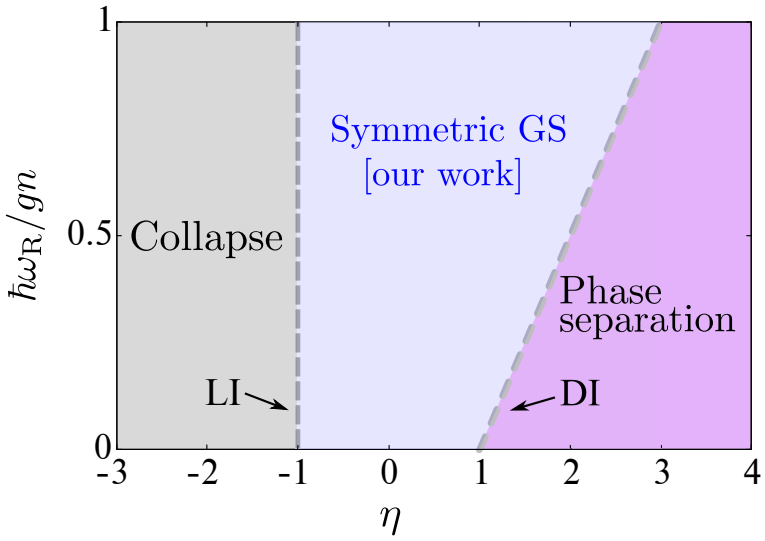

Figure 4.2: Phase diagram of a binary Bose superfluid with respect to the intercomponent coupling $\eta \equiv g_{12}/g$ and the Rabi coupling $\omega_{\rm R}$. We focus on the symmetric ground state (GS) with balanced densities realized in $-1 < \eta < 1+2\hbar\omega_{\rm R}/gn$. The boundary $\eta = -1$ is the boundary at which the superfluid collapse due to Landau instability (LI). The boundary $\eta = 1+2\hbar\omega_{\rm R}/gn$ is the boundary at which the GS changes to the phase separation state across the dynamical instability (DI).

where $\delta\Psi_a$ is the fluctuations written as

$$\begin{pmatrix} \delta\Psi_a(\boldsymbol{r},t) \\ \delta\Psi_a^*(\boldsymbol{r},t) \end{pmatrix} = e^{i(\boldsymbol{k}\cdot\boldsymbol{r}-Et/\hbar)} \begin{pmatrix} u_a \\ v_a \end{pmatrix}. \tag{4.13}$$

Inserting Eq. (4.12) into Eqs. (4.3), we obtain

$$E \begin{pmatrix} u_1 \\ v_1 \\ u_2 \\ v_2 \end{pmatrix} = \mathcal{M} \begin{pmatrix} u_1 \\ v_1 \\ u_2 \\ v_2 \end{pmatrix}, \tag{4.14}$$

with

$$\mathcal{M} = \begin{pmatrix} h_1 & gn_1 & g_{12}\sqrt{n_1n_2} - \hbar\omega_{\rm R} & g_{12}\sqrt{n_1n_2} \\ -gn_1 & -h_1 & -g_{12}\sqrt{n_1n_2} & -g_{12}\sqrt{n_1n_2} + \hbar\omega_{\rm R} \\ g_{12}\sqrt{n_1n_2} - \hbar\omega_{\rm R} & g_{12}\sqrt{n_1n_2} & h_2 & gn_2 \\ -g_{12}\sqrt{n_1n_2} & -g_{12}\sqrt{n_1n_2} + \hbar\omega_{\rm R} & -gn_2 & -h_2 \end{pmatrix}, \tag{4.15}$$

and $h_a = \varepsilon_k + 2gn_a + g_{12}n_{\bar{a}} - \mu$. In the miscible regime $n_1 = n_2 = n/2$, diagonalization of $\mathcal{M}$ gives

$$(E_k^{\pm})^2 = \left(\varepsilon_k - \mu + gn + \frac{1}{2}g_{12}n \pm \frac{1}{2}g_{12}n \mp \hbar\omega_{\rm R}\right)^2 - \left(\frac{g \pm g_{12}}{2}n\right)^2. \tag{4.16}$$

The chemical potential μ can be determined by minimizing the thermodynamic potential energy $E_{\rm int} - \mu N$ as

$$\mu = \frac{g + g_{12}}{2} n - \hbar\omega_{\rm R}. \tag{4.17}$$

Even though the two branches of elementary excitations (4.16) are gapped in general, by inserting the mean-field chemical potential in Eq. (4.17), one can obtain [183]

$$E_k^+ = \sqrt{\varepsilon_k \left(\varepsilon_k + (g + g_{12})n\right)}, \tag{4.18a}$$

$$E_k^- = \sqrt{\left(\varepsilon_k + 2\hbar\omega_{\rm R}\right)\left(\varepsilon_k + (g - g_{12})n + 2\hbar\omega_{\rm R}\right)}, \tag{4.18b}$$

which reads one gapless branch and one gapped branch with a finite Rabi coupling. The plus branch E_k^+ is real for $g > g_{12}$ while the minus branch E_k^- is real for $g_{12} < g + 2\hbar\omega_{\rm R}/n$ for any k. It indicates an oscillation around the stationary configuration and guarantees the linear stability of the miscible state. For $g_{12} > g + 2\hbar\omega_{\rm R}/n$, on the other hand, the minus branch E_k^- includes an imaginary part leading to the exponentially diverging fluctuations. It indicates the dynamical instability of the miscible state and the phase separation is favored as mentioned above.

4.3 Vortex excitations

In the following, we focus on a 2D binary Bose mixture. In Sec. 2.4, we discussed quantized vortices in a single-component Bose superfluid. In a binary Bose superfluid, the particle current is given by Eq. (4.7) resulting in the change of the expression of the vorticity. The superfluid velocity is given by

$$\boldsymbol{v}_{\rm s} = \frac{\boldsymbol{j}}{n} = \frac{\hbar}{m} \frac{n_1 \boldsymbol{\nabla}\theta_1 + n_2 \boldsymbol{\nabla}\theta_2}{n_1 + n_2}. \tag{4.19}$$

In a binary Bose mixture, it is convenient to write

$$\Psi \equiv \begin{pmatrix} \Psi_1 \\ \Psi_2 \end{pmatrix} = \sqrt{n} e^{-i\alpha/2} \begin{pmatrix} e^{-i\gamma/2} \cos\left(\dfrac{\beta}{2}\right) \\ e^{i\gamma/2} \sin\left(\dfrac{\beta}{2}\right) \end{pmatrix}, \tag{4.20}$$

where $\alpha = -(\theta_1 + \theta_2)$ is the total phase, $\gamma = \theta_2 - \theta_1$ is the relative phase, and β characterizes the population imbalance through $n_1 = n\cos^2(\beta/2)$ and $n_2 = n\sin^2(\beta/2)$ with $n = \Psi^\dagger\Psi = |\Psi_1|^2 + |\Psi_2|^2$. This set of three parameters (α, β, γ) can be regarded as Euler angles and Eq. (4.20) can be written as

$$\Psi(\alpha, \beta, \gamma) = e^{-i\gamma\hat{\sigma}_z/2} e^{-i\beta\hat{\sigma}_y/2} e^{-i\alpha\hat{\sigma}_z/2} \begin{pmatrix} \sqrt{n} \\ 0 \end{pmatrix}, \tag{4.21}$$

with $\hat{\sigma}_{x,y,z}$ the Pauli matrices and $0 \leq \alpha, \beta, \gamma \leq 2\pi$. Using (α, β, γ), we can write Eq. (4.19) as

$$\boldsymbol{v}_{\mathrm{s}} = -\frac{\hbar}{2m}\left(\boldsymbol{\nabla}\alpha + \cos\beta\boldsymbol{\nabla}\gamma\right), \tag{4.22}$$

which leads to the circulation

$$\Gamma = \oint_C \mathrm{d}\boldsymbol{r}\cdot\boldsymbol{v}_{\mathrm{s}} = -\frac{\kappa}{2}\left(q_\alpha + q_\gamma\cos\beta\right), \tag{4.23}$$

where C encloses vortices along which the density variation is uniform $\beta = \text{const.}$, and q_α and q_γ are the winding number for the total phase α and the relative phase γ respectively. Note that, in contrast to Eq. (2.31) in a single-component superfluid, Eq. (4.23) is no longer quantized because of the second term in Eq. (4.23) proportional to $\cos\beta$. In particular, with balanced densities $n_1 = n_2$ equivalent to $\beta = \pi/2$, $\Gamma = -\kappa q_\alpha/2$ indicates the half-quantized vortices emerge.

In general, the half-quantized vortices can be expressed as

$$\Psi^{(1)}_{\mathrm{HQV}} = \Psi(-\theta, \beta, -\theta) = \begin{pmatrix}\sqrt{n_1}e^{i\theta}\\ \sqrt{n_2}\end{pmatrix}, \tag{4.24a}$$

$$\Psi^{(2)}_{\mathrm{HQV}} = \Psi(-\theta, \beta, \theta) = \begin{pmatrix}\sqrt{n_1}\\ \sqrt{n_2}e^{i\theta}\end{pmatrix}. \tag{4.24b}$$

The former configuration represents the half-quantized vortex winding only the component 1 while the latter one represents the half-quantized vortex winding only the component 2 with θ the angle for the path encircling the vortices. On the other hand, one can express the integer vortices as

$$\Psi_{\mathrm{IV}} = \Psi(-2\theta, \beta, \gamma) = e^{i\theta}\begin{pmatrix}\sqrt{n_1}e^{-i\gamma/2}\\ \sqrt{n_2}e^{i\gamma/2}\end{pmatrix}, \tag{4.25}$$

which can take an arbitrary value of γ along the path θ.

Let us consider the half-quantized vortex-antivortex pairs. Denoting a vortex in component 1 with a unit charge as $\{1, 0\}$ and the one in component 2 with a unit charge $\{0, 1\}$, we represent the vortex-antivortex pairs as $\{1, 0\} \overset{r_0}{-} \{-1, 0\}$ in component 1 with the distance r_0 and $\{0, 1\} \overset{r_0}{-} \{0, -1\}$ in component 2. The configurations for the vortex-antivortex pairs are [73]

$$\{1, 0\} \overset{r_0}{-} \{-1, 0\}: \quad \Psi^{(1)}_{\mathrm{V-AV}} = \Psi(\theta^-_{r_0,0}, \beta, \theta^-_{r_0,0}) = \begin{pmatrix}\sqrt{n_1}e^{i\theta^-_{r_0,0}}\\ \sqrt{n_2}\end{pmatrix}, \tag{4.26a}$$

$$\{0, 1\} \overset{r_0}{-} \{0, -1\}: \quad \Psi^{(2)}_{\mathrm{V-AV}} = \Psi(\theta^-_{r_0,0}, \beta, -\theta^-_{r_0,0}) = \begin{pmatrix}\sqrt{n_1}\\ \sqrt{n_2}e^{i\theta^-_{r_0,0}}\end{pmatrix}, \tag{4.26b}$$

with

$$\theta_{r_0,\delta} \equiv \arctan\left(\frac{y-\delta/2}{x-r_0/2}\right), \tag{4.27}$$

and $\theta^{\pm}_{r_0,\delta} \equiv \theta_{r_0,\delta} \pm \theta_{-r_0,\delta}$.

A finite Rabi coupling between the two hyperfine states stabilizes a *vortex molecule*, which consists of two vortices with unit charges of different hyperfine states denoted as $[1,1]_{r_0} \equiv \{1,0\} \overset{r_0}{-} \{0,1\}$. Indeed, the energy shift due to the finite Rabi coupling in Eq. (4.8) reads

$$E_{\rm R} = -2\hbar\omega_{\rm R}\int \mathrm{d}\boldsymbol{r}\,|\Psi_1||\Psi_2|\cos\gamma. \tag{4.28}$$

The energy (4.28) takes the minimum at $\gamma = 0$ and maximum at $\gamma = \pi$. When the two vortices winding in Ψ_1 and Ψ_2 are fully overlapped, the relative phase vanishes everywhere. It implies that this Rabi coupling plays the role of attractive force between the two vortices of different hyperfine states resulting in the confinement of vortices. The configurations of the vortex molecule and the vortex molecule-antimolecule pair can be expressed as

$$[1,1]_{r_0}: \quad \Psi_{\rm M} = \Psi(\theta^{+}_{r_0,0}, \beta, \theta^{-}_{r_0,0}) = \begin{pmatrix} \sqrt{n_1}e^{i\theta_{r_0,0}} \\ \sqrt{n_2}e^{i\theta_{-r_0,0}} \end{pmatrix}, \tag{4.29a}$$

$$\begin{aligned}[1,1]_{\delta} \overset{r_0}{-} [-1,-1]_{\delta}: \quad \Psi_{\rm M-AM} &= \Psi(\theta^{-}_{r_0,\delta} + \theta^{-}_{r_0,-\delta}, \beta, \theta^{-}_{r_0,\delta} - \theta^{-}_{r_0,-\delta}) \\ &= \begin{pmatrix} \sqrt{n_1}e^{i\theta^{-}_{r_0,\delta}} \\ \sqrt{n_2}e^{i\theta^{-}_{r_0,-\delta}} \end{pmatrix},\end{aligned} \tag{4.29b}$$

respectively.

The inter-vortex interaction energies for each configuration of vortex-antivortex pairs in Eqs. (4.26) can be obtained by inserting Eqs. (4.26) into Eq. (4.2) under $V^{(1)}_{\rm ext} = V^{(2)}_{\rm ext} = 0$ as [73]

$$E[\Psi^{(1)}_{\rm V-AV}] = \frac{2\pi\hbar^2}{m}n_1 \ln\left(\frac{r_0}{\xi_1}\right) + \mathcal{E}_{\rm R} r_0, \tag{4.30a}$$

$$E[\Psi^{(2)}_{\rm V-AV}] = \frac{2\pi\hbar^2}{m}n_2 \ln\left(\frac{r_0}{\xi_2}\right) + \mathcal{E}_{\rm R} r_0, \tag{4.30b}$$

with $\mathcal{E}_{\rm R} \equiv \hbar\sqrt{\hbar\omega_{\rm R} n\sqrt{n_1 n_2}/m}$ and $\xi_{a=1,2} = \hbar/\sqrt{2mg_{aa}n_a}$ the vortex core size for the a-th component. Note that the Rabi coupling leads to a linear dependence of the energy on the inter-vortex distance in addition to the logarithmic dependence, which hinders the BKT transition due to the unbindings of the vortex-antivortex pairs. On the other hand, the energy for vortex molecule-antimolecule pairs can be calculated as

$$E[\Psi_{\rm M-AM}] = \frac{2\pi\hbar^2}{m}n \ln\left(\frac{r_0}{\xi}\right), \tag{4.31}$$

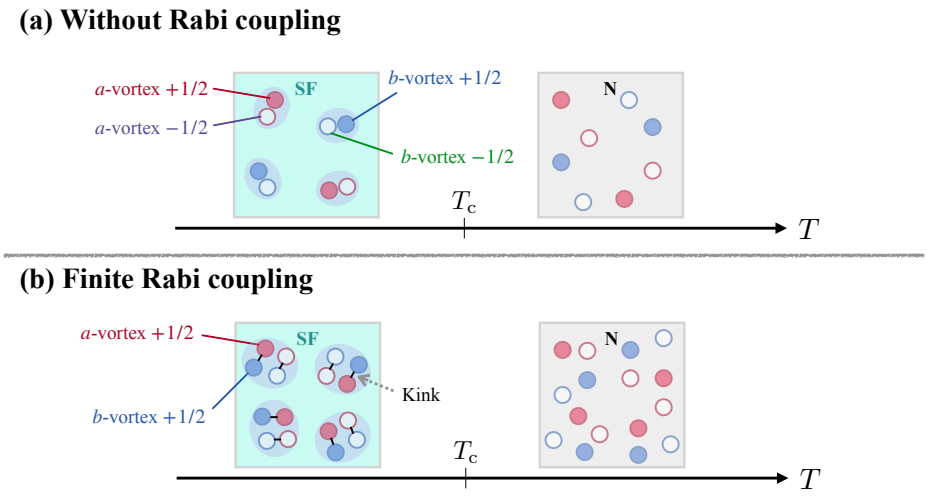

Figure 4.3: Schematic picture of the mechanism of BKT transitions in a binary Bose mixture (a) without Rabi coupling and (b) with finite Rabi coupling.

with $\xi = \sqrt{\xi_1 \xi_2}$. It has a logarithmic dependence on the inter-molecule distance indicating that the vortex molecule-antimolecule pairs play the role of topological excitations responsible for the BKT transition in a Rabi-coupled binary Bose mixture. The schematic picture of the BKT transition in a Rabi-coupled binary Bose superfluid is illustrated in Fig. 4.3.

The formation of the vortex molecules due to the Rabi coupling is analogous to the quark confinement in QCD [184]. Indeed, although the dimensionality is different from QCD, there are several attempts to demonstrate QCD by using the quantized vortices in a binary Bose superfluid [58, 61, 67, 70, 71, 74]. In the context of two-flavour QCD, a half-quantized vortex winding only the first component described by Eq. (4.24a) corresponds to the up-quark, and the one winding only the other component given by Eq. (4.24b) corresponds to the down-quark [71]. And the antiquarks correspond to each of the antivortices. The quark confinement is described by the formation of vortex molecules in Eq. (4.29a).

4.4 Berezinskii-Kosterlitz-Thouless transition

Based on the discussion in Sec. 4.3, we consider the BKT transition in a binary Bose mixture [91].

4.4.1 Superfluid density and critical temperature

In a binary Bose mixture with balanced densities $\alpha_{a=1,2} = n_a/n = 1/2$, we can obtain the following set of NK RG equations [73, 91, 185, 186]

$$\partial_l K(l)^{-1} = 4\pi^3 \Theta(\omega_{\rm R}) y(l)^2, \tag{4.32a}$$

$$\partial_l y(l) = \left[2 - \pi\Theta(\omega_{\rm R}) K(l)\right] y(l), \tag{4.32b}$$

where $\Theta(x)$ is the Heaviside step function with $\Theta(0) = 1/2$. It can be derived from the microscopic Lagrangian as in the single-component case. For details of the derivation, see Appendix A.4.2. The RG equations (4.32) give the modified NK criterion

$$k_{\rm B} T_{\rm c} = \frac{\pi\hbar^2}{2m} \Theta(\omega_{\rm R}) n_{\rm s}(T_{\rm c}), \tag{4.33}$$

at the BKT critical temperature $T_{\rm c}$. This NK criterion (4.33) is consistent with the Monte Carlo analysis in Ref. [73]. To calculate the RG flow, we use the initial conditions as $K(0) = J(0)/(k_{\rm B}T) = \hbar^2 n_{\rm s}^{(0)}(T)/(m k_{\rm B} T)$ and $\mu_{\rm v}(0) = \pi^2 \Theta(\omega_{\rm R}) J(0)/4$ [160, 187, 188, 189], where $n_{\rm s}^{(0)}(T)$ is calculated by

$$n_{\rm s}^{(0)}(T) = n - n_{\rm n}^{-}(T) - n_{\rm n}^{+}(T), \tag{4.34}$$

where

$$n_{\rm n}^{\pm}(T) = -\frac{1}{2} \int \frac{{\rm d}^2 \boldsymbol{k}}{(2\pi)^2} \frac{\hbar^2 k^2}{2m} f_T'(E_k^{\pm}), \tag{4.35}$$

is Landau's formula (3.29b) of the thermally activated normal density due to the elementary excitations. In the formula, $f_T'(E)$ is the derivative with respect to E of the Bose distribution function $f_T(E) = 1/[e^{E/(k_{\rm B}T)} - 1]$. The maximum value of the RG scale is related to the system size as $l_{\rm max} = \ln(L/\xi)$ with $\xi = \hbar/\sqrt{2mg(n/2)}$ the vortex core size. Here, we note that the higher-order derivative terms in the XY model can lead to corrections in the initial conditions for the RG flow. Indeed, it has been pointed out that the higher-order corrections are important for quantitatively accurate predictions of the BKT transition in XY models in particular for a small vortex chemical potential [190]. In our model of a binary Bose mixture, such a higher-order term of the superfluid velocity can arise and determine a quantitative change in our results with a small vortex chemical potential as well. In this Thesis, however, since they are expected to give moderate quantitative changes, we do not consider the effects of the spin-wave excitations on the vortex excitations, which will be the subject of future investigation including the functional RG analysis [190, 191].

The modification of the NK criterion in the absence of Rabi coupling reflects the half circulation of vorticity. With fractional parameters $\alpha_a = n_a/n$, for instance, each of the circulations for vortices $(\Psi_1, \Psi_2) = (\sqrt{n_1} e^{\pm i\theta_0}, \sqrt{n_2})$ with $\theta_0 = \arctan(y/x)$ is given by $\Gamma_1 = \pm 2\pi\alpha_1 \hbar/m$ (see Eq. (4.23)) [73]. For a population-balanced system $n_1 = n_2 = n/2$,

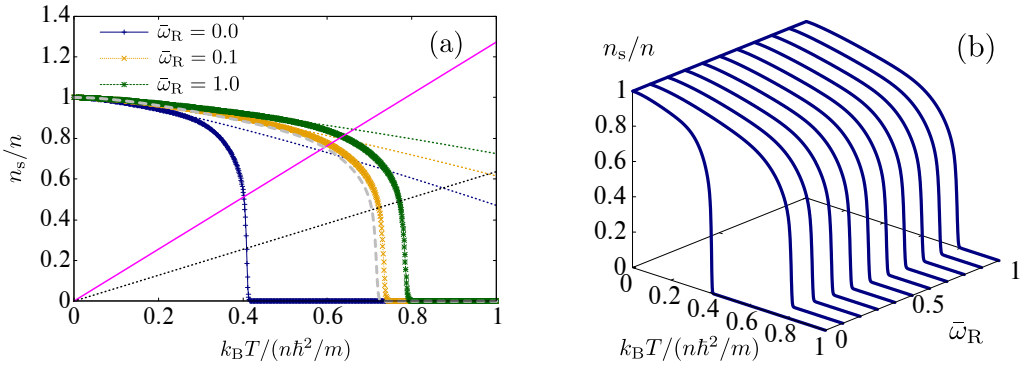

Figure 4.4: Renormalized superfluid fraction calculated with Eqs. (4.32) for $\tilde{g} = mg/\hbar^2 = 0.1$ and $\eta = g_{12}/g = 0$ [91]. The left panel (a) displays the results with $L/\xi = 200$ with $\bar{\omega}_R = \hbar\omega_R/(n\hbar^2/m) = 0.0, 0.1, 1.0$. The horizontal axis is the dimensionless temperature $2\pi/(n\lambda_T^2) = k_BT/(n\hbar^2/m)$. The grey dashed curve stands for the superfluid fraction in a single-component Bose gas with $\tilde{g} = 0.1$ calculated with Eqs. (2.74). The thin dotted curves represent the bare superfluid fraction given by Eq. (4.34). The thin solid line and thin dotted line stand for $k_BT = \pi\hbar^2 n_s(T)/(4m)$ and $k_BT = \pi\hbar^2 n_s(T)/(2m)$, respectively. The right panel (b) shows the 3D plot of the superfluid fraction as a function of the temperature and Rabi coupling.

in particular, $\alpha_{1,2} = 1/2$ gives rise to half vortices. In the presence of Rabi coupling, on the other hand, topological defects that lead to BKT transition are replaced with vortex molecule-antimolecule pairs instead of vortex-antivortex pairs [58, 73, 184]. The formation of vortex molecule pairs modifies the RG equations as in Eqs. (4.32), which recover the ones for the single-component case in Eqs. (2.74).

Figure 4.4 shows the renormalized superfluid fraction computed with Eqs. (4.32) for $\tilde{g} = mg/\hbar^2 = 0.1$ and $\eta \equiv g_{12}/g = 0$ with $L/\xi = 200$. Figure 4.4(a) displays the results with $\bar{\omega}_R = \hbar\omega_R/(n\hbar^2/m) = 0, 0.1, 1.0$. The horizontal axis is the dimensionless temperature $k_BT/(n\hbar^2/m) = 2\pi/(n\lambda_T^2)$ with $\lambda_T = [2\pi\hbar^2/(mk_BT)]^{1/2}$ being the thermal wavelength. The thin dotted curves stand for the bare superfluid fraction given by Eq. (4.34). Due to the finite system size, the discontinuity of the renormalized superfluid fraction in the thermodynamic limit $L \to \infty$ is smeared and altered to a continuous drop. In the single-component case plotted by the dashed curve, the superfluid fraction intersects with the thin dotted line $k_BT = \pi\hbar^2 n_s/(2m)$ at the BKT transition temperature as in Eq. (2.76) in the thermodynamic limit. In contrast, in a population-balanced binary Bose mixture, the superfluid fraction should intersect with the thin solid line $k_BT = \pi\hbar^2 n_s/(4m)$ in the absence of Rabi coupling at the BKT transition temperature as in Eq. (4.33) in the thermodynamic limit. With a finite Rabi coupling, on the other hand, the superfluid fraction intersects with the thin dotted line $k_BT = \pi\hbar^2 n_s/(2m)$ at the BKT transition temperature in the thermodynamic limit as in the single-component Bose gas. A larger value of Rabi coupling shifts the transition temperature to a higher one. The right panel Fig. 4.4(b) shows the 3D plot of the renormalized superfluid fraction to the Rabi coupling and the temperature.

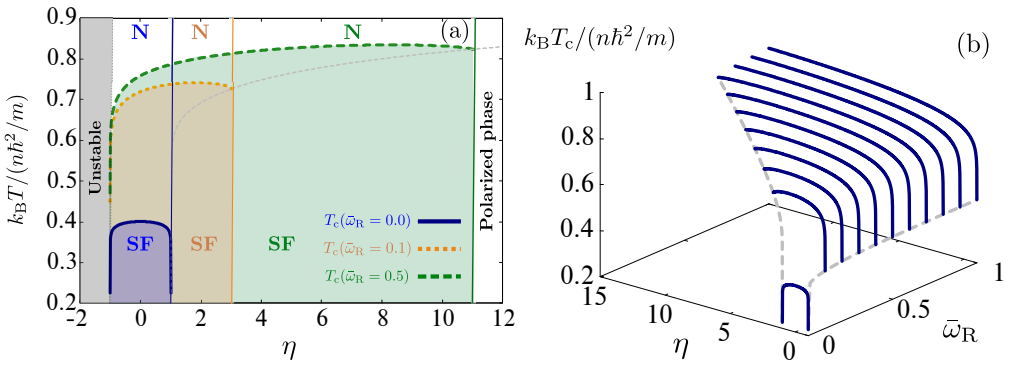

Figure 4.5: Phase diagram of the binary Bose mixture and the BKT transition temperature to inter-component coupling $\eta = g_{12}/g$ and Rabi coupling $\bar{\omega}_R$ [91]. Each of the curves in the left panel (a) represents the BKT transition temperature for $\tilde{g} = 0.1$ and $\bar{\omega}_R = 0.0, 0.1, 0.5$ below which the system is superfluid (SF). Above the transition temperature, it turns into a normal (N) phase with the vanishing superfluid fraction. The grey dotted curve in panel (a) represents the boundary at $\eta = 1+2\hbar\omega_R/(gn)$. Each of the vertical thin lines represents $\eta = 1+2\hbar\omega_R/(gn)$ for each Rabi coupling above which the population-balanced ground state changes to the polarized phase. For $\eta < -1$, the population-balanced ground state is unstable. The two dashed curves in the right panel (b) represent the boundaries of the stable region of the ground state with balanced densities at $\eta = -1$ and $\eta = 1 + 2\hbar\omega_R/(gn)$ respectively.

Figure 4.5 shows the phase diagram and the BKT transition temperature. In the left panel Fig. 4.5(a), each of the curves represents the intercomponent coupling dependence of the BKT transition temperature in the thermodynamic limit with $\tilde{g} = 0.1$ and $\bar{\omega}_R = 0, 0.1, 0.5$. The shaded region below the transition temperature is the superfluid phase with a finite superfluid density for each of the values of Rabi coupling, while the system is in the normal phase above the temperature. As one increases $\eta = g_{12}/g$ from -1, we can observe that the transition temperature first increases. Near $\eta = 1+2\hbar\omega_R/(gn)$, it reaches a maximum for each $\bar{\omega}_R$ and turns into a gradual decrease. In particular, at $\bar{\omega}_R = 0$, as displayed in Fig. 4.5(a), the BKT transition temperature is symmetric with respect to η and reaches its maximum at $\eta = 0$. This is a natural consequence of the two symmetric excitation spectra $E_k^{\pm} = \sqrt{\varepsilon_k \left[\varepsilon_k + gn\left(1 \pm \eta\right)\right]}$ for $\omega_R = 0$. Figure 4.5(b) displays the 3D plot of the BKT transition temperature to η and $\bar{\omega}_R$. It shows the monotonic increase of the transition temperature by increasing the Rabi coupling $\bar{\omega}_R$. This enhancement can be explained by the behavior of the energy gap in E_k^- due to the Rabi coupling. As one increases the Rabi coupling, the gap size also increases and the normal density n_n^- in Eq. (4.35) decreases while n_n^+ is unaffected. It results in an increase of the superfluid density in Eq. (4.34), thereby leading to an enhancement of the BKT transition temperature according to Eq. (4.33) by replacing the renormalized superfluid density with the bare one, which is a good approximation at low temperatures as illustrated in Fig. 4.4(a). The maximum value of the transition temperature scaled by the one in the single-component case is shown in Fig. 4.6 with varying Rabi coupling. It monotonically increases by increasing $\bar{\omega}_R$. Figure 4.6 also reveals that the

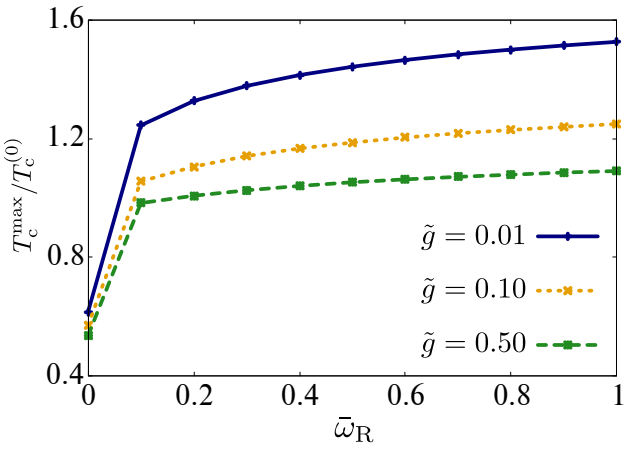

Figure 4.6: Maximum BKT transition temperature scaled by the transition temperature in the single-component case $T_c^{\max}/T_c^{(0)}$ with $\tilde{g} = 0.01, 0.1, 0.5$ [91].

ratio $T_c^{\max}/T_c^{(0)}$ is prominently enhanced as one decreases the intra-coupling strength $\tilde{g}$. This behavior comes from the monotonic increase of critical temperature $T_c^{(0)}$ in the single-component Bose gas faster than $T_c^{\max}$ by increasing $\tilde{g}$. In other words, $T_c^{(0)}$ in a single-component superfluid approaches zero by $g \to 0$ due to the Landau instability (2.52), while the transition temperature in a binary superfluid remains to be finite with a finite intercomponent coupling g_{12} even with $g \to 0$ because the system is still far from an ideal Bose gas.

4.4.2 Sound velocities

Let us consider the first and second sound velocities in a binary Bose mixture. The first and second sound velocities $c_{1,2}$ are the roots of Landau's two-fluid equation calculated from the free energy as we analyzed in Sec. 3.2. In a two-component Bose mixture, the free energy F at the mean-field level is given by

$$F = \frac{1+\eta}{4}\frac{gN^2}{L^2} - \hbar\omega_R N + L^2 k_B T \int \frac{d^2\boldsymbol{k}}{(2\pi)^2}\left[\ln\left(1 - e^{-E_k^-/(k_B T)}\right) + \ln\left(1 - e^{-E_k^+/(k_B T)}\right)\right]. \tag{4.36}$$

The first two terms in Eq. (4.36) correspond to the free energy at zero temperature, and the second line represents the contribution of thermal fluctuations. In the phononic regime at low temperatures without Rabi coupling $\omega_R = 0$, $E_k^+ = c_B \hbar k$ with $c_B = \sqrt{(1+\eta)gn/(2m)}$ and $E_k^- = c_- \hbar k$ with $c_- = \sqrt{(1-\eta)gn/(2m)}$ provide

$$\frac{F}{N} = \frac{1+\eta}{2}\frac{gn}{2} - \hbar\omega_R - \frac{\zeta(3)}{2\pi\hbar^2}\frac{(k_B T)^3}{n}\left(\frac{1}{c_-^2} + \frac{1}{c_B^2}\right), \tag{4.37a}$$

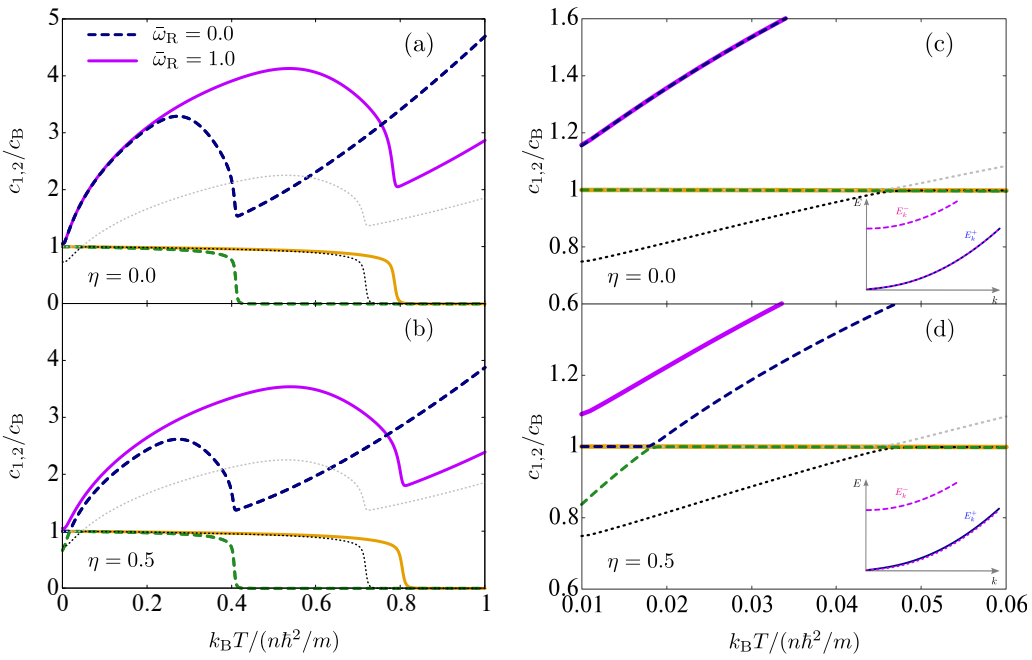

Figure 4.7: First sound and second sound velocities $c_{1,2}$ scaled by the Bogoliubov velocity c_B for $\tilde{g} = 0.1$ and $L/\xi = 200$ [91]. The inter-coupling is set to be $\eta = 0$ in the upper left panel (a), and $\eta = 0.5$ in the lower left panel (b). The dashed curves correspond to $\bar{\omega}_R = 0.0$ while the solid curves correspond to $\bar{\omega}_R = 1.0$. The thin dotted curves represent $c_{1,2}$ in a single-component Bose gas for $\tilde{g} = 0.1$. The low-temperature behavior is zoomed in the right panels (c) and (d). The insets in panels (c) and (d) illustrate the elementary excitations $E_k^{\pm}$. The solid curves stand for the gapless branch E_k^+, while the dotted and dashed curves represent E_k^- which is gapless for $\bar{\omega}_R = 0.0$ while gapped for $\bar{\omega}_R = 1.0$, respetively.

$$n_n = n_n^+ + n_n^- = \frac{3\zeta(3)}{2\pi\hbar^2}\frac{(k_BT)^3}{2m}\left(\frac{1}{c_-^4} + \frac{1}{c_B^4}\right), \tag{4.37b}$$

which results in

$$v_T = v_s = c_B, \quad v_L = \sqrt{\frac{c_-^{-2} + c_B^{-2}}{c_-^{-4} + c_B^{-4}}} = \sqrt{\frac{1-\eta}{1+\eta^2}}c_B, \tag{4.38}$$

at low temperatures. For $-1 < \eta \leq 0$, $v_L \geq v_s$ leads to $c_1 = v_L$ and $c_2 = v_s$. For $0 < \eta < 1$, $v_L < v_s$ leads to $c_1 = v_s$ and $c_2 = v_L$. With a finite Rabi coupling $\omega_R > 0$, on the other hand, the thermal contribution associated with the gapped branch E_k^- vanishes at low temperatures because the gapped mode is no longer occupied. Then, the free energy and normal density are given by

$$\frac{F}{N} = \frac{1+\eta}{2}\frac{gn}{2} - \hbar\omega_R - \frac{\zeta(3)}{2\pi\hbar^2}\frac{(k_BT)^3}{nc_B^2}, \tag{4.39a}$$

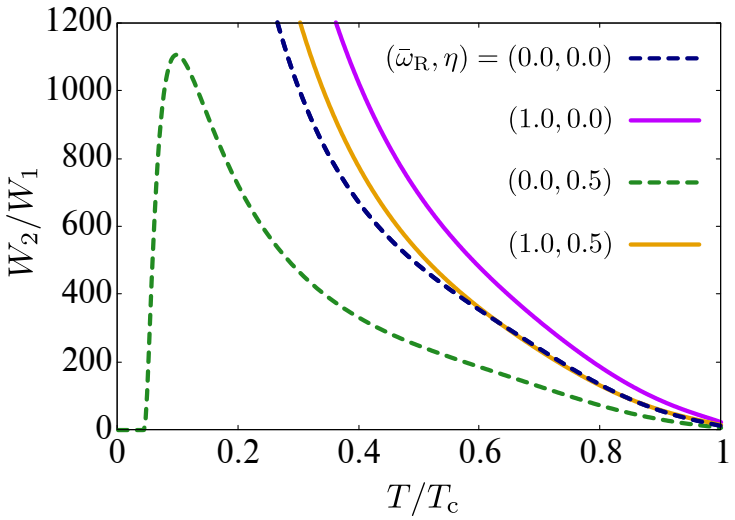

Figure 4.8: Ratio between the amplitude of the first sound and second sound W_2/W_1 in the dynamic structure factor.

$$n_n = \frac{3\zeta(3)}{2\pi\hbar^2}\frac{(k_B T)^3}{2mc_B^4}. \tag{4.39b}$$

The thermal part of free energy is identical to the one in the single-component case while the normal density is half of that in the single-component case in Eq. (3.29b) because of the prefactor 1/2 in Eqs. (4.35). As a result, the sound velocities at low temperatures change to

$$c_{1,2} = v_T = v_s = v_L = c_B, \tag{4.40}$$

at any value of inter-component coupling η. The difference from the single-component case in Eqs. (3.41) is ascribed to the modification of the normal density in Eqs. (4.39).

Figure 4.7 illustrates the first and second sound velocities for $\tilde{g} = 0.1$ and $\eta = 0, 0.5$ with $\bar{\omega}_R = 0.0, 1.0$. The upper branch is the first sound velocity c_1 and the lower branch is identified as the second sound velocity c_2, which survives as long as the superfluid density is finite. A finite Rabi coupling increases the critical temperature as shown in Fig. 4.4 and allows the second sound to be present up to a higher temperature. At the low-temperature limit in the absence of Rabi coupling, using the linear dispersions $E_k^+ \simeq c_B\hbar k$ and $E_k^- \simeq c_-\hbar k$, one finds Eqs. (4.38). For $\eta = 0$ as shown in Fig. 4.7(a), in particular, the first sound and second sound velocities coincide with each other $c_1 = c_2 = v_T = v_s = v_L = c_B$. The low-temperature behavior is shown in Fig. 4.7(c). With $0 < \eta < 1$ in the low-temperature regime without Rabi coupling, one observes $c_1 = v_s = v_T = c_B$ and $c_2 = v_L < c_B$ indicating that each of the sound modes is identified as the density mode and entropy mode respectively as illustrated by the dashed curves in Fig. 4.7(d). As one increases the temperature, the two branches exhibit a quasicrossing at which the density mode and entropy mode start to mix as in the case of a single-component

2D Bose gas plotted with the thin dotted curves in Fig. 4.7 or a 3D Bose gas [90, 151]. In contrast, the solid curves in Fig. 4.7 imply that a finite Rabi coupling suppresses the quasicrossing as shown in Fig. 4.7(d), which is distinct from a single-component 2D Bose gas. This behavior can be understood by the presence of a gapped mode. With a finite Rabi coupling, E_k^- is gapped out as shown in the insets of Figs. 4.7(c) and 4.7(d), and most thermally excited bosons occupy only the gapless mode $E_k^+ \simeq c_{\rm B}\hbar k$. Then, the major difference from the single-component case is only the additional prefactor $1/2$ in Eqs. (4.35) which affects the Landau velocity. Consequently, the Landau velocity is found to be identical to the Bogoliubov velocity which also coincides with the adiabatic velocity at low temperatures. It results in the suppression of quasicrossing at a low temperature. As explained in Sec. 3.2.2, the temperature at which the quasicrossing occurs characterizes the temperature above which the second sound can be detected by a density probe [192, 193, 194, 195]. From the experimental point of view, hence, the suppression of quasicrossing at finite temperature implies that the second sound mode is sensitive to a density probe even in the low-temperature regime, which can be tested with ultracold atom experiments [194, 196].

To discuss the detectability of the second sound, as in Sec. 3.3.1, we examine the dynamic structure factor (3.46) for the density response function. Figure 4.8 shows the ratio of the amplitude W_2/W_1 given by Eqs. (3.47) for $(\bar{\omega}_{\rm R}, \eta) = (0, 0), (1.0, 0.0), (0.0, 0.5)$, and $(1.0, 0.5)$. It clearly indicates that the ratio becomes smaller than unity $W_2/W_1 \ll 1$ in the low-temperature regime only for $(\bar{\omega}_{\rm R}, \eta) = (0.0, 0.5)$ while otherwise, it is much larger than unity. From this behavior, we can conclude that the second sound can be detected by a density probe even in the low-temperature regime unless $\bar{\omega}_{\rm R} = 0$ and $0 < \eta < 1$.

Chapter 5

Damped Langevin dynamics in Josephson junctions

This Chapter is devoted to the analyses of dynamics in a Bose Josephson junction and a superconducting Josephson circuit. First, we see the damped Langevin dynamics in an atomic Josephson junction in a head-to-tail configuration. It reveals that the Josephson coupling induces an intrinsic coupling between the Josephson mode and the other bath modes. The intrinsic coupling causes giant fluctuations in the relative phase. Secondly, we consider a resistively and capacitively shunted Josephson circuit. In contrast to the atomic Josephson junction, the resistor plays the role of a thermal bath and leads to extrinsic coupling with the superconducting phase. We clarify the effects of quantum fluctuations on the Langevin dynamics and coherence factor in the RCSJ circuit. Finally, we show the quantum correction to the Josephson frequency.

5.1 Josephson junctions

Josephson junctions were originally proposed as a system composed of an insulator sandwiched by two superconductors with the superconducting phases ϕ_1 and ϕ_2 as illustrated in Fig. 5.1(a) [197, 198, 199]. The relative superconducting phase $\phi = \phi_2 - \phi_1$ induces an AC Josephson current $I(t) = I_c \sin\phi(t)$ flowing across the insulator carried by the Cooper pairs. This transport phenomenon is the original AC Josephson effect. The superconductors can be replaced with atomic superfluids as in Fig. 5.1(b). Atomic Josephson junctions consist of two atomic superfluids trapped in a double-well potential and separated by a potential barrier as shown in Fig. 5.1(b). The two separated superfluids are coupled by a tunnel coupling J responsible for the Josephson oscillations of the population imbalance and relative superfluid phase. Generally, the potential height can be asymmetric as in Fig. 5.1(b) though we consider only the symmetric case for simplicity throughout this Thesis. These two-terminal setups with ultracold atoms are useful in particular to investigate transport properties [200, 201, 202, 203, 204, 205, 206, 207, 208, 209, 210, 211, 212] or relaxation dynamics

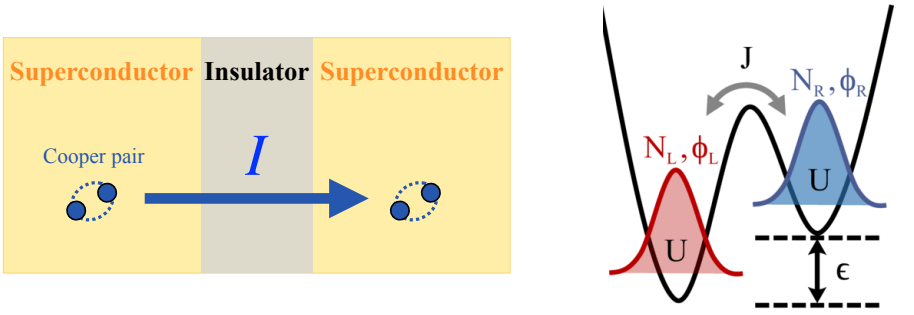

(a) Superconducting Josephson junction (b) Atomic Josephson junction

Figure 5.1: Schematic figures of (a) superconducting Josephson junction and (b) atomic Josephson junction [42].

[42].

Although the Josephson effect itself is a quantum mechanical phenomenon, we should observe the influence of quantum fluctuations on the Josephson dynamics. In Sec. 5.2, we consider a Bose-Josephson junction to reveal the Langevin dynamics of Josephson modes. Next, by analyzing the Josephson dynamics in a superconducting Josephson circuit subject to quantum fluctuations, we clarify the difference from the atomic Josephson junction in Sec. 5.3. Section 5.4 presents the quantum correction to the frequency of the Josephson oscillation.

5.2 Bose Josephson junction

We start with quasi-1D two weakly-interacting Bose gases with the system size L described by

$$\mathcal{L}_{\rm BJJ} = \sum_{a=1,2}\left[i\hbar\Psi_a^*\partial_t\Psi_a - \frac{\hbar^2}{2m}|\partial_x\Psi_a|^2 - \frac{g}{2}|\Psi_a|^4\right] + \frac{J(x)}{2}\left[\Psi_1^*\Psi_2 + \Psi_2^*\Psi_1\right], \tag{5.1}$$

with g the interaction strength and $J(x)$ the Josephson coupling dependent on spatial coordinates. This model is analogous to the binary Bose superfluid considered in Chap. 4, but the spatial dependence of the Josephson coupling $J(x)$, which was a uniform Rabi coupling in a binary Bose superfluid, characterizes the dynamics in this Bose-Josephson junction. Moreover, Eq. (5.1) does not include a intercomponent coupling term $g_{12}|\Psi_1|^2|\Psi_2|^2$ due to the spatial separation. One can consider two typical

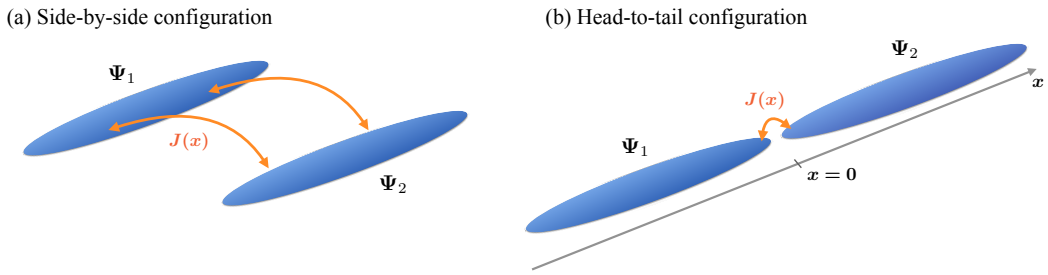

Figure 5.2: Schematic figures of (a) side-by-side configuration and (b) head-to-tail configuration in a BJJ.

cases:

$$J(x) = \begin{cases} J_0 & \text{(side-by-side)}, \\ J_0 L\delta(x) & \text{(head-to-tail)}. \end{cases} \tag{5.2}$$

These two configurations are sketched in Fig. 5.2. Here, J_0 characterizes the strength of the tunnel coupling. In the following subsections, we work on these two cases. We perform the polar decomposition of the complex Bose field of a-th quasi-condensate $\Psi_a(x,t)$ as

$$\Psi_a(x,t) = \sqrt{n_a(x,t)} e^{i\phi_a(x,t)}, \tag{5.3}$$

where $n_a(x,t) = |\Psi_a(x,t)|^2$ is the density and ϕ_a is the phase of the a-th quasi-condensate. We introduce the average density, population imbalance, total phase, and relative phase as

$$\begin{aligned} \bar{n} &= \frac{n_1 + n_2}{2}, \qquad & \zeta &= \frac{n_1 - n_2}{2\bar{n}}, \\ \bar{\phi} &= \phi_1 + \phi_2, \qquad & \phi &= \phi_1 - \phi_2. \end{aligned} \tag{5.4}$$

By inserting Eq. (5.3) into Eq. (5.1) with Eqs. (5.4), the Lagrangian density can be written as

$$\mathcal{L}_{\mathrm{BJJ}}[\zeta,\phi] = -\hbar\bar{n}\zeta\dot{\phi} - \frac{\hbar^2\bar{n}}{4m}\left[\frac{(\partial_x\zeta)^2}{1-\zeta^2} + (\partial_x\phi)^2\right] - g\bar{n}^2\zeta^2 + J(x)\bar{n}\sqrt{1-\zeta^2}\cos\phi, \tag{5.5}$$

with $\dot{\bar{n}} = \dot{\bar{\phi}} = 0$ and $\partial_x\bar{n} = \partial_x\bar{\phi} = 0$. By assuming a small population imbalance $|\zeta| \ll 1$, the saddle-point approximation by inserting the equation of motion $\zeta = -\hbar\dot{\phi}/[2g\bar{n} + J(x)\cos\phi]$ provides the simplified Lagrangian only with respect to the relative phase as

$$\mathcal{L}_\phi = \frac{\hbar}{4g}\dot{\phi}^2 - \frac{\hbar^2\bar{n}}{4m}(\partial_x\phi)^2 + J(x)\bar{n}\cos\phi, \tag{5.6}$$

within the Josephson regime $J(x) \ll 2g\bar{n}$.

5.2.1 Side-by-side configuration

Let us first consider the side-by-side configuration $J(x) = J_0$, which is the uniform Josephson coupling as sketched in Fig. 5.2(a). We perform mode expansion of the relative phase as

$$\phi(x,t) = \frac{1}{\sqrt{L}} \sum_{n=0}^{\infty} \Phi_n(x) q_n(t), \tag{5.7}$$

with

$$\Phi_n(x) = \frac{1}{\sqrt{L}} \cos(k_n x), \tag{5.8}$$

and $k_n = n\pi/L$. Here, $\{\Phi_n(x)\}_{n=1}^{\infty}$ is an orthonormal basis satisfying

$$\int_0^L \mathrm{d}x\, \Phi_n^*(x)\Phi_m(x) = \delta_{nm}. \tag{5.9}$$

Using this mode expansion (5.7), the Lagrangian can be expressed as

$$L_\phi = \int_0^L \mathrm{d}x\, \mathcal{L}_\phi \quad = \sum_{n=0}^{\infty} \left[\frac{M}{2} \dot{q}_n(t)^2 - \frac{M\tilde{\omega}_n^2}{2} q_n(t)^2 \right], \tag{5.10}$$

with $M = \hbar^2/2gL$, $\omega_n = ck_n$, $c = \sqrt{g\bar{n}/m}$, and

$$\tilde{\omega}_n \equiv \sqrt{\omega_n^2 + \Omega^2}, \tag{5.11}$$

where $\Omega = \sqrt{J_0\bar{n}/ML}$ is the Josephson frequency. The Lagrangian (5.10) indicates that the system is described by independent decoupled harmonic oscillators with frequency $\tilde{\omega}_n$, which absorbs the effects of Josephson coupling. It does not allow us to describe the damping effects in the Josephson mode. To discuss the damped dynamics in the side-by-side configuration, we need to incorporate the higher-order contributions in ϕ.

5.2.2 Head-to-tail configuration

In a head-to-tail configuration $J(x) = J_0 L\delta(x)$ illustrated in Fig. 5.2(b), on the other hand, the damped dynamics can be described in a simpler manner. The mode expansion (5.7) gives

$$L_\phi = \sum_{n=0}^{\infty} \left[\frac{M}{2} \dot{q}_n(t)^2 - \frac{M\omega_n^2}{2} q_n(t)^2 \right] + J_0 L\bar{n} \cos\left(\frac{1}{L} \sum_{n=0}^{\infty} q_n(t) \right). \tag{5.12}$$

In contrast to the side-by-side configuration described by Eq. (5.10), the Josephson coupling gives an additional contribution as in the last term in Eq. (5.12)

To elucidate the dynamics of the Josephson mode, we perform a canonical transformation

$$Q_0(t) = \sum_{n=0}^{\infty} q_n(t), \qquad Q_{n\geq 1}(t) = q_n(t), \tag{5.13}$$

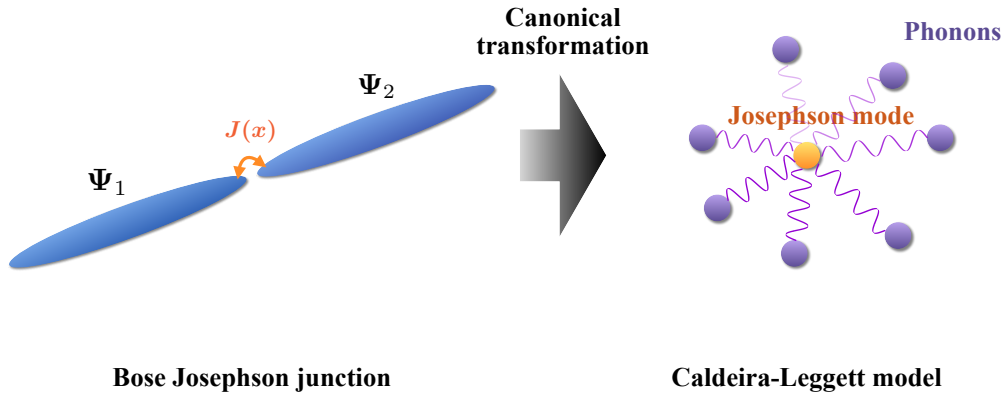

Figure 5.3: Mapping from the Bose Josephson junction in a head-to-tail configuration to the Caldeira-Leggett-type model.

which results in

$$L_\phi = \frac{M}{2}\left[\dot{Q}_0(t) - \sum_{n=1}^{\infty}\dot{Q}_n(t)\right]^2 + \sum_{n=1}^{\infty}\left[\frac{M}{2}\dot{Q}_n(t)^2 - \frac{M\omega_n^2}{2}Q_n(t)^2\right] + J_0 L\bar{n}\cos\left(\frac{Q_0(t)}{L}\right). \tag{5.14}$$

The Hamiltonian reads

$$H_\phi = \frac{P_0^2}{2M} - J_0 L\bar{n}\cos\phi_0 + \sum_{n=1}^{\infty}\left[\frac{(P_n+P_0)^2}{2M} + \frac{M\omega_n^2}{2}Q_n^2\right], \tag{5.15}$$

with $P_n = \partial L_\phi/\partial\dot{Q}_n$ the canonical momenta and

$$\phi_0(t) \equiv \phi(0,t) = \frac{Q_0(t)}{L}, \tag{5.16}$$

the Josephson mode. The obtained Hamiltonian (5.15) is called *velocity-coupling model*, which involves an intrinsic coupling between the Josephson mode ϕ_0 and the phononic bath modes Q_n through the momentum. It describes the dynamics of Josephson mode in contact with a thermal bath similar to the Caldeira-Leggett (CL) model [213]. For details on the CL model, see Appendix D. Namely, through the canonical transformation (5.13), we mapped the Bose Josephson system described by Eq. (5.12) to the CL-type model (see Fig. 5.3). However, this intrinsic coupling with bath modes is in stark contrast

to the extrinsic coupling in the standard CL model. Indeed, the Hamilton equations

$$\dot{Q}_0 = \frac{P_0}{M} + \sum_{n=1}^{\infty} \frac{P_n + P_0}{M}, \qquad \dot{Q}_{n\geq 1} = \frac{P_n + P_0}{M}$$
$$\dot{P}_0 = -J_0 \bar{n} \sin\phi_0, \qquad \dot{P}_{n\geq 1} = -M\omega_n^2 Q_n, \tag{5.17}$$

lead to a generalized Langevin equation

$$\ddot{\phi}_0(t) + \int_0^t \mathrm{d}t'\, \gamma[\phi(t'); t-t']\dot{\phi}_0(t') + \Omega^2 \sin\phi_0(t) = \xi_\phi(t) - \gamma_0 \delta(t) \sin\phi_0(0). \tag{5.18}$$

Here, the damping kernel is defined by

$$\gamma[\phi(t'); t-t'] \equiv \Omega^2 \sum_{n=1}^{\infty} \cos\left[\omega_n (t-t')\right] \cos\phi_0(t'). \tag{5.19}$$

Up to the linear order in ϕ_0, Eq. (5.18) can be written as

$$\ddot{\phi}_0(t) + \int_0^t \mathrm{d}t'\, \gamma(t-t')\dot{\phi}_0(t') + \Omega^2 \phi_0(t) = \xi_\phi(t) - \gamma_0 \delta(t) \phi_0(0), \tag{5.20}$$

with

$$\gamma(t-t') = \Omega^2 \sum_{n=1}^{\infty} \cos\left[\omega_n (t-t')\right], \tag{5.21}$$

which is simplified as

$$\gamma(t-t') = \gamma_0 \delta(t-t'), \tag{5.22}$$

with $\gamma_0 \equiv J_0 \bar{n}/Mc$ the damping constant in the continuum limit. The stochastic noise is related to the initial distributions of the infinite number of bath modes as

$$\xi_\phi(t) \equiv -\frac{1}{L} \sum_{n=1}^{\infty} \left[\omega_n^2 \cos(\omega_n t) Q_n(0) + \omega_n \sin(\omega_n t) \dot{Q}_n(0)\right]. \tag{5.23}$$

By assuming that the phonons are initially in thermal equilibrium at temperature T, the noise satisfies

$$\langle \xi_\phi(t) \rangle = 0, \tag{5.24a}$$

$$\chi_\phi(t,t') \equiv \frac{1}{2}\langle\{\xi_\phi(t), \xi_\phi(t')\}\rangle = -\int_{-\infty}^{\infty} \frac{\mathrm{d}\omega}{2\pi} e^{i\omega(t-t')} \frac{\gamma\omega^2}{ML\Omega^2} \hbar\omega \coth\left(\frac{\hbar\omega}{2k_\mathrm{B}T}\right), \tag{5.24b}$$

where the ensemble average $\langle \cdots \rangle$ in Eqs. (5.24) is performed with respect to the bath Hamiltonian of thermal phonons given by [92]

$$H_\mathrm{B} = \sum_{n=1}^{\infty} \left(\frac{P_n^2}{2M} + \frac{M\omega_n^2}{2} Q_n^2\right). \tag{5.25}$$

The second term on the right-hand side of Eq. (5.18) is the negligible initial slippage term.

In a similar manner, we can obtain the Langevin equation with respect to the population imbalance. Based on the assumption of the canonical commutation relation between the phase and density, it is reasonable to perform the mode expansion of the population imbalance in terms of the momentum as

$$\zeta(x,t) = \frac{P_0(t)}{\hbar\bar{n}} + \frac{\sqrt{L}}{\hbar\bar{n}} \sum_{n=1}^{\infty} \Phi_n(x) \left[P_n(t) + P_0(t)\right], \tag{5.26}$$

and we can identify the Josephson mode as

$$\zeta_0(t) = \frac{P_0(t)}{\hbar\bar{n}}. \tag{5.27}$$

From Eqs. (5.17), we can derive the generalized Langevin equation

$$\ddot{\zeta}_0(t) + \int_0^t \mathrm{d}t'\, \gamma(t-t')\dot{\zeta}_0(t') + \Omega^2\zeta_0(t) = \xi_\zeta(t). \tag{5.28}$$

Here, we have omitted the initial slippage term. The stochastic noise is defined as

$$\xi_\zeta(t) = -\frac{\Omega^2}{\hbar\bar{n}} \sum_{n=1}^{\infty} \left[\cos(\omega_n t) P_n(0) + \frac{\sin(\omega_n t)}{\omega_n} \dot{P}_n(0)\right], \tag{5.29}$$

which satisfies

$$\langle \xi_\zeta(t) \rangle = 0, \tag{5.30a}$$

$$\chi_\zeta(t,t') \equiv \frac{1}{2}\langle\{\xi_\zeta(t), \xi_\zeta(t')\}\rangle = \int_{-\infty}^{\infty} \frac{\mathrm{d}\omega}{2\pi} e^{i\omega(t-t')} \frac{M\gamma\Omega^2}{\hbar^2\bar{n}^2} \hbar\omega \coth\left(\frac{\hbar\omega}{2k_\mathrm{B}T}\right). \tag{5.30b}$$

In the classical limit $k_\mathrm{B}T \gg \hbar\omega$, Eqs. (5.24b) and (5.30b) reduce to

$$\chi_\phi(t,t') = -\frac{\gamma_0}{M\Omega^2} k_\mathrm{B}T \frac{\mathrm{d}^2}{\mathrm{d}t^2}\delta(t-t'), \tag{5.31a}$$

$$\chi_\zeta(t,t') = \frac{\gamma_0 M\Omega^2}{\hbar^2\bar{n}^2} k_\mathrm{B}T\delta(t-t'). \tag{5.31b}$$

Note that Eq. (5.31b) recovers the classical FDT while Eq. (5.31a) involves additional time derivatives.

In the low-temperature limit $k_\mathrm{B}T \ll \hbar\omega$, on the other hand, Eqs. (5.24b) and (5.30b) reduce to

$$\chi_\phi(t,t') = -\int_{-\infty}^{\infty} \frac{\mathrm{d}\omega}{2\pi} e^{i\omega(t-t')} \frac{\gamma\omega^2}{ML\Omega^2} \hbar|\omega|, \tag{5.32a}$$

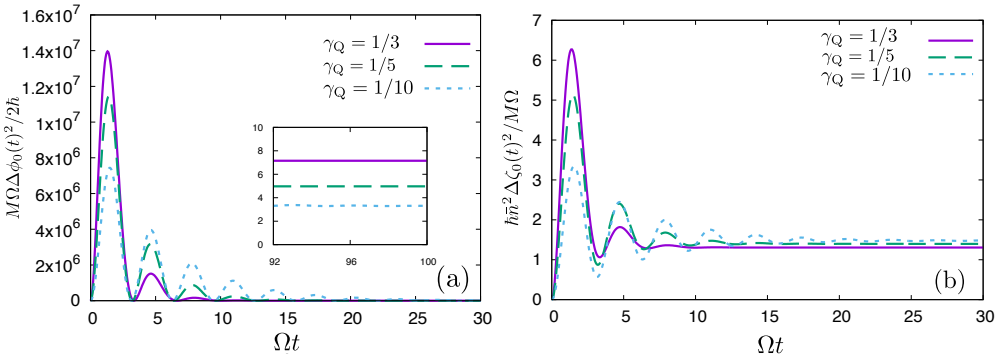

Figure 5.4: Variances of the Josephson modes for relative phase (panel (a)) and population imbalance (panel (b)) at $k_{\rm B}T = 0.01\hbar\Omega$ [92].

$$\chi_\zeta(t,t') = \int_{-\infty}^{\infty} \frac{{\rm d}\omega}{2\pi} e^{i\omega(t-t')} \frac{M\gamma\Omega^2}{\hbar^2\bar{n}^2}\hbar|\omega|. \tag{5.32b}$$

Note that both Eqs. (5.32a) and (5.32b) explicitly exhibit the ultraviolet divergences due to the quantum fluctuations at zero temperature [214, 215, 216, 217, 218]. These divergences are present also at any temperature as in Eqs. (5.24b) and (5.30b) except in the classical limit. In particular, Eq. (5.32a) reveals that the phase mode is subject to larger fluctuations as $\sim |\omega|^3$ in the ultraviolet region.

5.2.3 Effects of quantum fluctuations on correlation functions

Based on the Langevin equations (5.20) and (5.28), we elucidate the effects of quantum fluctuations on autocorrelation functions. The variances are given by

$$\begin{aligned}\Delta\phi_0(t)^2 &\equiv \langle\phi_0(t)^2\rangle - \langle\phi_0(t)\rangle^2 = \int_0^t {\rm d}s \int_0^t {\rm d}s'\, \chi_\phi(s,s') g^{\rm R}(t-s) g^{\rm R}(t-s') \\ &= \frac{2\hbar}{M\Omega}\frac{\gamma_{\rm Q}}{1-\gamma_{\rm Q}^2}\int_{-\infty}^{\infty} {\rm d}x\, x^3 \coth\left(\frac{\hbar\Omega}{2k_{\rm B}T}x\right) G_x(t) G_{-x}(t),\end{aligned} \tag{5.33a}$$

$$\begin{aligned}\Delta\zeta_0(t)^2 &\equiv \langle\zeta_0(t)^2\rangle - \langle\zeta_0(t)\rangle^2 = \int_0^t {\rm d}s \int_0^t {\rm d}s'\, \chi_\zeta(s,s') g^{\rm R}(t-s) g^{\rm R}(t-s') \\ &= \frac{M\Omega}{\hbar\bar{n}^2}\frac{\gamma_{\rm Q}}{1-\gamma_{\rm Q}^2}\int_{-\infty}^{\infty} {\rm d}x\, x \coth\left(\frac{\hbar\Omega}{2k_{\rm B}T}x\right) G_x(t) G_{-x}(t).\end{aligned} \tag{5.33b}$$

Here, we set $x \equiv \omega/\Omega$ and $\gamma_{\rm Q} \equiv \gamma_0/2\Omega$, and introduced the retarded response function

$$g^{\rm R}(t) \equiv \frac{\sin\left(\Omega\sqrt{1-\gamma_{\rm Q}^2}\,t\right)}{\Omega\sqrt{1-\gamma_{\rm Q}^2}} e^{-\gamma_0 t/2}\Theta(t), \tag{5.34}$$

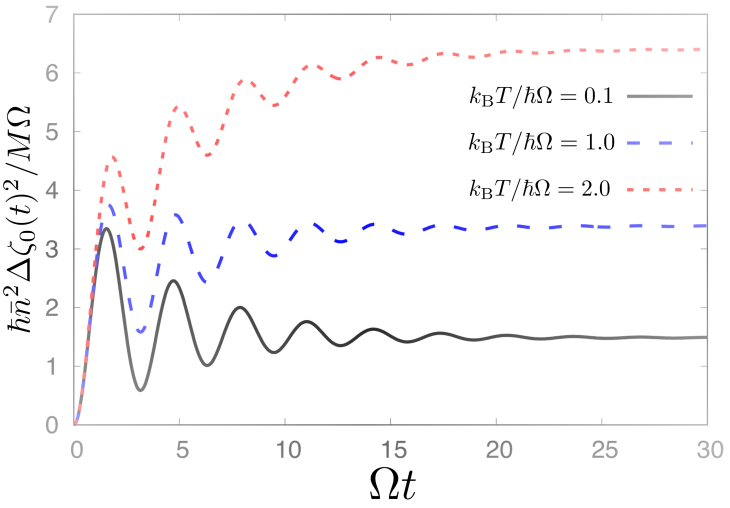

Figure 5.5: Thermal effects on the dynamics of the variances of population imbalance [92].

and

$$G_x(t) \equiv \frac{1}{(ix+\gamma_Q)^2+\gamma_Q^2-1} \times \left[\sqrt{1-\gamma_Q^2}\left[1-e^{-(ix+\gamma_Q)\Omega t}\cos\left(\Omega\sqrt{1-\gamma_Q^2}t\right)\right]-(ix+\gamma_Q)\sin\left(\Omega\sqrt{1-\gamma_Q^2}t\right)\right]. \tag{5.35}$$

Figure 5.4 shows the variances of Eqs. (5.33) at $k_BT = 0.01\hbar\Omega$ in the underdamped regime $\gamma_Q < 1$. The ultraviolet cutoff frequency is chosen to be $\omega_{max} = c\pi N/\Omega L$ with $c = 10^{-3}\,\mathrm{ms}^{-1}$, $N = 10^3$, $\Omega = 10^2\,\mathrm{s}^{-1}$, and $L = 1\,\mu\mathrm{m}$ [42]. Figure 5.4(a) clearly shows that the variance $\Delta\phi_0(t)^2$, related to the relative phase of the Josephson mode, oscillates until it reaches an asymptotic value in the long-time limit, as shown in the inset. The huge initial oscillations are crucially dependent on the cutoff ω_{max}, and the asymptotic value strongly depends on the choice of γ_Q. It is worth noting that a smaller damping constant γ_Q leads to a smaller asymptotic value. The variance $\Delta\zeta_0(t)^2$ of the population imbalance of the Josephson mode in Fig. 5.4(b) also oscillates in time, reaching asymptotically a finite value. Here, the asymptotic value also strongly depends on the damping parameter γ_Q and a smaller γ_Q leads to a larger asymptotic value.

The temperature dependence of the variance of population imbalance is displayed in Fig. 5.5. The figure shows that the asymptotic value $\Delta\zeta_0(\infty)^2$ grows by increasing the temperature. We have verified that the phase variance $\Delta\phi_0(\infty)^2$ also exhibits the similar behavior. These results are fully consistent with the ones obtained in Ref. [219] for the quadratic fluctuations of the damped harmonic oscillator in thermal equilibrium.

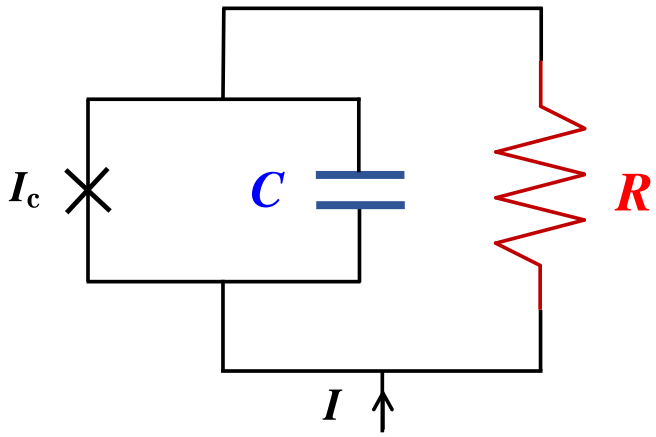

Figure 5.6: RCSJ circuit with resistance R and capacitance C that we study in Sec. 5.3. Here, I_c represents the critical current in the Josephson junction and I is the external current.

5.3 Superconducting Josephson circuit

A resistively and capacitively shunted Josephson (RCSJ) junction illustrated in Fig. 5.6 is a useful platform to investigate quantum dynamics [220, 221, 222, 223, 224] and a good example that shows damped dynamics similar to the BJJ in a head-to-tail configuration discussed in the last section. In this section, we show that the superconducting phase in the RCSJ circuit also exhibits damped Langevin dynamics and illustrate the differences from the BJJ. The dynamics of a RCSJ circuit is described by

$$C\dot{V}(t) + \frac{V(t)}{R} + \frac{\partial U_{\rm wash}(\phi)}{\partial \phi} = \eta(t), \tag{5.36a}$$

$$\dot{\phi}(t) = \frac{2eV(t)}{\hbar}, \tag{5.36b}$$

where $\phi(t)$, $V(t)$, C, and R are the superconducting phase, voltage, capacitance, and resistance, respectively. In Eq. (5.36a),

$$U_{\rm wash}(\phi) = -I_{\rm c}\cos\phi(t) - I\phi(t), \tag{5.37}$$

is the tilted washboard potential with the critical current $I_{\rm c}$ [225, 226]. For a small external current $I < I_{\rm c}$, the washboard potential has potential minima at $\sin\phi = I/I_{\rm c}$ while if the external current exceeds $I_{\rm c}$, it has no potential minimum and it may drive the phase into a running state as shown in Fig. 5.7. Throughout this section, we consider the case with a small external current as in Fig. 5.7(a) excluding the running state. Equation (5.36b) provides the relation between the phase and the voltage. In Eq. (5.36b), e is the elementary charge. We deal with the phase, voltage, and current noise as classical quantities. Then, the current noise $\eta(t)$ in Eq. (5.36a), which originates from the shunted resistor, satisfies

$$\langle \eta(t) \rangle = 0, \tag{5.38a}$$

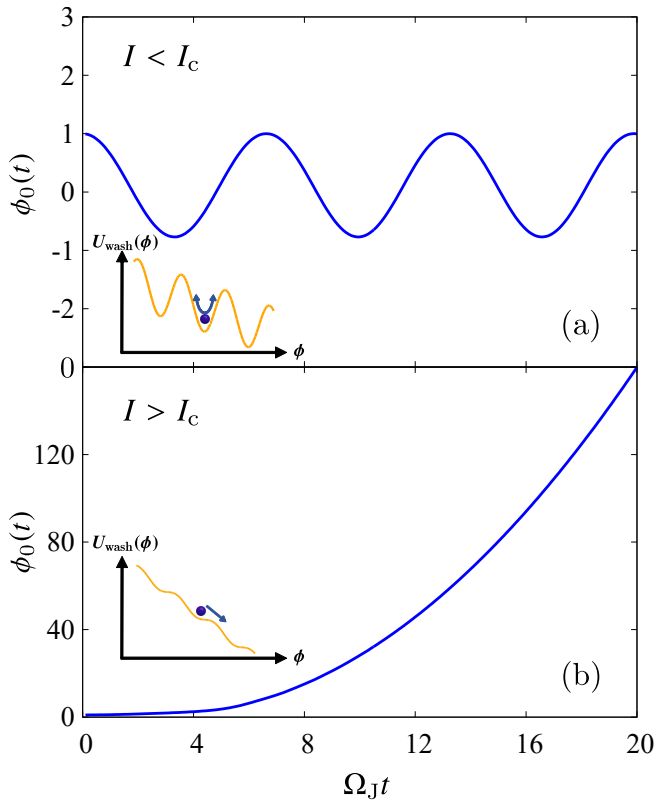

Figure 5.7: Deterministic part of the superconducting phase $\phi_0(t)$ subject to the washboard potential in Eq. (5.37) in the absence of friction [93]. We set the initial condition $\phi_0(0) = 1$ and $\dot{\phi}_0(0) = 1$ for brevity. The upper panel (a) shows the case of $I < I_c$, while the lower panel (b) displays the case of $I > I_c$. In the former case, the phase oscillates around an extremum of the washboard potential. On the other hand, in the latter case, the potential has no extremum leading to the running state with respect to the phase.

$$\Gamma(\omega) \equiv \int_{-\infty}^{\infty} \mathrm{d}t \, \langle \eta(t)\eta(0) \rangle \, e^{-i\omega t} = \frac{2}{R}\hbar\omega \coth\left(\frac{\hbar\omega}{2k_{\mathrm{B}}T}\right). \tag{5.38b}$$

The average $\langle \cdots \rangle$ stands for the Gaussian average with respect to the colored noise $\eta(t)$. The stochastic current noise $\eta(t)$ is equivalent to the noise in Eq. (5.28) satisfying Eqs. (5.30) in a head-to-tail BJJ. In the classical limit $\hbar\omega \ll k_{\mathrm{B}}T$, Eq. (5.38b) reproduces the classical FDT. On the other hand, at $T = 0$, Eq. (5.38b) results in $\Gamma(\omega) \to 2\hbar|\omega|/R$ [213, 227]. The ω dependence of the correlation in Eqs. (5.38) indicates that the quantum noise $\eta(t)$ is the colored noise and approaches the white one in the classical limit. This current noise spectrum of Eq. (5.38b) has been experimentally measured in Ref. [228] and includes the zero-point fluctuations in the shunted resistor.

Equations (5.36) provide the equation of motion with respect to the superconducting

phase ϕ as [229]

$$\frac{\hbar C}{2e}\ddot{\phi}(t) + \frac{\hbar}{2eR}\dot{\phi}(t) + \frac{\partial U_{\rm wash}(\phi)}{\partial \phi} = \eta(t). \tag{5.39}$$

The solution of Eq. (5.39) can be written as

$$\phi(t) = \phi_0(t) + \delta\phi(t), \tag{5.40}$$

where ϕ_0 is the deterministic part of the superconducting phase and $\delta\phi$ represents the stochastic part due to the current noise. By assuming $|\delta\phi(t)| \ll |\phi_0(t)|$, each of the components satisfies [229]

$$\frac{\hbar C}{2e}\ddot{\phi}_0(t) + \frac{\hbar}{2eR}\dot{\phi}_0(t) + \frac{\partial U_{\rm wash}(\phi_0)}{\partial \phi_0} = 0, \tag{5.41}$$

$$\frac{\hbar C}{2e}\delta\ddot{\phi}(t) + \frac{\hbar}{2eR}\delta\dot{\phi}(t) + I_{\rm c}\cos\phi_0(t)\delta\phi(t) = \eta(t). \tag{5.42}$$

In Ref. [229], Brandt *et al.* have employed the approximation $|\delta\phi(t)| \ll |\phi_0(t)|$ under the assumption of the small current noise. We also adopt this assumption throughout this section. Hereafter, we use the following notations

$$\Omega_{\rm J}^2 \equiv \frac{2e}{\hbar}\frac{I_{\rm c}}{C} = \frac{2\pi I_{\rm c}}{\Phi_0 C}, \qquad \Omega_{\rm RC} \equiv \frac{1}{2RC}, \tag{5.43}$$

where $\Phi_0 = h/(2e)$ is the magnetic flux quantum, $\Omega_{\rm J}$ is the Josephson plasma frequency, and $\Omega_{\rm RC}$ is related to the resistance leading to damping in phase dynamics; one can write Eqs. (5.41) and (5.42) as

$$\ddot{\phi}_0 + 2\Omega_{\rm RC}\dot{\phi}_0 + \Omega_{\rm J}^2 \sin\phi_0 = \Omega_{\rm J}^2 \frac{I}{I_{\rm c}}, \tag{5.44}$$

$$\delta\ddot{\phi} + 2\Omega_{\rm RC}\delta\dot{\phi} + \Omega_{\rm J}^2\delta\phi\cos\phi_0 = \Omega_{\rm J}^2\frac{\eta}{I_{\rm c}}. \tag{5.45}$$

5.3.1 Linear analysis in the absence of external current

We focus on the linear regime in which the washboard potential in Eq. (5.37) can be well approximated to a harmonic potential in addition to the term that involves the small external current corresponding to the upper case in Fig. 5.7(a). In the linear regime $\sin\phi_0 \simeq \phi_0$ and $\cos\phi_0 \simeq 1$ in the absence of the external current $I = 0$, the equations of motion (5.44) and (5.45) read

$$\ddot{\phi}_0 + 2\Omega_{\rm RC}\dot{\phi}_0 + \Omega_{\rm J}^2\phi_0 = 0, \tag{5.46}$$

$$\delta\ddot{\phi} + 2\Omega_{\rm RC}\delta\dot{\phi} + \Omega_{\rm J}^2\delta\phi = \frac{\Omega_{\rm J}^2}{I_{\rm c}}\eta. \tag{5.47}$$

We can obtain the root of this approximated equation of motion as

$$\phi(t) = \phi_0(t) + \int_0^t \mathrm{d}t_1\, G(t-t_1)\eta(t_1), \tag{5.48}$$

and the two-point correlation function

$$\left\langle \phi(t)\phi(t') \right\rangle = \phi_0(t)\phi_0(t') + \int_0^t \mathrm{d}t_1 \int_0^{t'} \mathrm{d}t_2\, G(t-t_1)G(t'-t_2)\left\langle \eta(t_1)\eta(t_2) \right\rangle, \tag{5.49}$$

where $\phi_0(t)$ is the solution of Eq. (5.46), and

$$G(t) = \frac{\Omega_\mathrm{J}^2}{I_\mathrm{c}} \frac{e^{-\Omega_\mathrm{RC}t}}{\sqrt{\Omega_\mathrm{J}^2 - \Omega_\mathrm{RC}^2}} \sin\left(\sqrt{\Omega_\mathrm{J}^2 - \Omega_\mathrm{RC}^2}\, t\right)\Theta(t). \tag{5.50}$$

The correlation function (5.49) is analogous to Eqs. (5.33) in a BJJ at $t = t'$. By using Eqs. (5.38), the second term in the right-hand-side of Eq. (5.49) can be written as

$$\int_0^t \mathrm{d}t_1 \int_0^{t'} \mathrm{d}t_2\, G(t-t_1)G(t'-t_2)\left\langle \eta(t_1)\eta(t_2) \right\rangle = \int_{-\infty}^{\infty} \frac{\mathrm{d}\omega}{2\pi} \Gamma(\omega) G_t(\omega) G_{t'}(-\omega) e^{i\omega(t-t')}. \tag{5.51}$$

where

$$\begin{aligned} G_t(\omega) &\equiv \int_0^t \mathrm{d}t_1\, G(t_1) e^{-i\omega t_1} \\ &= \frac{\Omega_\mathrm{J}^2}{2I_\mathrm{c}} \frac{1}{\sqrt{\Omega_\mathrm{J}^2 - \Omega_\mathrm{RC}^2}} \left[\frac{e^{i\left(i\Omega_\mathrm{RC} + \sqrt{\Omega_\mathrm{J}^2 - \Omega_\mathrm{RC}^2} - \omega\right)t} - 1}{i\Omega_\mathrm{RC} + \sqrt{\Omega_\mathrm{J}^2 - \Omega_\mathrm{RC}^2} - \omega} - \frac{e^{i\left(i\Omega_\mathrm{RC} - \sqrt{\Omega_\mathrm{J}^2 - \Omega_\mathrm{RC}^2} - \omega\right)t} - 1}{i\Omega_\mathrm{RC} - \sqrt{\Omega_\mathrm{J}^2 - \Omega_\mathrm{RC}^2} - \omega} \right]. \end{aligned} \tag{5.52}$$

Note that Eq. (5.49) is real, while Eq. (5.52) is a complex function. The dynamics in the absence of the noise as a solution of Eq. (5.44) is

$$\phi_0(t) = \frac{2\pi V_0}{\Phi_0} \frac{e^{-\Omega_\mathrm{RC}t}}{\sqrt{\Omega_\mathrm{J}^2 - \Omega_\mathrm{RC}^2}} \sin\left(\sqrt{\Omega_\mathrm{J}^2 - \Omega_\mathrm{RC}^2}\, t\right). \tag{5.53}$$

Consequently, we finally obtain the correlation function including the quantum noise as

$$\left\langle \phi(t)\phi(t') \right\rangle = \phi_0(t)\phi_0(t') + \frac{2}{R} \int_{-\infty}^{\infty} \frac{\mathrm{d}\omega}{2\pi} \hbar\omega \coth\left(\frac{\hbar\omega}{2k_\mathrm{B}T}\right) G_t(\omega) G_{t'}(-\omega) e^{i\omega(t-t')}. \tag{5.54}$$

The frequency integral in Eq. (5.54) involves a logarithmic ultraviolet divergence due to the zero-point fluctuations in the noise spectrum [228, 230]. In our calculations below, we restrict the energy range as $-\Delta \leq \hbar\omega \leq \Delta$, where Δ is the energy gap of

the superconductor. This superconducting gap is related to the critical current by the Ambegaokar-Baratoff formula [231, 232]

$$I_{\rm c} = \frac{\pi\Delta}{2eR}\tanh\left(\frac{\Delta}{2k_{\rm B}T}\right). \tag{5.55}$$

One may think that, according to Eq. (5.53), $\phi_0(t\to\infty)\to 0$ leads to the breakdown of the approximation $|\delta\phi(t)| \ll |\phi_0(t)|$ that we assumed for Eqs. (5.41) and (5.42). It is true that the higher order contributions of $\delta\phi(t)$ can affect the correlations. In the long-time limit in which ϕ_0 vanishes, however, the results under the approximation can be valid. Setting $\phi_0(t) = 0$ in the absence of the external current, one obtains

$$\delta\ddot{\phi} + 2\Omega_{\rm RC}\delta\dot{\phi} + \Omega_{\rm J}^2\sin\delta\phi = \Omega_{\rm J}^2\frac{\eta}{I_{\rm c}}. \tag{5.56}$$

Hence, within the linear regime with respect to $\delta\phi$, we obtain the identical equation as Eq. (5.47) and our results would be valid even in the long-time limit.

Figure 5.8(a) shows the dynamics of the autocorrelation function of the relative phase $\langle\phi^2(t)\rangle$ for $k_{\rm B}T = 0.1\hbar\Omega_{\rm J}$ with different damping. In the following, we fix $2e\Omega_{\rm J}/I_{\rm c} = 10^{-2}$ and $V_0 = \hbar\Omega_{\rm J}/(2e)$ for simplicity. Experimentally, in Ref. [233] for instance, they used $I_{\rm c} = 9.489$ μA and $\Omega_{\rm J} = 67.4$ GHz, which corresponds to $2e\Omega_{\rm J}/I_{\rm c} \simeq 2.3\times10^{-3}$ and $V_0 \simeq 2.2\times10^{-5}$ V. Based on these experimental values, we chose the fixed parameter $2e\Omega_{\rm J}/I_{\rm c} = 10^{-2}$. One can see that the correlation is suppressed as one increases the damping coefficient $\Omega_{\rm RC}/\Omega_{\rm J}$. This is a natural behavior because the large damping constant leads to an earlier exponential decay of the phase correlation according to Eq. (5.50). In addition, the energy gap $\Delta \sim \Omega_{\rm J}/\Omega_{\rm RC}$ at low temperatures as an energy cutoff in Eq. (5.54) is also responsible for this strong suppression with a smaller resistance. In the experiment in Ref. [233], Devoret *et al.* measured $R = 190$ Ω and $C = 6.35$ pF resulting in $\Omega_{\rm RC}/\Omega_{\rm J} \simeq 6.2\times10^{-3}$, which corresponds to the case with a tiny damping constant. Only in the long-time limit $t\to\infty$ does the energy integral in Eq. (5.54) converge without any cutoff energy. Remarkably, we found that the asymptotic correlation still depends on the damping constant as a consequence of quantum fluctuations in the current noise.

In the long-time limit, the correlation functions can also be obtained through Fourier analysis [198, 234]. Performing the Fourier transformation on Eq. (5.47), we obtain [234]

$$\delta\tilde{\phi}(\omega) \equiv \int_{-\infty}^{\infty} {\rm d}t\,\delta\phi(t)e^{-i\omega t} = \alpha(\omega)\Omega_{\rm J}^2\frac{\tilde{\eta}(\omega)}{I_{\rm c}}, \tag{5.57}$$

where $\tilde{\eta}(\omega) \equiv \int_{-\infty}^{\infty}{\rm d}t\,\eta(t)e^{-i\omega t}$ and

$$\alpha(\omega) \equiv \frac{1}{-\omega^2 + 2i\Omega_{\rm RC}\omega + \Omega_{\rm J}^2}. \tag{5.58}$$

Interestingly, $\alpha(\omega)$ is equivalent to the long-time limit of $G_t(\omega)$ in Eq. (5.52) as

$$\alpha(\omega) = \frac{I_{\rm c}}{\Omega_{\rm J}^2}G_{t\to\infty}(\omega). \tag{5.59}$$

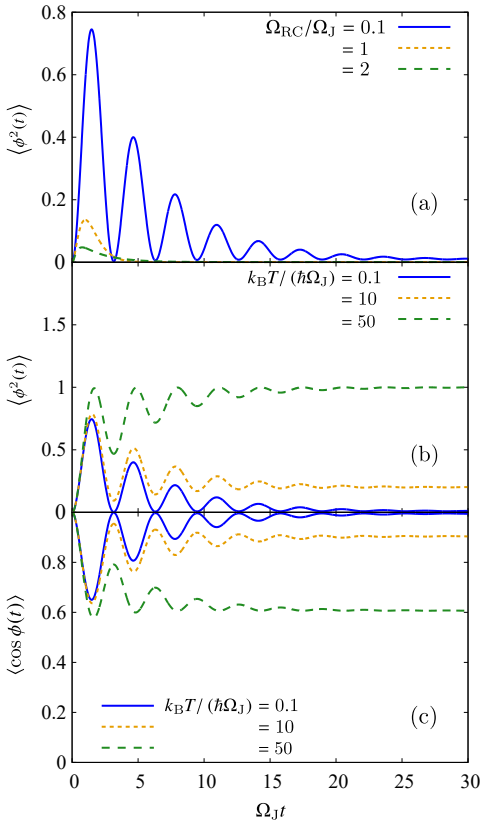

Figure 5.8: Time evolution of the autocorrelation function with respect to the phase $\phi(t)$ [93]. The upper panel (a) displays the results for $k_BT/(\hbar\Omega_J) = 0.1$. The blue solid, orange dotted, and green dashed lines respectively stand for the results for $\Omega_{RC}/\Omega_J = 0.1$ (underdamped), $\Omega_{RC}/\Omega_J = 1$ (critically damped), and $\Omega_{RC}/\Omega_J = 2$ (overdamped). The panel (b) displays the results for $\Omega_{RC}/\Omega_J = 0.1$. The blue solid, orange dotted, and green dashed lines respectively stand for the results for $k_BT/(\hbar\Omega_J) = 0.1, 10, 50$. The lower panel (c) displays the coherence factor for $\Omega_{RC}/\Omega_J = 0.1$. We set $2e\Omega_J/I_c = 10^{-2}$ and $V_0 = \hbar\Omega_J/(2e)$.

As a result, the time-independent autocorrelation function with respect to the phase in the long-time limit can be obtained as [234]

$$\left\langle \phi^2(t\to\infty)\right\rangle = \frac{2\Omega_J^4}{RI_c^2}\int_{-\infty}^{\infty}\frac{d\omega}{2\pi}\hbar\omega\coth\left(\frac{\hbar\omega}{2k_BT}\right)|\alpha(\omega)|^2. \tag{5.60}$$

In particular, in the underdamped limit $\Omega_{RC} \ll \Omega_J$, by virtue of the following relation

$$2\Omega_{RC}\omega|\alpha(\omega)|^2 \to \frac{\pi}{2\Omega_J}\left[\delta(\omega-\Omega_J)+\delta(\omega+\Omega_J)\right], \tag{5.61}$$

one obtains

$$\left\langle \phi^2(t\to\infty)\right\rangle \to \frac{2e\Omega_J}{I_c}\coth\left(\frac{\hbar\Omega_J}{2k_BT}\right). \tag{5.62}$$

which is consistent with the classical limit

$$\left\langle \phi^2(t\to\infty)\right\rangle_{\rm cl} = \frac{2e\Omega_{\rm J}}{I_{\rm c}}\frac{2k_{\rm B}T}{\hbar\Omega_{\rm J}}, \tag{5.63}$$

with $\Gamma(\omega) \to 4k_{\rm B}T/R$ under $\hbar\omega \ll k_{\rm B}T$. In a similar manner, one can write the autocorrelation function with respect to the voltage as well. It is given by

$$\left\langle V^2(t\to\infty)\right\rangle = \left(\frac{\Phi_0}{2\pi}\right)^2 \frac{2\Omega_{\rm J}^4}{RI_c^2}\int_{-\infty}^{\infty}\frac{{\rm d}\omega}{2\pi}\hbar\omega\coth\left(\frac{\hbar\omega}{2k_{\rm B}T}\right)\omega^2|\alpha(\omega)|^2. \tag{5.64}$$

This frequency integral is logarithmically divergent, which is distinct from the case of phase correlation in Eq. (5.60). Only in the underdamped limit, however, it converges and reduces to

$$\left\langle V^2(t\to\infty)\right\rangle \to \left(\frac{\hbar\Omega_{\rm J}}{2e}\right)^2\frac{2e\Omega_{\rm J}}{I_{\rm c}}\coth\left(\frac{\hbar\Omega_{\rm J}}{2k_{\rm B}T}\right), \tag{5.65}$$

which is also consistent with the classical limit

$$\left\langle V^2(t\to\infty)\right\rangle_{\rm cl} = \left(\frac{\hbar\Omega_{\rm J}}{2e}\right)^2\frac{2e\Omega_{\rm J}}{I_{\rm c}}\frac{2k_{\rm B}T}{\hbar\Omega_{\rm J}}. \tag{5.66}$$

In the classical limit, in contrast, the asymptotic correlation functions are independent of the damping. In other words, the dependence of the asymptotic autocorrelations on the resistance reflects the quantum effects. This manifestation of the quantum effect as the dependence on the resistance of the correlations in the long-time limit can be measured experimentally. In the underdamped limit $\Omega_{\rm RC} \ll \Omega_{\rm J}$, in particular, it reduces to $2e\Omega_{\rm J}/I_{\rm c}\cdot\coth\left[\hbar\Omega_{\rm J}/\left(2k_{\rm B}T\right)\right]$, which recovers the classical asymptotic value $2k_{\rm B}T/\left(\hbar\Omega_{\rm J}\right)$ in the classical limit $k_{\rm B}T \gg \hbar\Omega_{\rm J}$.

Figure 5.8(b) illustrates the numerical results with different temperatures in the underdamped regime $\Omega_{\rm RC} = 0.1\Omega_{\rm J}$. It shows that the autocorrelation is enhanced in the high-temperature region due to the dominant thermal fluctuations compared to the low-temperature region in which quantum fluctuations dominate over thermal ones. It also indicates that the asymptotic value gets closer to the classical one $2k_{\rm B}T/\left(\hbar\Omega_{\rm J}\right)$ in Eq. (5.63) as one increases temperature, as expected.

Figure 5.8(c) displays the time evolution of the coherence factor for $\Omega_{\rm RC} = 0.1\Omega_{\rm J}$. Using the Gaussian property of the noise η, one can compute it by

$$\left\langle\cos\phi(t)\right\rangle = \cos\phi_0(t)e^{-\left[\left\langle\phi^2(t)\right\rangle-\phi_0^2(t)\right]/2}. \tag{5.67}$$

Figure 5.8(c) shows that the coherence decays earlier at a higher temperature, which indicates that thermal fluctuations destroy the coherence. The asymptotic values of the coherence factor are dependent on the damping, as illustrated in Fig. 5.9. The dependence on $\Omega_{\rm RC}$ reflects the dependence of the variance as in Eq. (5.67). One can see that the decay of coherence at a higher temperature gets gradual with larger damping. This behavior can be interpreted that the large friction suppresses the deviation of the coherence due to thermal fluctuations, while the coherence would be destroyed by thermal

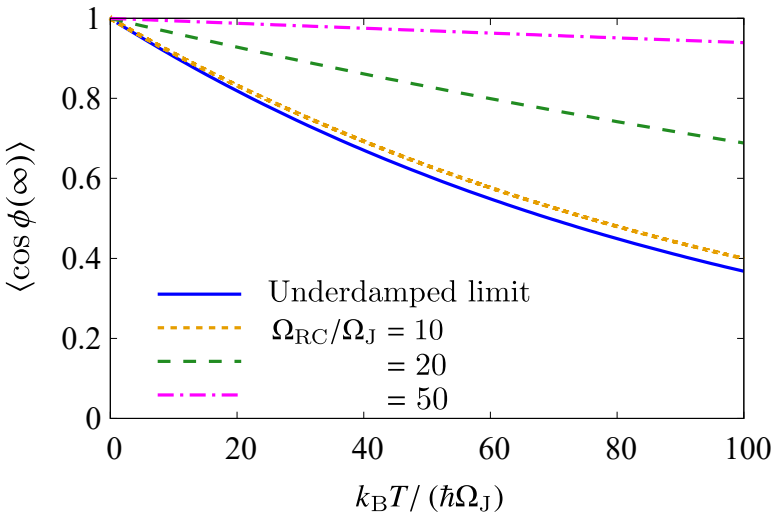

Figure 5.9: Temperature dependence of the coherence factor in the long-time limit $\langle \cos\phi(t\to\infty)\rangle$ [93]. The solid curve stands for the result in the underdamped limit $\Omega_{\rm RC}/\Omega_{\rm J}\to 0$. The dotted, dashed, and dotted-dashed curves represent the results for $\Omega_{\rm RC}/\Omega_{\rm J}=10,20,50$, respectively, obtained by Eq. (5.60). We set $2e\Omega_{\rm J}/I_{\rm c}=10^{-2}$ and $V_0=\hbar\Omega_{\rm J}/(2e)$.

fluctuations with small friction. However, the figure indicates that even in the underdamped limit $\Omega_{\rm RC}/\Omega_{\rm J}\to 0$, the coherence keeps finite as $\langle\cos\phi(\infty)\rangle\to\exp\left[-e\Omega_{\rm J}/I_{\rm c}\right]$ at $T=0$. This result implies that a supercurrent flows even in the underdamped limit at $T=0$ contrary to the picture of the Schmid-Bulgadaev transition, which claims that the junction is insulating with a resistance above a critical resistance [235, 236]. This consequence is consistent with the recent work in Ref. [237, 238] on the absence of the Schmid-Bulgadaev transition.

In a similar manner, one can obtain the dynamics of the voltage in the absence of noise as

$$\begin{aligned} V_0(t) &= \frac{\Phi_0}{2\pi}\dot{\phi}_0(t) \\ &= V_0\frac{e^{-\Omega_{\rm RC}t}}{\sqrt{1-\Omega_{\rm RC}^2/\Omega_{\rm J}^2}}\left[-\frac{\Omega_{\rm RC}}{\Omega_{\rm J}}\sin\left(\sqrt{\Omega_{\rm J}^2-\Omega_{\rm RC}^2}t\right)+\sqrt{1-\frac{\Omega_{\rm RC}^2}{\Omega_{\rm J}^2}}\cos\left(\sqrt{\Omega_{\rm J}^2-\Omega_{\rm RC}^2}t\right)\right], \end{aligned} \tag{5.68}$$

and the two-point correlation of the voltage as

$$\begin{aligned} \left\langle V(t)V(t')\right\rangle = V_0(t)V_0(t') + \left(\frac{\Phi_0}{2\pi}\right)^2\frac{2}{R}\int_{-\infty}^{\infty}\frac{{\rm d}\omega}{2\pi}\hbar\omega\coth\left(\frac{\hbar\omega}{2k_{\rm B}T}\right)e^{i\omega(t-t')} \\ \times\left[\partial_t G_t(\omega)+i\omega G_t(\omega)\right]\left[\partial_{t'}G_{t'}(-\omega)-i\omega G_{t'}(-\omega)\right]. \end{aligned} \tag{5.69}$$

Figure 5.10(a) illustrates the dynamics of the autocorrelation function of the voltage $\langle V^2(t)\rangle$ for $k_{\rm B}T=0.1\hbar\Omega_{\rm J}$ with several values of the damping constant. Similar to that

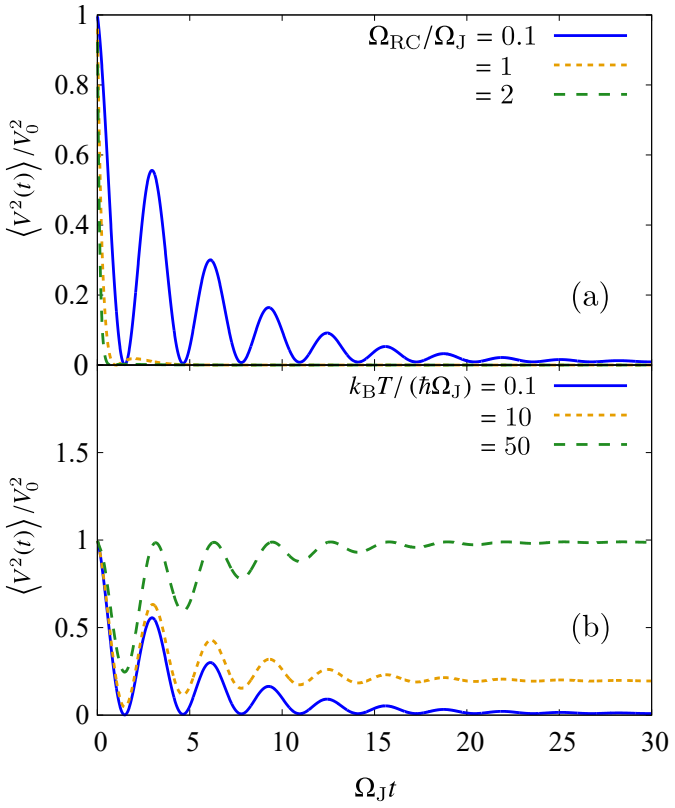

Figure 5.10: Autocorrelation function of the voltage $\langle V^2(t)\rangle$ [93]. The upper panel (a) displays the results for $k_{\rm B}T/(\hbar\Omega_{\rm J}) = 0.1$. The blue solid, orange dotted, and green dashed curves stand for the results for $\Omega_{\rm RC}/\Omega_{\rm J} = 0.1$ (underdamped), $\Omega_{\rm RC}/\Omega_{\rm J} = 1$ (critically damped), and $\Omega_{\rm RC}/\Omega_{\rm J} = 2$ (overdamped), respectively. The lower panel (b) displays the results for $\Omega_{\rm RC}/\Omega_{\rm J} = 0.1$. The blue solid, orange dotted, and green dashed curves stand for the results for $k_{\rm B}T/(\hbar\Omega_{\rm J}) = 0.1, 10, 50$, respectively. We set $2e\Omega_{\rm J}/I_{\rm c} = 10^{-2}$ and $V_0 = \hbar\Omega_{\rm J}/(2e)$.

of the phase in Fig. 5.8(a), one can see that the correlation of the voltage is strongly suppressed as one increases $\Omega_{\rm RC}/\Omega_{\rm J}$. The asymptotic correlation in the long-time limit is also dependent on $\Omega_{\rm RC}$ as in Eq. (5.64) as a consequence of the quantum fluctuations similar to the phase correlation. As well as the phase correlation, we expect that this dependence on the damping constant can also be experimentally observed. The difference from the phase correlation is that, even in the long-time limit, the integral in Eq. (5.69) does not converge in general. The voltage correlation in Eq. (5.69) indeed converges only in the classical limit with any damping, or in the underdamped limit with any temperature regime. In the underdamped limit, the asymptotic value converges to $2e\Omega_{\rm J}/I_{\rm c}\cdot V_0^2\coth\left[\hbar\Omega_{\rm J}/(2k_{\rm B}T)\right]$, which recovers the classical limit. Figure 5.10(b) shows the results with different temperature for $\Omega_{\rm RC} = 0.1\Omega_{\rm J}$. As well as the phase correlation in Fig. 5.8(b), Fig. 5.10(b) indicates that thermal fluctuations enhance the correlation of voltage over a long time.

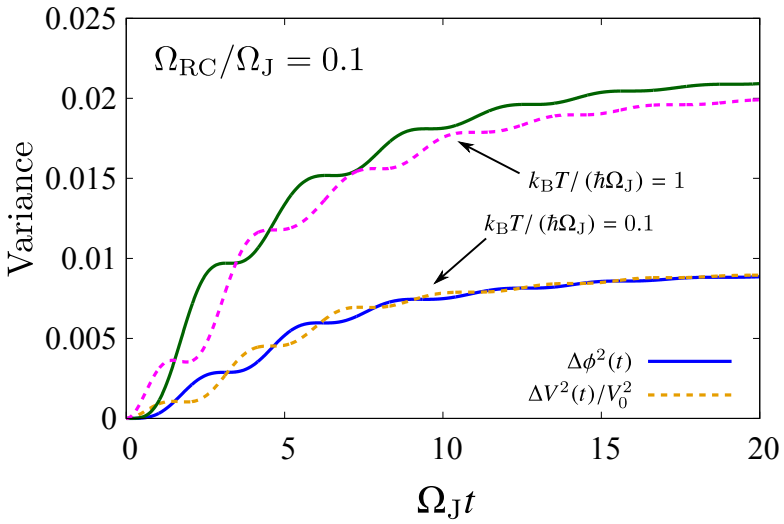

Figure 5.11: Dynamics of the variances of the superconducting phase and voltage with $\Omega_{\rm RC}/\Omega_{\rm J} = 0.1$ and $k_{\rm B}T = 0.1\hbar\Omega_{\rm J}$, $\hbar\Omega_{\rm J}$.

Let us remark on the differences from the head-to-tail BJJ case analyzed in Sec. 5.2. In the RCSJ circuit, the phase variance shown in Fig. 5.8(a) is less enhanced compared to the one in a BJJ displayed in Fig. 5.4(a). The giant fluctuations in the relative phase in a BJJ originate from the intrinsic coupling between the Josephson mode and bath modes based on the velocity-coupling model, while the RCSJ circuit involves only extrinsic coupling as in the standard CL model. Furthermore, the variance of the conjugate variable exhibits in-phase oscillations in a BJJ as obtained in Figs. 5.4 while it exhibits out-of-phase oscillations in a RCSJ circuit as shown in Fig. 5.11. The conjugate variable is the population imbalance in a BJJ, while it is the voltage in a RCSJ circuit. This different oscillatory behavior is also the consequence of the intrinsic coupling with bath modes in a head-to-tail BJJ.

5.3.2 Effects of external current

In the presence of the external current I, instead of Eq. (5.46), the deterministic part of the superconducting phase is governed by [239]

$$\ddot{\phi}_0 + 2\Omega_{\rm RC}\dot{\phi}_0 + \Omega_{\rm J}^2\phi_0 = \Omega_{\rm J}^2\frac{I}{I_{\rm c}}, \tag{5.70}$$

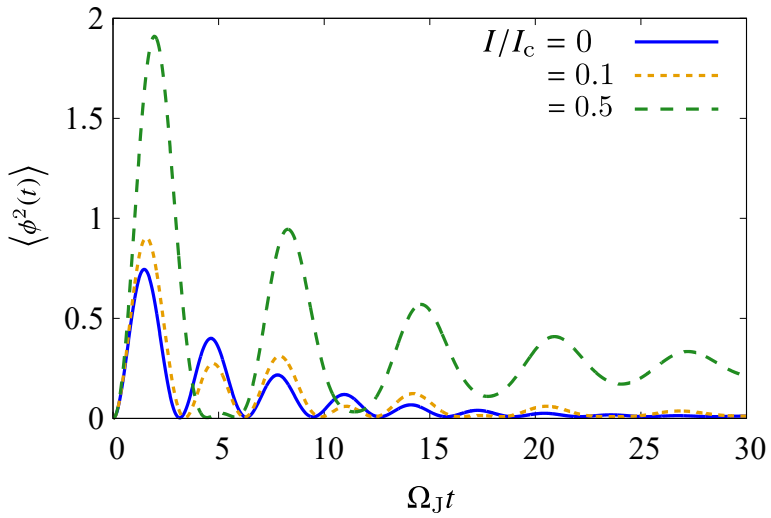

Figure 5.12: Autocorrelation function $\langle \phi^2(t) \rangle$ for $\Omega_{RC}/\Omega_J = 0.1$ and $k_B T/(\hbar\Omega_J) = 0.1$ [93]. The blue solid, orange dotted, and green dashed lines respectively stand for the results for $I/I_c = 0, 0.1, 0.5$. We set $2e\Omega_J/I_c = 10^{-2}$ and $V_0 = \hbar\Omega_J/(2e)$.

and the resulting deterministic part of the phase ϕ_0 is given by

$$\phi_0(t) = \frac{\Omega_J}{\sqrt{\Omega_J^2 - \Omega_{RC}^2}} \left[\left(\frac{2\pi V_0}{\Phi_0 \Omega_J} - \frac{\Omega_{RC}}{\Omega_J} \frac{I}{I_c} \right) e^{-\Omega_{RC} t} \sin\left(\sqrt{\Omega_J^2 - \Omega_{RC}^2}\, t \right) \right.$$
$$\left. + \sqrt{1 - \left(\frac{\Omega_{RC}}{\Omega_J} \right)^2} \frac{I}{I_c} \left[1 - e^{-\Omega_{RC} t} \cos\left(\sqrt{\Omega_J^2 - \Omega_{RC}^2}\, t \right) \right] \right], \tag{5.71}$$

which recovers Eq. (5.53) in $I = 0$. Since we are working within the linear regime, the transition to the running state due to the tilted washboard potential is absent in this case and the external current just shifts and intensifies the deterministic part of the phase instead, as shown in Fig. 5.12. With a larger external current, the magnitude of phase correlation is more intensified and shifted. In order to justify the linear approximation we employed above, it is required to use the relatively small external current. Under the original washboard potential in Eq. (5.37), with a large external current, the potential has no extremum and the phase flows away from the initial phase as illustrated in Fig. 5.7(b). This running state strongly enhances the deterministic part of the phase correlation $\langle \phi_0^2(t) \rangle$ in the long-time regime, which would make the noise contribution negligible. With a sufficiently small current, on the other hand, the phase should oscillate around an extremum of the potential as shown in Fig. 5.7(a), and the linear approximation is expected to well describe the dynamics. Based on this discussion, we used three relatively small values of external current $I/I_c = 0, 0.1, 0.5$ in Fig. 5.12. In $t \to \infty$, the correlation function asymptotically approaches the nonzero asymptotic value of the deterministic part $\phi_0^2(t \to \infty) \to I/I_c$ plus that of the variance.

5.4 Quantum correction to Josephson frequency

In the last two sections, we considered the effects of quantum fluctuations on the dynamics of correlation functions. In addition, the Josephson frequency itself is also subject to quantum corrections. In this final section, we show the quantum correction to the Josephson frequency through effective action formalism, which can be verified also by another approach through equations of motion discussed in Appendix E [94].

Let us start with the action of the simplest Josephson junction: a spatially zero-dimensional Bose Josephson junction given by

$$\begin{aligned} S_{\rm BJJ}[\Psi_1,\Psi_1^*,\Psi_2,\Psi_2^*] &= \int \mathrm{d}t\, L_{\rm BJJ}[\Psi_1,\Psi_1^*,\Psi_2,\Psi_2^*] \\ &= \int \mathrm{d}t \left[\sum_{a=1,2} \left(i\hbar\,\Psi_a^*\dot{\Psi}_a - \frac{U}{2}|\Psi_a|^4 \right) + \frac{J}{2}\left(\Psi_1^*\Psi_2 + \Psi_2^*\Psi_1\right) \right], \end{aligned} \tag{5.72}$$

where $\Psi_a(t)$ is the adimensional complex field of bosons in the ath site at real-time t, U is the on-site interaction strength of particles, J is the tunneling energy, and dot stands for the time-derivative. The Madelung transformation $\Psi_a(t) = \sqrt{N_a(t)}e^{i\phi_a(t)}$ with the number of bosons $N_a(t)$ and the phase angle $\phi_a(t)$ in the ath site leads to the BJJ action $S_{\rm BJJ}[\phi,z,\bar{\phi},N] = \int \mathrm{d}t\, L_{\rm BJJ}[\phi,z,\bar{\phi},N]$ with

$$L_{\rm BJJ}[\phi,z,\bar{\phi},N] = \frac{i\hbar}{2}\dot{N} - \frac{U}{4}N^2 + \frac{\hbar}{2}N\left(z\dot{\phi} - \dot{\bar{\phi}}\right) - \frac{U}{4}N^2z^2 + \frac{J}{2}N\sqrt{1-z^2}\cos\phi, \tag{5.73}$$

and

$$\begin{aligned} N(t) &= N_1(t) + N_2(t), \quad z(t) = \frac{N_1(t) - N_2(t)}{N(t)}, \\ \bar{\phi}(t) &= \phi_1(t) + \phi_2(t), \quad \phi(t) = \phi_2(t) - \phi_1(t). \end{aligned} \tag{5.74}$$

The relative action only in terms of the relative quantities $S[\phi,z] = \int \mathrm{d}t\, L(\phi,z)$ can be obtained by integrating out the total number of bosons $N(t)$ and the total phase $\bar{\phi}(t)$ as

$$\begin{aligned} \int \mathcal{D}\phi\mathcal{D}z\, e^{iS[\phi,z]/\hbar} &= \int \mathcal{D}\Psi_1\mathcal{D}\Psi_1^*\mathcal{D}\Psi_2\mathcal{D}\Psi_2^*\, e^{iS_{\rm BJJ}[\Psi_1,\Psi_1^*,\Psi_2,\Psi_2^*]/\hbar} \\ &= \int \mathcal{D}\phi\mathcal{D}z \int \mathcal{D}N\, e^{i\int \mathrm{d}t\left[L_{\rm BJJ}[\phi,z,\bar{\phi},N] - \hbar\dot{N}\bar{\phi}/2\right]/\hbar} \int \mathcal{D}\bar{\phi}\, e^{i\int \mathrm{d}t\dot{N}\bar{\phi}/2}. \end{aligned} \tag{5.75}$$

The integral with respect to $\bar{\phi}$ in Eq. (5.75) yields $\delta[\dot{N}]$ and the total number of boson N turns out to be a constant of motion. Consequently, the relative Lagrangian is found to be

$$L[\phi,z] = \frac{\hbar N}{2}z\dot{\phi} - \frac{UN^2}{4}z^2 + \frac{JN}{2}\sqrt{1-z^2}\cos\phi. \tag{5.76}$$

Here, we omitted negligible constants that stem from the Jacobian for the Madelung transformation in Eq. (5.75).

One of the simplest approximations to analyze the quantum dynamics governed by Eq. (5.76) is the saddle-point (mean-field) approximation. Within this saddle-point approximation, we focus only on the configurations extremizing the action satisfying the Euler-Lagrange equations given by

$$\hbar\dot{\phi} = J\frac{z}{\sqrt{1-z^2}}\cos\phi + UNz, \qquad \hbar\dot{z} = -J\sqrt{1-z^2}\sin\phi. \tag{5.77}$$

Equations (5.77) describe the mean-field dynamics of the macroscopic quantum tunneling in the Josephson junction.

5.4.1 Josephson oscillations in the linear regime

In the regime with small amplitude of oscillations $|\phi(t)| \ll 1$ and $|z(t)| \ll 1$, the relative Lagrangian (5.76) is simplified as

$$L^{(\mathrm{quad})}[\phi, z] = \frac{\hbar N}{2}z\dot{\phi} - \frac{JN}{4}\phi^2 - \frac{JN+UN^2}{4}z^2. \tag{5.78}$$

The quadratic Lagrangian (5.78) produces the linearized equations of motion:

$$\hbar\dot{\phi} = (J+UN)z, \qquad \hbar\dot{z} = -J\phi, \tag{5.79}$$

which are equivalent to two sets of uncoupled harmonic equations as

$$\ddot{\phi} + \Omega^2\phi = 0, \qquad \ddot{z} + \Omega^2 z = 0, \tag{5.80}$$

with the Josephson frequency

$$\Omega = \frac{\sqrt{J(J+UN)}}{\hbar} = \begin{cases} \Omega_{\mathrm{R}} = \dfrac{J}{\hbar} & (UN/J \ll 1), \\ \Omega_{\mathrm{J}} = \dfrac{\sqrt{JUN}}{\hbar} & (UN/J \gg 1). \end{cases} \tag{5.81}$$

In the Rabi regime $UN/J \ll 1$, the Josephson frequency (5.81) reduces to the Rabi frequency Ω_{R}. In the Josephson regime $UN/J \gg 1$, on the other hand, it reduces to Ω_{J}.

5.4.2 Effective phase action

To consider quantum corrections to the standard Josephson frequency (5.81), we first derive the phase action. Expanding the relative Lagrangian (5.76) up to the Gaussian level with respect to the population imbalance $z(t)$, we obtain

$$L[\phi, z] = \frac{\hbar N}{2}z\dot{\phi} - \frac{UN^2 + JN\cos\phi}{4}z^2 + \frac{JN}{2}\cos\phi. \tag{5.82}$$

One may think that a phase action can be obtained by naively integrating out the population imbalance $z(t)$ as we performed in Eq. (5.75) in terms of N and $\bar{\phi}$. However,

the second term involving ϕ proportional to z^2 indeed produces a modification of the resulting kinetic term and path-integral measure. To precisely discuss this procedure of integrating out population imbalance, we introduce a path-integral propagator for the phase

$$K(\phi_{\rm f}, t_{\rm f}|\phi_{\rm i}, t_{\rm i}) = \int_{\{\phi_{\rm i}, t_{\rm i}\}}^{\{\phi_{\rm f}, t_{\rm f}\}} \mathcal{D}\phi \int \mathcal{D}z\, e^{iS[\phi,z]/\hbar}, \tag{5.83}$$

with $S[\phi, z] = \int {\rm d}t\, L[\phi, z]$ and $L[\phi, z]$ given by Eq. (5.82). To perform the integral over the $z(t)$ paths, it is useful to use the time-sliced representation of the propagator. In that case, the paths are subdivided into n time infinitesimal steps $\delta t = (t_{\rm f} - t_{\rm i})/n$, and one lets n to be infinity at the end of the calculation. The path integral over $z(t)$ is then performed as an n-fold integral over the variables z_j with $j = 1, \cdots, n$. Performing these integrals, we find

$$K(\phi_{\rm f}, t_{\rm f}|\phi_{\rm i}, t_{\rm i}) = \left(\prod_{j=1}^{n-1} \int_0^{2\pi} {\rm d}\phi_j\right) \prod_{j=1}^{n} K_{\rm inf}(\phi_j, t_j|\phi_{j-1}, t_{j-1}), \tag{5.84}$$

where the infinitesimal propagator is found to be

$$K_{\rm inf}(\phi_j, \delta t|\phi_{j-1}, 0) = \sqrt{\frac{\hbar N}{(UN + J\cos\phi_j) 4\pi i \delta t}} \times \exp\left[-\frac{\hbar N(\phi_j - \phi_{j-1})^2}{4i(UN + J\cos\phi_j)\delta t} + \frac{i}{2\hbar} JN\delta t \cos\phi_j\right]. \tag{5.85}$$

The prefactor of the exponential in Eq. (5.85) is a normalization factor that ensures the condition

$$\lim_{\delta t \to 0} K_{\rm inf}(\phi_j, \delta t|\phi_{j-1}, 0) = \delta(\phi_j - \phi_{j-1}). \tag{5.86}$$

This prefactor is crucial to remove the divergence resulting from the quantum fluctuations of $\phi(t)$ [240]. By setting $n \to \infty$, the exponential phase factor for the $\phi(t)$ path can be represented as $\exp[iS_0[\phi]/\hbar]$ with the phase action

$$S_0[\phi] = \int {\rm d}t \left[\frac{N\hbar^2}{4\,(UN + J\cos\phi)}\dot{\phi}^2 + \frac{JN}{2}\cos\phi\right], \tag{5.87}$$

and the full propagator in Eq. (5.83) is given by

$$K(\phi_{\rm f}, t_{\rm f}|\phi_{\rm i}, t_{\rm i}) = \int_{\{\phi_{\rm i}, t_{\rm i}\}}^{\{\phi_{\rm f}, t_{\rm f}\}} \mathcal{D}\phi\, e^{iS_0[\phi]/\hbar}. \tag{5.88}$$

In Eq. (5.88), the path-integral measure is related to the prefactor in Eq. (5.85) as

$$\int \mathcal{D}\phi = \lim_{n\to\infty} \prod_{j=1}^{n} \int_{-\pi}^{\pi} \frac{{\rm d}\phi_j}{\sqrt{(U + J\cos\phi_j/N)\, 4\pi i\delta t/\hbar}}. \tag{5.89}$$

Note that the phase action $S_0[\phi]$ can be also obtained by inserting the linearized equation of motion $z = \hbar\dot{\phi}/(UN + J\cos\phi)$ into Eq. (5.82).

5.4.3 One-loop correction to Josephson frequency

In the Josephson regime $UN \gg J$, the integral measure (5.89) no longer depends on $\phi(t)$ and the phase action reduces to

$$S_{\mathrm{J}}[\phi] = \int \mathrm{d}t \left[\frac{M_{\mathrm{J}}}{2} \dot{\phi}^2 - V[\phi] \right], \tag{5.90}$$

with $M_{\mathrm{J}} = \hbar^2/2U$ and $V[\phi] = M_{\mathrm{J}} \Omega_{\mathrm{J}}^2 \cos\phi/2$. Thanks to the negligible higher-order contributions of ϕ in the kinetic term, Eq. (5.87) is simplified to Eq. (5.90). It is the familiar action of a capacitively shunted superconducting Josephson circuit in which the population imbalance of Cooper pairs is tiny $|z(t)| \ll 1$ but the total number of Cooper pairs N is large. In this framework, $I_{\mathrm{c}} = eJN/\hbar$ corresponds to the critical electric current and $C = 2e^2/U$ corresponds to the electric capacitance appeared in Sec. 5.3 [241].

To determine quantum corrections to the Josephson frequency Ω_{J}, we consider the quantum effective action $\Gamma_{\mathrm{J}}[\phi]$. It is a modified expression of the original phase action $S_{\mathrm{J}}[\phi]$ taking into account quantum corrections. Extremization of $\Gamma_{\mathrm{J}}[\phi]$ provides the exact equation of motion for the expectation value of the field $\phi(t)$. First, we rewrite the potential term in Eq. (5.90) as

$$V[\phi] = \frac{M_{\mathrm{J}} \Omega_{\mathrm{J}}^2}{2} \phi^2 + \tilde{V}[\phi], \tag{5.91}$$

with

$$\tilde{V}[\phi] = M_{\mathrm{J}} \Omega_{\mathrm{J}}^2 (1 - \cos\phi) - \frac{M_{\mathrm{J}} \Omega_{\mathrm{J}}^2}{2} \phi^2 = \lambda \phi^4 + \mathcal{O}\big(\phi^6\big), \tag{5.92}$$

with the four-point coupling constant $\lambda = -JN/48$. Within the effective action formalism, it is the potential $\tilde{V}[\phi]$ that encodes quantum fluctuations [242]. Up to the quadratic order in the derivative expansion [242, 243, 244], the quantum effective action is given by

$$\Gamma_{\mathrm{J}}[\phi] = \int \mathrm{d}t \left[\frac{Z[\phi]}{2} \dot{\phi}^2 - V_{\mathrm{eff}}[\phi] \right], \tag{5.93}$$

where

$$Z[\phi] = M_{\mathrm{J}} + Z_1[\phi] + Z_2[\phi] + \cdots, \tag{5.94}$$

is the effective mass with $Z_{n=1,2,\cdots} \propto \hbar^n$ and

$$V_{\mathrm{eff}}[\phi] = V[\phi] + V_{\mathrm{eff}}^{(1)}[\phi] + V_{\mathrm{eff}}^{(2)}[\phi] + \cdots, \tag{5.95}$$

is the effective potential with $V_{\mathrm{eff}}^{(n=1,2,\cdots)} \propto \hbar^n$ represented as $\hbar$ expansions, or equivalently, loop expansions [242]. In particular, to the first order of the $\hbar$ expansions, we find

$$Z_1[\phi] = \frac{\hbar}{32 M_{\mathrm{J}}^2} \frac{\left[\partial_\phi^3 \tilde{V}[\phi]\right]^2}{\left[\Omega_{\mathrm{J}}^2 + \dfrac{1}{M_{\mathrm{J}}} \partial_\phi^2 \tilde{V}[\phi]\right]^{5/2}}, \tag{5.96}$$

and

$$V_{\rm eff}^{(1)}[\phi] = \frac{\hbar}{2}\left[\sqrt{\Omega_{\rm J}^2 + \frac{1}{M_{\rm J}}\partial_\phi^2 \tilde{V}[\phi]} - \Omega_{\rm J}\right]. \tag{5.97}$$

Note that the original potential $V[\phi]$ must be convex so that Eqs. (5.96) and (5.97) are real. This is realized in the domain $|\phi| < \sqrt{2}$, which has already been satisfied under $|\phi| \ll 1$ that makes the approximation from Eq. (5.87) to Eq. (5.90) valid. By extremizing $\Gamma_{\rm J}[\phi]$, the equation of motion with the one-loop correction reads

$$[M_{\rm J} + Z_1[\phi]]\,\ddot{\phi} + \frac{\partial_\phi Z_1[\phi]}{2}\dot{\phi}^2 + \partial_\phi\left[V[\phi] + V_{\rm eff}^{(1)}[\phi]\right] = 0. \tag{5.98}$$

The equation of motion (5.98) is obtained by the second-order derivative expansion and neglecting higher-order contributions of $\hbar$. This approximation is valid under [242]

$$\left|\frac{\lambda\phi^4}{M_{\rm J}\Omega_{\rm J}^2\phi^2/2}\right| \ll 1. \tag{5.99}$$

By inserting the oscillator length $\phi = \sqrt{\hbar/M_{\rm J}\Omega_{\rm J}}$ into Eq. (5.99), one obtains another condition

$$\left|\frac{2\hbar\lambda}{M_{\rm J}^2\Omega_{\rm J}^3}\right| \ll 1. \tag{5.100}$$

The condition (5.99) reads $|\phi| \ll 2\sqrt{3}$ which is already satisfied under $|\phi| \ll 1$. The latter one (5.100) reads $UN/J \ll 36N^2$. This condition indicates that the approximation is valid under a sufficiently small ratio between the onsite interaction energy and the tunneling energy within the Josephson regime $1 \ll UN/J \ll 36N^2$. The effective mass $Z_1[\phi]$ turns out to give higher-order contributions and provides no correction to the Josephson frequency. Up to the quadratic level of ϕ, the one-loop effective potential is found to be

$$V_{\rm eff}^{(1)}[\phi] = \frac{\hbar\Omega_{\rm J}}{2}\left(\sqrt{\cos\phi} - 1\right) \simeq \frac{3\lambda}{M_{\rm J}\Omega_{\rm J}}\phi^2 = -\frac{\sqrt{JUN}}{8\hbar}\phi^2. \tag{5.101}$$

As a result, we obtain the one-loop correction to the Josephson frequency as

$$\Omega_{\rm J}^{(1)} = \Omega_{\rm J}\sqrt{1 - \frac{1}{2}\sqrt{\frac{U}{JN}}}. \tag{5.102}$$

Obviously, Eq. (5.102) recovers $\Omega_{\rm J}$ in Eq. (5.81) for $N \gg 1$. In a capacitively shunted superconducting Josephson circuit, Eq. (5.102) reads

$$\Omega_{\rm p}^{(1)} = \Omega_{\rm p}\sqrt{1 - \frac{1}{2}\sqrt{\frac{2e^3}{\hbar C I_{\rm c}}}}, \tag{5.103}$$

with $\Omega_{\rm p} = \sqrt{2e\hbar I_{\rm c}/\hbar C}$ being the Josephson plasma frequency. Based on the experiments of the Bose Josephson junction with ^{87}Rb atoms trapped in a double-well potential reported in Ref. [42], the number of bosons is typically $N = 2500$ and the ratio between the interaction and tunneling energy is $UN/2J \sim 10^2$. These experimental data produce $(\Omega_{\rm J} - \Omega_{\rm J}^{(1)})/\Omega_{\rm J} \simeq 0.1\%$, which indicates that the one-loop correction slightly reduces the Josephson frequency. One could observe the effect of this quantum correction more significantly in the deep Josephson regime by increasing the ratio UN/J at fixed N, in other words, by increasing the onsite interaction strength U or decreasing the Josephson coupling J under Eq. (5.100) because $\Omega_{\rm J}^{(1)}/\Omega_{\rm J} = (1 - \Omega_{\rm J}/2N\Omega_{\rm R})^{1/2}$ with $\Omega_{\rm J}/\Omega_{\rm R} = \sqrt{UN/J}$. In a superconducting Josephson circuit, the typical experimental value $2e\Omega_{\rm p}/I_{\rm c} = 2(2e^3/\hbar C I_{\rm c})^{1/2} \simeq 2.3 \times 10^{-3}$ in Ref. [233] results in $(\Omega_{\rm p} - \Omega_{\rm p}^{(1)})/\Omega_{\rm p} \simeq 0.03\%$, which slightly reduces the plasma frequency in the order of 10^{-4}. A larger value of $2e\Omega_{\rm p}/I_{\rm c}$ could amplify the quantum correction.

Our obtained results of one-loop quantum correction to the Josephson frequency in Eq. (5.102) can be also verified by another approach through the equation of motion. For the details, see Appendix E. Experimentally, our results can be tested not only in an atomic Josephson junction but also in a superconducting Josephson circuit.

Chapter 6

Conclusion

In this PhD thesis, we theoretically investigated multicomponent superfluidity from the viewpoint of the BKT transition in a 2D atomic superfluid and Josephson dynamics in atomic Josephson junctions and superconducting Josephson circuits.

In Chap. 2, we overviewed fundamental knowledge of quantum fluids to proceed with the discussion in the following chapters. In particular, we explained quantized vortices in superfluids, which are responsible for the BKT transition in 2D.

In Chap. 3, we presented the theoretical framework to study sound modes based on Tisza-Landau's two-fluid hydrodynamics. We analyzed the first and second sound velocities in a single-component collisional Bose superfluid in D-dimension including the beyond-mean-field quantum correction. It revealed the distinct behaviors of the hybridization temperature characterizing the hybridization of density and entropy modes in a D-dimensional superfluid. In 2D, in particular, our results of sound velocities are in fair agreement with the recent experimental data.

Chapter 4 was devoted to the study of 2D binary Bose superfluids and the BKT transition. In contrast to a single-component superfluid considered in Chap. 2, multicomponent superfluids have half-quantized vortices and vortex molecules. We clarified the BKT transition resulting from these exotic vortex excitations. The BKT transition temperature turned out to be amplified by increasing the Rabi coupling, while it behaves nonmonotonically with respect to the two-body intercomponent coupling. The enhancement of the superfluid transition temperature can be understood from the two branches of elementary excitations. In addition, we analyzed the first and second sound velocities in the binary Bose mixture. We found the parameter regime in which the hybridization is hindered. In particular, the hybridization is suppressed by a finite Rabi coupling due to the gapped elementary excitations, which can be tested experimentally with ultracold atoms.

In Chap. 5, we clarified the dynamical properties of the multicomponent superfluid focusing on Josephson junctions. We showed that a Bose Josephson junction can be mapped to a Caldeira-Leggett-type system in which the Josephson mode is coupled to the bath modes through an intrinsic coupling. As a result, the Josephson mode exhibits

damped Langevin dynamics and the correlation functions are amplified by the quantum fluctuations. The Josephson mode in a superconducting Josephson circuit also shows the damped Langevin dynamics, but the dynamics of correlation functions are different from that in the Bose Josephson junction due to the extrinsic coupling through the resistance. Finally, we elucidated the quantum correction also to the Josephson frequencies via the effective action formalism. Our results of dynamics in multicomponent superfluids would provide a wide application to a broad range of junction systems.

Acknowledgment

I sincerely thank my supervisor Prof. Luca Salasnich for his support in all aspects of my life as a PhD student in Padova. His support and advice were crucial to me and my fruitful life as a PhD student in Padova is fully owing to him. Through the collaborations with Prof. Andrea Perali in Camerino and Prof. Jacques Tempere in Antwerp, I have learned a lot and they inspired my research interests. The former PhD student Andrea Tononi helped me a lot especially during the early period of my stay in Padova and through the research collaboration. The collaborations with the former Master student Francesco Binanti and the PhD student Giovanni Midei in Camerino also stimulated my research activities. I would like to thank all of these collaborators. I have been supported by the PhD fellowship of Fondazione Cassa di Risparmio Padova e Rovigo during the three years of my PhD and acknowledge their financial support.

Finally, I would like to express my greatest acknowledgment to my family in Japan.

Appendix A

Nelson-Kosterlitz renormalization group analysis

This Appendix is devoted to the derivation of the Nelson-Kosterlitz renormalization group equations in a 2D Bose superfluid. First, we see the suppression of amplitude fluctuations in a 2D Bose superfluid allowing us to focus only on the phase fluctuations. Then, we show the connection between a 2D dilute Bose superfluid and the XY model employing Popov's treatment. Next, we show the equivalence of the XY model with the sine-Gordon model in the presence of vortices. Starting from the equivalent sine-Gordon model, we derive the Nelson-Kosterlitz renormalization group equations through a correlation function.

A.1 Suppression of amplitude fluctuations

Let us consider the fluctuations of the uniform superfluid order parameter given by

$$\hat{\Psi}(\boldsymbol{r}) = \Psi + \delta\hat{\Psi}(\boldsymbol{r}), \tag{A.1}$$

similar to Eq. (4.12). To distinguish the amplitude and phase fluctuations, we decompose the field operator as

$$\hat{\Psi}(\boldsymbol{r}) = \sqrt{n + \delta\hat{n}(\boldsymbol{r})}e^{i\hat{\theta}(\boldsymbol{r})}. \tag{A.2}$$

In this manner, the amplitude and phase fluctuation fields are related to $\delta\hat{\Psi}(\boldsymbol{r})$ as

$$\delta\hat{n}(\boldsymbol{r}) = \sqrt{n}\left[\delta\hat{\Psi}^{\dagger}(\boldsymbol{r}) + \delta\hat{\Psi}(\boldsymbol{r})\right], \qquad \hat{\theta}(\boldsymbol{r}) = \frac{i}{2\sqrt{n}}\left[\delta\hat{\Psi}^{\dagger}(\boldsymbol{r}) - \delta\hat{\Psi}(\boldsymbol{r})\right]. \tag{A.3}$$

From the Bose commutation relation in Eq. (2.2) with respect to $\hat{\Psi}(\boldsymbol{r})$, the relation (A.3) yields

$$[\delta\hat{n}(\boldsymbol{r}), \hat{\theta}(\boldsymbol{r})] = i\delta(\boldsymbol{r} - \boldsymbol{r}'), \tag{A.4}$$

indicating that the density and phase fluctuation fields are conjugated. Inserting Eq. (A.2) into Eq. (2.1) under Eq. (2.15) and $V_{\rm ext}(\boldsymbol{r}) = 0$, up to the quadratic order of $\delta\hat{\Psi}(\boldsymbol{r})$, we obtain

$$\hat{H} = \int \mathrm{d}\boldsymbol{r} \left[-\frac{\hbar^2}{2m} \left[\frac{1}{4n} \delta\hat{n}^\dagger(\boldsymbol{r}) \boldsymbol{\nabla}^2 \delta\hat{n}(\boldsymbol{r}) + n\hat{\theta}^\dagger(\boldsymbol{r}) \boldsymbol{\nabla}^2 \hat{\theta}(\boldsymbol{r}) \right] + \frac{g}{2} \delta\hat{n}^\dagger(\boldsymbol{r}) \delta\hat{n}(\boldsymbol{r}) \right]. \tag{A.5}$$

Here, we omitted a constant mean-field energy term. The Fourier expansions

$$\delta\hat{n}(\boldsymbol{r}) = \sum_{\boldsymbol{k}} e^{i\boldsymbol{k}\cdot\boldsymbol{r}} \delta\hat{n}_{\boldsymbol{k}}, \qquad \delta\hat{n}^\dagger(\boldsymbol{r}) = \sum_{\boldsymbol{k}} e^{-i\boldsymbol{k}\cdot\boldsymbol{r}} \delta\hat{n}^\dagger_{\boldsymbol{k}}, \tag{A.6a}$$

$$\hat{\theta}(\boldsymbol{r}) = \sum_{\boldsymbol{k}} e^{i\boldsymbol{k}\cdot\boldsymbol{r}} \hat{\theta}_{\boldsymbol{k}}, \qquad \hat{\theta}^\dagger(\boldsymbol{r}) = \sum_{\boldsymbol{k}} e^{-i\boldsymbol{k}\cdot\boldsymbol{r}} \hat{\theta}^\dagger_{\boldsymbol{k}}, \tag{A.6b}$$

with $\delta\hat{n}_{\boldsymbol{k}} = \delta\hat{n}^\dagger_{-\boldsymbol{k}}$ and $\hat{\theta}_{\boldsymbol{k}} = \hat{\theta}^\dagger_{-\boldsymbol{k}}$ give [50]

$$\hat{H} = \sum_{\boldsymbol{k}} \left[\frac{\varepsilon_k + 2gn}{4n} \delta\hat{n}^\dagger_{\boldsymbol{k}} \delta\hat{n}_{\boldsymbol{k}} + n\varepsilon_k \hat{\theta}^\dagger_{\boldsymbol{k}} \hat{\theta}_{\boldsymbol{k}} \right]. \tag{A.7}$$

Under the Bogoliubov transformation

$$\begin{aligned} \hat{\gamma}_{\boldsymbol{k}} &= u_{\boldsymbol{k}} \delta\hat{n}_{\boldsymbol{k}} + v_{\boldsymbol{k}} \hat{\theta}_{\boldsymbol{k}}, \\ \hat{\gamma}^\dagger_{-\boldsymbol{k}} &= u^*_{-\boldsymbol{k}} \delta\hat{n}_{\boldsymbol{k}} + v^*_{-\boldsymbol{k}} \hat{\theta}_{\boldsymbol{k}}, \end{aligned} \tag{A.8}$$

with the choice of the coherence factors

$$u_{\boldsymbol{k}} = \sqrt{\frac{E_k}{4n\varepsilon_k}}, \qquad v_{\boldsymbol{k}} = \frac{i}{2u_{\boldsymbol{k}}} = i\sqrt{\frac{n\varepsilon_k}{E_k}}, \tag{A.9}$$

and $E_k = \sqrt{\varepsilon_k(\varepsilon_k + 2gn)}$, we can diagonalize Eq. (A.7) and obtain

$$\hat{H} = \sum_{\boldsymbol{k}} E_k \hat{\gamma}^\dagger_{\boldsymbol{k}} \hat{\gamma}_{\boldsymbol{k}}, \tag{A.10}$$

in addition to a constant ground state energy.

To see the magnitude of each of the fluctuations, let us consider $\Delta n \equiv \sum_{\boldsymbol{k}} \Delta n_{\boldsymbol{k}}$ and $\Delta\theta \equiv \sum_{\boldsymbol{k}} \Delta\theta_{\boldsymbol{k}}$ with [245]

$$\Delta n_{\boldsymbol{k}} \equiv \langle \delta\hat{n}^\dagger_{\boldsymbol{k}} \delta\hat{n}_{\boldsymbol{k}} \rangle = \mathrm{Tr} \left[e^{-\beta\hat{H}} \delta\hat{n}^\dagger_{\boldsymbol{k}} \delta\hat{n}_{\boldsymbol{k}} \right] = n\frac{\varepsilon_k}{E_k} \left[2f_T(E_k) - 1 \right], \tag{A.11a}$$

$$\Delta\theta_{\boldsymbol{k}} \equiv \langle \hat{\theta}^\dagger_{\boldsymbol{k}} \hat{\theta}_{\boldsymbol{k}} \rangle = \mathrm{Tr} \left[e^{-\beta\hat{H}} \hat{\theta}^\dagger_{\boldsymbol{k}} \hat{\theta}_{\boldsymbol{k}} \right] = \frac{1}{4n} \frac{E_k}{\varepsilon_k} \left[2f_T(E_k) - 1 \right]. \tag{A.11b}$$

First of all, the relative weight of the fluctuations at each momentum is

$$\frac{\Delta n_{\boldsymbol{k}}}{\Delta\theta_{\boldsymbol{k}}} = 4n^2 \frac{k^2}{k^2 + 8\pi\eta_2 n}, \tag{A.12}$$

where η_2 is the gas parameter in 2D defined by Eq. (3.33). Equation (A.12) indicates that, in the low-temperature regime in which only the low momentum states are occupied, the amplitude fluctuations are less significant than the phase fluctuations $\Delta n_{\boldsymbol{k}}/\Delta\theta_{\boldsymbol{k}} \to 0$. In the short-wavelength regime, the magnitude of the amplitude fluctuations becomes comparable to the one of phase fluctuations $\Delta n_{\boldsymbol{k}}/\Delta\theta_{\boldsymbol{k}} \sim 1$. On the other hand, in the higher temperature regime $k_{\rm B}T \gg E_k$, the Bose distribution function can be simplified as $f_T(E_k) \simeq k_{\rm B}T/E_k$ and the momentum summation results in

$$\frac{\Delta n}{n^2} = \frac{2}{n\lambda_T^2} \ln\left(\frac{k_{\rm B}T}{2gn}\right). \tag{A.13}$$

Consequently, Eq. (A.13) shows the suppression of the amplitude fluctuations in a 2D Bose gas also in the higher temperature regime $k_{\rm B}T \gg E_k$ as long as $n\lambda_T^2 \gg 1$, namely $E_k \ll k_{\rm B}T \ll 2\pi n\hbar^2/m$.

A.2 Popov's treatment

In Eq. (2.58), we used the substitution of the superfluid density $|\Psi|^2 \to n_{\rm s}$. We derive this substitution through Popov's treatment in this section [50, 246]. In Sec. A.1, we saw that the phase fluctuations are dominant rather than the amplitude fluctuations in 2D. Based on this discussion, we decompose the Bose field Ψ into the fast varying variable $\tilde{\Psi}$ and the slowly varying variable θ as

$$\Psi(\boldsymbol{r}) = \tilde{\Psi}(\boldsymbol{r})e^{i\theta(\boldsymbol{r})}. \tag{A.14}$$

We consider grand canonical Hamiltonian with a chemical potential μ, a normal fluid velocity $\boldsymbol{v}_{\rm n}$, and superfluid velocity $\boldsymbol{v}_{\rm s}$ given by

$$\begin{aligned} K &= \int {\rm d}\boldsymbol{r} \left[\frac{\hbar^2}{2m}|\boldsymbol{\nabla}\Psi(\boldsymbol{r})|^2 + g|\Psi(\boldsymbol{r})|^4\right] - \mu N - \boldsymbol{v}_{\rm n}\cdot\boldsymbol{P} - \boldsymbol{s}\cdot\boldsymbol{I} \\ &= \int {\rm d}\boldsymbol{r} \left[\frac{\hbar^2}{2m}|(-i\hbar\boldsymbol{\nabla} - m\boldsymbol{v}_{\rm n})\,\Psi(\boldsymbol{r})|^2 + \left(g|\Psi(\boldsymbol{r})|^2 - \mu - \frac{mv_{\rm n}^2}{2}\right)|\Psi(\boldsymbol{r})|^2 - \hbar\boldsymbol{s}\cdot\boldsymbol{\nabla}\theta\right], \end{aligned} \tag{A.15}$$

with

$$\boldsymbol{P} = \frac{i\hbar}{2}\int {\rm d}\boldsymbol{r}\,[(\boldsymbol{\nabla}\Psi^*)\Psi - \Psi^*\boldsymbol{\nabla}\Psi], \tag{A.16}$$

being the total momentum and

$$\boldsymbol{I} = \hbar\int {\rm d}\boldsymbol{r}\,\boldsymbol{\nabla}\theta, \tag{A.17}$$

being the topological invariant and its conjugate variable $\boldsymbol{s}$ associated with the superfluid velocity $\boldsymbol{v}_{\rm s}$. The thermodynamic potential is given by

$$\Omega[T,\mu,\boldsymbol{v}_{\rm n},\boldsymbol{s}] = -\frac{1}{\beta}\ln Z[T,\mu,\boldsymbol{v}_{\rm n},\boldsymbol{s}], \qquad Z[T,\mu,\boldsymbol{v}_{\rm n},\boldsymbol{s}] = {\rm Tr}[e^{-\beta K}]. \tag{A.18}$$

The thermodynamic potential produces the ensemble averages as

$$\langle \boldsymbol{P} \rangle = -\frac{\partial \Omega}{\partial \boldsymbol{v}_{\rm n}}, \quad \langle \boldsymbol{I} \rangle = -\frac{\partial \Omega}{\partial \boldsymbol{s}}, \quad \langle N \rangle = -\frac{\partial \Omega}{\partial \mu}. \tag{A.19}$$

The definition of the grand canonical Hamiltonian (A.15) gives a relation

$$\Omega[T, \mu, \boldsymbol{v}_{\rm n}, \boldsymbol{s}] = \Omega \left[T, \mu + \frac{m v_{\rm n}^2}{2}, 0, \boldsymbol{s} \right] - V m \boldsymbol{v}_{\rm n} \cdot \boldsymbol{s}. \tag{A.20}$$

Equation (A.20) is a general relation independent of the interactions [50]. In $\boldsymbol{v}_{\rm n} \to 0$, Eq. (A.20) yields

$$m \boldsymbol{v}_{\rm n} \frac{\partial \Omega}{\partial \mu} - \frac{\partial \Omega}{\partial \boldsymbol{v}_{\rm n}} = V m \boldsymbol{s}, \tag{A.21}$$

which is equivalent to

$$\langle \boldsymbol{P} \rangle = V m \left(\langle n \rangle \boldsymbol{v}_{\rm n} + \boldsymbol{s} \right), \tag{A.22}$$

with $\langle n \rangle = \langle N \rangle / V$ being the average density. The current density given by (3.28) is related to the total momentum as $\boldsymbol{J} = \langle \boldsymbol{P} \rangle / mV$ and Eqs. (A.22) and (3.18) give

$$\boldsymbol{s} = n_{\rm s} \left(\boldsymbol{v}_{\rm s} - \boldsymbol{v}_{\rm n} \right). \tag{A.23}$$

Here, we introduce the *macroscopic* superfluid density by

$$\boldsymbol{v}_{\rm s} = \frac{1}{mV} \langle \boldsymbol{I} \rangle = -\frac{1}{mV} \frac{\partial \Omega}{\partial \boldsymbol{s}}. \tag{A.24}$$

Indeed, in $\boldsymbol{v}_{\rm n} \to 0$, $\boldsymbol{J} \to \boldsymbol{s} = n_{\rm s} \boldsymbol{v}_{\rm s}$ and

$$\boldsymbol{v}_{\rm s} = \frac{\boldsymbol{s}}{n_{\rm s}} = -\frac{1}{mV} \frac{\partial \Omega}{\partial \boldsymbol{s}}. \tag{A.25}$$

By acting $\boldsymbol{\nabla}_{\boldsymbol{s}} \cdot$ on Eq. (A.25) and using $\boldsymbol{\nabla}_{\boldsymbol{s}} \cdot \boldsymbol{s} = D$, Eq. (A.25) reads

$$\frac{1}{n_{\rm s}} = -\frac{1}{DmV} \boldsymbol{\nabla}_{\boldsymbol{s}}^2 \Omega \Big|_{s \to 0}, \tag{A.26}$$

With $\mathrm{d}\boldsymbol{s} = n_{\rm s} \, \mathrm{d}\boldsymbol{v}_{\rm s}$ and $\Omega[T, \mu, \boldsymbol{v}_{\rm n}, \boldsymbol{s}] = -\mathcal{P}[T, \mu, \boldsymbol{v}_{\rm n}, \boldsymbol{v}_{\rm s}] V$ with $\mathcal{P}[T, \mu, \boldsymbol{v}_{\rm n}, \boldsymbol{v}_{\rm s}]$ the pressure, we find the formula of the superfluid density as

$$n_{\rm s} = -\frac{1}{Dm} \boldsymbol{\nabla}_{\boldsymbol{v}_{\rm s}}^2 \mathcal{P}[T, \mu, 0, \boldsymbol{v}_{\rm s}] \Big|_{\boldsymbol{v}_{\rm s} \to 0}. \tag{A.27}$$

The Euclidean action corresponding to the grand canonical Hamiltonian (A.15) is given by

$$\begin{aligned} S_{\rm E}[\Psi] = & \int_0^{\hbar\beta} \mathrm{d}\tau \int \mathrm{d}\boldsymbol{r} \left[\hbar \Psi^* \partial_\tau \Psi + \frac{\hbar^2}{2m} |\boldsymbol{\nabla} \Psi|^2 + g |\Psi|^4 - \mu |\Psi|^2 \right. \\ & \left. - \frac{i\hbar}{2} \boldsymbol{v}_{\rm n} \cdot \left[(\boldsymbol{\nabla} \Psi^*) \Psi - \Psi^* \boldsymbol{\nabla} \Psi \right] - \boldsymbol{s} \cdot \boldsymbol{\nabla} \theta \right] \\ = & \, S_{\rm E}[\tilde{\Psi}] + \int_0^{\hbar\beta} \mathrm{d}\tau \int \mathrm{d}\boldsymbol{r} \left[\left(i\hbar \partial_\tau \theta + \frac{\hbar^2}{2m} (\boldsymbol{\nabla} \theta)^2 \right) |\tilde{\Psi}|^2 + \frac{i\hbar^2}{2m} \boldsymbol{\nabla} \theta \cdot \left[(\boldsymbol{\nabla} \Psi^*) \Psi - \Psi^* \boldsymbol{\nabla} \Psi \right] \right]. \end{aligned} \tag{A.28}$$

The second term in Eq. (A.28) gives shifts to the chemical potential and the normal fluid velocity as

$$\mu \to \tilde{\mu} = \mu - i\hbar\partial_\tau\theta - \frac{\hbar^2}{2m}(\boldsymbol{\nabla}\theta)^2, \tag{A.29a}$$

$$\boldsymbol{v}_{\rm n} \to \tilde{\boldsymbol{v}}_{\rm n} = \boldsymbol{v}_{\rm n} - \frac{\hbar}{m}\boldsymbol{\nabla}\theta. \tag{A.29b}$$

The partition function is given by

$$Z_{\rm E} = \int \mathcal{D}\Psi\mathcal{D}\Psi^*\, e^{-S_{\rm E}[\Psi]/\hbar} = \int \mathcal{D}\theta\, Z_\theta, \tag{A.30}$$

with

$$Z_\theta = \prod_j Z_j, \qquad Z_j = \int_{(\Delta\tau_j,\Delta V_j)} \mathcal{D}\tilde{\Psi}\, e^{-S_{\rm E}[\Psi]/\hbar}. \tag{A.31}$$

Here, in Eq. (A.31), we divide the system volume and imaginary time path into parts $\hbar\beta = \sum_j \Delta\tau_j$, $V = \sum_j \Delta V_j$ such that the spacetime variation of the superfluid phase θ is locally slow in each cell: $\partial_\tau\theta = $ const. and $\boldsymbol{\nabla}\theta = $ const. and there is no correlation between the different cells. Then, by performing the path integral in terms of $\tilde{\Psi}$ within each cell, one finds

$$\begin{aligned} Z_j &= \exp\Big[-\Delta\tau_j\Omega[0,\tilde{\mu},\tilde{\boldsymbol{v}}_{\rm n},0]/\hbar\Big] = \exp\Big[\Delta\tau_j\Delta V_j\mathcal{P}[0,\tilde{\mu},\tilde{\boldsymbol{v}}_{\rm n},0]/\hbar\Big] \\ &= \exp\Big[\Delta\tau_j\Delta V_j\mathcal{P}[0,\mu - i\hbar\partial_\tau\theta, \boldsymbol{v}_{\rm n}=0, \boldsymbol{v}_{\rm s}=\hbar\boldsymbol{\nabla}\theta/m]/\hbar\Big]. \end{aligned} \tag{A.32}$$

In the last equality, we used Eq. (A.20). In $\boldsymbol{v}_{\rm n} \to 0$, we find

$$Z_\theta = e^{-S_{\rm E}[\theta]/\hbar}, \tag{A.33}$$

with

$$\begin{aligned} S_{\rm E}[\theta] &= -\int_0^{\hbar\beta} {\rm d}\tau \int {\rm d}\boldsymbol{r}\, \mathcal{P}_0[\mu - i\hbar\partial_\tau\theta, \boldsymbol{v}_{\rm s} = \hbar\theta/m] \\ &= \int_0^{\hbar\beta} {\rm d}\tau \int {\rm d}\boldsymbol{r} \left[-\mathcal{P}_0[\mu,0] + i\hbar\partial_\tau\theta\, \frac{\partial\mathcal{P}_0[\mu,0]}{\partial\mu} - \frac{v_{\rm s}^2}{2D}\boldsymbol{\nabla}^2_{\boldsymbol{v}_{\rm s}}\mathcal{P}_0 + \cdots\right], \end{aligned} \tag{A.34}$$

with $\mathcal{P}_0[\mu, \boldsymbol{v}_{\rm s}]$ being the pressure at zero temperature and $\boldsymbol{v}_{\rm n} = 0$. Note that odd powers of $\boldsymbol{v}_{\rm s} = \hbar\boldsymbol{\nabla}\theta/m$ vanishes by the spatial inversion symmetry. In particular with time-independent superfluid phase $\theta(\boldsymbol{r})$, the formula of the superfluid density (A.27) leads to

$$S_{\rm E}[\theta] = \int_0^{\hbar\beta} {\rm d}\tau \int {\rm d}\boldsymbol{r}\, \frac{\hbar^2 n_{\rm s}}{2m}(\boldsymbol{\nabla}\theta)^2, \tag{A.35}$$

up to the quadratic order of $\boldsymbol{v}_{\rm s} = \hbar\boldsymbol{\nabla}\theta/m$. Equation (A.35) coincides with Eq. (2.58), which is obtained just by inserting the Madelung transformation (2.57) and substituting $n \to n_{\rm s}$. Consequently, this substitution turns out to be equivalent to Poppov's treatment integrating out fast amplitude variable.

A.3 Sine-Gordon model

In this section, we show another approach to derive the NK RG equations (2.74) through the 2D sine-Gordon model given by

$$S_{\mathrm{sG}}[\phi] = S_0[\phi] - \frac{2\hbar g_{\mathrm{sG}}}{(2\pi\alpha)^2}\int \mathrm{d}^2\boldsymbol{r}\cos(2\phi), \tag{A.36}$$

with

$$S_0[\phi] = \frac{\hbar}{4\pi K_{\mathrm{sG}}}\int \mathrm{d}^2\boldsymbol{r}\,(\boldsymbol{\nabla}\phi)^2, \tag{A.37}$$

and $\phi(\boldsymbol{r})$ being the analytic real field where K_{sG} and g_{sG} are the coefficients of the kinetic term and cosine potential, respectively, and α is the short-range cutoff.

A.3.1 Equivalence to XY model

Using the identity $\cos(2\phi) = \sum_{\sigma=\pm1} e^{2i\sigma\phi}/2$, we can perturbatively calculate the partition function for the sine-Gordon model

$$Z_{\mathrm{sG}} = \int \mathcal{D}\phi\, e^{-S_{\mathrm{sG}}[\phi]/\hbar} \tag{A.38}$$

as

$$\begin{aligned} Z_{\mathrm{sG}} &= \sum_{n=0}^{\infty}\frac{1}{n!}\left(\frac{g_{\mathrm{sG}}}{2\pi^2}\right)^n \int\left(\prod_{j=1}^{n}\mathrm{d}^2\boldsymbol{x}_j\right)\int \mathcal{D}\phi\, e^{-S_0[\phi]/\hbar}\cos\left[2\phi(\boldsymbol{x}_1)\right]\cdots\cos\left[2\phi(\boldsymbol{x}_n)\right] \\ &= \sum_{n=0}^{\infty}\frac{1}{n!}\left(\frac{g_{\mathrm{sG}}}{4\pi^2}\right)^n \int\left(\prod_{j=1}^{n}\mathrm{d}^2\boldsymbol{x}_j\right)\sum_{\{\sigma_j\}=\pm1}\left\langle e^{2i\sum_{j=1}^{n}\sigma_j\phi(\boldsymbol{x}_j)}\right\rangle_0, \end{aligned} \tag{A.39}$$

where $\boldsymbol{x}_j = \boldsymbol{r}_j/\alpha$ is the dimensionless length scaled by the short-range cutoff and $\langle O\rangle_0 \equiv Z_0^{-1}\int \mathcal{D}\phi\, O[\phi]e^{-S_0[\phi]/\hbar}$ with $Z_0 = \int \mathcal{D}\phi\, e^{-S_0[\phi]/\hbar}$. The ensemble average in Eq. (A.39) can be computed as

$$\begin{aligned} \left\langle e^{2i\sum_{j=1}^{n}\sigma_j\phi(\boldsymbol{x}_j)}\right\rangle_0 &= \frac{1}{Z_0}\int \mathcal{D}\phi\, e^{2i\sum_{j=1}^{n}\sigma_j\phi(\boldsymbol{r}_j)}e^{-S_0[\phi]/\hbar} \\ &= e^{4K_{\mathrm{sG}}\sum_{i<j}\sigma_i\sigma_j\ln|\boldsymbol{x}_i-\boldsymbol{x}_j|}. \end{aligned} \tag{A.40}$$

Here, the Gaussian integral imposes the neutral condition $\sum_{j=1}^{n}\sigma_j = 0$ requiring $n = 2N$ is even. Using Eq. (A.40), one obtains

$$Z_{\mathrm{sG}} = \sum_{N=0}^{\infty}\frac{1}{(N!)^2}\left(\frac{g_{\mathrm{sG}}}{4\pi^2}\right)^{2N}\int\left(\prod_{j=1}^{2N}\mathrm{d}^2\boldsymbol{x}_j\right)\, e^{8\pi K_{\mathrm{sG}}\sum_{i<j}^{2N}\sigma_i\sigma_j C(\boldsymbol{x}_i-\boldsymbol{x}_j)}. \tag{A.41}$$

Comparing Eq. (A.41) and Eq. (2.66) with unit vortex charges $q_j = \sigma_j$, we find that the sine-Godron model and the singular part of the XY model in Sec. 2.6 are equivalent with the correspondence of

$$\pi K = 2K_{\rm sG}, \qquad y = \frac{g_{\rm sG}}{4\pi^2}. \tag{A.42}$$

Namely, $K_{\rm sG}$ plays the same role of the phase stiffness (scaled by the temperature) in the XY model, while the coupling constant of the cosine potential $g_{\rm sG}$ corresponds to the vortex fugacity. Since the vortices discussed in the XY model are described only by the topological part of the partition function (2.66), this equivalence is useful to derive the equivalent RG equations (2.74) through the sine-Gordon model.

A.3.2 Derivation of renormalization group equations

Based on the correspondence with the sine-Gordon model proven in Sec. A.3.1, we derive the NK RG equations (2.74) from the sine-Gordon model. To this end, we introduce a correlation function

$$R(\boldsymbol{r}_1 - \boldsymbol{r}_2) = \left\langle e^{i\phi(\boldsymbol{r}_1)} e^{-i\phi(\boldsymbol{r}_2)} \right\rangle = \frac{1}{Z_{\rm sG}} \int \mathcal{D}\phi \, e^{i\phi(\boldsymbol{r}_1)} e^{-i\phi(\boldsymbol{r}_2)} e^{-S_{\rm sG}[\phi]/\hbar}. \tag{A.43}$$

First of all, the lowest contribution without the cosine potential term is given by

$$R_0(\boldsymbol{r}_1 - \boldsymbol{r}_2) = \left\langle e^{i\phi(\boldsymbol{r}_1)} e^{-i\phi(\boldsymbol{r}_2)} \right\rangle_0 = e^{-2\pi K_{\rm sG} C(\boldsymbol{r}_1 - \boldsymbol{r}_2)}. \tag{A.44}$$

with $C(\boldsymbol{r}) = \ln(|\boldsymbol{r}|/\alpha)/2\pi$. Including the effects of the cosine potential perturbatively up to $\mathcal{O}\big(g_{\rm sG}^2\big)$, one finds the correlation function as

$$\begin{aligned} R(\boldsymbol{r}_1 - \boldsymbol{r}_2) &= R_0(\boldsymbol{r}_1 - \boldsymbol{r}_2) \\ &+ \frac{1}{2}\left(\frac{g_{\rm sG}}{4\pi^2\alpha^2}\right)^2 \sum_{\sigma_1=\pm 1} \sum_{\sigma_2=\pm 1} \int \mathrm{d}^2\boldsymbol{r}' \int \mathrm{d}^2\boldsymbol{r}'' \left[\left\langle e^{i\phi(\boldsymbol{r}_1)} e^{-i\phi(\boldsymbol{r}_2)} e^{2i\sigma_1\phi(\boldsymbol{r}')} e^{-2i\sigma_2\phi(\boldsymbol{r}'')} \right\rangle_0 \right. \\ &\left. - \left\langle e^{i\phi(\boldsymbol{r}_1)} e^{-i\phi(\boldsymbol{r}_2)} \right\rangle_0 \left\langle e^{2i\sigma_1\phi(\boldsymbol{r}')} e^{-2i\sigma_2\phi(\boldsymbol{r}'')} \right\rangle_0 \right] \end{aligned} \tag{A.45}$$

To evaluate Eq. (A.45), it is useful to employ the formula [185]

$$\left\langle \prod_j e^{iA_j\phi(\boldsymbol{r}_j)} \right\rangle_0 = \exp\left[2\pi K_{\rm sG} \sum_{i<j} A_i A_j C(\boldsymbol{r}_i - \boldsymbol{r}_j) \right], \tag{A.46}$$

only if $\sum_j A_j = 0$. Unless the neutral condition is satisfied, the correlation function vanishes. It indicates that only $\sigma_1 = \sigma_2$ gives a non-zero contribution to Eq. (A.45).

The formula (A.46) results in

$$
\begin{aligned}
&R(\boldsymbol{r}_1-\boldsymbol{r}_2) = R_0(\boldsymbol{r}_1-\boldsymbol{r}_2)\\
&+\frac{g_{\mathrm{sG}}^2}{32\pi^4\alpha^4}\sum_{\sigma_1=\pm1}\int \mathrm{d}^2\boldsymbol{r}'\int \mathrm{d}^2\boldsymbol{r}''\, e^{-2\pi K_{\mathrm{sG}}C(\boldsymbol{r}_1-\boldsymbol{r}_2)}e^{-8\pi K_{\mathrm{sG}}C(\boldsymbol{r}'-\boldsymbol{r}'')}\left[e^{4\pi\sigma_1 K_{\mathrm{sG}}D(\boldsymbol{r}_1,\boldsymbol{r}_2;\boldsymbol{r}',\boldsymbol{r}'')}-1\right]\\
&= R_0(\boldsymbol{r}_1-\boldsymbol{r}_2)\left[1+\frac{g_{\mathrm{sG}}^2}{32\pi^4\alpha^4}\sum_{\sigma_1=\pm1}\int \mathrm{d}^2\boldsymbol{r}'\int \mathrm{d}^2\boldsymbol{r}''\, e^{-8\pi K_{\mathrm{sG}}C(\boldsymbol{r}'-\boldsymbol{r}'')}\left[e^{4\pi\sigma_1 K_{\mathrm{sG}}D(\boldsymbol{r}_1,\boldsymbol{r}_2;\boldsymbol{r}',\boldsymbol{r}'')}-1\right]\right],
\end{aligned}
\tag{A.47}
$$

with $D(\boldsymbol{r}_1,\boldsymbol{r}_2;\boldsymbol{r}',\boldsymbol{r}'') = C(\boldsymbol{r}_1-\boldsymbol{r}')-C(\boldsymbol{r}_1-\boldsymbol{r}'')-C(\boldsymbol{r}_2-\boldsymbol{r}')+C(\boldsymbol{r}_2-\boldsymbol{r}'')$. Using $\boldsymbol{R}=(\boldsymbol{r}'+\boldsymbol{r}'')/2$ and $\boldsymbol{r}=\boldsymbol{r}'-\boldsymbol{r}''$ and assuming $r \ll R$, one can expand the integrand in Eq. (A.47) as

$$
\begin{aligned}
e^{4\pi\sigma_1 K_{\mathrm{sG}}D(\boldsymbol{r}_1,\boldsymbol{r}_2;\boldsymbol{r}',\boldsymbol{r}'')} &= e^{4\pi\sigma_1 K_{\mathrm{sG}}\boldsymbol{r}\cdot\boldsymbol{\nabla}_{\boldsymbol{R}}[C(\boldsymbol{r}_1-\boldsymbol{R})-C(\boldsymbol{r}_2-\boldsymbol{R})]}\\
&= 1+4\pi\sigma_1 K_{\mathrm{sG}}\boldsymbol{r}\cdot\boldsymbol{\nabla}_{\boldsymbol{R}}\left[C(\boldsymbol{r}_1-\boldsymbol{R})-C(\boldsymbol{r}_2-\boldsymbol{R})\right]\\
&+8\pi^2 K_{\mathrm{sG}}\left[\boldsymbol{r}\cdot\boldsymbol{\nabla}_{\boldsymbol{R}}\left[C(\boldsymbol{r}_1-\boldsymbol{R})-C(\boldsymbol{r}_2-\boldsymbol{R})\right]\right]^2+\mathcal{O}\big(r^3\big).
\end{aligned}
\tag{A.48}
$$

The second term proportional to σ_1 in Eq. (A.48) vanishes after performing the summation $\sum_{\sigma_1=\pm1}$. This expansion reduces Eq. (A.47) to

$$
\begin{aligned}
&R(\boldsymbol{r}_1-\boldsymbol{r}_2) = R_0(\boldsymbol{r}_1-\boldsymbol{r}_2)\\
&\times\left[1+\frac{g_{\mathrm{sG}}^2}{4\pi^2\alpha^4}\int \mathrm{d}^2\boldsymbol{R}\int \mathrm{d}^2\boldsymbol{r}\, e^{-8\pi K_{\mathrm{sG}}C(\boldsymbol{r})}K_{\mathrm{sG}}^2\left[\boldsymbol{r}\cdot\boldsymbol{\nabla}_{\boldsymbol{R}}\left[C(\boldsymbol{r}_1-\boldsymbol{R})-C(\boldsymbol{r}_2-\boldsymbol{R})\right]\right]^2\right]\\
&= R_0(\boldsymbol{r}_1-\boldsymbol{r}_2)\Bigg[1-\frac{g_{\mathrm{sG}}^2}{8\pi^2\alpha^4}\int \mathrm{d}^2\boldsymbol{R}\int \mathrm{d}^2\boldsymbol{r}\, e^{-8\pi K_{\mathrm{sG}}C(\boldsymbol{r})}K_{\mathrm{sG}}^2 r^2\\
&\times\left[C(\boldsymbol{r}_1-\boldsymbol{R})-C(\boldsymbol{r}_2-\boldsymbol{R})\right]\boldsymbol{\nabla}_{\boldsymbol{R}}^2\left[C(\boldsymbol{r}_1-\boldsymbol{R})-C(\boldsymbol{r}_2-\boldsymbol{R})\right]\Bigg]\\
&= R_0(\boldsymbol{r}_1-\boldsymbol{r}_2)\left[1+\frac{g_{\mathrm{sG}}^2}{2\pi^2\alpha^4}K_{\mathrm{sG}}^2 C(\boldsymbol{r}_1-\boldsymbol{r}_2)\int_{r>\alpha}\mathrm{d}^2\boldsymbol{r}\, r^2 e^{-8\pi K_{\mathrm{sG}}C(\boldsymbol{r})}\right].
\end{aligned}
\tag{A.49}
$$

The last equality in Eq. (A.49) follows from $\boldsymbol{\nabla}_{\boldsymbol{r}}^2 C(\boldsymbol{r}) = \delta^2(\boldsymbol{r})$. By setting $R(\boldsymbol{r}_1-\boldsymbol{r}_2) = e^{-2\pi K_{\mathrm{eff}}C(\boldsymbol{r}_1-\boldsymbol{r}_2)}$, the effective coupling strength K_{eff} reads

$$
\begin{aligned}
K_{\mathrm{eff}} &= K_{\mathrm{sG}}-\frac{g_{\mathrm{sG}}^2}{4\pi^3\alpha^4}K_{\mathrm{sG}}^2\int_{r>\alpha}\mathrm{d}^2\boldsymbol{r}\, r^2 e^{-8\pi K_{\mathrm{sG}}C(\boldsymbol{r})}\\
&= K_{\mathrm{sG}}-\frac{y_{\mathrm{sG}}^2}{2}K_{\mathrm{sG}}^2\int_1^\infty \mathrm{d}x\, x^{3-4K_{\mathrm{sG}}},
\end{aligned}
\tag{A.50}
$$

with $x = r/\alpha$. Up to $\mathcal{O}\big(g_{\mathrm{sG}}^2\big)$, Eq. (A.50) can be written as

$$
K_{\mathrm{eff}}^{-1} = K_{\mathrm{sG}}^{-1}+\frac{g_{\mathrm{sG}}^2}{2\pi^2}\int_1^\infty \mathrm{d}x\, x^{3-4K_{\mathrm{sG}}}.
\tag{A.51}
$$

As we performed in Eqs. (2.72), by splitting the integral at the boundary $x = b = e^{\mathrm{d}l} = 1 + \mathrm{d}l$ and introducing

$$\tilde{K}_{\mathrm{sG}}^{-1} = K_{\mathrm{sG}}^{-1} + \frac{g_{\mathrm{sG}}^2}{2\pi^2}\int_1^b \mathrm{d}x\, x^{3-4K_{\mathrm{sG}}}, \qquad \tilde{g}_{\mathrm{sG}} = g_{\mathrm{sG}} b^{2-2K_{\mathrm{sG}}}, \tag{A.52}$$

Eq. (A.51) can be written as

$$K_{\mathrm{eff}}^{-1} = \tilde{K}_{\mathrm{sG}}^{-1} + \frac{\tilde{g}_{\mathrm{sG}}^2}{2\pi^2}\int_1^\infty \mathrm{d}x'\, x'^{3-4\tilde{K}_{\mathrm{sG}}}, \tag{A.53}$$

after rescaling $x' = x/b$, which is equivalent to Eq. (A.51). Equations (A.52) yield

$$\partial_l K_{\mathrm{sG}}(l)^{-1} = \frac{1}{2\pi^2} g_{\mathrm{sG}}(l)^2, \tag{A.54a}$$

$$\partial_l g_{\mathrm{sG}}(l) = \left[2 - 2K_{\mathrm{sG}}(l)\right] g_{\mathrm{sG}}(l). \tag{A.54b}$$

Under the mapping (A.42), Eqs. (A.54) are found to be identical to the NK RG equations (2.74).

A.4 Renormalization group equations for a binary Bose superfluid

In this section, we give the detailed calculation for the derivation of the NK RG equations (4.32) in a Rabi-coupled binary Bose mixture illustrating the difference from the single-component Bose superfluid. The Lagrangian density for a two-component Bose mixture is given by

$$\mathcal{L} = \sum_{a=1,2}\left[i\hbar\Psi_a^*\partial_t\Psi_a - \frac{\hbar^2}{2m}|\boldsymbol{\nabla}\Psi_a|^2 - \frac{g}{2}|\Psi_a|^4\right] - g_{12}|\Psi_1|^2|\Psi_2|^2 + \hbar\omega_{\mathrm{R}}\left[\Psi_1^*\Psi_2 + \Psi_2^*\Psi_1\right]. \tag{A.55}$$

The Madelung transformation (4.4) with a uniform density n_a and time-independent superfluid phase $\theta_a(\boldsymbol{r})$ gives

$$\mathcal{L}_\theta[\theta_1,\theta_2] = -\frac{J_1}{2}(\boldsymbol{\nabla}\theta_1)^2 - \frac{J_2}{2}(\boldsymbol{\nabla}\theta_2)^2 + 2\hbar\omega_{\mathrm{R}}\tilde{n}\cos\left(\theta_1 - \theta_2\right), \tag{A.56}$$

where $\tilde{n} \equiv \sqrt{n_1 n_2}$ and $J_{a=1,2} = \hbar^2 n_a/m = \alpha_a J$ with $J = \hbar^2 n_{\mathrm{s}}/m$ being the total phase stiffness. Here, we omitted constant terms $-g(n_1^2+n_2^2)/2 - g_{12}\tilde{n}^2$. According to Popov's treatment introduced in Sec. A.2, n_a can be interpreted as the superfluid density of each component. In particular, with balanced densities $\alpha_1 = \alpha_2 = 1/2$, we have $J_1 = J_2 = J/2$. The Lagrangian (A.56) yields the equations of motion

$$J_1\boldsymbol{\nabla}^2\theta_1 = 2\hbar\omega_{\mathrm{R}}\sin\left(\theta_1 - \theta_2\right), \qquad J_2\boldsymbol{\nabla}^2\theta_2 = -2\hbar\omega_{\mathrm{R}}\sin\left(\theta_1 - \theta_2\right). \tag{A.57}$$

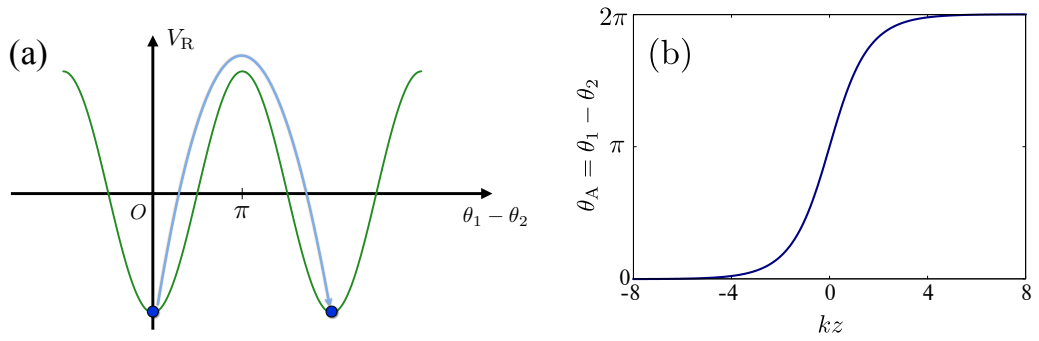

Figure A.1: Sine-Gordon kink in a Rabi-coupled binary Bose superfluid. (a) shows Rabi coupling potential $V_{\rm R}=-2\hbar\omega_{\rm R}\tilde{n}\cos(\theta_1-\theta_2)$. (b) shows the kink solution (A.60).

A.4.1 Sine-Gordon kinks with a finite Rabi coupling

Without Rabi coupling $\omega_{\rm R}=0$, the Lagrangian (A.55) is invariant under the U(1) transformation of each component $\mathrm{U}(1)_1$: $\Psi_1\to e^{i\varphi_1}\Psi_1$ or $\mathrm{U}(1)_2$: $\Psi_2\to e^{i\varphi_2}\Psi_2$, and hosts $\mathrm{U}(1)_1\times\mathrm{U}(1)_2$ symmetry. On the other hand, with a finite Rabi coupling, only $\mathrm{U}(1)_{1+2}$ symmetry holds. Indeed, moving on to the basis $\theta_\pm=(\theta_1\pm\theta_2)/\sqrt{2}$, Eq. (A.56) reads $\mathcal{L}_\theta=\mathcal{L}_+ + \mathcal{L}_-$ with

$$\mathcal{L}_+ = -\frac{\hbar^2 n}{4m}(\boldsymbol{\nabla}\theta_+)^2, \tag{A.58a}$$

$$\mathcal{L}_- = -\frac{\hbar^2 n}{4m}(\boldsymbol{\nabla}\theta_-)^2 + 2\hbar\omega_{\rm R}\tilde{n}\cos(\sqrt{2}\theta_-), \tag{A.58b}$$

for balanced densities $n_1=n_2$. Equations (A.58) indicate that $\mathrm{U}(1)_{1-2}$ symmetry is explicitly broken by the Rabi coupling while $\mathrm{U}(1)_{1+2}$ symmetry is preserved. Figure A.1(a) illustrates the Rabi coupling potential $V_{\rm R}=-2\hbar\omega_{\rm R}\tilde{n}\cos(\theta_1-\theta_2)$. Winding $\theta_1-\theta_2$: $0\to 2\pi$ requires overcoming a potential barrier located at $\theta_1-\theta_2=\pi$ corresponding to a kink.

Equations of motion (A.57) correspond to the local minima of the energy. They read [184]

$$\theta_1=\alpha_2\theta_{\rm A}, \qquad \theta_2=-\alpha_1\theta_{\rm A}, \tag{A.59}$$

with

$$\theta_{\rm A}=4\arctan e^{kz}, \qquad k^2=\frac{2m\omega_{\rm R}}{\hbar}\frac{n}{\tilde{n}}. \tag{A.60}$$

Equations (A.59) are the kink solutions, which are dependent only on one spatial coordinate z. Here, k^{-1} is the characteristic length of the kink and the tension is given by $\sigma=8n\sqrt{2\hbar^3\omega_{\rm R}/m}(\tilde{n}/n)^{3/2}$ [184]. Figure A.1(b) shows the kink solution $\theta_{\rm A}=\theta_1-\theta_2$.

A.4.2 Derivation of renormalization group equations

Without the Rabi coupling $\omega_{\mathrm{R}} = 0$, by inserting Eqs. (A.57) into Eq. (A.56) to eliminate θ_2, one obtains the optimized Lagrangian

$$\mathcal{L}_{\theta}^{\mathrm{opt}}[\theta_1] = -\frac{J_1}{2}(\boldsymbol{\nabla}\theta_1)^2 = -\frac{J}{4}(\boldsymbol{\nabla}\theta_1)^2, \tag{A.61}$$

with balanced densities $\alpha_1 = \alpha_2 = 1/2$. With a finite Rabi coupling, on the other hand, by inserting the kink solution (A.59) into Eq. (A.56), we obtain

$$\mathcal{L}_{\theta}^{\mathrm{opt}}[\theta_1] = -J_1(\boldsymbol{\nabla}\theta_1)^2 + \mathcal{O}\big(\boldsymbol{\nabla}^4\big) = -\frac{J}{2}(\boldsymbol{\nabla}\theta_1)^2 + \mathcal{O}\big(\boldsymbol{\nabla}^4\big), \tag{A.62}$$

which is identical to the single-component XY model (2.58). Compared to the case with no Rabi coupling or the single-component case described by Eq. (A.61), the effective phase stiffness in the Lagrangian (A.62) is modified as $J_1 \to 2J_1 = J$ due to the coupling between the two components through the sine-Gordon kink. This modification of the effective phase stiffness leads to the change of the NK RG equations (4.32) with a finite Rabi coupling. Indeed, with a finite Rabi coupling $\omega_{\mathrm{R}} > 0$, Eq. (A.62) is identical to the single-component XY model (2.58) and gives the identical NK RG equations (2.74) by following the same procedure in Sec. A.3.2. In the absence of the Rabi coupling $\omega_{\mathrm{R}} = 0$, on the other hand, the phase stiffness is halved as in Eq. (A.61) and consequently, the phase stiffness in the NK RG equations (4.32) are also halved.

Appendix B

Algebraic long-range order in two-dimensional Bose superfluids

In this Appendix, we explain the details of the calculation of the single-body density matrix in Eq. (2.78). Performing the Fourier transformation

$$\theta(\boldsymbol{r}) = \sum_{\boldsymbol{q}} \theta_{\boldsymbol{q}} e^{i\boldsymbol{q}\cdot\boldsymbol{r}}, \tag{B.1}$$

we can write the XY action in Eq. (2.58) as

$$S_{\mathrm{XY}}[\theta] = \frac{\hbar K}{2} \sum_{\boldsymbol{q}} q^2 \theta_{\boldsymbol{q}} \theta^*_{\boldsymbol{q}}. \tag{B.2}$$

The single-body density matrix in Eq. (2.77) can be evaluated as

$$\begin{aligned}
\rho_1(\boldsymbol{r},\boldsymbol{r}') &= n \left\langle e^{-i[\theta(\boldsymbol{r})-\theta(\boldsymbol{r}')]} \right\rangle_{\mathrm{XY}} \\
&= n \left\langle e^{-i\sum_{\boldsymbol{q}} \theta_{\boldsymbol{q}} \left(e^{i\boldsymbol{q}\cdot\boldsymbol{r}} - e^{i\boldsymbol{q}\cdot\boldsymbol{r}'}\right)} \right\rangle_{\mathrm{XY}} = n \left\langle e^{-i\sum_{\boldsymbol{q}} \tilde{\theta}_{\boldsymbol{q}} \left(e^{i\boldsymbol{q}\cdot\boldsymbol{R}} - 1\right)} \right\rangle_{\mathrm{XY}} \\
&= n \frac{\int \prod_{\boldsymbol{q}'} \mathrm{d}\tilde{\theta}_{\boldsymbol{q}'}\, \mathrm{d}\tilde{\theta}^*_{\boldsymbol{q}'}\, e^{-S_{\mathrm{XY}}[\theta]/\hbar} e^{-i\sum_{\boldsymbol{q}} \tilde{\theta}_{\boldsymbol{q}} \left(e^{i\boldsymbol{q}\cdot\boldsymbol{R}} - 1\right)}}{\int \prod_{\boldsymbol{q}'} \mathrm{d}\tilde{\theta}_{\boldsymbol{q}'}\, \mathrm{d}\tilde{\theta}^*_{\boldsymbol{q}'}\, e^{-S_{\mathrm{XY}}[\theta]/\hbar}}.
\end{aligned} \tag{B.3}$$

with $\tilde{\theta}_{\boldsymbol{q}} \equiv \theta_{\boldsymbol{q}} e^{i\boldsymbol{q}\cdot\boldsymbol{r}'}$ and $\boldsymbol{R} \equiv \boldsymbol{r} - \boldsymbol{r}'$. By performing the Gaussian integral in Eq. (B.3), the single-body density matrix reads

$$\rho_1(\boldsymbol{r},\boldsymbol{r}') = n \exp\left[\sum_{\boldsymbol{q}} \frac{\cos\left(\boldsymbol{q}\cdot\boldsymbol{R}\right) - 1}{K q^2}\right]. \tag{B.4}$$

Here, the wavenumber summation is expressed as

$$\sum_{\boldsymbol{q}} \frac{\cos\left(\boldsymbol{q}\cdot\boldsymbol{R}\right) - 1}{q^2} = \int_0^\infty \frac{\mathrm{d}q}{2\pi} \frac{1}{q} \int_0^{2\pi} \frac{\mathrm{d}\varphi}{2\pi} \left[\cos\left(qR\cos\varphi\right) - 1\right]. \tag{B.5}$$

For $qR < 1$, one can write $\cos(qR\cos\varphi) \simeq 1$. For $qR \gg 1$, $\cos(qR\cos\varphi)$ rapidly oscillates and can be negligible after summation. As a result, by introducing an ultraviolet cutoff R_c^{-1}, Eq. (B.5) can be evaluated as

$$\sum_{\boldsymbol{q}} \frac{\cos(\boldsymbol{q}\cdot\boldsymbol{R})-1}{q^2} \simeq \int_{R^{-1}}^{R_c^{-1}} \frac{\mathrm{d}q}{2\pi}\frac{1}{q} = \frac{1}{2\pi}\ln\left(\frac{R_c}{R}\right), \tag{B.6}$$

and we obtain

$$\rho_1(\boldsymbol{r},\boldsymbol{r}') = n\exp\left[\frac{1}{2\pi K}\ln\left(\frac{R_c}{R}\right)\right] = n\left(\frac{|\boldsymbol{r}-\boldsymbol{r}'|}{R_c}\right)^{-\eta(T)}, \tag{B.7}$$

with the exponent $\eta(T)$ given by Eq. (2.79).

Appendix C

Dimensional regularization

This Appendix summarizes the dimensional regularization used in Sec. 3.3. Within the mean-field level, we are usually free from any divergence, making the mean-field analysis easy. However, once we include quantum corrections, ultraviolet divergences frequently appear as in Sec. 3.3. To treat this problem, we employ the *dimensional regularization* developed by 't Hooft and Veltman [153]. Historically, in the one-loop calculations of Feynman diagrams, first Pauli and Villars invented a regularization procedure by adding regulators with a cutoff parameter to make the integrand decays faster with respect to the momentum. Gupta improved the Pauli-Villars regularization to preserve gauge invariance in Abelian gauge theory. However, this Pauli-Villars-Gupta regularization does not preserve gauge invariance of vector fields in non-Abelian gauge theory. 't Hooft and Veltman developed dimensional regularization preserving the gauge invariance in non-Abelian gauge theory [153].

Dimensional regularization exploits the analytic continuation of an integral extending the dimensions to complex. Let us remember the Gamma function

$$s^{-z} = \frac{1}{\Gamma(z)} \int_0^\infty \mathrm{d}t\, e^{-st} t^{z-1}, \tag{C.1}$$

for $s \neq 0$. Equation (C.1) is well-defined with

$$\mathrm{Re}[s] \geq 0, \qquad 0 < \mathrm{Re}[z] < 1. \tag{C.2}$$

If $\mathrm{Im}[s] \leq 0$, we can bend the integral path to the imaginary axis as

$$s^{-z} = \frac{i^z}{\Gamma(z)} \int_0^\infty \mathrm{d}t\, e^{-ist} t^{z-1}. \tag{C.3}$$

Now Eq. (C.3) no longer requires the condition $\mathrm{Re}[s] \geq 0$ and well-defined with $\mathrm{Im}[s] < 0$ and $\mathrm{Re}[z] > 0$.

To compute the quantum correction

$$F_{\mathrm{Q}} = \frac{1}{2} \sum_{\boldsymbol{p}} E_p = \frac{\Omega_D L^D}{2(2\pi)^D} \int_0^\infty \mathrm{d}p\, p^{D-1} \sqrt{\frac{p^2}{2m}\left(\frac{p^2}{2m} + 2\mu\right)}, \tag{C.4}$$

with $\mu = gn$ in Sec. 3.3, we introduce Euler's beta function defined by

$$B(x,y) = \int_0^\infty \mathrm{d}t\, \frac{t^{x-1}}{(1+t)^{x+y}} = \frac{\Gamma(x)\Gamma(y)}{\Gamma(x+y)}. \tag{C.5}$$

Then, Eq. (C.4) reads

$$F_\mathrm{Q} = \frac{L^D \Omega_D \mu}{2(2\pi)^D} \left(\frac{4m\mu}{\hbar^2}\right)^{D/2} B\left(\frac{D+1}{2}, -\frac{D+2}{2}\right). \tag{C.6}$$

Equation (C.6) involves $\Gamma(x)$ with $x < 0$ according to Eq. (C.5). Note that to obtain Eq. (C.6), the condition $\mathrm{Re}[-D/2 - 1] > 0$ is required. However, once we obtain the expression of Eq. (C.6), it gives us the extension to an arbitrary complex dimension D as long as it is a holomorphic function in terms of D. An important feature of dimensional regularization is that the divergence of the original momentum summation (C.4) is inherited to the isolated poles with respect to the dimension D. Indeed, $\Gamma(z)$ has isolated poles at $z = 0, -1, -2, \cdots$ and the infinite product representation

$$\frac{1}{\Gamma(z)} = z e^{\gamma z} \prod_{n=1}^\infty \left(1 + \frac{z}{n}\right) e^{-z/n}, \tag{C.7}$$

gives

$$\Gamma(-n+\varepsilon) = \frac{(-1)^n}{n!}\left[\frac{1}{\varepsilon} + \psi(n+1) + \mathcal{O}(\varepsilon)\right], \tag{C.8}$$

with $\varepsilon \ll 1$ and $\psi(z) \equiv \Gamma'(z)/\Gamma(z)$ being the digamma function. In particular, $\psi(1) = -\gamma$ where $\gamma = 0.5772\cdots$ is the Euler-Mascheroni constant.

For the three-dimensional case $D = 3$, Eq. (C.5) has no pole and Eq. (C.6) reads [154]

$$F_\mathrm{Q} = L^3 \frac{8}{15\pi^2} \left(\frac{m\mu}{\hbar^2}\right)^{3/2} \mu. \tag{C.9}$$

For the one-dimensional case $D = 1$ as well, Eq. (C.6) reads

$$F_\mathrm{Q} = -L \frac{2}{3\pi} \sqrt{\frac{m\mu}{\hbar^2}}\, \mu. \tag{C.10}$$

For the two-dimensional case $D = 2$, on the other hand, Eq. (C.5) has an isolated pole in $\Gamma(-2)$ and requires careful treatment with Eq. (C.8). To this end, we write Eq. (C.6) for $D = 2$ as

$$\frac{F_\mathrm{Q}}{L^2} = \frac{\kappa^\varepsilon \Omega_D \mu}{2(2\pi)^{D_-}} \left(\frac{4m\mu}{\hbar^2}\right)^{D_-/2} B\left(\frac{D_- + 1}{2}, -\frac{D_- + 2}{2}\right), \tag{C.11}$$

with κ being a regulator with the dimension of wavenumber and $D_- = D - \varepsilon = 2 - \varepsilon$. The expansion (C.8) and $x^\varepsilon = 1 + \varepsilon \ln x + \mathcal{O}(\varepsilon^2)$ give

$$\begin{aligned}
\frac{F_\mathrm{Q}}{L^2} &= -\frac{\mu}{2\sqrt{\pi}} \frac{m\mu}{\pi\hbar^2} \left[1 + \frac{\varepsilon}{2} \ln\left(\frac{\pi\hbar^2\kappa}{m\mu}\right) + \mathcal{O}(\varepsilon^2)\right] B\left(\frac{D_- + 1}{2}, -\frac{D_- + 2}{2}\right) \\
&= -\frac{m\mu^2}{4\pi\hbar^2} \left[\frac{1}{\varepsilon} + \frac{\ln 16 - 2\gamma - 1}{4} + \frac{1}{2} \ln\left(\frac{\pi\hbar^2\kappa^2}{m\mu}\right) + \mathcal{O}(\varepsilon)\right].
\end{aligned} \tag{C.12}$$

We perform *minimal subtraction* that subtracts the infinity $1/\varepsilon$ in $\varepsilon \to 0$ in Eq. (C.12). As a result, at zero temperature, the free energy in Eq. (3.32) is modified by the quantum correction as

$$\frac{F_0}{L^2} = \frac{\mu^2}{g} - \frac{m\mu^2}{8\pi\hbar^2} \ln\left(\frac{4\pi\hbar^2\kappa^2}{m\mu e^{2\gamma+1/2}}\right). \tag{C.13}$$

With $\kappa = 1/a_{2\mathrm{D}}$ and $\mu = gn$, Eq. (C.13) gives the 2D result in Eq. (3.34). The identical result can be obtained also through the renormalization of the coupling constant g, or the momentum-cutoff regularization [154].

Appendix D

Caldeira-Leggett model

This Appendix is devoted to the outline of the Caldeira-Leggett (CL) model, which describes the quantum Brownian motion [213]. It consists of a system coupled with a number of phonons. After the first analysis by Caldeira and Leggett in 1983, it has been applied to a variety range of physics such as SQUID [247].

The Hamiltonian of the CL model is given by

$$\hat{H}_{\rm CL} = \hat{H}_0 + \sum_n \left[\frac{\hat{p}_n^2}{2m} + \frac{m\omega_n^2}{2} \left(\hat{x}_n - \frac{\kappa_n}{m\omega_n^2} \hat{x} \right)^2 \right], \tag{D.1}$$

with

$$\hat{H}_0 = \frac{\hat{p}^2}{2M} + V(\hat{x}), \tag{D.2}$$

being the Hamiltonian of a particle subject to a potential $V(\hat{x})$ satisfying the canonical commutation relation $[\hat{x}, \hat{p}] = i\hbar$. In Eq. (D.1), κ_n represents the coupling strength between the particle and the n-th harmonic oscillator with the mass m and frequency ω_n in the thermal bath. The harmonic oscillators also satisfy the canonical commutation relation $[\hat{x}_n, \hat{p}_m] = i\hbar\delta_{n,m}$. One can decompose Eq. (D.1) into

$$\hat{H}_{\rm CL} = \hat{H}_0 + \hat{H}_{\rm int} + \hat{H}_{\rm B} + \hat{H}_{\rm c}, \tag{D.3}$$

with

$$H_{\rm int} = -\hat{x} \sum_n \kappa_n \hat{x}_n, \tag{D.4}$$

being the interaction term with the thermal bath described by

$$\hat{H}_{\rm B} = \sum_n \left(\frac{\hat{p}_n^2}{2m} + \frac{m\omega_n^2}{2} \hat{x}_n^2 \right). \tag{D.5}$$

The counter term $\hat{H}_{\rm c} = \hat{x}^2 \sum_n \kappa_n^2 / 2m\omega_n^2$ can be absorbed into the potential term as $V_{\rm c}(\hat{x}) = V(\hat{x}) + \hat{H}_{\rm c}$.

Heisenberg equations read

$$\frac{\mathrm{d}\hat{x}(t)}{\mathrm{d}t} = \frac{\hat{p}(t)}{M}, \quad \frac{\mathrm{d}\hat{p}(t)}{\mathrm{d}t} = -V_{\mathrm{c}}'(\hat{x}) + \sum_n \kappa_n \hat{x}_n(t), \tag{D.6}$$

$$\frac{\mathrm{d}\hat{x}_n(t)}{\mathrm{d}t} = \frac{\hat{p}_n(t)}{m}, \quad \frac{\mathrm{d}\hat{p}_n(t)}{\mathrm{d}t} = -m\omega_n^2 \hat{x}_n(t) + \kappa_n \hat{x}(t). \tag{D.7}$$

Equations (D.6) and (D.7) give

$$\begin{aligned}
\hat{x}_n(t) &= \hat{x}_n(0)\cos(\omega_n t) + \frac{\hat{p}_n(0)}{m\omega_n}\sin(\omega_n t) + \frac{\kappa_n}{m\omega_n}\int_0^t \mathrm{d}s\, \hat{x}(s)\sin[\omega_n(t-s)] \\
&= \hat{x}_n(0)\cos(\omega_n t) + \frac{\hat{p}_n(0)}{m\omega_n}\sin(\omega_n t) \\
&+ \frac{\kappa_n}{m\omega_n^2}\left[\hat{x}(t) - \cos(\omega_n t)\hat{x}(0) - \int_0^t \mathrm{d}s\, \frac{\hat{p}(s)}{M}\cos[\omega_n(t-s)]\right].
\end{aligned} \tag{D.8}$$

Inserting Eq. (D.8) into Eqs. (D.6), we can obtain the quantum Langevin equation

$$\frac{\mathrm{d}\hat{p}(t)}{\mathrm{d}t} + \int_0^t \mathrm{d}s\, \Gamma(t-s)\frac{\hat{p}(s)}{M} + V'(\hat{x}) = \hat{\xi}(t) - \Gamma(t)\hat{x}(0), \tag{D.9}$$

where

$$\Gamma(t) = \sum_n \frac{\kappa_n^2}{m\omega_n^2}\cos(\omega_n t), \tag{D.10}$$

is the damping kernel and

$$\hat{\xi}(t) = \sum_n \kappa_n \left[\hat{x}_n(0)\cos(\omega_n t) + \frac{\hat{p}_n(0)}{m\omega_n}\sin(\omega_n t)\right], \tag{D.11}$$

is the stochastic noise. The second term in the right-hand-side of Eq. (D.9) is the initial slippage term and negligible apart from $t = 0$ if $\Gamma(t)$ decays fast enough.

By assuming the initial thermal equilibrium of the bath with temperature T and denoting the thermal average with $\hat{H}_{\mathrm{B}}$ as $\langle\cdots\rangle_{\mathrm{B}}$, Eq. (D.11) provides

$$\langle\hat{\xi}(t)\rangle_{\mathrm{B}} = 0, \tag{D.12}$$

$$\chi(t) = \frac{1}{2}\langle\{\hat{\xi}(t), \hat{\xi}(0)\}\rangle_{\mathrm{B}} = \sum_n \frac{\kappa_n^2}{2m\omega_n}\coth\left(\frac{\hbar\omega_n}{2k_{\mathrm{B}}T}\right)\cos(\omega_n t). \tag{D.13}$$

Introducing a spectral density

$$J(\omega) = \sum_n \frac{\kappa_n^2}{2m\omega_n}\delta(\omega - \omega_n), \tag{D.14}$$

one can write Eqs. (D.10) and (D.13) as

$$\Gamma(t) = 2\int_0^\infty \mathrm{d}\omega\, \frac{J(\omega)}{\omega}\cos(\omega t), \tag{D.15}$$

$$\chi(t) = \hbar\int_0^\infty \mathrm{d}\omega\, J(\omega)\coth\left(\frac{\hbar\omega}{2k_\mathrm{B}T}\right)\cos(\omega t). \tag{D.16}$$

The Fourier transformations of Eqs. (D.15) and (D.16) lead to the second FDT

$$\tilde{\chi}(\omega) = \frac{\hbar\omega}{2}\coth\left(\frac{\hbar\omega}{2k_\mathrm{B}T}\right)\tilde{\Gamma}(\omega). \tag{D.17}$$

In the classical limit $\hbar\omega/k_\mathrm{B}T \to 0$, one recovers the classical FDT

$$\tilde{\chi}(\omega) = k_\mathrm{B}T\tilde{\Gamma}(\omega). \tag{D.18}$$

In particular, with an Ohmic spectral density

$$J(\omega) = \frac{\gamma}{\pi}\omega, \tag{D.19}$$

the damping kernel (D.15) reduces to

$$\Gamma(t) = 2\gamma\delta(t), \tag{D.20}$$

which is Markovian without memory effects. The quantum Langevin equation (D.9) reduces to

$$\frac{\mathrm{d}\hat{p}(t)}{\mathrm{d}t} + \gamma\frac{\hat{p}(t)}{M} + V'(\hat{x}) = \hat{\xi}(t) - 2\gamma\delta(t)\hat{x}(0), \tag{D.21}$$

where the noise in the classical limit reduces to

$$\chi(t) = 2\gamma k_\mathrm{B}T\delta(t). \tag{D.22}$$

In general, the damping kernel (D.15) is non-local in time, which makes the quantum Langevin equation non-Markovian with memory effects.

Appendix E

Alternative derivation of quantum correction to Josephson frequency

In this Appendix, we give the Hamiltonian description of the phase dynamics in Sec. 5.4, and provide another approach to obtain the one-loop correction to the Josephson frequency (5.102) derived through effective action formalism in Sec. 5.4.

E.1 Hamiltonian and phase wavefunction

The term $\hbar N z\dot{\phi}/2$ in the relative Lagrangian (5.76) implies that the phase $\phi(t)$ and the population imbalance $z(t)$ are canonically conjugated allowing us to introduce canonical momentum

$$p_\phi = \frac{\hbar N}{2} z, \tag{E.1}$$

and the Hamiltonian reads

$$H = p_\phi \dot{\phi} - L[\phi, z] = \frac{U}{\hbar^2} p_\phi^2 - \frac{JN}{2}\sqrt{1 - \frac{4}{\hbar^2 N^2} p_\phi^2}\cos\phi, \tag{E.2}$$

which is the Hamiltonian of a nonrigid pendulum [248]. The Hamilton equations give Eqs. (5.77).

For the phase action (5.87), the Lagrangian is

$$L_0[\phi] = \frac{N\hbar^2 \dot{\phi}^2}{4\left(UN + J\cos\phi\right)} + \frac{JN}{2}\cos\phi, \tag{E.3}$$

and the canonical momentum reads

$$p_\phi = \frac{\partial L_0}{\partial \dot{\phi}} = \frac{N\hbar^2}{2\left(UN + J\cos\phi\right)}\dot{\phi}. \tag{E.4}$$

Then, the phase Hamiltonian is given by

$$H_0 = \frac{UN + J\cos\phi}{\hbar^2 N} p_\phi^2 - \frac{JN}{2}\cos\phi. \tag{E.5}$$

Equation (E.5) can be obtained by expanding Eq. (E.2) up to the quadratic level of p_ϕ.

First quantization $p_\phi \to \hat{p}_\phi = -i\hbar\partial_\phi$ allows us to obtain the time-dependent Schrödinger equation

$$i\hbar\partial_t \Psi(\phi, t) = \hat{H}_0 \Psi(\phi, t), \tag{E.6}$$

with the phase wavefunction $\Psi(\phi, t)$ and

$$\hat{H}_0 = -\left(U + \frac{J}{N}\cos\phi\right)\partial_\phi^2 - \frac{JN}{2}\cos\phi. \tag{E.7}$$

This quantized Hamiltonian (E.7) is related to the phase action (5.87) as

$$\langle\phi_{\rm f}|\, e^{-i\hat{H}_0(t_{\rm f}-t_{\rm i})/\hbar}\,|\phi_{\rm i}\rangle = \int \mathcal{D}\phi\mathcal{D}p_\phi\, e^{i\int_{t_{\rm i}}^{t_{\rm f}} {\rm d}t\left[p_\phi\dot{\phi} - H_0\right]/\hbar} = \int \mathcal{D}\phi\, e^{iS_0[\phi]/\hbar}. \tag{E.8}$$

E.2 Alternative derivation of one-loop correction

In this section, we provide an alternative derivation of the one-loop correction to the Josephson frequency obtained in Eq. (5.102) through equations of motion. This approach is analogous to the one developed recently to determine beyond-mean-field corrections to the critical temperature in two-band superconductors [249]. The equation of motion derived from Eq. (5.90) reads

$$M_{\rm J}\ddot{\phi} + M_{\rm J}\Omega_{\rm J}^2 \sin\phi = 0. \tag{E.9}$$

Then, we decompose the phase field into the mean-field part $\phi_0(t)$ and the small fluctuation part $\tilde{\phi}(t)$ encoding quantum fluctuations as

$$\phi(t) = \phi_0(t) + \tilde{\phi}(t). \tag{E.10}$$

Up to the quadratic level of $\tilde{\phi}(t)$, Eq. (E.9) gives

$$M_{\rm J}\ddot{\phi}_0 + M_{\rm J}\ddot{\tilde{\phi}} + M_{\rm J}\Omega_{\rm J}^2\left(1 - \frac{\tilde{\phi}^2}{2}\right)\sin\phi_0 + M_{\rm J}\Omega_{\rm J}^2\tilde{\phi}\cos\phi_0 = 0. \tag{E.11}$$

We consider performing an ensemble average with respect to $\tilde{\phi}$ defined by

$$\langle O\rangle = \frac{1}{Z}\int \mathcal{D}\tilde{\phi}\, O[\tilde{\phi}]\, e^{iS_{\rm J}^{(\rm quad)}[\tilde{\phi}]/\hbar}, \tag{E.12}$$

with

$$S_{\rm J}^{(\rm quad)}[\tilde{\phi}] = \int {\rm d}t\left(\frac{M_{\rm J}}{2}\dot{\tilde{\phi}}^2 - \frac{M_{\rm J}\Omega_{\rm J}^2}{2}\tilde{\phi}^2\right), \tag{E.13}$$

being the quadratic Josephson action in terms of $\tilde{\phi}$ and $Z = \int \mathcal{D}\tilde{\phi}\, e^{iS_{\rm J}^{(\rm quad)}[\tilde{\phi}]/\hbar}$. Performing the ensemble average, one obtains

$$\langle\tilde{\phi}\rangle = 0, \qquad \langle\tilde{\phi}^2\rangle = \sqrt{\frac{U}{JN}}, \tag{E.14}$$

and Eq. (E.11) yields

$$M_{\mathrm{J}}\ddot{\phi}_0 + M_{\mathrm{J}}\Omega_{\mathrm{J}}^2\left(1 - \frac{1}{2}\sqrt{\frac{U}{JN}}\right)\sin\phi_0 = 0. \tag{E.15}$$

Compared with Eq. (E.9), Eq. (E.15) indicates that the Josephson frequency Ω_{J} is modified to Eq. (5.102). Consequently, we have verified our result of Eq. (5.102) obtained via effective action formalism. We considered the ensemble average with respect to the quadratic action (E.13), which requires that the quartic and higher-order contributions are negligible. It corresponds to the condition (5.99) required from the validity of the second-order derivative expansion in the effective action in Sec. 5.4.3, and the other condition (5.100) follows as well.

Bibliography

[1] P. Kapitza, Viscosity of Liquid Helium below the λ-Point, Nature **141**, 74 (1938).

[2] J. F. Allen and A. D. Misener, Flow of Liquid Helium II, Nature **141**, 75 (1938).

[3] L. Tisza, Transport Phenomena in Helium II, Nature **141**, 913 (1938).

[4] L. D. Landau, Two-fluid model of liquid helium. II, J. Phys. **5**, 71 (USSR) (1941).

[5] L. D. Landau and E. M. Lifshitz, *Fluid Mechanics* (Pergamon, Oxford, U.K., 1987).

[6] S. Balibar, The Discovery of Superfluidity, J. Low Temp. Phys. **146**, 441-470 (2007).

[7] S. Balibar, Laszlo Tisza and the two-fluid model of superfluidity, Comptes Rendus Physique **18**, 586-591 (2017).

[8] S. N. Bose, Plancks Gesetz und Lichtquantenhypothese, Z. Phys. **26**, 178 (1924).

[9] A. Einstein, Quantentheorie des einatomigen idealen Gases, Ber. Berl. Akad. 261 (1924); 3 (1925).

[10] F. London, The λ-Phenomenon of Liquid Helium and the Bose-Einstein Degeneracy, Nature **141**, 643 (1938).

[11] M. H. Anderson, J. R. Ensher, M. R. Matthews, C. E. Wieman, and E. A. Cornell, Observation of Bose-Einstein Condensation in a Dilute Atomic Vapor, Science **269**, 198 (1995).

[12] K. B. Davis, M. O. Mewes, M. R. Andrews, N. J. van Druten, D. S. Durfee, D. M. Kurn, and W. Ketterle, Bose-Einstein Condensation in a Gas of Sodium Atoms, Phys. Rev. Lett. **75**, 3969 (1995).

[13] D. S. Jin, J. R. Ensher, M. R. Matthews, C. E. Wieman, and E. A. Cornell, Collective Excitations of a Bose-Einstein Condensate in a Dilute Gas, Phys. Rev. Lett. **77**, 420 (1996).

[14] J. Kasprzak, M. Richard, S. Kundermann, A. Baas, P. Jeambrun, J. M. J. Keeling, F. M. Marchetti, M. H. Szymańska, R. André, J. L. Staehli, V. Savona, P. B. Littlewood, B. Deveaud, and L. S. Dang, Bose-Einstein condensation of exciton polaritons, Nature (London) **443**, 409 (2006).

[15] A. Amo, J. Lefrère, S. Pigeon, C. Adrados, C. Ciuti, I. Carusotto, R. Houdré, E. Giacobino, and A. Bramati, Superfluidity of polaritons in semiconductor microcavities, Nat. Phys. **5**, 805-810 (2009).

[16] I. Carusotto and C. Ciuti, Quantum fluids of light, Rev. Mod. Phys. **85**, 299 (2013).

[17] D. Sanvitto and S. Kéna-Cohen, The road towards polaritonic devices, Nat. Mater. **15**, 1061 (2016).

[18] M. Yamaguchi and T. Ogawa, *Equilibrium to Nonequilibrium Condensation in Driven-Dissipative Semiconductor Systems, in Principles and Methods of Quantum Information Technologies*, Lecture Notes in Physics, edited by Y. Yamamoto and K. Semba (Springer Japan, Tokyo, 2016).

[19] G. E. Volovik, *The Universe in a Helium Droplet* (Oxford University Press, New York, 2003).

[20] M. Sato and Y. Ando, Topological superconductors: a review, Rep. Prog. Phys. **80**, 076501 (2017).

[21] D. Fausti, R. I. Tobey, N. Dean, S. Kaiser, A. Dienst, M. C. Hoffmann, S. Pyon, T. Takayama, H. Takagi, and A. Cavalleri, Light-Induced Superconductivity in a Stripe-Ordered Cuprate, Science **331**, 189 (2011).

[22] M. Mitrano, A. Cantaluppi, D. Nicoletti, S. Kaiser, A. Perucchi, S. Lupi, P. Di Pietro, D. Pontiroli, M. Riccò, S. R. Clark, D. Jaksch, and A. Cavalleri, Possible light-induced superconductivity in K_3C_{60} at high temperature, Nature **530**, 461 (2016).

[23] M. Köhl, H. Moritz, T. Stöferle, K. Günter, and T. Esslinger, Fermionic Atoms in a Three Dimensional Optical Lattice: Observing Fermi Surfaces, Dynamics, and Interactions, Phys. Rev. Lett. **94**, 080403 (2005).

[24] M. Horikoshi, S. Nakajima, M. Ueda, and T. Mukaiyama, Measurement of Universal Thermodynamic Functions for a Unitary Fermi Gas, Science **327**, 442 (2010).

[25] M. J. H. Ku, A. T. Sommer, L. W. Cheuk, and M. W. Zwierlein, Revealing the Superfluid Lambda Transition in the Universal Thermodynamics of a Unitary Fermi Gas, Science **335**, 563 (2012).

[26] C. J. Pethick and H. Smith, *Bose-Einstein Condensation in Dilute Gases* (Cambridge University Press, Cambridge, 2008).

[27] D. M. Bauer, M. Lettner, C. Vo, G. Rempe, and S. Dürr, Control of a magnetic Feshbach resonance with laser light, Nat. Phys. **5**, 339-342 (2009).

[28] C. A. Regal, M. Greiner, and D. S. Jin, Observation of Resonance Condensation of Fermionic Atom Pairs, Phys. Rev. Lett. **92**, 040403 (2004).

[29] M. W. Zwierlein, C. A. Stan, C. H. Schunck, S. M. F. Raupach, A. J. Kerman, and W. Ketterle, Condensation of Pairs of Fermionic Atoms near a Feshbach Resonance, Phys. Rev. Lett. **92**, 120403 (2004).

[30] L. D. Carr, C. W. Clark, and W. P. Reinhardt, Stationary solutions of the one-dimensional nonlinear Schrödinger equation. II. Case of attractive nonlinearity, Phys. Rev. A **62**, 063611 (2000).

[31] H. E. Nistazakis, D. J. Frantzeskakis, and B. A. Malomed, Collisions between spatiotemporal solitons of different dimensionality in a planar waveguide, Phys. Rev. E **64**, 026604 (2001).

[32] R. Kanamoto, H. Saito, and M. Ueda, Quantum phase transition in one-dimensional Bose-Einstein condensates with attractive interactions, Phys. Rev. A **67**, 013608 (2003).

[33] L. Amico, A. Osterloh, F. Cataliotti, Quantum Many Particle Systems in Ring-Shaped Optical Lattices, Phys. Rev. Lett. **95**, 063201 (2005).

[34] M. Crosta, A. Fratalocchi, and S. Trillo, Bistability and instability of dark-antidark solitons in the cubic-quintic nonlinear Schrödinger equation, Phys. Rev. A **84**, 063809 (2011).

[35] M. Cominotti, D. Rossini, M. Rizzi, F. Hekking, and A. Minguzzi, Optimal Persistent Currents for Interacting Bosons on a Ring with a Gauge Field, Phys. Rev. Lett. **113**, 025301 (2014).

[36] L. Salasnich, Bright solitons in ultracold atoms, Opt. Quant. Electron. **49**, 409 (2017).

[37] A. Tononi, Y. Wang, and L. Salasnich, Quantum solitons in spin-orbit-coupled Bose-Bose mixtures, Phys. Rev. A **99**, 063618 (2019).

[38] R. Ravisankar, T. Sriraman, L. Salasnich, and P. Muruganandam, Quenching dynamics of the bright solitons and other localized states in spin-orbit coupled Bose-Einstein condensates, J. Phys. B: At. Mol. Opt. Phys. **53**, 195301 (2020).

[39] A. Cidrim, L. Salasnich, and T. Macrì, Soliton trains after interaction quenches in Bose mixtures, New J. Phys. **23**, 023022 (2021).

[40] K. Furutani and L. Salasnich, Superfluid properties of bright solitons in a ring, Phys. Rev. A **105**, 033320 (2022).

[41] M. Gring, M. Kuhnert, T. Langen, T. Kitagawa, B. Rauer, M. Schreitl, I. Mazets, D. Adu Smith, E. Demler, and J. Schmiedmayer, Relaxation and Prethermalization in an Isolated Quantum System, Science **33**, 1318 (2012).

[42] M. Pigneur, T. Berrada, M. Bonneau, T. Shumm, E. Demler, and J. Schmiedmayer, Relaxation to a Phase-Locked Equilibrium State in a One-Dimensional Bosonic Josephson Junction, Phys. Rev. Lett. **120**, 173601 (2018).

[43] M. Greiner, O. Mandel, T. Esslinger, T. W. Hänsch, and I. Bloch, Quantum phase transition from a superfluid to a Mott insulator in a gas of ultracold atoms, Nature **415**, 39-44 (2002).

[44] R. Hanai, A. Edelman, Y. Ohashi, and P. B. Littlewood, Non-Hermitian Phase Transition from a Polariton Bose-Einstein Condensate to a Photon Laser, Phys. Rev. Lett. **122**, 185301 (2019).

[45] D. D. Osheroff, R. C. Richardson, and D. M. Lee, Evidence for a New Phase of Solid ^{3}He, Phys. Rev. Lett. **28**, 885 (1972).

[46] D. L. Stein and M. C. Cross, Phase Transitions in Two-Dimensional Superfluid ^{3}He, Phys. Rev. Lett. **42**, 504 (1979).

[47] D. Vollhardt and P. Wölfle, *The Superfluid Phases of Helium 3* (Taylor & Francis, 1990).

[48] A. F. Andreev and E. P. Bashkin, Three-velocity hydrodynamics of superfluid solutions, Zh. Eksp. Teor. Fiz. **69**, 319 (1975) [Sov. Phys. JETP **42**, 164 (1975)].

[49] D. V. Fil and S. I. Shevchenko, Nondissipative drag of superflow in a two-component Bose gas, Phys. Rev. A **72**, 013616 (2005).

[50] B. Svistunov, E. Babaev, and N. Prokof'ev, *Superfluid States of Matter* (Boca Raton: CRC Press, 2015).

[51] J. Nespolo, G. E. Astrakharchik, and A. Recati, Andreev- Bashkin effect in superfluid cold gases mixtures, New J. Phys. **19**, 125005 (2017).

[52] P. Konietin and V. Pastukhov, 2D dilute Bose mixture at low temperatures, J. Low Temp. Phys. **190**, 256 (2018).

[53] V. Karle, N. Defenu, and T. Enss, Coupled superfluidity of binary Bose mixtures in two dimensions, Phys. Rev. A **99**, 063627 (2019).

[54] J. H. Kim, D. Hong, and Y. Shin, Observation of two sound modes in a binary superfluid gas, Phys. Rev. A **101**, 061601(R) (2020).

[55] D. Romito, C. Lobo, and A. Recati, Linear response study of collisionless spin drag, Phys. Rev. Research **3**, 023196 (2021).

[56] E. J. Mueller and T.-L. Ho, Two-Component Bose-Einstein Condensates with a Large Number of Vortices, Phys. Rev. Lett. **88**, 180403 (2002).

[57] K. Kasamatsu, M. Tsubota, and M. Ueda, Vortex Phase Diagram in Rotating Two-Component Bose-Einstein Condensates, Phys. Rev. Lett. **91**, 150406 (2003).

[58] K. Kasamatsu, M. Tsubota, and M. Ueda, Vortex Molecules in Coherently Coupled Two-Component Bose-Einstein Condensates, Phys. Rev. Lett. **93**, 250406 (2004).

[59] K. Kasamatsu, M. Tsubota, and M. Ueda, Vortices in Multicomponent Bose-Einstein Condensates, Int. J. Mod. Phys. B **19**, 1835 (2005).

[60] K. Kasamatsu and M. Tsubota, Vortex sheet in rotating two-component Bose-Einstein condensates, Phys. Rev. A **79**, 023606 (2009).

[61] M. Eto, K. Kasamatsu, M. Nitta, H. Takeuchi, and M. Tsubota, Interaction of half-quantized vortices in two-component Bose-Einstein condensates, Phys. Rev. A **83**, 063603 (2011).

[62] A. Aftalion, P. Mason, and J. Wei, Vortex-peak interaction and lattice shape in rotating two-component Bose-Einstein condensates, Phys. Rev. A **85**, 033614 (2012).

[63] P. Kuopanportti, J. A. M. Huhtamäki, and M. Möttönen, Exotic vortex lattices in two-species Bose-Einstein condensates, Phys. Rev. A **85**, 043613 (2012).

[64] M. Eto and M. Nitta, Vortex trimer in three-component Bose- Einstein condensates, Phys. Rev. A **85**, 053645 (2012).

[65] M. Eto and M. Nitta, Vortex graphs as N-omers and $\mathbb{C}P^{N-1}$ skyrmions in N-component Bose-Einstein condensates, Europhys. Lett. **103**, 60006 (2013).

[66] M. Cipriani and M. Nitta, Crossover between integer and fractional vortex lattices in coherently coupled two-component Bose-Einstein condensates, Phys. Rev. Lett. **111**, 170401 (2013).

[67] M. Cipriani and M. Nitta, Vortex lattices in three-component Bose-Einstein condensates under rotation: Simulating colorful vortex lattices in a color superconductor, Phys. Rev. A **88**, 013634 (2013).

[68] D. S. Dantas, A. R. P. Lima, A. Chaves, C. A. S. Almeida, G. A. Farias, and M. V. Milosĕvić, Bound vortex states and exotic lattices in multicomponent Bose-Einstein condensates: The role of vortex-vortex interaction, Phys. Rev. A **91**, 023630 (2015).

[69] K. Kasamatsu, M. Eto, and M. Nitta, Short-range intervortex interaction and interacting dynamics of half-quantized vortices in two-component Bose-Einstein condensates, Phys. Rev. A **93**, 013615 (2016).

[70] M. Tylutki, L. P. Pitaevskii, A. Recati, and S. Stringari, Confinement and precession of vortex pairs in coherently coupled Bose-Einstein condensates, Phys. Rev. A **93**, 043623 (2016).

[71] M. Eto and M. Nitta, Confinement of half-quantized vortices in coherently coupled Bose-Einstein condensates: Simulating quark confinement in a QCD-like theory, Phys. Rev. A **97**, 023613 (2018).

[72] B. M. Uranga and A. Lamacraft, Infinite lattices of vortex molecules in Rabi-coupled condensates, Phys. Rev. A **97**, 043609 (2018).

[73] M. Kobayashi, M. Eto, M. Nitta, Berezinskii-Kosterlitz-Thouless Transition of Two-Component Bose Mixtures with Intercomponent Josephson Coupling, Phys. Rev. Lett. **123**, 075303 (2019).

[74] M. Eto, K. Ikeno and M. Nitta, Collision dynamics and reactions of fractional vortex molecules in coherently coupled Bose-Einstein condensates, Phys. Rev. Research **2**, 033373 (2020).

[75] K. Yagi, T. Hatsuda, and Y. Miake, *Quark-Gluon Plasma* (Cambridge University Press, Cambridge, 2005).

[76] H. Tajima, S. Tsutsui, T. M. Doi, and K. Iida, Cooper triples in attractive three-component fermions: Implication for hadron quark crossover, Phys. Rev. Research, **4**, L012021 (2022).

[77] S. Akagami, H. Tajima, and K. Iida, Possible Condensation of Cooper Triples, JPS Conf. Proc. **38**, 011010 (2023).

[78] H. Tajima, S. Tsutsui, T. M. Doi, and K. Iida, Density-Induced Hadron-Quark Crossover via the Formation of Cooper Triples, Symmetry **15**, 333 (2023).

[79] E. R. Elliott, D. C. Aveline, N. P. Bigelow, P. Boegel, S. Botsi, E. Charron, J. P. D ' Incao, P. Engels, T. Estrampes, N. Gaaloul, J. R. Kellogg, J. M. Kohel, N. E. Lay, N. Lundblad, M. Meister, M. E. Mossman, G. Müller, H. Müller, K. Oudrhiri, L. E. Phillips, A. Pichery, E. M. Rasel, C. A. Sackett, M. Sbroscia, W. P. Schleich, R. J. Thompson, J. R. Williams, Quantum Gas Mixtures and Dual-Species Atom Interferometry in Space, arXiv:2306.15223.

[80] T. van Zoest, N. Gaaloul, Y. Singh, H. Ahlers, W. Herr, S. T. Seidel, W. Ertmer, E. Rasel, M. Eckart, E. Kajari, S. Arnold, G. Nandi, W. P. Schleich, R. Walser, A. Vogel, K. Sengstock, K. Bongs, W. Lewoczko-Adamczyk, M. Schiemangk, T. Schuldt, A. Peters, T. Könemann, H. Müntinga, C. Lämmerzahl, H. Dittus, T. Steinmetz, T. W. Hänsch, J. Reichel, Bose-Einstein Condensation in Microgravity, Science **328**, 1540 (2010).

[81] E. R. Elliott, M. C. Krutzik, J. R. Williams, J. R. Thompson, and D. C. Aveline, NASA's Cold Atom Lab (CAL): system development and ground test status, npj Microgravity **4**, 16 (2018).

[82] N. Lundblad, R. A. Carollo, C. Lannert, M. J. Gold, X. Jiang, D. Paseltiner, N. Sergay, and D. C. Aveline, Shell potentials for microgravity Bose-Einstein condensates, npj Microgravity **5**, 30 (2019).

[83] G. Condon, M. Rabault, B. Barrett, L. Chichet, R. Arguel, H. Eneriz-Imaz, D. Naik, A. Bertoldi, B. Battelier, P. Bouyer, and A. Landragin, All-Optical Bose-Einstein Condensates in Microgravity, Phys. Rev. Lett. **123**, 240402 (2019).

[84] A. Tononi, F. Cinti, and L. Salasnich, Quantum Bubbles in Microgravity, Phys. Rev. Lett. **125**, 010402 (2020).

[85] D. C. Aveline, J. R. Williams, E. R. Elliott, C. Dutenhoffer, J. R. Kellogg, J. M. Kohel, N. E. Lay, K. Oudrhiri, R. F. Shotwell, N. Yu, and R. J. Thompson, Observation of Bose-Einstein condensates in an Earth-orbiting research lab, Nature **582**, 193-197 (2020).

[86] K. Frye *et al.*, The Bose-Einstein Condensate and Cold Atom Laboratory, EPJ Quant. Technol. **8**, 1 (2021).

[87] R. A. Carollo, D. C. Aveline, B. Rhyno, S. Vishveshwara, C. Lannert, J. D. Murphree, E. R. Elliott, J. R. Williams, R. J. Thompson, and N. Lundblad, Observation of ultracold atomic bubbles in orbital microgravity, Nature **606**, 281-286 (2022).

[88] R. J. Thompson, D. Aveline, S. W. Chiow, E. R. Elliott, J. R. Kellogg, J. M. Kohel, M. S. Sbroscia, L. Phillips, C. Schneider, J. R. Williams, N. Bigelow, P. Engels, N. Lundblad, C. A. Sackett, and L. Woerner, Exploring the quantum world with a third generation ultra-cold atom facility, Quantum Sci. Technol. **8**, 014007 (2023).

[89] A. Tononi and L. Salasnich, Low-dimensional quantum gases in curved geometries, Nat. Rev. Phys. **5**, 398-405 (2023).

[90] K. Furutani, A. Tononi, and L. Salasnich, Sound modes in collisional superfluid Bose gases, New. J. Phys. **23**, 043043 (2021).

[91] K. Furutani, A. Perali, and L. Salasnich, Berezinskii-Kosterlitz-Thouless phase transition with Rabi coupled bosons, Phys. Rev. A **107**, L041302 (2023).

[92] F. Binanti, K. Furutani, and L. Salasnich, Dissipation and fluctuations in elongated bosonic Josephson junctions, Phys. Rev. A **103**, 063309 (2021).

[93] K. Furutani and L. Salasnich, Quantum and thermal fluctuations in the dynamics of a resistively and capacitively shunted Josephson junction, Phys. Rev. B **104**, 014519 (2021).

[94] K. Furutani, J. Tempere, and L. Salasnich, Quantum effective action for the bosonic Josephson junction, Phys. Rev. B **105**, 134510 (2022).

[95] O. Penrose and L. Onsager, Bose-Einstein Condensation and Liquid Helium, Phys. Rev. **104**, 576 (1956).

[96] N. D. Mermin and H. Wagner, Absence of Ferromagnetism or Antiferromagnetism in One- or Two-Dimensional Isotropic Heisenberg Models, Phys. Rev. Lett. **17**, 1133 (1966).

[97] P. C. Hohenberg, Existence of Long-Range Order in One and Two Dimensions, Phys. Rev. **158**, 383 (1967).

[98] E. P. Gross, Structure of a quantized vortex in boson systems, Nuovo Cimento **20**, 454 (1961).

[99] L. P. Pitaevskii, Vortex lines in an imperfect Bose gas, Sov. Phys. JETP **13**, 451 (1961).

[100] F. London, *Superfluids*, John Wiley (1954).

[101] R. P. Feynman, Application of quantum mechanics to liquid helium, Progress in Low Temperature Physics, vol. 1 North-Holland 16 (1955).

[102] W. F. Vinen, The detection of single quanta circulation in liquid helium II, Proc. Roy. Soc. London A, **260**, 218 (1961).

[103] N. Manton and P. Sutcliffe, *Topological Solitons* (Cambridge University Press, Cambridge, 2004).

[104] T. Ellis and P. V. E. McClintock, The Breakdown of Superfluidity in Liquid ^{4}He V. Measurement of the Landau Critical Velocity for Roton Creation, Phil. Trans. Roy. Soc. A **315**, 259 (1985).

[105] V. L. Berezinskii, Destruction of Long-range Order in One-dimensional and Two-dimensional Systems Possessing a Continuous Symmetry Group. II. Quantum Systems, Sov. Phys. JETP **34**, 610 (1972).

[106] J. M. Kosterlitz and D. J. Thouless, Ordering, metastability and phase transitions in two-dimensional systems, J. Phys. C: Solid State Phys. **6**, 1181 (1973).

[107] D. R. Nelson and J. M. Kosterlitz, Universal Jump in the Superfluid Density of Two-Dimensional Superfluids, Phys. Rev. Lett. **39**, 1201 (1977).

[108] J. W. Kane and L. P. Kadanoff, Long-range order in superfluid helium, Phys. Rev. **155**, 80 (1967).

[109] J. R. Clow and J. D. Reppy, Temperature dependence of superfluid critical velocities near T_λ, Phys. Rev. Lett. **19**, 291 (1967).

[110] G. Kukich, R. P. Henkel, and J. D. Reppy, Decay of Superfluid "Persistent Currents " , Phys. Rev. Lett. **21**, 197 (1968).

[111] D. J. Amit, Phase transition in HeII films, Phys. Lett. A **26**, 448 (1968); New form for the thermodynamic potential of HeII near T_λ, **26**, 466 (1968).

[112] R. S. Kagiwada, J. C. Fraser, I. Rudnick, and D. Bergman, Superflow in Helium films: third sound measurements, Phys. Rev. Lett. **22**, 338 (1969).

[113] R. P. Henkel, E. N. Smith, and J. D. Reppy, Temperature dependence of the superfluid healing length, Phys. Rev. Lett. **23**, 1276 (1969).

[114] M. Chester, L. C. Yang, and J. B. Stephens, Quartz microbalance studies of an adsorbed Helium film, Phys. Rev. Lett. **29**, 211 (1972).

[115] M. Chester and L. C. Yang, Superfluid fraction in thin Helium films, Phys. Rev. Lett. **31**, 1377 (1973).

[116] M. H. W. Chan, A. W. Yanof, and J. D. Reppy, Superfluidity of thin ^{4}He films, Phys. Rev. Lett. **32**, 1347 (1974).

[117] J. E. Berthold, D. J. Bishop, and J. D. Reppy, Superfluid Transition of ^{4}He Films Adsorbed on Porous Vycor Glass, Phys. Rev. Lett. **39**, 348 (1977).

[118] D. J. Bishop and J. D. Reppy, Study of the Superfluid Transition in Two-Dimensional ^{4}He Films, Phys. Rev. Lett. **40**, 1727 (1978).

[119] D. J. Bishop and J. D. Reppy, Study of the superfluid transition in two-dimensional ^{4}He films, Phys. Rev. B **22**, 5171 (1980).

[120] D. J. Bishop, J. E. Berthold, J. M. Parpia, and J. D. Reppy, Superfluid density of thin ^{4}He films adsorbed in porous Vycor glass, Phys. Rev. B **24**, 5047 (1981).

[121] V. Kotsubo and G. A. Williams, Kosterlitz-Thouless Superfluid Transition for Helium in Packed Powders, Phys. Rev. Lett. **53**, 691 (1984).

[122] P. Minnhagen, The two-dimensional Coulomb gas, vortex unbinding, and superfluid-superconducting films, Rev. Mod. Phys. **59**, 1001 (1987).

[123] G. Agnolet, D. F. McQueeney, and J. D. Reppy, Kosterlitz-Thouless transition in helium films, Phys. Rev. B **39**, 8934 (1989).

[124] Z. Hadzibabic, P. Krüger, M. Cheneau, B. Battelier, and J. Dalibard, Berezinskii-Kosterlitz-Thouless crossover in a trapped atomic gas, Nature **441**, 1118 (2006).

[125] P. Cladé, C. Ryu, A. Ramanathan, K. Helmerson, and W. D. Phillips, Observation of a 2D Bose gas: from thermal to quasicondensate to superfluid, Phys. Rev. Lett. **102**, 170401 (2009).

[126] S. Tung, G. Lamporesi, D. Lobser, L. Xia, and E. A. Cornell, Observation of the presuperfluid regime in a two-dimensional Bose gas, Phys. Rev. Lett. **105**, 230408 (2010).

[127] K. Martiyanov, V. Makhalov, and A. Turlapov, Observation of a two-dimensional Fermi gas of atoms, Phys. Rev. Lett. **105**, 030404 (2010).

[128] P. Dyke, E. D. Kuhnle, S. Whitlock, H. Hu, M. Mark, S. Hoinka, M. Lingham, P. Hannaford, and C. J. Vale, Crossover from 2D to 3D in a weakly interacting Fermi gas, Phys. Rev. Lett. **106**, 105304 (2011).

[129] T. Yefsah, R. Desbuquois, L. Chomaz, K. J. Günter, and J. Dalibard, Exploring the Thermodynamics of a Two-Dimensional Bose Gas, Phys. Rev. Lett. **107**, 130401 (2011).

[130] C.-L. Hung, X. Zhang, N. Gemelke, and C. Chin, Observation of scale invariance and universality in two-dimensional Bose gases, Nature **470**, 236 (2011).

[131] M. Feld, B. Fröhlich, E. Vogt, M. Koschorreck, and M. Köhl, Observation of a pairing pseudogap in a two-dimensional Fermi gas, Nature **480**, 75 (2011).

[132] A. T. Sommer, L. W. Cheuk, M. J. H. Ku, W. S. Bakr, and M. W. Zwierlein, Evolution of fermion pairing from three to two dimensions, Phys. Rev. Lett. **108**, 045302 (2012).

[133] M. Koschorreck, D. Pertot, E. Vogt, B. Fröhlich, M. Feld, and M. Köhl, Attractive and repulsive Fermi polarons in two dimen- sions, Nature **485**, 619 (2012).

[134] E. Vogt, M. Feld, B. Fröhlich, D. Pertot, M. Koschorreck, and M. Köhl, Scale invariance and viscosity of a two-dimensional Fermi gas, Phys. Rev. Lett. **108**, 070404 (2012).

[135] R. Desbuquois, L. Chomaz, T. Yefsah, J. Léonard, J. Beugnon, C. Weitenberg, and J. Dalibard, Superfluid behaviour of a two-dimensional Bose gas, Nature Physics **8**, 645 (2012).

[136] L.-C. Ha, C.-L. Hung, X. Zhang, U. Eismann, S.-K. Tung, and C. Chin, Strongly Interacting Two-Dimensional Bose Gases, Phys. Rev. Lett. **110**, 145302 (2013).

[137] M. G. Ries, A. N. Wenz, G. Zürn, L. Bayha, I. Boettcher, D. Kedar, P. A. Murthy, M. Neidig, T. Lompe, and S. Jochim, Observation of Pair Condensation in the Quasi-2D BEC-BCS Crossover, Phys. Rev. Lett. **114**, 230401 (2015).

[138] R. J. Fletcher, M. Robert-de-Saint-Vincent, J. Man, N. Navon, R. P. Smith, K. G. H. Viebahn, and Z. Hadzibabic, Connecting Berezinskii-Kosterlitz-Thouless and BEC Phase Transitions by Tuning Interactions in a Trapped Gas, Phys. Rev. Lett. **114**, 255302 (2015).

[139] P. A. Murthy, I. Boettcher, L. Bayha, M. Holzmann, D. Kedar, M. Neidig, M. G. Ries, A. N. Wenz, G. Zürn, and S. Jochim, Observation of the Berezinskii-Kosterlitz-Thouless phase transition in an ultracold Fermi gas, Phys. Rev. Lett. **115**, 010401 (2015).

[140] J. L. Ville, R. Saint-Jalm, É. Le Cerf, M. Aidelsburger, S. Nascimbène, J. Dalibard, and J. Beugnon, Sound Propagation in a Uniform Superfluid Two-Dimensional Bose Gas, Phys. Rev. Lett. **121**, 145301 (2018).

[141] M. Bohlen, L. Sobirey, N. Luick, H. Biss, T. Enss, T. Lompe, and H. Moritz, Sound Propagation and Quantum-Limited Damping in a Two-Dimensional Fermi Gas, Phys. Rev. Lett. **124**, 240403 (2020).

[142] L. Sobirey, N. Luick, M. Bohlen, H. Biss, H. Moritz, and T. Lompe, Observation of superfluidity in a strongly correlated two-dimensional Fermi gas, Science **372**, 844 (2021).

[143] P. Christodoulou, M. Gałka, N. Dogra, R. Lopes, J. Schmitt, and Z. Hadzibabic, Observation of first and second sound in a BKT superfluid, Nature **594**, 191-194 (2021).

[144] W. H. Nitsche, N. Y. Kim, G. Roumpos, C. Schneider, M. Kamp, S. Höfling, A. Forchel, and Y. Yamamoto, Algebraic order and the Berezinskii-Kosterlitz-Thouless transition in an exciton-polariton gas, Phys. Rev. B **90**, 205430 (2014).

[145] D. Caputo, D. Ballarini, G. Dagvadorj, C. Sánchez Muñoz, M. De Giorgi, L. Dominici, K. West, L. N. Pfeiffer, G. Gigli, F. P. Laussy, M. H. Szymańska, and D. Sanvitto, Topological order and thermal equilibrium in polariton condensates, Nat. Mater. **17**, 145 (2018).

[146] K. Epstein, A. M. Goldman, and A. M. Kadin, Vortex-Antivortex Pair Dissociation in Two-Dimensional Superconductors, Phys. Rev. Lett. **47**, 534 (1981).

[147] A. F. Hebard and A. T. Fiory, Critical-Exponent Measurements of a Two-Dimensional Superconductor, Phys. Rev. Lett. **50**, 1603 (1983).

[148] W. Zhao, Q. Wang, M. Liu, W. Zhang, Y. Wang, M. Chen, Y. Guo, K. He, X. Chen, Y. Wang, J. Wang, X. Xie, Q. Niu, L. Wang, X. Ma, J. K. Jain, M. H. W. Chan, and Q.-K. Xue, Evidence for Berezinskii-Kosterlitz-Thouless transition in atomically flat two-dimensional Pb superconducting films, Solid State Commun. **165**, 59 (2013).

[149] Z. Lin, C. Mei, L. Wei, Z. Sun, S. Wu, H. Huang, S. Zhang, C. Liu, Y. Feng, H. Tian, H. Yang, J. Li, Y. Wang, G. Zhang, Y. Lu, Y. Zhao, Quasi-two-dimensional superconductivity in $FeSe_{0.3}Te_{0.7}$ thin films and electric-field modulation of superconducting transition, Sci. Rep. **5**, 14133 (2015).

[150] I. M. Khalatnikov, *An Introduction to the Theory of Superfluidity* (Benjamin, New York, U.S., 1965).

[151] L. Verney, L. Pitaevskii, and S. Stringari, Hybridization of first and second sound in a weakly interacting Bose gas, EPL **111**, 40005 (2015).

[152] L. A. Sidorenkov, M. K. Tey, R. Grimm, Y.-H. Hou, L. Pitaevskii, and S. Stringari, Second sound and the superfluid fraction in a Fermi gas with resonant interactions, Nature **498**, 78-81 (2013).

[153] G. 't Hooft, M. Veltman, Regularization and renormalization of gauge fields, Nuclear Phys. B **44**, 189 (1972).

[154] L. Salasnich and F. Toigo, Zero-point energy of ultracold atoms, Phys. Rep. **640**, 1 (2016).

[155] T. D. Lee and C. N. Yang, Low-Temperature Behavior of a Dilute Bose System of Hard Spheres. II. Nonequilibrium Properties, Phys. Rev. **113**, 1406 (1959).

[156] A. Griffin and E. Zaremba, First and second sound in a uniform Bose gas, Phys. Rev. A **56**, 4839 (1997).

[157] E. Taylor, H. Hu, X.-J. Liu, L. P. Pitaevskii, A. Griffin, and S. Stringari, First and second sound in a strongly interacting Fermi gas, Phys. Rev. A **80**, 053601 (2009).

[158] H. Hu, E. Taylor, X.-J. Liu, S. Stringari, and A. Griffin, Second sound and the density response function in uniform superfluid atomic gases, New J. Phys. **12**, 043040 (2010).

[159] T. D. Lee, K. Huang and C. N. Yang, Eigenvalues and Eigenfunctions of a Bose System of Hard Spheres and Its Low-Temperature Properties, Phys. Rev. **106**, 1135 (1957).

[160] G. Bighin and L. Salasnich, Vortices and antivortices in two-dimensional ultracold Fermi gases, Sci. Rep. **7**, 45702 (2017).

[161] C. Mora and Y. Castin, Ground State Energy of the Two-Dimensional Weakly Interacting Bose Gas: First Correction Beyond Bogoliubov Theory, Phys. Rev. Lett. **102**, 180404 (2009).

[162] J. Dalibard, Fluides quantiques de basse dimension et transition de Kosterlitz-Thouless (Collège de France Lecture Notes) (2016).

[163] N. Prokof'ev, O. Ruebenacker, and B. Svistunov, Critical Point of a Weakly Interacting Two-Dimensional Bose Gas, Phys. Rev. Lett. **87**, 270402 (2001).

[164] N. Prokof'ev N and B. Svistunov, Two-dimensional weakly interacting Bose gas in the fluctuation region, Phys. Rev. A **66**, 043608 (2002).

[165] C.-L. Hung, X. Zhang, N. Gemelke, and C. Chin, Observation of scale invariance and universality in two-dimensional Bose gases, Nature **470**, 236 (2011).

[166] A. Rançon and N. Dupuis, Universal thermodynamics of a two-dimensional Bose gas, Phys. Rev. A **85**, 063607 (2012).

[167] T. Ozawa and S. Stringari, Discontinuities in the First and Second Sound Velocities at the Berezinskii-Kosterlitz-Thouless Transition, Phys. Rev. Lett. **112**, 025302 (2014).

[168] M. Ota and S. Stringari, Second sound in a two-dimensional Bose gas: From the weakly to the strongly interacting regime, Phys. Rev. A **97**, 033604 (2018).

[169] G. De Rosi, G. E. Astrakharchik, and S. Stringari, Thermodynamic behavior of a one-dimensional Bose gas at low temperature, Phys. Rev. A **96**, 013613 (2017).

[170] A. Cappellaro and L. Salasnich, Finite-range corrections to the thermodynamics of the one-dimensional Bose gas, Phys. Rev. A **96**, 063610 (2017).

[171] M. R. Andrews, D. M. Kurn, H.-J. Miesner, D. S. Durfee, C. G. Townsend, S. Inouye, and W. Ketterle, Propagation of Sound in a Bose-Einstein Condensate, Phys. Rev. Lett. **79**, 553 (1997).

[172] R. Meppelink, S. B. Koller, and P. van der Straten, Sound propagation in a Bose-Einstein condensate at finite temperatures, Phys. Rev. A **80**, 043605 (2009).

[173] A. L. Gaunt, T. F. Schmidutz, I. Gotlibovych, R. P. Smith, and Z. Hadzibabic, Bose-Einstein Condensation of Atoms in a Uniform Potential, Phys. Rev. Lett. **110**, 200406 (2013).

[174] T. A. Hilker, L. H. Dogra, C. Eigen, J. A. P. Glidden, R. P. Smith, and Z. Hadzibabic, First and Second Sound in a Compressible 3D Bose Fluid, Phys. Rev. Lett. **128**, 223601 (2022).

[175] M. R. Matthews, B. P. Anderson, P. C. Haljan, D. S. Hall, M. J. Holland, J. E. Williams, C. E. Wieman, and E. A. Cornell, Watching a Superfluid Untwist Itself: Recurrence of Rabi Oscillations in a Bose-Einstein Condensate, Phys. Rev. Lett. **83**, 3358 (1999).

[176] J. Williams, R. Walser, J. Cooper, E. A. Cornell, and M. Holland, Excitation of a dipole topological state in a strongly coupled two-component Bose-Einstein condensate, Phys. Rev. A **61**, 033612 (2000).

[177] T. Zibold, E. Nicklas, C. Gross, and M. K. Oberthaler, Classical Bifurcation at the Transition from Rabi to Josephson Dynamics, Phys. Rev. Lett. **105**, 204101 (2010).

[178] E. Nicklas, H. Strobel, T. Zibold, C. Gross, B. A. Malomed, P. G. Kevrekidis, and M. K. Oberthaler, Rabi Flopping Induces Spatial Demixing Dynamics, Phys. Rev. Lett. **107**, 193001 (2011).

[179] S. De, D. L. Campbell, R. M. Price, A. Putra, Brandon M. Anderson, and I. B. Spielman, Quenched binary Bose-Einstein condensates: Spin-domain formation and coarsening, Phys. Rev. A **89**, 033631 (2014).

[180] E. Nicklas, M. Karl, M. Höfer, A. Johnson, W. Muessel, H. Strobel, J. Tomkovič, T. Gasenzer, and M. K. Oberthaler, Observation of Scaling in the Dynamics of a Strongly Quenched Quantum Gas, Phys. Rev. Lett. **115**, 245301 (2015).

[181] M. W. Zwierlein, Z. Hadzibabic, S. Gupta, and W. Ketterle, Spectroscopic Insensitivity to Cold Collisions in a Two-State Mixture of Fermions, Phys. Rev. Lett. **91**, 250404 (2003).

[182] C. P. Search and P. R. Berman, Manipulating the speed of sound in a two-component Bose-Einstein condensate, Phys. Rev. A **63**, 043612 (2001).

[183] M. Abad and A. Recati, A study of coherently coupled two-component Bose-Einstein condensates, Eur. Phys. J. D **67**, 148 (2013).

[184] D. T. Son and M. A. Stephanov, Domain walls of relative phase in two-component Bose-Einstein condensates, Phys. Rev. A. **65**, 063621 (2002).

[185] T. Giamarchi, *Quantum Physics in One Dimension*, International Series of Monographs on Physics (Oxford University Press, Oxford, U.K., 2003).

[186] A. Altland and B. Simons, *Condensed Matter Field Theory* (Cambridge University Press, Cambridge, U.K., 2010).

[187] P. Minnhagen and M. Nylén, Charge density of a vortex in the Coulomb-gas analogy of superconducting films, Phys. Rev. B **9**, 5768 (1985).

[188] U. Al Khawaja, J. O. Andersen, N. P. Proukakis, and H. T. C. Stoof, Low dimensional Bose gases, Phys. Rev. A **66**, 013615 (2002).

[189] W. Zhang, G.-D. Lin, and L.-M. Duan, Berezinskii-Kosterlitz-Thouless transition in a trapped quasi-two-dimensional Fermi gas near a Feshbach resonance, Phys. Rev. A **78**, 043617 (2008).

[190] I. Maccari, N. Defenu, L. Benfatto, C. Castellani, and T. Enss, Interplay of spin waves and vortices in the two-dimensional XY model at small vortex-core energy, Phys. Rev. B **102**, 104505 (2020).

[191] M. Kobayashi, G. Fejős, C. Chatterjee, and M. Nitta, Vortex confinement transitions in the modified Goldstone model, Phys. Rev. Research **2**, 013081 (2020).

[192] M. Ota and S. Stringari, Second sound in a two-dimensional Bose gas: From the weakly to the strongly interacting regime, Phys. Rev. A **97**, 033604 (2018).

[193] H. Hu, E. Taylor, X.-J. Liu, S. Stringari, and A. Griffin, Second sound and the density response function in uniform superfluid atomic gases, New J. Phys. **12**, 043040 (2010).

[194] R. Meppelink, S. B. Koller, and P. van der Straten, Sound propagation in a Bose-Einstein condensate at finite temperatures, Phys. Rev. A **80**, 043605 (2009).

[195] A. Tononi, A. Cappellaro, G. Bighin, and L. Salasnich, Propagation of first and second sound in a two-dimensional Fermi superfluid, Phys. Rev. A **103**, L061303 (2021).

[196] J. H. Kim, D. Hong, and Y. Shin, Observation of two sound modes in a binary superfluid gas, Phys. Rev. A **101**, 061601(R) (2020).

[197] B. D. Josephson, Possible new effects in superconductive tunnelling, Phys. Lett. **1**, 251-3 (1962).

[198] B. D. Josephson, Coupled Superconductors, Rev. Mod. Phys. **36**, 216 (1964).

[199] A. Barone, and G. Paternò, *Physics and Applications of the Josephson Effect* (Wiley, New York, 1982).

[200] J.-P. Brantut, J. Meineke, D. Stadler, S. Krinner, and T. Esslinger, Conduction of Ultracold Fermions Through a Mesoscopic Channel, Science **337**, 1069-71 (2012).

[201] D. Stadler, S. Krinner, J. Meineke, J.-P. Brantut, and T. Esslinger, Observing the drop of resistance in the flow of a superfluid Fermi gas, Nature **491**, 736-9 (2012).

[202] J.-P. Brantut, C. Greiner, J. Meineke, D. Stadler, S. Krinner, C. Kollath, T. Esslinger, and A. Georges, A Thermoelectric Heat Engine with Ultracold Atoms, Science **342**, 713-5 (2013).

[203] S. Krinner, D. Stadler. D. Husmann, J.-P. Brantut, and T. Esslinger, Observation of quantized conductance in neutral matter, Nature **517**, 64-7 (2015).

[204] S. Krinner, D. Stadler, J. Meineke, J.-P. Brantut, and T. Esslinger, Observation of a Fragmented, Strongly Interacting Fermi Gas, Phys. Rev. Lett. **115**, 045302 (2015).

[205] D. Husmann, S. Uchino, S. Krinner, M. Lebrat, T. Giamarchi, T. Esslinger, and J.-P. Brantut, Connecting strongly correlated superfluids by a quantum point contact, Science **350**, 1498-501 (2015).

[206] S. Krinner, M. Lebrat, D. Husmann, C. Greiner, J.-P. Brantut, and T. Esslinger, Mapping out spin and particle conductances in a quantum point contact, Proc. Natl. Acad. Sci. **113**, 8144-9 (2016).

[207] M. Lebrat, P. Grišins, D. Husmann, S. Häusler, L. Corman, T. Giamarchi, J.-P. Brantut, and T. Esslinger, Band and Correlated Insulators of Cold Fermions in a Mesoscopic Lattice, Phys. Rev. X **8**, 011053 (2018).

[208] D. Husmann, M. Lebrat, S. Häusler, J.-P. Brantut, L. Corman, and T. Esslinger, Breakdown of the Wiedemann-Franz law in a unitary Fermi gas, Proc. Natl. Acad. Sci. **115**, 8563-8 (2018).

[209] G. Salerno, H. M. Price, M. Lebrat, S. Häusler, T. Esslinger, L. Corman, J.-P. Brantut, and N. Goldman, Quantized Hall Conductance of a Single Atomic Wire: A Proposal Based on Synthetic Dimensions, Phys. Rev. X **9**, 041001 (2019).

[210] S. Krinner, T. Esslinger, and J.-P. Brantut, Two-terminal transport measurements with cold atoms, J. Phys.: Condens. Matter **29**, 343003 (2017).

[211] G. Valtolina, A. Burchianti, A. Amico, E. Neri, K. Xhani, J. A. Seman, A. Trombettoni, A. Smerzi, M. Zaccanti, M. Inguscio, and G. Roati, Josephson effect in fermionic superfluids across the BEC-BCS crossover, Science **350**, 1505-8 (2015).

[212] M. Kanàsz-Nagy, L. Glazman, T. Esslinger, and E. A. Demler, Anomalous Conductances in an Ultracold Quantum Wire, Phys. Rev. Lett. **117**, 255302 (2016).

[213] A. O. Caldeira and A. J. Leggett, Quantum tunnelling in a dissipative system, Ann. Phys. (N.Y.) **149**, 374 (1983).

[214] H. B. Callen and T. A. Welton, Irreversibility and Generalized Noise, Phys. Rev. **83**, 34 (1951).

[215] H. Metiu and G. Schön, Description of Quantum Noise by a Langevin Equation, Phys. Rev. Lett. **53**, 13 (1984).

[216] G. W. Ford, J. T. Lewis, and R. F. O'Connell, Quantum Langevin equation, Phys. Rev. A **37**, 4419 (1988).

[217] P. Hänggi and G. Ingold, Fundamental aspects of quantum Brownian motion, Chaos **15**, 026105 (2005).

[218] S. Diehl, Noise gets marginal, Nat. Phys. **6**, 721 (2010).

[219] H. Grabert, U, Weiss, and P. Talkner, Quantum theory of the damped harmonic oscillator, Z. Phys. B **55**, 87 (1984).

[220] R. Yagi, S.-i. Kobayashi, and Y. Ootuka, Phase Diagram for Superconductor-Insulator Transition in Single Small Josephson Junctions with Shunt Resistor, J. Phys. Soc. Jpn. **66**, 3722 (1997).

[221] G.-L. Ingold and H. Grabert, Effect of Zero Point Phase Fluctuations on Josephson Tunneling, Phys. Rev. Lett. **83**, 3721 (1999).

[222] N. Kimura and T. Kato, Temperature dependence of zero-bias resistances of a single resistance-shunted Josephson junction, Phys. Rev. B **69**, 012504 (2004).

[223] A. Blais, A. L. Grimsmo, S. M. Girvin, and A. Wallraff, Circuit quantum electrodynamics, Rev. Mod. Phys. **93**, 025005 (2021).

[224] M. Houzet and L. I. Glazman, Critical Fluorescence of a Transmon at the Schmid Transition, Phys. Rev. Lett. **125**, 267701 (2020).

[225] S. L. Lukyanov and P. Werner, Resistively shunted Josephson junctions: quantum field theory predictions versus Monte Carlo results, J. Stat. Mech. P06002 (2007).

[226] J. A. Blackburn, M. Cirillo, and N. G.-Jensen, A survey of classical and quantum interpretations of experiments on Josephson junctions at very low temperatures, Phys. Rep. **611**, 1-33 (2016).

[227] E. D. Torre, E. Demler, T. Giamarchi, and E. Altman, Quantum critical states and phase transitions in the presence of non-equilibrium noise, Nat. Phys. **6**, 806 (2010).

[228] R. H. Koch, D. J. Van Harlingen, and J. Clarke, Measurements of quantum noise in resistively shunted Josephson junctions, Phys. Rev. B **26**, 74 (1982).

[229] F. T. Brandt, J. Frenkel, and J. C. Taylor, Noise in resistively shunted Josephson junctions, Phys. Rev. B **82**, 014515 (2010).

[230] R. H. Koch, D. J. Van Harlingen, and J. Clarke, Quantum-Noise Theory for the Resistively Shunted Josephson Junction, Phys. Rev. Lett. **45**, 2132 (1980).

[231] V. Ambegaokar and A. Baratoff, Tunneling Between Superconductors, Phys. Rev. Lett. **10**, 486 (1963).

[232] J. A. Sauls, Andreev bound states and their signatures, Phil. Trans. R. Soc. A **376** (2018).

[233] M. H. Devoret, J. M. Martinis, and J. Clarke, Measurements of Macroscopic Quantum Tunneling out of the Zero-Voltage State of a Current-Biased Josephson Junction, Phys. Rev. Lett. **55**, 1908 (1985).

[234] G. W. Ford, J. T. Lewis, and R. F. O'Connell, Dissipative Quantum Tunneling: Quantum Langevin Equation Approach, Phys. Lett. A **128**, 29 (1988).

[235] A. Schmid, Diffusion and Localization in a Dissipative Quantum System, Phys. Rev. Lett. **51**, 1506 (1983).

[236] S. A. Bulgadaev, Phase diagram of a dissipative quantum system, JETP Lett. **39**, 315 (1984).

[237] A. Murani, N. Bourlet, H. le Sueur, F. Portier, C. Altimiras, D. Esteve, H. Grabert, J. Stockburger, J. Ankerhold, and P. Joyez, Absence of a Dissipative Quantum Phase Transition in Josephson Junctions, Phys. Rev. X **10**, 021003 (2020).

[238] K. Masuki, H. Sudo, M. Oshikawa, and Y. Ashida, Absence versus Presence of Dissipative Quantum Phase Transition in Josephson Junctions, Phys. Rev. Lett. **129**, 087001 (2022).

[239] Y. Levinson, Quantum noise in a current-biased Josephson junction, Phys. Rev. B **67**, 184504 (2003).

[240] F. Bastianelli and P. van Nieuwenhuizen, Path Integrals and Anomalies in Curved Space (Cambridge University Press, Cambridge, U.K., 2006).

[241] N. Nagaosa, *Quantum Field Theory in Condensed Matter Physics* (Springer, Berlin, 2013).

[242] G. Jona-Lasinio, Relativistic field theories with symmetry-breaking solutions, Nuovo Cimento **34**, 1790 (1964).

[243] S. Coleman and E. Weinberg, Radiative Corrections as the Origin of Spontaneous Symmetry Breaking, Phys. Rev. D. **7**, 1888 (1973).

[244] F. Cametti, G. Jona-Lasinio, C. Presilla, and F. Toninelli, Comparison between quantum and classical dynamics in the effective action formalism, in New Directions in Quantum Chaos, Proceedings of International School of Physics "Enrico Fermi", Course CXLIII, Varenna, 1999, edited by G. Casati, I. Guarnieri, and U. Smilansky (IOS Press, Amsterdam, 2000), pp. 431-448.

[245] H. T. C. Stoof, K. B. Gubbels, and D. B. M. Dickerscheid, *Ultracold Quantum Fluids*, (Springer, New York, 2009).

[246] V. N. Popov, *Functional Integrals in Quantum Field Theory and Statistical Physics* (Reidel, Dordrecht, the Netherlands, 1983).

[247] *The SQUID Handbook: Applications of SQUIDs and SQUID Systems*, edited by J. Clarke and A. I. Braginski (John Wiley & Sons, New York, 2006).

[248] A. Smerzi, S. Fantoni, S. Giovanazzi, and S. R. Shenoy, Quantum Coherent Atomic Tunneling between Two Trapped Bose-Einstein Condensates, Phys. Rev. Lett. **79**, 4950 (1997).

[249] L. Salasnich, A. A. Shanenko, A. Vagov, J. Albino Aguiar, and A. Perali, Screening of pair fluctuations in superconductors with coupled shallow and deep bands: A route to higher-temperature superconductivity, Phys. Rev. B **100**, 064510 (2019).